DUCTILE FRACTURE OF MAGNESIUM ALLOYS: CHARACTERIZATION AND MODELING

A Dissertation

by

BABAK KONDORI

Submitted to the Office of Graduate and Professional Studies of
Texas A&M University
in partial fulfillment of the requirements for the degree of

DOCTOR OF PHILOSOPHY

Chair of Committee,	A.A. Benzerga
Committee Members,	D.C. Lagoudas
	I. Karaman
	R. Arroyave
Head of Department,	I. Karaman

May 2015

Major Subject: Materials Science and Engineering

ABSTRACT

Magnesium alloys are prime potential candidates for lightweight structural applications because of their superior specific stiffness and strength. However, their effective insertion in transportation vehicles hinges on improving their ductility and developing cost-effective forming technologies. Here, the processes of damage initiation and accumulation to fracture are investigated at ambient temperature, experimentally and theoretically, in two Mg alloys, AZ31 and WE43. Material AZ31 exhibits strong basal texture whereas WE43 has a weak non-basal texture with quasi-isotropic properties. The microstructural characterization is carried out on the initial materials aiming at determining the texture, the grain size/shape distribution as well as the chemical composition, volume fraction, shape and spatial arrangement of second-phase particles. The macroscopic plastic flow anisotropy is characterized using round tensile bars and compression pins along three principal and three off-axes orientations. Semi-continuous measurement of diameter contraction in two orthogonal directions enabled the monitoring of relative volume change and strain-ratio evolution. The data is used to model the plastic anisotropy of the materials using models from the literature. A significant increase in volume is measured during plastic deformation. Macroscopic fracture loci, along two principal and one off-axis directions, are obtained for each material using round notched bars of varying notch acuity so as to study the effect of stress triaxiality and directionality on flow and fracture. It was found that notched AZ31 bars exhibit higher failure strain than uniaxial specimens. Second phase particles and deformation twins are identified as critical sites for damage initiation. Experiments also indicate that WE43 and AZ31 display significantly different sensitivities to stress triaxiality. Substantial drop in the failure

strains of WE43 with increasing triaxiality is attributed to intergranular fracture. Image analysis is performed on specimens deformed to incipient and complete fracture to infer the distribution properties of voids and particles. A micromechanics-based continuum damage model is used to rationalize the main experimental trends and explore conflicting hypotheses. The model has two components: (i) a shape-dependent void growth; and (ii) a shape-dependent void/crack coalescence part. The results provide the groundwork for understanding the effects of microstructural and loading variables on damage and fracture in magnesium alloys.

DEDICATION

To Sara

ACKNOWLEDGEMENTS

I would like to thank my advisor Dr. Amine Benzerga for his constant encouragement, guidance and financial support without which this project would not have been done. I would like to thank him for encouraging my research and allowing me to grow as a research scientist. His guidance on research as well as my career has been priceless. I would also like to thank my committee members, Drs. Dimitris Lagoudas, Ibrahim Karaman and Raymundo Arryave for serving as my committee members. I am grateful to Drs. Alan Needleman and Mohammad Naraghi for attending my defense and their brilliant comments and suggestions. I am grateful to Rodney Inmon, Miriam Brown in the Aerospace Department and Jan Gerston in the Materials Science and Engineering Department, at Texas A&M University. All of you have been there to support me when I required help.

I would like to thank my wife, Sara, for the love, kindness and support she has given me during the past seven years. Words cannot express how grateful I am to her for all of the sacrifices that she has made. Furthermore I would also like to thank my parents and sisters for their endless love and support. Besides my family, I had a group of friends who supported me during this program and encouraged me to strive towards my goals. I would also like express appreciation to Drs. Shyam M. Keralavarma, Ebubekir Dogan and Majid Tabesh, who were very helpful to me during my PhD program.

Progress in research is not possible without scientific collaboration. I would like to thank Dr. Morgeneyer for the tomography analysis. Finally, I would like to thank the Qatar Foundation for the financial support of this project and Magnesium Elektron North America Inc. for the free material coupons.

TABLE OF CONTENTS

Page

LIST OF FIGURES

LIST OF TABLES

TABLE Page

NOMENCLATURE

Nomenclature

$\Psi^{KB}(\sigma; f, W, e_3, h)$	Yield function of material with voids before mico-scale localization
$\Psi^{BL}(\sigma; \chi, W, e_3)$	yield function of the material with voids after microscale localization $\equiv$ Coalescence yield function
$\bar{\sigma}$	flow stress of the matrix
f	void volume fraction
W	void aspect ratio
e_3	direction of the applied load which coincides with the void axis
$\mathbb{h}$	Anisotropy tensor in the space of deviatoric stresses
χ	ligament ratio
λ	cell aspect ratio (not idependent of f, χ, W)
ε_f	strain to failure (at onset of localization at material point level)
T	stress triaxiality ratio

1. INTRODUCTION

1.1 Motivation

Magnesium (Mg) has the lowest density of all structural metals (1.74 g/cm^3). Mg alloys are endowed with superior specific stiffness and strength, which make them ideal material candidates for lightweight structural applications, notably in the transportation industries [1]. In spite of notable potential properties, there are shortcomings that prevent large-scale applications of Mg alloys in the abovementioned industries. Among the drawbacks of Mg alloys, one could mention their reduced mechanical properties at high temperatures (higher than 200°C) that prevent their use as parts such as engine blocks and transmission cases in car industries. Another challenge facing their implementation as wrought products in load-bearing components is their relatively low ductility and catastrophic failure after limited necking, which limits their formability at room temperature.

Over the past decade, much experimental and modeling effort has been devoted to tailoring the properties of Mg alloys to meet the needs of industry. This includes understanding the plastic flow and strengthening of Mg alloys [2–8], their tension-compression asymmetry, plastic flow anisotropy and propensity for twinning under favorable loading conditions [9–11]. These studies have provided in-depth understanding about the active deformation mechanisms in Mg alloys when loaded uniaxially along different directions or during processing routes such as rolling and Equal Angle Angular Extrusion (ECAE).

Despite these studies, little research has been devoted to damage and fracture of Mg alloys [12–14]. Although microstructural manipulations through alloying, grain refinement or texture design [15–17] hold the promise of developing strong

and damage-resistant alloys, in-depth incorporation of damage and fracture properties in alloy design methods is still lacking. In many cases, only the effects of carefully designed texture or precipitates on the activation of various deformation mechanisms are studied whereas their role in fracture, especially under complex loading schemes, is left unexplored. In spite of several valuable studies on the deformation and fracture of Mg alloys, and recently their rare earth (RE) containing family, there are areas in which current understanding is limited and further research is necessary.

Firstly, studies on fracture of Mg alloys are almost entirely limited to uniaxial loading. While a broad range of information could be extracted from these studies, the effect of loading variables and hydro-static stresses on the deformation mechanisms in Mg alloys are left largely unexplored. It is known that motion of edge dislocations is not significantly affected by hydro-static stresses. On the other hand, the effect of loading conditions on the deformation twinning and motion of screw dislocations is not fully understood. How these known deformation mechanisms in magnesium are affected by changes in loading conditions is still unclear.

Without systematic understanding of these effects, common assumptions in analytical and computational studies could also be questioned. For example, recent work by Kondori and Benzerga [18] showed that, unlike most material systems, there is a significant increase in volume during both uniaxial tension and compression of AZ31. Note that 'constant volume' is usually assumed in crystal plasticity models, even in those applied to Mg alloys [19]. Davidson et al. [20] studied the effect of hydrostatic pressure on fracture of hot-extruded pure magnesium. It was observed that ductility is initially increased linearly with pressure, a behavior attributed to prevention of either intergranular fracture or void nucleation and growth. Following this linear region, ductility increased drastically over a narrow pressure range while fracture was controlled by shear bands. It was argued that pressure prohibits frac-

ture mechanisms, which depend upon normal tensile stresses. Using a thick Al rim surrounding Mg compression pins, Sankaran et al. [21] achieved strain of order of 2 in Mg. The high value of attained strain was attributed to the effect of compressive hydro-static pressure and the support provided by thick Al rim. It was argued that Al rim restrains the bifurcation of the flow into a single shear band although no rationale was presented to support this idea.

Recently, the effect of stress-state triaxiality, T, on fracture of hot-rolled AZ31 alloy was also studied [18,22]. It was shown that failure strain (crack initiation and final fracture) increases as the triaxiality is increased from uniaxial to triaxial loading. This trend contrasts with what is observed in most material systems. The increased failure strain in notched bar specimens compared to uniaxial bars was attributed to (i) transition from slanted fracture driven by shear localization during uniaxial loading to flat fracture in notched samples; (ii) transition from twin-controlled fracture in uniaxial bars to void coalescence-dominated fracture in notched specimens; and (iii) the effect of plastic anisotropy and activation of new deformation systems (probably extension twinning) under traixial loading. These findings illustrate the significant effects of loading condition on formability and ductility of Mg alloys. It is not clear how the loading condition affects the fracture behavior of WE series alloys. Other question is whether mere texture weakening and reduced anisotropy leads to more ductile alloys in all loading conditions.

Another area in which further research is required is damage evolution (after initiation and before failure). In many cases, the study of fracture in Mg alloys is focused on the identification of damage initiation mechanisms such as deformation twins [12,23] or second phase particles [24]. While damage initiation is an important stage of the fracture process, it is usually the growth of these defects and their interactions with each other that define ductility. Limited research has been dedicated to

experimental study of voids and microcracks after initiation or the effect of a macroscopic main cracks on the deformation system in their immediate vicinity [25–28]. In the case of RE containing alloys, fracture mechanism (including damage initiation, growth and their interactions), even under uniaxial loading, are still unknown.

The third unexplored area in the fracture of Mg alloys, is shear localization effects. Structural instabilities could occur in alloys with strong anisotropy [29]. Most fracture studies of magnesium alloys in the literature cover those case in which failure happens via shear localization [12, 20]. In this condition, structural instability instead of intrinsic behavior of the material is the cause of fracture. Moreover, damage zone during shear localization is limited to a very narrow region that makes the study of damage mechanisms extremely difficult, if not impossible. Since shear localization is closely connected to plastic flow properties of the matrix, it is necessary to fully characterize macroscopic plastic anisotropy (especially for RE-containing alloys which very limited information is available in the literature). In addition, void/microcrack growth is a signature of plastic deformation of the matrix. Thus, plastic anisotropy characterization in these alloys is of utmost importance.

Finally, it should be mentioned that alloying and processing affect the anisotropic flow properties of polycrystalline Mg. Primary processing, such as extrusion or rolling, generally leads to a strong basal texture. This is the case in pure magnesium and many Mg alloys such as AZ31 and ZK60. Alloying affects the strength, texture and possibly the propensity for twinning, but also leads to the formation of second-phase particles, some of which can play a role in the ductile fracture process [13, 24, 30]. Knowledge of how texture, twinning and second-phase particles affect the damage process across a wide range of stress states is still lacking.

These shortcomings are present while, over the past fifty years, the ductile fracture community has developed various models, tool, methods and even standards

that have been employed successfully in many industries such as nuclear, oil and gas and aerospace. Using the knowledge from this community, this study addresses these shortcomings as the first step towards a complete characterization of damage initiation and progression mechanisms in Mg alloys under multiaxial stress states. More specifically, the current study evaluates the fracture properties of two magnesium alloys (i.e., AZ31 and WE43) using carefully designed experiments at a range of triaxialities. AZ31 is selected for this study because it is the most commonly used Mg alloy in the industry and its production cost is rather low compared to other Mg alloys. Most of the studies on wrought Mg alloys in the literature are also done on this alloy. Thus, there is a vast collection of data available on the properties of this alloy. WE43, which has been recently developed, offers superior room- and high temperature mechanical properties compared to other Mg alloys. High yield strength, allegedly isotropic plastic response and acceptable uniaxial strain to fracture are among the properties that makes this alloy one of the most promising Mg alloys for Aerospace industries [31]. One drawback of this alloys is its high production cost due to the presence of Y, RE elements and Zr in its composition. However, this alloys could be used in aerospace industries where performance and safety outpoint cost. Study of these two alloys offers information on the most technologically relevant (AZ31) and the most advanced Mg alloy (WE43) up to this date.

Employing sophisticated micromechanical-based constitutive frameworks, it is attempted to identify the microscopic fracture mechanisms active in Mg alloys and their effect on macroscopic response. Here, the attention is focused on the evolution of damage after initiation and the interaction between voids. In addition, in attempt to evaluate plastic anisotropy, interrupted uniaxial tension and compression experiments are performed on the studied Mg alloys. The results of these experiments provide a database for plastic anisotropy characterization. The completeness

of data is such that it could be used to calibrate and test predictive capabilities of any model in the literature addressing flow in anisotropic matrices. To circumvent the difficulties associated with shear failure during deformation of Mg alloys, round and cylindrical specimens were employed since axisymmetric deformation states decrease the propensity for shear localization [29].

1.2 Significance of the research

Understanding the mechanisms of damage and fracture in Mg alloys could potentially lead to improved alloy design methods and processing routes. This study is focused on the ductile fracture of magnesium alloys at room temperature with attention to the effects that loading parameters and microstructural variables have on overall behavior. Up to this point, the literature has remained elusive about the effect of known deformation mechanisms and microstructural features on damage tolerance and fracture properties of magnesium. This study is the first systematic study on the damage and fracture in Mg alloys. The knowledge acquired from this work could be employed as a road map for development of new, damage- tolerant and ductile magnesium alloys by improving the design of new manufacturing routs that render materials with textures beneficial to ductility properties. The present study on the damage and fracture properties across a wide range of stress states along different directions enables the identification of (i) various damage mechanisms in Mg alloy; (ii) the effect of processing texture; and (iii) the influence of directionality in microstructure on failure properties and its mechanisms.

Although great information on the behavior of material could be extracted from uniaxial experiments, the behavior at complex stress states should be studied as well. The loading condition that material encounters at service is often complex and far from uniaxial. The current study appreciates these variations and investigates

the behavior of Mg alloys at various triaxialities. The data on plastic anisotropy of Mg alloys in the literature could also be affected by the fact that in most studies, e.g., [12, 14], rectangular-prismatic tensile specimens are typically used, which are known to favor shear-like fracture, even in materials that are more ductile and less anisotropic than Mg. Under such circumstances, the material adjacent to the slanted fracture surface does not display much damage by cavitation or otherwise. In other words, shear failure obscures the intrinsic damage mechanisms as it becomes increasingly difficult to decouple the fracture behavior from plastic instability. One of the advantages of this study is the attempt to circumvent the difficulties associated with shear failure by use cylindrical specimens, since axisymmetric deformation states decrease the propensity for shear localization [29]; another way is avoid sear localization to introduce a notch so as to induce a damage process zone in the specimen. This methos is also explored in this research.

The results of the current study have far reaching applications. The alloys used in this study could be considered as model materials for Hexagonal Close-Packed (HCP) crystal structure. Thus, results of this project are applicable to other HCP materials. Knowledge developed from this study could also be used in the general framework of anisotopic material, in which anisotropy in both microscale (in the unit cell level) and macroscale (originating from macroscopic texture) are present. In addition, extensive microstructural investigations were also done on initial material, fractured specimens and specimens stopped after macroscopic crack initiation using both traditional metallography and 3D X-ray tomography (see Section 7 and 6). The results of such studies showed that voids at failure exhibit much less longitudinal growth compared to other material systems. This put Mg alloys in the class of materials failing after limited void growth. Some technologically important alloys such as high strength Al alloys and steels are also put in this class. Thus, information

from this study could be extended to those materials as well.

Presently, there are various phenomenological and crystal plasticity-based methods for modeling plastic flow anisotropy. However, there is limited data available for testing and validating such sophisticated approaches. (This is especially true for materials with tension compression asymmetry.) Usually, there are several materials parameters in the models that should be calibrated using existing experimental results. Large numbers of these parameters on the one hand and lack of experimental under different loading conditions from other leads to exhaustion of existing data. The situation is such that there are very limited options available to test models. Models, in such conditions, are often tested against the data acquired under very similar loading conditions. In some cases lack of discriminating experiments forces the researchers to test the models against the same data employed for model calibration. This work presents the result of a series of experiments in tension and compression along various directions of two processed magnesium alloys where flow properties and strain ratios are reported. Such set of data could be used as an acid test for the existing models in the literature and help improve them by identifying their shortcomings. In addition, two commonly used models for anisotropy, i.e. Hill 1948 and Cazacu-Pluncket-Barlat (CPB), are evaluated against the data. Finally, it should be noted that there are some studies that use methodology very close the current one to characterize plastic anisotropy in AZ31 [32].

Unfortunately, a closer look shows that these studies are done only in either tension or compression, never both. Some inconsistencies are also found in their data. Considering the activity of polar deformation mechanisms such as deformation twinning and significant tension compression asymmetry in Mg alloy, it seems necessary for such experiments to be done in both tension and compression. These shortcomings require a systematic study to fully characterize plastic anisotropy in Mg alloys and extract their material parameters.

1.3 Goal

Any attempt to improve mechanical properties and room temperature formability of Mg alloys requires fundamental understanding of their damage and failure. Current understanding is limited to uniaxial loading and does not fully recognize the mechanistic aspects of shear failure. This research aims at the characterization and modeling of plastic anisotropy and stress triaxiality effects on damage and fracture in Mg alloys. Some of the practical implications of meeting this goal may include a better understanding of the role of plastic anisotropy in fracture, engineering this anisotropy (through texture optimization or other microstructural manipulations) and identifying stress states for which damage tolerance is enhanced in processing operations and load-bearing applications.

1.4 Objectives

With the overall goal in mind, the followings are identified as objectives of this study.

1. Characterize the mechanical behavior of both AZ31 and WE43 alloy, with particular attention to 3D plastic flow anisotropy.

2. Investigate the effects of stress state triaxiality on the fracture of both alloys.

3. Examine the mechanisms of damage initiation and accumulation using fractography, quantitative metallography and high-resolution tomography.

4. Implement 3D constitutive relations for coupled plasticity and damage that account for anisotropy as well as the nucleation, growth and coalescence of voids and microcracks.

5. Study various scenarios for predicting the nominal fracture loci for both alloys, guided by systematic parameter sensitivity analyses.

2. BACKGROUND

2.1 Magnesium and its alloys: Fundamentals

2.1.1 Magnesium and its alloys: History

Magnesium is the lightest structural material with low density of $\rho = 1.74$ g/cm^3. Sir Humphrey Davy at 1808 was the first to isolate Mg element using electrolysis [33]. Provided it is alloyed with proper elements, magnesium can exhibit superior specific stiffness and strength that makes it ideal material choice for lightweight structural applications, notably in the transportation industries [1]. By application of Mg in car industries pistons in 1921, their production started to increase in coming years before world war II. Volkswagen Beetle (1938) and B36 United States bombers (1950s) are among other structural applications of Mg alloys.

The use of Mg alloys after World War II, however, was dropped significantly due to its high production cost and low corrosion resistance. Finding ways to reduce their production cost (via low cost die-casting) and increase their corrosion resistance (by adding Mn element), has lead to significant increase in production of Mg and its alloys in recent years [34, 35]. Figure 1 shows the substantial increase in the production of die-cast magnesium components in Europe in a recent seventeen-year period. The same trend is also observed in U.S. and other developed countries.

2.1.2 Magnesium: Crystal structure

Crystalline structure of Magnesium is Hegxagonal Closed Packed (H.C.P) with $c/a = 1.624$, which is very close to an idea H.C.P structure where $c/a = 1.633$ [36]. Although Mg exhibits elastically isotropic behavior [37], there is a significant plastic anisotropy in its yield and flow stress as well as strain ratios. In Mg's H.C.P structure,

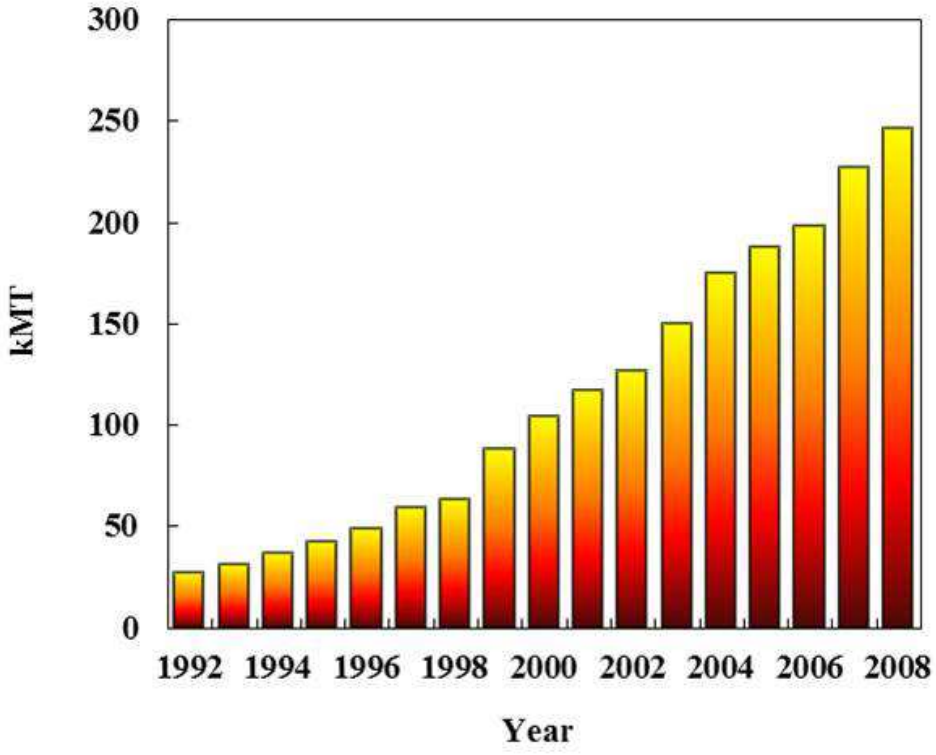

Figure 1: Increase in pressure die-cast components in Europe from 1991 to 1997 [34].

the basal planes (planes at the base of hexagon) have highest atomic compactness. The direction of maximum atomic compactness in this material is ¡a¿≡ $\langle 11\bar{2}0 \rangle$. Other planes and directions have considerably lower atomic compactness. Since atomic compactness affect the motion of dislocations and other agents of deformation (such as deformation twins) substantially, the difference in compactness properties along various directions gives rise to a significant anisotropy in plastic response of Mg in the scale of single crystals. In poly-crystalline materials with randomly oriented grains, this grain-scale anisotropy is not relevant. However, deformation of Mg poly-crystals (e.g., processing and forming) will rearrange the grains to a preferred orientation.

This is called processing/deformation induced texture. If the texture is strong, as in the case of most wrought Mg alloys, poly-crystal exhibit anisotropic properties similar to that of a single-crystal. In the literature, the strong texture and its associated anisotropy are held responsible for the limited formability/ductility of wrought Mg alloys [38, 39].

2.1.3 Alloying effect

Aluminum (Al): Aluminum, as the most favorable alloying element for magnesium, improves die-castability and mechanical properties of magnesium at room temperature without significantly raising its density. As a result, the most commonly used magnesium alloys are those based on Mg-Al, such as AZ31, AM60 and AZ91. These alloys constitute more than 90% of the total magnesium in the market for structural applications. A part of the added aluminum dissolves into the matrix and improves the mechanical properties of magnesium through solid solution hardening. Accordion to the Mg-Al phase diagram [40] presented in Figure 2, aluminum content higher than $2wt\%$, leads to formation of a new $\beta - Mg_{17}Al_{12}$ phase as particles and precipitates, improving room-temperature mechanical properties of the alloys by hindering dislocation motion. Moreover, the $\beta - Mg_{17}Al_{12}$ phase has a low melting point of about 437°C, which improves die castability. However, this phase softens readily at high temperatures ($T > 130$°C) and, thus, has deleterious effects on the creep properties.

Rare Earth: Rare earth elements improve cast-ability of magnesium and reduces the porosity in the final cast products [41]. These elements strengthen Mg through solid solution and precipitation hardening both at room and high temperatures [42–44]. RE elements are effective in improving strength and corrosion resistance by formation of stable precipitates in the Mg matrix or at its grain boundaries. Recent

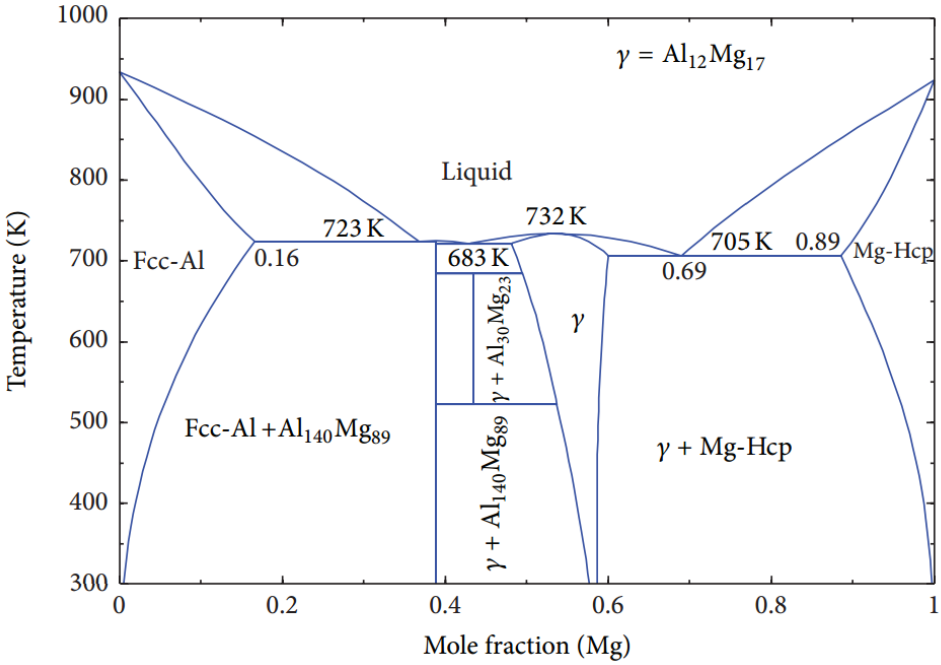

Figure 2: Mg-Al phase diagram [40].

studies indicate that the macroscopic texture is weakened through using rare earth (RE) alloying elements [45–48]. Figure 3 shows the phase diagram of two Mg-RE binary systems (i.e., Mg-Nd and Mg-Y).

Zinc (Zn): Zinc is the alloying element that is mostly used along with Al. No new phases in the Mg-Al-Zn alloy system is formed when the Al/Zn ratio is over 3:1 [49]. Zing improves castability of Mg but also increases the propensity for micro-porosity formation. The strength of Mg is increased by adding Zn via solid solution and precipitation hardening. On the other hand, the probability of hot-shortness is also increased as Zn is added to the system. Zinc could improve Mg's properties by removing impurities such as Cu and their deleterious effects [50].

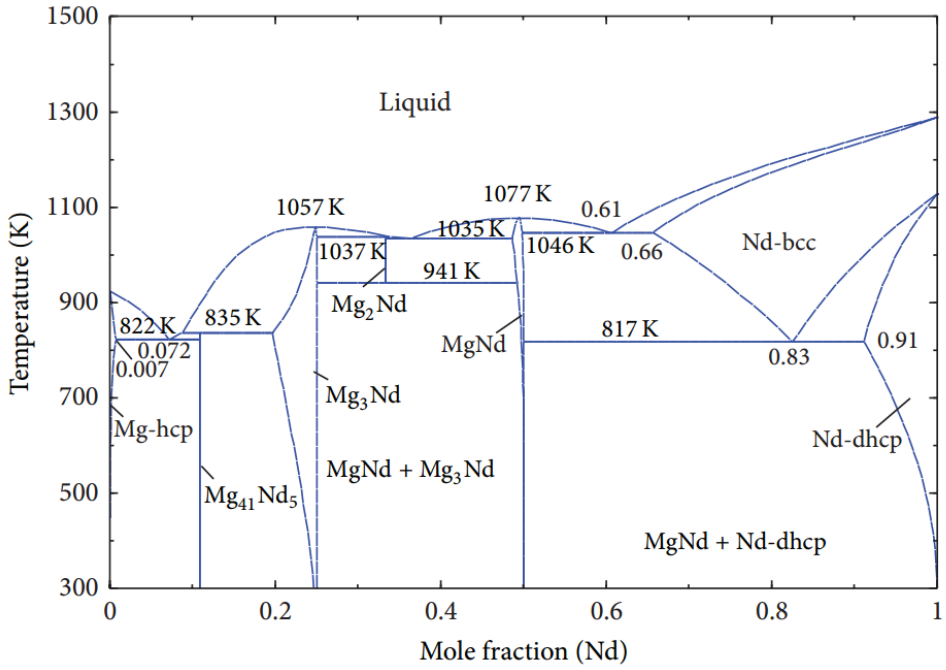

(a)

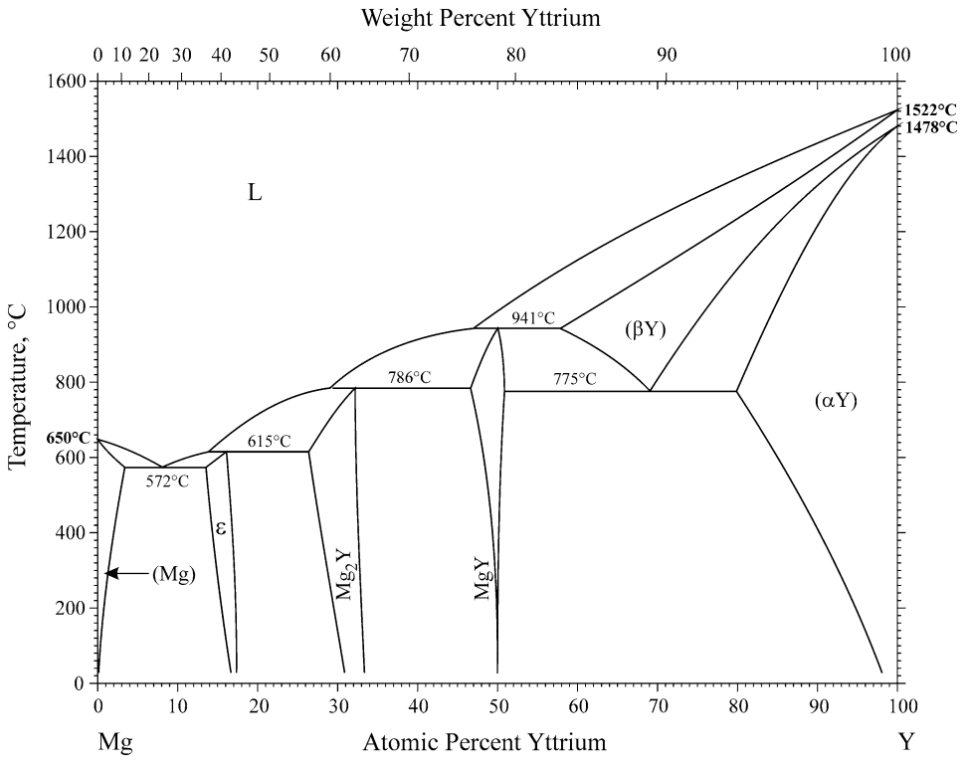

(b)

Figure 3: (a) Mg-Nd phase diagram [36] (b) Mg-Y phase diagram [51]. Here the phase ε has the chemical composition of $Mg_{48}Y_{10}$

Mangenese (Mn): The most important effect of Mn is to reduce solubility of Fe in Mg by forming Mn-Fe compounds. This increases the corrosion- and creep-resistance of Mg products. The remaining Mn will (i) form Mn rich particles or (ii) participate in formation of Al-Mn rich particles. Phase diagram of Mg-Mn, as shown in Figure 4, does not show any second phase particle between the two elements [52]. Strengthening effect of these elements are negligible [33, 53].

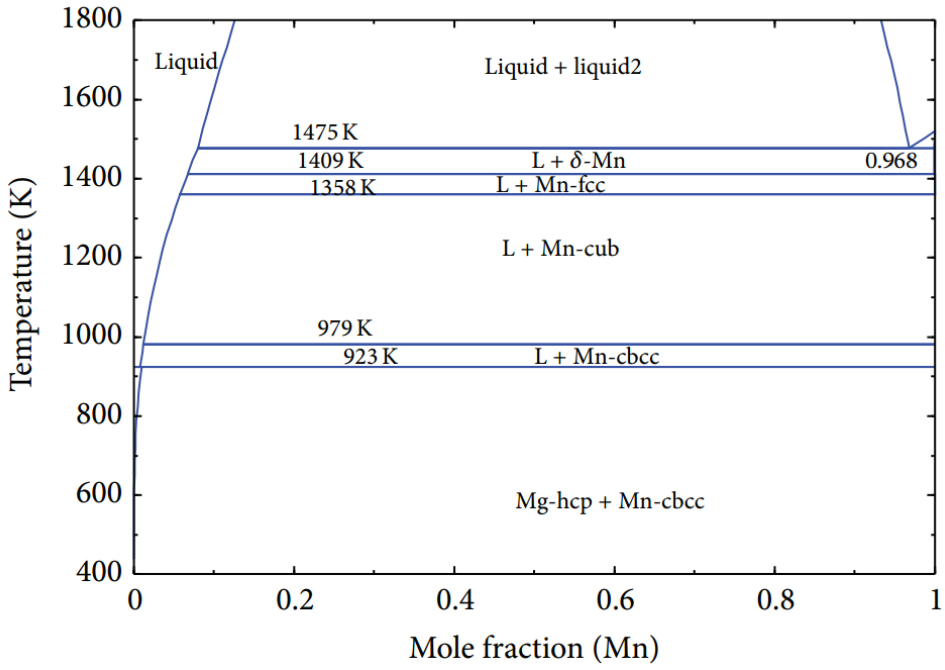

Figure 4: Mg-Mn phase diagram [54].

2.2 Deformation modes

Characteristics of plastic deformation in SC Mg and textured wrought Mg alloys are tension/compression asymmetry in yield strength, significant plastic anisotropy (in flow strength as well as strain ratios), and S-shaped stress-strain response during

elongation/compression $\parallel/\perp$ to c-axis. These characteristics stem from the fact that different deformation systems are activated each time the loading direction is altered. Thus, to understand the anisotropy in plastic deformation and overall mechanical response of Mg alloys, it is necessary to gain knowledge about the details of operative deformation systems in this material. Figure 5 illustrates the most important active deformation mechanisms in Mg alloys. Deformation twinning and dislocation glide play important roles in the mechanical response of these alloys.

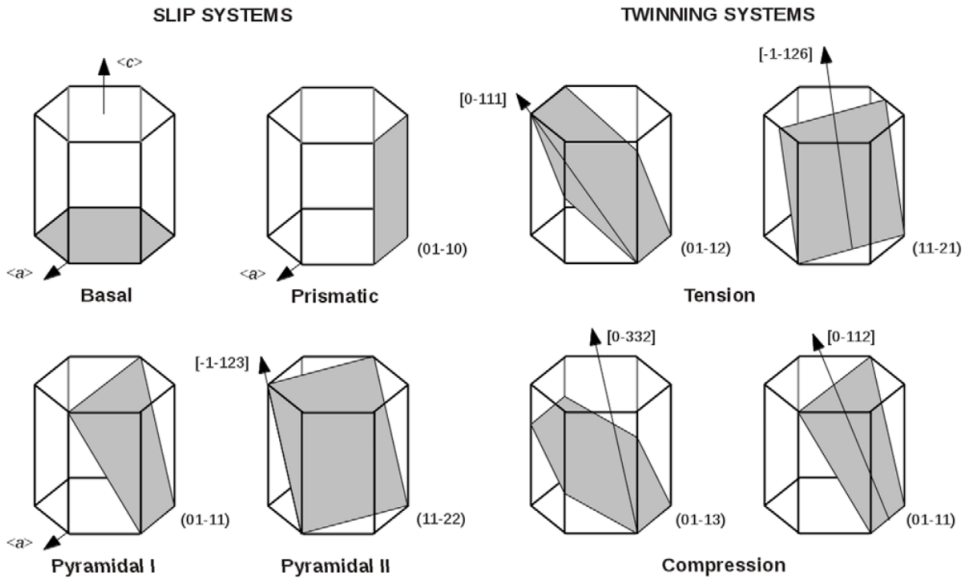

Figure 5: Various deformation systems in a magnesium signle-crystal [55].

The essentials of dislocation and twin plasticity are as follow. Dislocation plasticity is mediated by individual events of dislocation glide on multiple but distinctive "slip planes". Each glide event takes place after the applied shear stress (resolved on the slip plane and along the direction of Burgers vector) reaches a critical resolved shear stress (CRSS). Dislocation glide causes a small perturbation in the lattice by

breaking and formation of atomic bonds in the vicinity of dislocation line. Each glide event develops small strain field in size of Burgers vector associated with the dislocation. Cumulative effect of these strain fields leads to the overall deformation in the crystal. Reversing the direction of applied load leads to reversing the motion of dislocation. In contrast to slip, deformation twin produces a homogeneous shear over a three-dimensional region. The motion preserves the crystal structure and only changes crystal orientation [56, 57]. Unlike dislocation glide, the total strain that a twin could produce is limited [56,57]. Twinning has a property that is called "polarity", meaning that it could get activated under a certain loading condition but not necessarily under reversed loading [58]. Deformation twins usually exhibit a platelet morphology which is caused by the energetic barriers against their formation [57]. Similar to the CRSS of dislocations, it is possible to associate a CRSS to a twin system.

As mentioned before, depending on the direction of applied deformation, different deformation systems get activated in magnesium alloys. In the following, common deformation systems of magnesium are presented according to an ascending order of their CRSS values. Due to its very low CRSS, basal $\{0001\}\langle 11\bar{2}0\rangle$ dislocation glide becomes activated in almost any type of applied deformation and contributes in accommodating the imposed deformation [2, 59, 60]. The CRSS of basal slip has been experimentally and numerically determined. This value is very low [61, 62] and could be as low as 0.5 MPa [63]. It has been argued that easy activation of basal slip could cause shear localization in contraction $\{10\bar{1}1\} < 10\bar{1}2 >$ and double twins and lead to premature failure [12,14,23]. Basal $\{0001\}\langle 11\bar{2}0\rangle$ slip provides two independent slip systems.

Extension $\{10\bar{1}2\} < 10\bar{1}1 >$ twinning is the primary mode of twinning in magnesium, which becomes activated when a single-crystal in elongated along its c-axis

or compressed perpendicular to this direction. This condition is equivalent to in-plane compression (IPC) or out-of-plane tension (OPT) in rolled poly-crystalline Mg plates with basal texture. Activation extension twinning is the origin of tension/compression asymmetry and the S-shaped stress-strain response of many magnesium alloys during IPC and OPT [39]. The matrix experience a rotation of 86° after undergoing extension twinning. Unlike dislocation activity, the amount of strain produced by twinning is limited. For example, during extension twinning, the maximum shear strain produced in a completely twinned matrix is 0.13 [64]. This shear strain is equivalent to 0.065 axial strain along the c-axis. Extension twinning is believed to be beneficial to ductility properties of Mg alloys by enhancing the extent of uniform deformation [10]. These twins is easily activated if proper loading condition is present. The CRSS of extension twins is between 25 and 35 MPa [39].

Prismatic $\{10\bar{1}0\}\langle 11\bar{2}0\rangle$ slip is an active deformation systems at both room and high temperatures when deformation is applied perpendicular to the basal planes' normal [65, 66]. For poly-crystalline Mg alloys, this condition is satisfied for any in-plane deformation. Prismatic slip has lower CRSS in ploy-crystalline Mg compare to single-crystal case and its activation becomes easier at smaller grain sizes. This CRSS reduction is rationalized by the effects of grain boundary compatibility stresses [3]. Prismatic slip exhibit high sensitivity to temperature as well. The ratio of the CRSS of prismatic slip with respect to basal slip drops from 87 at room temperature to 1 3 at 286°C [66]. This temperature dependence is attributed to the narrow core structure of these dislocations. Similar to basal slip, Prismatic $\{10\bar{1}0\}\langle 11\bar{2}0\rangle$ slip offers two independent deformation systems. Neither basal nor prismatic dislocations produce any shear along the c-axis of the Mg crystal.

Pyramidal $\langle c+a\rangle$ ($\{11\bar{2}2\}$ $\langle\bar{1}\bar{1}23\rangle$) slip is a dislocation system that provides deformation along the c-axis of Mg crystals. It is a difficult system to activate at

room temperature because of (i) its high CRSS [67,68] and (ii) easy dissociation into sessile $\{c\}$ dislocations, which suppresses continuous slip [69]. Similar to prismatic dislocations, motion of pyramidal $\langle c+a \rangle$ dislocations is sensitive to temperature. The CRSS of this slip system is significantly reduced at elevated temperatures. Easy activation of dislocation slip on non-basal planes leads to reduced flow stress and increased formability [9, 70].

Contraction ($\{10\bar{1}1\} < 10\bar{1}2 >$) and double twins $\{10\bar{1}1\} - \{10\bar{1}2\} < 10\bar{1}1 >$ are other deformation twin variants that could be activated in Mg alloys. These twins do not often form in the microstructure unless the strain in the matrix is higher than 5%. These twin systems are deemed as detrimental for ductility properties because of two reason. As a result of favorable orientation of the crystal inside contraction and double twins, localized activity of basal slip in the twinned regions triggers shear localization and leads to premature failure [4, 23, 71, 72]. Significant accommodation strains and formation of large surface steps are also proposed as the origins for deleterious effects of contraction and double twins on ductility [14, 23].

2.3 Some of the yield functions used to describe anisotropy in Mg alloys

Yield models such as Tresca (1864), which is based on the maximum shear stress, and von Mises (1913), based on distortion energy, are applicable to isotropic materials. Although these models offer many capabilities and are useful in understanding plastic deformation of materials, they are not applicable to materials with anisotropic properties such as wrought and textured materials as well as directionally reinforced composites. The first model to describe yield in an incompressible anisotropic matrix was proposed by Hill [73]. Hill formulated the von Mises criterion for a material with orthotropic axis of symmetry. This quadratic criterion is originally presented

as follows:

$$f(\sigma) = F(\sigma_y - \sigma_z)^2 + G(\sigma_x - \sigma_z)^2 + H(\sigma_x - \sigma_y)^2 + 2L\tau_{yz}^2 + 2M\tau_{xz}^2 + 2N\tau_{xy}^2 = 1 \quad (2.1)$$

where F, G,...,N are the materials constant. If stresses are expressed along the principal axis of orthotropy, it is the case that:

$$F(\sigma_2 - \sigma_3)^2 + G(\sigma_1 - \sigma_3)^2 + H(\sigma_1 - \sigma_2)^2 = 1 \quad (2.2)$$

It is also possible to introduce anisotropy as a linear transformation of the Cauchy stress acting on the material [74]. Benzerga and Besson [75] re-derived Hill (1948) yield criterion as a linear transformation, based on the framework proposed in Ref. [76]. Hereafter, this model is referred to as Hill48. The yield function in this model takes the following form:

$$\mathcal{F} = \frac{3}{2}\,\sigma : \mathbb{p} : \sigma - \bar{\sigma}^2 = \frac{3}{2}\,\sigma^{'} : \mathbb{h} : \sigma^{'} - \bar{\sigma}^2 \quad (2.3)$$

where:

$\sigma^{'} = \sigma - 1/3\ tr(\sigma)\mathbf{I}$: The stress deviator;

$\mathbb{p}$: The forth order Hill deviatoric anisotropy tensor;

$\mathbb{h}$: The forth order macroscopic anisotropy tensor in the space of deviatoric stresses;

$\bar{\sigma}$: The flow stress in an arbitrarily chosen reference direction (in this study we will use L as a reference flow stress).

The relationship between $\mathbb{p}$ and $\mathbb{h}$ is as follows:

$$\mathbb{p} = \mathbb{J} : \mathbb{h} : \mathbb{J} \quad (2.4)$$

where $\mathbb{J}$ is the forth-order deviatoric projection operator $\mathbb{J} = \mathbb{I} - \frac{1}{3}\mathbf{I}\bigotimes\mathbf{I}$ with $\mathbb{I}$ and $\mathbf{I}$ being the forth- and second-order identity tensors, respectively.

The anisotropy of the material is therefore fully characterized by identifying the coefficients of the anisotropy tensor, i.e. $\mathbb{p}$ or $\mathbb{h}$. Equation 2.6 shows an example of simplified deviatoric anisotropy tensor for the case of an orthotropic material with no tension–compression asymmetry.

$$\mathbb{h} = \begin{bmatrix} h_{11} & h_{12} & h_{13} & 0 & 0 & 0 \\ h_{12} & h_{22} & h_{23} & 0 & 0 & 0 \\ h_{13} & h_{23} & h_{33} & 0 & 0 & 0 \\ 0 & 0 & 0 & h_{44} & 0 & 0 \\ 0 & 0 & 0 & 0 & h_{55} & 0 \\ 0 & 0 & 0 & 0 & 0 & h_{66} \end{bmatrix} \tag{2.5}$$

For the principal axis of orthotropy, the anisotropiy tensor $\mathbb{h}$ becomes:

$$\mathbb{h} = \begin{bmatrix} h_L & 0 & 0 & 0 & 0 & 0 \\ 0 & h_T & 0 & 0 & 0 & 0 \\ 0 & 0 & h_S & 0 & 0 & 0 \\ 0 & 0 & 0 & h_{TS} & 0 & 0 \\ 0 & 0 & 0 & 0 & h_{LS} & 0 \\ 0 & 0 & 0 & 0 & 0 & h_{LT} \end{bmatrix} \tag{2.6}$$

Using normality flow rule, one can also identify material parameters for this yield criterion based on strain ratios. The advantage of this model is that it is analytically simple and identification of its material parameters is easy. In fact, all the parameters could be identified using uniaxial tests. Despite the fact that this criterion renders an elliptical yield surface and works well for many materials such

as BBC metals, it has several shortcomings. Using this model leads to error in representation of (i) earing during deep-drawing of FCC metals, (ii) yield surface in material showing tension/compression asymmetry [77] and (iii) yield surface in materials where non-schmid effects are present [78]. In spite of these disadvantages and due to its simplicity, Hill quadratic anisotropic criterion is widely used in metal forming industry and is adopted for analytical works requiring a description of plastic anisotropy [75, 79].

To take into account the effect of tension/compression asymmetry and strength differential effects, Cazacu et al. [80] proposed an extension to Drucker's isotropic yield criterion. In addition to the second invariant of stress deviator, this model takes the third invariant into account. This yield function is as follows:

$$f(\mathbb{L}\sigma^{'}) = \left(\left|(\mathbb{L}\sigma^{'})_1\right| - k(\mathbb{L}\sigma^{'})_1\right)^2 + \left(\left|(\mathbb{L}\sigma^{'})_2\right| - k(\mathbb{L}\sigma^{'})_2\right)^2 + \left(\left|(\mathbb{L}\sigma^{'})_3\right| - k(\mathbb{L}\sigma^{'})_3\right)^2 \tag{2.7}$$

where $\sigma^{'i}$ is the principal value of Cauchy stress deviator. $\mathbb{L}$ is the linear transformation that incorporates the anisotropy of the matrix. Using Voigt's notation, the components of $\mathbb{L}$ are:

$$[\mathbb{L}] = \begin{bmatrix} L_{11} & L_{12} & L_{13} & 0 & 0 & 0 \\ h_{12} & L_{22} & L_{23} & 0 & 0 & 0 \\ L_{13} & L_{23} & L_{33} & 0 & 0 & 0 \\ 0 & 0 & 0 & L_{44} & 0 & 0 \\ 0 & 0 & 0 & 0 & L_{55} & 0 \\ 0 & 0 & 0 & 0 & 0 & L_{66} \end{bmatrix} \tag{2.8}$$

The $(\mathbb{L}\sigma^{'})_i$s (i = 1, 2 and 3) are the principle stresses of the transformed ap-

plied Cauchy stresses. The parameter k represents the effect of tension/compression asymmetry and is defined as follows:

$$k = \frac{1 - h\left(\frac{\sigma_T}{\sigma_C}\right)}{1 + h\left(\frac{\sigma_T}{\sigma_C}\right)} \tag{2.9}$$

where

$$h\left(\frac{\sigma_T}{\sigma_C}\right) = \sqrt{\frac{2 - \left(\frac{\sigma_T}{\sigma_C}\right)^2}{2\left(\frac{\sigma_T}{\sigma_C}\right)^2 - 1}} \tag{2.10}$$

Here, σ_T is yield stress in tension while σ_C is its compressive counterpart. From Equation 2.10, it follows that for the parameter k to be real, $1/\sqrt{2} \leqslant \frac{\sigma_T}{\sigma_C} \leqslant \sqrt{2}$. This model requires more than ten fitting parameters to fully characterize the anisotropy of the matrix. This prevents its application to industrial problems. In addition, the presence of absolute functions in the formulation requires a systematic study on the possibilities for each $(\mathbb{L}\sigma')_i$, which has not been done, up to this date. It is also claimed that this model is able to accurately predict the yield function in materials with tension/compression asymmetry, especially with H.C.P structure. Up to this date, however, the model has been tested against limited experiments such as in-plane loading where anisotropy is marginal. In other occasions, the stress state of the experiments used to test this model is identical or similar to those used for model calibration.

2.4 Fracture in Mg alloys

2.4.1 Fracture in Mg alloys with strong basal texture

A commonly accepted understanding of fracture under uniaxial tensile loading perpendicular to the c axis is as follows [4]. Subsequent to basal slip, anisotropic plastic flow leads to stress concentrations, for example at grain boundaries, which are

then accommodated by $\{10\bar{1}2\}$ extension twinning [64]. Concomitant with prismatic $\langle a \rangle$ slip, the latter produces a strain transverse to the loading direction but normal to the c axis. While some details pertain to the hardening behavior that ensues, it is clear that a transverse strain along the c axis can only be produced by so-called contraction twins and, to some extent, $\langle c + a \rangle$ dislocations. The former concentrate large shears which lead to failure by strain incompatibility at the twin boundaries or inside the twins. Clear evidence of twin-sized microcracks parallel to $\{10\bar{1}1\}$ $\{10\bar{1}2\}$ contraction double twins has recently been documented in different alloys [12, 14].

It is emphasized that the above mechanisms pertain to uniaxial loading conditions. How the plastic anisotropy plays out under more complex triaxial loading states, which are encountered during processing or in service, remains unexplored. In addition, in most studies, e.g., [12, 14], rectangular-prismatic tensile specimens are typically used, which are known to favor shear-like fracture, even in materials that are more ductile, and less anisotropic than Mg. Under such circumstances, the material adjacent to the slanted fracture surface does not display much damage, by cavitation or otherwise. In other words, shear failure obscures the intrinsic damage mechanisms as it becomes increasingly difficult to decouple the fracture behavior from the plastic instability. Furthermore, ductility is often invoked to mean the tensile elongation of an initially smooth bar. In materials with limited post-necking deformation, this property is more a measure of the hardening capacity of the alloy than it is a measure of the material's resistance to damage accumulation and cracking. To our knowledge, there has been no systematic study of load triaxiality effects on the ductile fracture of Mg alloys.

2.4.2 Fracture in Mg-RE alloys

Traditionally, this lack of ductility is attributed to their HCP crystal structure [9]. It is argued that HCP crystal structure offers limited number of independent deformation systems which gives rise to incompatible strains and results in low ductility. Similar effects are postulated for polycrystalline magnesium alloys exhibiting strong texture [38, 81], although some contributions from grain boundaries to activation of non-basal slip [3], deformation twinning, grain boundary sliding (GBS) [4] and, thus, overall ductility are rationalized. In short, lack of sufficient slip systems is generally held responsible for the limited formability/ductility of wrought Mg alloys [38, 39]. However, the literature remains elusive on the issue of how plastic anisotropy affects ductility for triaxial loading conditions.

According to this rationale, many research works in magnesium community have been dedicated to texture weakening using rare earth (RE) alloying elements to reduce the anisotropy in formed magnesium alloy [45–48]. Other researchers have tried to change the CRSS of different deformation systems via addition of various alloying elements to form solid solution [67, 82] or precipitates on certain crystallographic planes [83, 84] and achieve better ductility and formability. The latter method also includes, but is not limited to, using RE alloying elements. For example, using experiments on AZ91 and Z5 alloys and utilizing simple Orowan-based calculation, Robson et al. [82, 85] showed that development of plate-like precipitates on basal planes (i.e. basal plates) is effective in prohibiting twin growth and, thus, reducing tension-compression asymmetry and plastic anisotropy. Up to this date, development of RE containing alloys stands out as the most promising route for producing ductile and formable Mg alloys for structural application. At dilute limits, RE containing alloys suffer from low yield strength ($\sim$ 60 MPa) although exhibit remarkable strain

to failure under compression parallel to rolling direction (strain to maximum load higher than 0.50) and tensile ductility close to that of AZ31 (between 0.13 and 0.22 depending on the used RE element) [48]. To achieve higher strength, yttrium (Y) and higher concentrations of RE elements are used [31]. Strain to failure of these Y- and RE-concentrated alloys under uniaxail loading is, however, reduced to values comparable or slightly inferior to that of AZ31 with similar heat treatment condition (compare results in Ref. [9, 13, 22] with those in Ref. [86, 87]). Combination of very high specific strength (ultimate strength of ∼400 MPa) and acceptable uniaxial fracture strain (∼0.15) makes these alloys attractive candidates for aerospace and defense applications where manufacturing cost is of limited importance. Added cost of alloying elements and their required manufacturing specifications, makes automotive industries reluctant to utilize these alloys.

Microscopically, contraction and double twinning are proposed as the main origins of damage in Mg alloys [12, 14]. Under uniaxial tension, deformation in pure magnesium and Mg alloys such as AZ31 with strong basal texture is accommodated by $\langle a \rangle$ type basal and prismatic dislocations in addition to extension twins, depending on the direction of load. Contraction and double twinning and $\langle c+a \rangle$ dislocations are also active, although with much less intensity. It is argued that because of strong basal texture and favorable orientation of slip planes inside contraction and double twins, localized activity of basal slip in the twinned regions triggers shear localization and leads to final failure [4, 23, 71, 72]. Significant accommodation strains and formation of large surface steps are also proposed as the origins for deleterious effects of contraction and double twins on ductility [14, 23]. It is while extension twins are proposed as beneficial for ductility properties by increasing the extent of uniform deformation prior to shear localization and fracture in slanted mode [10, 23]. On the other hand, in RE containing Mg alloys where the texture is less pronounced and

anisotropy is not as significant, contraction twins are active with higher intensity. As a result, numerous regions with localized shear form while each region has less intense localization compare to pure Mg and AZ31 [88]. In this condition, the failure in shear band, supposedly, happens at significantly higher strains. Higher activity of prismatic slip and its effect on the deformation twinning could also lead to less catastrophic shear band formation in these alloys as well [47, 89].

Incorporation of damage and fracture properties in design methods, in an in-depth fashion, is still lacking. In the case of Mg alloys, usually the effect of carefully designed texture or precipitates only on the activation of various deformation mechanisms are studies and their role in fracture specially under complex loading schemes are left unexplored. The case of WE alloy series is a good example of this shortcoming. In spite of several valuable studies on the deformation and fracture of Mg alloys, and recently their RE containing family, there are still unexplored areas which limit our understanding of ductility in Mg alloys. One could divide these area into three major ones:

This work is focused on the study deformation, fracture and its mechanisms in an RE rich Mg alloys, WE43. Processing texture in this alloys is weakened due to high concentrations of Y and RE elements. By preforming a series of interrupted uniaxial tension and compression experiments, the plastic anisotropy in WE43 is characterized. Round uniaxial and notched bar specimens are used to study the effect of loading condition (i.e. stress state triaxiality) on fracture strain of these alloys. Anisotropy in fracture properties is also characterized by performing fracture experiments along various directions. Finally, connection between macroscopic response and damage at microscopic scale is established.

2.4.3 Need for modeling

To guide alloy development attempts, understanding of the fundamental mechanisms leading to damage and fracture is essential. Failure to account for fracture properties could lead to development of alloys with unexpected fracture properties to an extend that its application to real-world situation is jeopardized. Up to this point, most of studies in the Mg community have been focused on deformation mechanisms in magnesium alloys and adopted the viewpoint in which fracture is a mere consequence of attaining a critical strain. Other research efforts are dedicated to the identification of damage initiation mechanisms such as deformation twins [12, 23] or second phase particles [24]. Although damage initiation is an important stage in the fracture process, it is usually the growth of these defects and their interactions with each other that determines the fracture strain and ductility. Limited studies are dedicated to experimental study of voids and microcracks after initiation or the effect of a macroscopic main cracks on the deformation system in their immediate vicinity [25–28]. In this regard, fracture mechanics community has developed sophisticated models for ductile failure in the past several decades [79, 90, 91, 91–93]. Some of these models are able to accurately predict the interaction of voids and microcracks in anisotropic media and render valuable insight on how fracture proceeds after damage initiation. These types of studies have not been carried out in the case of magnesium alloys. It is the case that observation of deep dimples that covers most of the fracture surfaces [18, 23] partially justifies the application ductile fracture models. In addition, failure in Mg alloys under uniaxial loading (even in round specimens [18]) happens by shear localization [12, 20]. In this condition, structural instabilities instead of intrinsic behavior of the material is the cause of fracture. It is crucial to separate structural instabilities from intrinsic fracture behavior of Mg

alloys. In spite of the existence of advanced models, simulating the observed trends in Mg fracture experiments is still challenging. Identification of variables that lead to failure strains close to the experimentally observed ones could shed light on the underlying mechanisms for fracture.

In this thesis, the mechanisms of damage accumulation to fracture during deformation is studied. No attempt has been devoted to evaluating the fracture toughness or investigating crack propagation in a boundary value problem. Instead, fracture strain, as a property that represents ductility, is studied. One of the most important variables that influence the fracture strain of the material is stress state triaxiality. Thus, the fracture locus (i.e., fracture strain in a range of triaxialities) are studied. Note that fracture locus is neither, in general, unique nor considered an intrinsic property of the studied material. Under strictly proportional loading (when stress triaxiality remains constant), however, the fracture locus is intrinsic to the material. The intrinsic fracture locus is considered here. It is worth noting that the intrinsic fracture locus is not directly accessible to experimental measurements because it is almost impossible to achieve proportional loading, all the way to fracture in laboratory condition. The complex stress state in front of a freshly formed crack and developed neck during uniaxial tension are examples of non-proportionalities developed inside material during loading. The closest condition to a proportional loading is achieved by using notched bars in which triaxiality variations are minimal. The fracture locus in such experiments (and their associated range of triaxialities) are close to the intrinsic one. Thus, the results form notched bar experiments are used in the study of fracture strains.

The objective of the current modeling effort is to study the effect of various microstrucutal parameters such as matrix plastic anisotropy, void shape and distribution on the overall fracture properties of materials. Such studies help better

understanding of failure in materials via ductile fracture mechanisms. The results are used as a guide to understand fracture in materials with anisotropic matrix such as magnesium alloys. Finally, the mistrostrucutal parameters of the current AZ31 and WE43 alloys are employed to predict the fracture strains of these alloy at various triaxialities and rationalize the experimentally measured fracture locus.

2.5 Ductile fracture in metals: Fundamentals

The most common mechanism responsible for failure in metals at ambient temperature is Ductile fracture. This mechanism involves nucleation, growth and coalescence of microvoids. Ductile failure usually takes place after significant deformation (i.e. considerable void growth prior to coalescence). There are, however, cases where fracture occurs after limited strain, as low as 1%. This is the case for materials with significant impurity, high strength alloys and metal matrix composites. Figure 6 presents schematics of different stages of ductile fracture process where the initial material with second phase particles is deformed. Nucleation of voids usually occur at second phase particles (Figure 6b).

After void nucleation, continued plastic deformation of the matrix around nucleated voids leads to void growth (Figure 6c). Void growth can be, thus, viewed as signature of plastic deformation of the matrix. Void growth continues until it is terminated by coalescence where the localized growth or shear localization in the inter-void ligaments kicks in. Multiple voids could coalesce and lead to formation of a macroscopic crack after which load-bearing capacity of the material is diminished significantly. This manifests itself as a sudden macroscopic load drop (Figure 6d). In the following subsections, various stages of ductile fracture are described in more details.

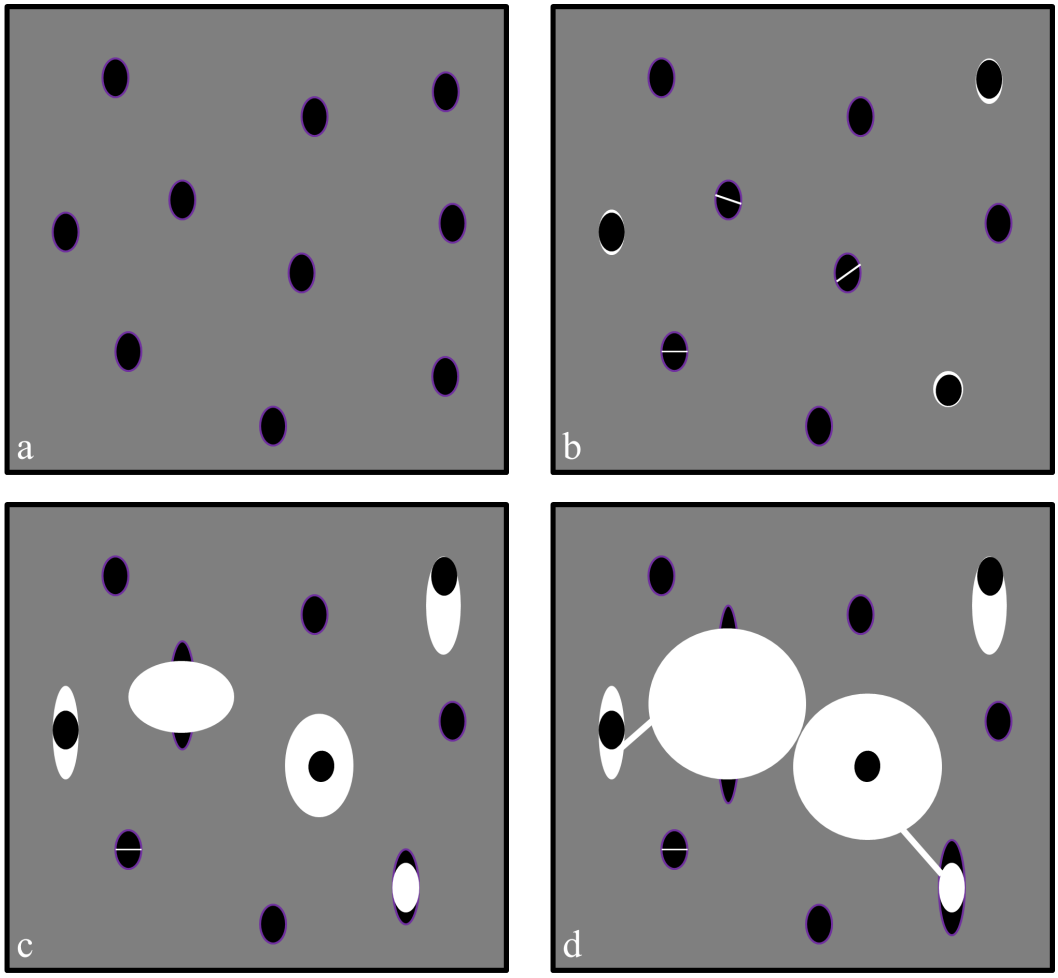

Figure 6: Schematic of different stages of ductile fracture. (a) Initially void-free matrix containing second phase particles. (b) Void nucleation by particle cracking or particle/matrix interface de-cohesion. (c) Void growth. (d) Coalescence of voids.

2.5.1 Ductile fracture in metals: Nucleation

Pioneering work on fracture via ductile fracture [94–96] showed that in structural materials in where alloying elements and second phase particles are present, void nucleation usually occurs after some straining and by particle/matrix interface de-cohesion (Figure 7a) or particle cracking (Figure 7b). If the material is very pure

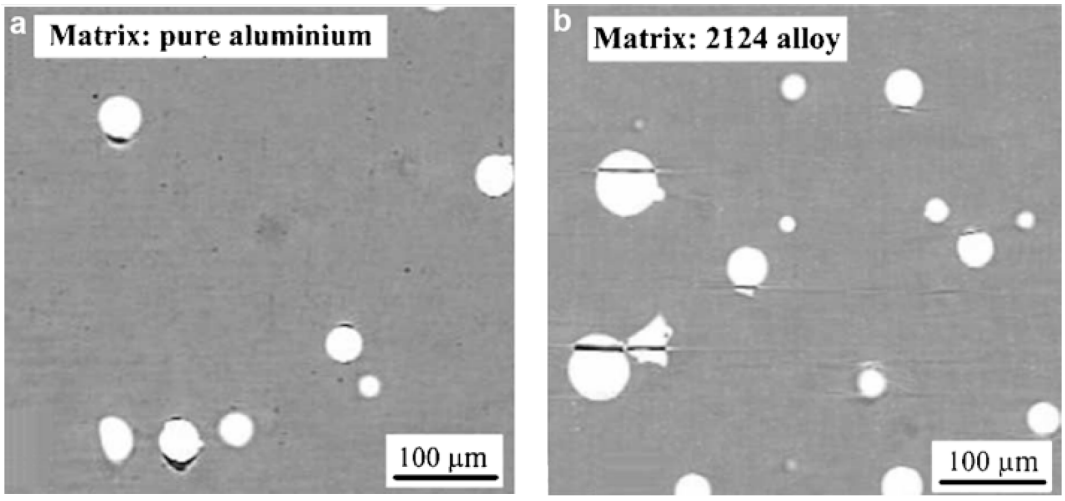

Figure 7: Void nucleation by (a)particle/matrix interface de-cohesion, (b) particle cracking [97].

and does not contain second phase particles, voids can initiate at the intersection of slip bands where dislocations from different slip systems meet. Vacancies could cluster and form voids, as well.

Depending on the properties of matrix, particles and their interface, the mode of nucleation could change. Table 1 summarizes these effects. Experimental studies to define the nucleation criterion have led to stress- [95, 97, 98] and strain-based criteria [96, 99]. The modeling activities in this area include those assuming perfect bonding between matrix and particles to investigate the local distribution of plastic strain and stresses [97, 100]. Cohesive separation (as proposed by Needleman) [101, 102] and no bonding at interface [103, 104] have also been studied.

Table 1: Effect of materials and loading parameters on microscopic mode of void nucleation.

Parameter	Type	Trend	
		Decohesion	Cracking
Matrix Yield Strength		↘	↗
Matrix hardening exponent		↘	↗
Particle elongation		↘	↗
Particle stiffness		↗	↗
Load orientation	Axial	↘	↗
	Transverse	↗	↘
Load Triaxiality		↗	↘

2.5.2 Ductile fracture in metals: Growth

In ductile materials void growth is responsible for most of the elongation before failure. Continued plastic deformation of the matrix after void nucleation usually results in volumetric growth of voids (shear and compressive loading are instances where it is not true) and change in their shapes [105]. Although it is a very important stage of ductile fracture, void growth usually has a very weak effect on the overall macroscopic response. Stress triaxiality has a strong influence on the void growth and evolution of its shape. Triaxiality, which is the ratio of hydrostatic stress to the von Mises equivalent stress, is defined as follows:

$$T = \frac{\sigma_m}{\sigma_{eq}} \tag{2.11}$$

where σ_m is the hydrostatic stress and σ_{eq} is the von Mises equivalent stress defines as $\sigma_{eq} = \sqrt{(3/2)\sigma' : \sigma'}$. Here σ' is stress deviator.

The rate of void growth is reported to increase exponentially with increasing triaxiality [106]. In general, most of triaxiality effects in ductile fracture originates from its influence on void growth. Void growth could be studied experimentally by optical or scanning electron microscopy of interrupted experiment. Three dimensional (3D) X-ray tomography (both ex-situ and in-situ) could also provide extensive information about void growth.

Because of the relationship between material porosity and ductile failure, the ability to accurately describe the evolution of voids in a ductile metal is crucial in order to accurately predict the failure of the material. The first attempts to study void growth was done by McClintock and Rice & Tracey [107, 108] which were limited isolates voids in an infinite medium. Unfortunately, computational constraints make it prohibitively expensive to model each of the micro-voids in most engineering structures; therefore, the method of explicitly tracking the evolution of each micro-void is not practical at this time. An alternative to explicitly tracking the evolution of each void (i.e., tracking microscopic, or local, quantities) is to incorporate the effects of the micro-voids into the macroscopic, or average, properties (such as macroscopic stress, strain, yielding, etc). Since the rate of dilatation of the porous solid is related to the void growth rate, plastic potentials for the porous solid must be developed in order to describe the void growth. The most widely used plastic potential for porous solids was proposed by Gurson [90]. This model is limited to cylindrical and spherical voids in an isotropic, perfect plastic solid. To derive an analytic expression for the plastic potential (and, thus, the yield criterion, assuming associated plasticity), Gurson performed a limit load analysis on a RVE. The void growth models used in this dissertation are extensions of the Gurson's model [90] to

account for matrix plastic flow anisotropy and void shape. In Gurson's analysis, it was assumed that the virgin material (void-free) obeys the classical von Mises yield criterion. To obtain the plastic potential, Gurson minimized the plastic energy for a specific velocity field compatible with uniform strain -rate boundary-conditions. Thus, the obtained criterion was an upper bound of the exact plastic potential (since the plastic energy was minimized for only one velocity field rather than complete set of kinematically admissible velocity fields).

Note that the original Gurson's model is for single voids in a RVE in the shape of a sphere or cylinder. The details of this model are as follow:

1. Geometry:

   The RVE is a hollow spheroid containing a confocal spheroidal cavity. In such an RVE, microstructural variables are porosity volume fraction f, void aspect ratio, W, and void axis, $\mathbf{e}_3$.

2. Plasticity model:

   The orthotropic, associated Hill flow theory is used for the matrix, cf. equations (8.1). The orthotropy axes are not necessarily aligned with the voids. Here, L, T and S refer to the principal directions of plate.

3. Velocity fields:

$$\forall \mathbf{x} \in \Omega \backslash \omega, \quad v_i(\mathbf{x}) = A v_i^A(\mathbf{x}) + \beta_{ij} x_j, \tag{2.12}$$

   As above, scalar A and symmetric tensor $\boldsymbol{\beta}$ are parameters (with $\beta_{kk} = 0$). Here, $\boldsymbol{\beta}$ is not necessarily axisymmetric if one admits the ensuing approximations.

A widely used modification of Gurson's spherical yield criterion was suggested in

Tvergaard [109, 110] based on comparisons with finite element calculations of shear band instabilities (where the instability is determined by a loss of ellipticity of the governing equations). Calculations by Tvergaard were meant to represent a periodic array of spherical voids that were arranged such that hexagonal representative volume elements (RVEs) could be fit together to form the structure. (The cylindrical RVE used in the calculations was an approximation of the hexagonal RVE.) Recent extension of this model enables detailed materials behavior such as void shape [92, 111, 112] and anisotropy of matrix [75, 79] being taken into account. A quite similar yield function for porous medium to that of Gurson could be obtained using general thermodynamic principles [113].

2.5.3 Ductile fracture in metals: Coalescence

Consideration of failure by void growth (where voids grow till they touching each other, "void impingement", leads to substantial overestimation of ductility. Physically, void growth continues till a critical configuration is attained. After this critical stage, entitled as onset of "coalescence", localized and directional growth of voids interrupts the homogeneous and stable one. The localized flow in the inter-void region leads to substantially higher rate of void growth. Coalescence could occur via internal necking in the ligaments between voids, shear band formation called "void-sheet" coalescence and necklace coalescence. There are many attempts to model coalescence

Micromechanical evidence for internal necking were first provided using cell model calculations using finite element calculations [114, 115] where elastic unloading of the regions above and below voids leads to very high growth rates in the intervoid ligaments. The first attempt to model coalescence by internal necking was done by Thomason [116] in two dimensions. Tvergaard and Needleman [91] attempted to take

coalescence into account by modifying Gurson's spherical yield criterion to develop GTN model. Attempts to develop heuristic and purely analytical closed form yield function for coalescence in three dimensions (Such as Ref. [93, 117, 118]) are those that account for discontinuity in the velocity gradient fields in the to-be-homogenized RVE.

3. EXPERIMENTAL APPROACH

3.1 Starting materials and characterization of initial microstructure

Two alloys are used in this study. The first alloy is a 1.25" (32 mm) thick hot-rolled AZ31B plate (2.5-3.5% Al, 0.7-1.3% Zn, 0.2-1.0% Mn) provided by Magnesium Elektron company in the H24 condition (strain hardened and partially annealed) [119]. The other alloy is a 1.5" (38 mm) thick hot-rolled WE43 (3.7-4.3% Y, 2.4-4.4% RE, 0.4% Zr min) plate, also provided by Magnesium Elektron company, in the T5 condition (strain hardened, solid solution and artificially aged). The plates are reported to three principal directions, rolling or longitudinal (L), transverse (T) and short-transverse or through-thickness (S); see Figure 8b. To study the mirostructure of the material, metallographic samples from different planes were cut using a diamond saw, ground with SiC paper and fine polished using 1, 0.3 and 0.05 μm alumina suspensions. Water was used during grinding only. Isopropyl alcohol was used for rinsing and sometimes acetone as ultrasonic cleanser. For etching, acetic picral solution (4.2 g picric acid, 10 ml acetic acid, 70 ml ethanol and 10 ml water) was used for 5s. In some occasions, Nital solution (5% concentration) was also used to reveal microstructure of WE43 alloy. Optical Microscopy (OM) and Scanning Electron microscopy (SEM) were both used for microstructural observations.

The average grain size and its distribution were determined using the line intercept method [120] and *ImageJ* image analyzing software. Compositional variations in the microstructure and the identification of second phase particles were determined using energy dispersion spectroscopy (EDS) and wavelength dispersion spectroscopy (WDS) in SEM. Crystallographic texture measurements were carried out using a Bruker-AXS D8 X-ray diffractometer (XRD) with Cu Kα radiation on a sample

from the plate's mid-section in the L–S plane to get (0002) and $(10\bar{1}0)$ pole figures using a 5° grid size and an 85° sample tilt.

3.2 Mechanical behavior characterization

Compression and tension specimens were cut out along the three principal directions (i.e., L, T and S directions) in addition to three off axis ones (i.e., 45° between pairs of principal directions). A schematic of the specimen orientation with respect to the plate is shown in Figure 8b. The specimens were deformed either to crack initiation or complete fracture. One of the principal directions was systematically marked on both ends of each specimen to enable tracking of the microstructural orientations with respect to the sample geometry. Cylindrical specimens were used exclusively so as to deconvolute, as much as possible, structural instability effects from material's intrinsic properties. Specimens' geometry is sketched in Figure 8a. The same experiments enabled to measure (i) the yield and flow behavior of the material; (ii) the evolution of plastic anisotropy with plastic strain; and (iii) the strains to failure. At least two specimens were used for each type of test. To increase confidence when scatter was large, up to two additional tests were carried out.

3.2.1 Uniaxial compression

Compression tests were carried out on a servo-hydraulic MTS machine (Model 318.25) with a load cell capacity of 250kN at a strain rate of 10^{-3}s^{-1}. A pure nickel anti-seize lubricant was used to prevent early barreling. Each test was interrupted at regular strain intervals and the specimen was unloaded to enable the measurement of its current height, H, and two lateral diameters along the principal directions(Φ_X). The associated strain to these measurements are calculated according to the following equations.

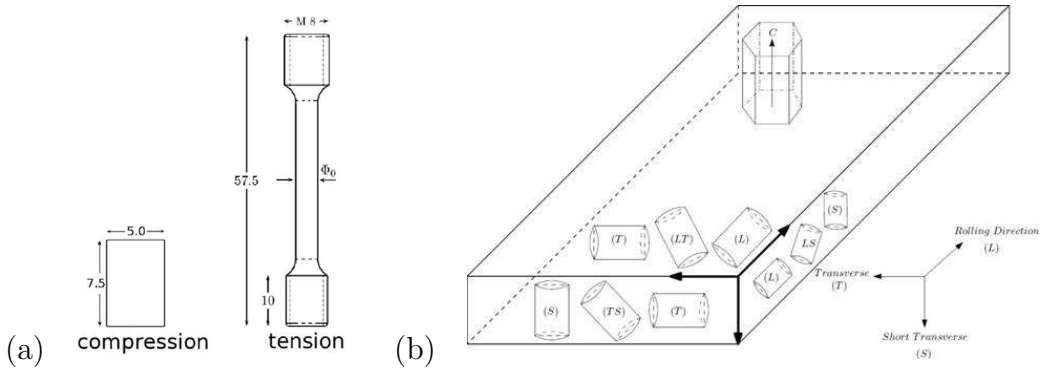

Figure 8: (a) Geometry of the specimens for uniaxial tension and compression experiments. (b) Various directions along which uniaxial tests were carried out.

$$\varepsilon_{\text{axial}} = \ln\left(\frac{H}{H_0}\right); \quad \varepsilon_{\text{X}} = \ln\left(\frac{\Phi_{\text{X}}}{\Phi_0}\right), \tag{3.1}$$

where Φ_X stands for lateral diameter along L, T, S, LT, LS or TS and the superscript 0 refers to initial values. The accuracy on lateral strains (ε_{X}) is 0.1%.

An example is presented in the following. For compression along L direction and after each unloading, current height (H) and diameters (Φ_{T} and Φ_{S}) were measured. True axial and lateral strains were defined as:

$$\varepsilon_{\text{L}} = \ln\left(\frac{H}{H_0}\right); \quad \varepsilon_{\text{X}} = \ln\left(\frac{\Phi_{\text{X}}}{\Phi_0}\right). \tag{3.2}$$

Here Φ_X stands for lateral diameter along T and S direction. Anisotropy ratio in such tests could be used to quantify the plastic anisotropy. For loading parallel to L direction, this ratio is defined as:

$$R^{\text{L}} = \frac{\varepsilon_{\text{T}}}{\varepsilon_{\text{S}}} \tag{3.3}$$

Similar definitions are introduced for experiments along other directions, according to a permutation between L, T, and S. In the case off-axis experiments, anisotropy ratio is always defined as lateral strain along the off-axis direction divided by the lateral strain along the principal direction. The followings are the definition of anisotropy ratio for experiments along T, S, LT, LS and TS direction.

$$R^{\mathrm{T}} = \frac{\varepsilon_{\mathrm{S}}}{\varepsilon_{\mathrm{L}}}, \quad R^{\mathrm{S}} = \frac{\varepsilon_{\mathrm{L}}}{\varepsilon_{\mathrm{T}}}, \quad R^{\mathrm{LT}} = \frac{\varepsilon_{\mathrm{TL}}}{\varepsilon_{\mathrm{S}}}, \quad R^{\mathrm{LS}} = \frac{\varepsilon_{\mathrm{SL}}}{\varepsilon_{\mathrm{T}}}, \quad R^{\mathrm{TS}} = \frac{\varepsilon_{\mathrm{ST}}}{\varepsilon_{\mathrm{L}}} \tag{3.4}$$

Most compression tests were continued until the pins failed in shear. A distinct load drop was observed before the specimen split in two pieces. The value of axial strain at the load drop is taken as a measure of strain to failure initiation, ε_{i}. In addition, a strain to complete fracture, ε_{f}, was defined on the basis of cross-sectional area variation:

$$\varepsilon_{\mathrm{f}} = \ln\left(\frac{A_{\mathrm{f}}}{A_0}\right) \equiv \varepsilon_{X1}\Big|_{\mathrm{f}} + \varepsilon_{X2}\Big|_{\mathrm{f}} \tag{3.5}$$

where X1 and X2 are the measured lateral diameters. As an example, strain to fracture for loading along L direction is:

$$\varepsilon_{\mathrm{f}} = \ln\left(\frac{A_{\mathrm{f}}}{A_0}\right) \equiv \varepsilon_{\mathrm{T}}\Big|_{\mathrm{f}} + \varepsilon_{\mathrm{S}}\Big|_{\mathrm{f}}. \tag{3.6}$$

Here, the area of the fractured specimen, A_{f}, was measured post-mortem in OM. Also, $\varepsilon_{\mathrm{T}}\big|_{\mathrm{f}}$ and $\varepsilon_{\mathrm{S}}\big|_{\mathrm{f}}$ are the lateral strains in $(3.1)_2$ taken at failure. The identification in $(3.6)_2$ assumes an elliptical shape for the fractured cross-section. An alternative measurement of A_{f} assuming an oval shape led to small differences in evaluating ε_{f}.

3.2.2 Uniaxial tension

Uniaxial tension experiments were carried out at an initial strain rate of $10^{-3}\mathrm{s}^{-1}$ on a servo-hydraulic MTS machine (Model 380.50) equipped with a 250kN load cell.

True axial strain was measured prior to necking using a laser extensometer over a gauge length of ~ 30 mm. Also, a radial extensometer (of which details will follow) was used to measure the diameter reduction in real time. This measurement was made along a certain direction depending on the loading direction (diameter along S, S, L, S, T and L were measured for loading parallel to L, T, S, LT, LS and TS, respectively). In addition, each test was paused at regular strain intervals in order to measure the lateral diameters using a caliper (accuracy better than 0.005mm). This method expedited measurements of plastic anisotropy as compared with the unloading–reloading method used in the compression tests. True axial and lateral strains were defined similar to Equation (3.1) substituting the gauge length l for H in $(3.1)_1$. All AZ31 tensile specimens failed in shear. However, this occurred after necking. In the case of WE43 uniaxial bars, necking was much limited and some of the specimen showed flat mode of failure depending on their loading direction. Although post-necking deformation is small, it is generally important to distinguish between failure initiation and complete fracture as in the case of compression. Ideally, the strain to failure initiation is defined as:

$$\varepsilon_{\mathrm{i}} = \left| \ln \left(\frac{A_{\mathrm{i}}}{A_0} \right) \right| \equiv |\varepsilon_{X1}| \Big|_{\mathrm{i}} + |\varepsilon_{X2}| \Big|_{\mathrm{i}} \tag{3.7}$$

where $X1$ and $X2$ refer to two perpendicular directions subject to measurement. For instance, during loading parallel to L direction, the above equations become:

$$\varepsilon_{\mathrm{i}} = \left| \ln \left(\frac{A_{\mathrm{i}}}{A_0} \right) \right| \equiv |\varepsilon_{\mathrm{T}}| \Big|_{\mathrm{i}} + |\varepsilon_{\mathrm{S}}| \Big|_{\mathrm{i}} \tag{3.8}$$

A robust estimate of ε_{i} thus requires a measurement of A_{i} (the area of the cross-section at the neck at crack initiation). To interrupt a tensile test at incipient

cracking is quite challenging. Therefore, in most tests the last value recorded for the axial strain was used as a lower-bound estimate of ε_{i}. In general, this identification can lead to errors because of necking. Exceptionally, one test along LT direction was interrupted successfully at the load drop (i.e., at crack initiation). This case enabled to estimate the error made by identifying ε_{i} with the last recorded value of ε_{L} at about 4%.

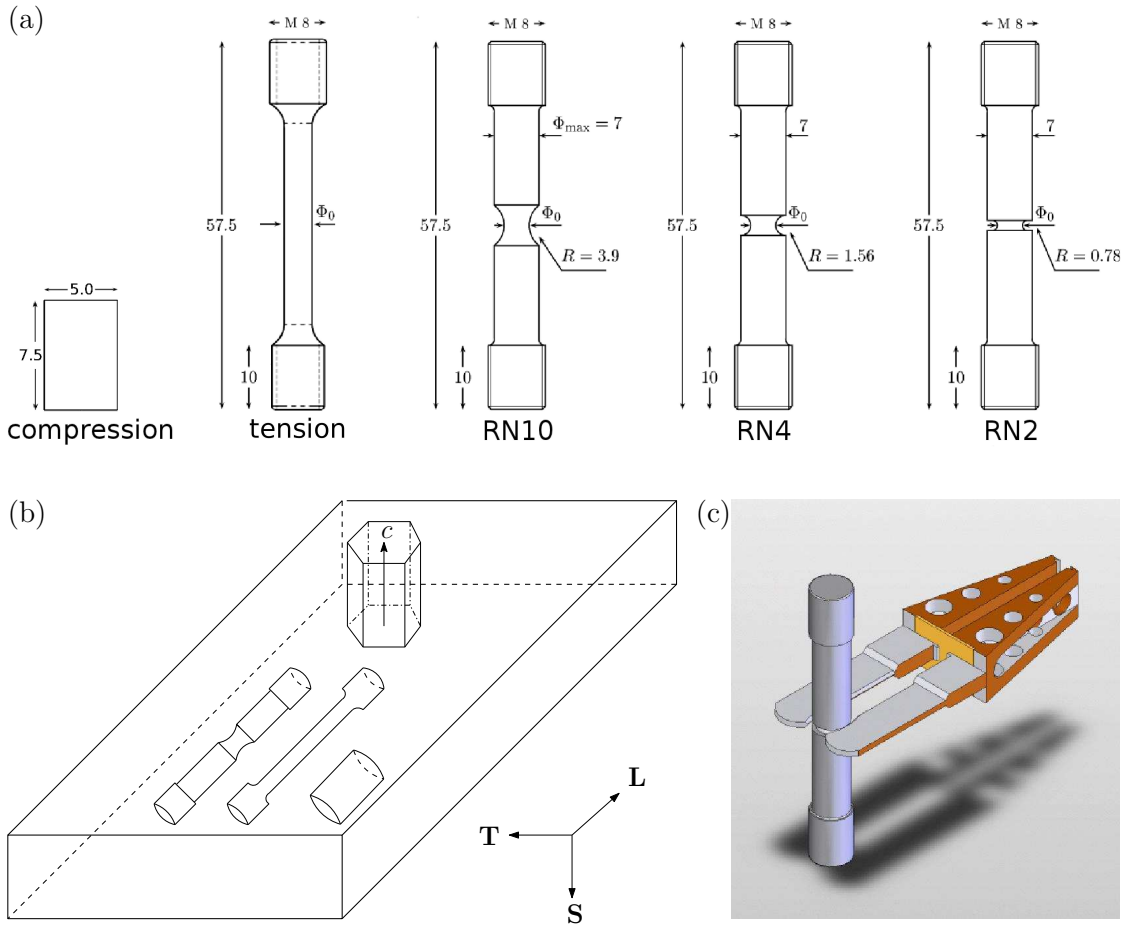

Figure 9: (a) Geometry and (b) orientation of round specimens used. (c) Custom-made knives for a radial extensometer, here mounted on the RN2 specimen.

3.2.3 Notched bar experiments

Notched bars are usually employed in fracture studies because (i) a triaxial stress state is developed in the notched region and effect of triaxialoty on fracture properties could be investigates; (ii) Notch introduces a damage zone which facilitates investigation of different fracture mechanisms; Finally (iii) in strongly anisotropic materials such as Mg, the introduction of notch enables the investigation of the effect of triaxial loading on plastic anisotropy [121, 122]. In order to study the effect of stress triaxiality on the deformation and fracture of AZ31, round notched (RN) specimens with three different notch geometries (to provide a range of triaxialities) were used [121].

Inside the notch, the stress state is triaxial. In addition to the major axial stress, Σ, there are two equal minor (principal) stresses, each denoted by $\sigma < \Sigma$. Let $\theta \equiv \sigma/\Sigma$. Each notched bar is essentially characterized by a certain level of θ. The stress triaxiality, T, is defined as the ratio of the hydrostatic stress to the von Mises effective stress. For axisymmetric loading, T is related to θ through:

$$T \equiv \frac{1}{3} \operatorname{sign} \Sigma \, \frac{2\theta + 1}{|1 - \theta|}. \tag{3.9}$$

Alternatively, each bar is labeled based on the notch severity parameter, ζ, equal to ten times the notch radius to specimen diameter at the notch. Three values of ζ were explored and the corresponding specimens are denoted by RNζ, Figure 9a. There is a direct relation between notch severity and stress triaxiality. The lower the value of ζ the higher the levels of stress triaxiality, as inferred from finite-element calculations [122]. Taking the notch height as a gauge length, a nominal strain rate of $3 \times 10^{-4} s^{-1}$ was imposed in all cases. In the notched bars, the use of an axial extensometer would be pointless unless the gauge is restricted to the height of the

notch, which is difficult given the size of our specimens. Instead, the instantaneous diameter along a certain direction (for example, S direction for loading along L) was continuously measured thanks to a custom-made radial extensometer. The latter consists of two knives (Figure 9c) made of a superalloy material mounted on an MTS clip-on displacement gage 632.02E-20 (not shown), which is commonly used in standard fracture toughness tests. As in the compression of pins, some notched bar experiments were interrupted and the specimens were unloaded several times to measure the anisotropy ratios, especially at incipient macroscopic crack formation. Unlike the situation in initially smooth tensile bars or compression pins, the plastic strains are spatially nonuniform in the gauge section of a notched bar. Hence, the following definitions are typically adopted; see Ref. [121]:

$$\bar{\varepsilon}_{\mathrm{X}} = \ln\left(\frac{\Phi_{\mathrm{X}}}{\Phi_0}\right), \tag{3.10}$$

$$\begin{cases} R^{\mathrm{L}} = \dfrac{\bar{\varepsilon}_{\mathrm{T}}}{\bar{\varepsilon}_{\mathrm{S}}}, \quad R^{\mathrm{T}} = \dfrac{\bar{\varepsilon}_{\mathrm{S}}}{\bar{\varepsilon}_{\mathrm{L}}}, \quad R^{\mathrm{S}} = \dfrac{\bar{\varepsilon}_{\mathrm{L}}}{\bar{\varepsilon}_{\mathrm{T}}}, \\ \\ R^{\mathrm{LT}} = \dfrac{\varepsilon_{TL}}{\bar{\varepsilon}_{\mathrm{S}}}, \quad R^{\mathrm{LS}} = \dfrac{\varepsilon_{SL}}{\bar{\varepsilon}_{\mathrm{T}}}, \quad R^{\mathrm{TS}} = \dfrac{\varepsilon_{ST}}{\bar{\varepsilon}_{\mathrm{L}}} \end{cases} \tag{3.11}$$

$$\bar{\varepsilon}_{\mathrm{f}} = \varepsilon_T\Big|_{\mathrm{f}} + \varepsilon_S\Big|_{\mathrm{f}}, \quad \bar{\varepsilon}_{\mathrm{i}} = \varepsilon_T\Big|_{\mathrm{i}} + \varepsilon_S\Big|_{\mathrm{i}}, \tag{3.12}$$

where the bar stands for spatial averaging over the minimum-diameter section (absolute values taken where appropriate). These definitions are the counterpart of equations $(3.1)_1$ and (3.4)–(3.7) in uniaxial bars. Most tests were stopped after crack initiation and before final fracture (after detecting a significant macroscopic load drop) but some were continued to final fracture. Crack initiation is detected by

a sudden drop in the load-displacement curve where is it marked by a black dot in some load-deflection graphs (see Figure 2.9 in Ref. [123] for further background on this identification). For each notch geometry, one specimen was taken to complete fracture then subsequent ones were interrupted at crack initiation.

3.3 Fractography and post deformation microstructural analyses

In the literature, two methods are typically used to identify damage initiation sites [123]. The first, more straightforward, consists of observing fracture surfaces in SEM. If void formation from second phase particles occurs and there is residual void–particle contact post-mortem, as would prevail in low triaxiality fracture, particles would be observed at the bottom of dimples. This is the standard method for identifying second-phase particles inside dimples by means of dispersion spectroscopy. The second, more tedious, consists of interrupting mechanical tests and subsequently sectioning the specimens using Electric discharge machining (EDM) and searching (in OM or SEM) for some evidence of void formation [121]. Each method has its advantages. The disadvantage of the first is that mere observation of particles on the fracture surface does not necessarily inform on the extent to which they were involved in the fracture process. The disadvantage of the second is that it only samples through two-dimensional sections. In general, a combination of both is necessary to obtain a full picture. This has been accomplished in the present study. In material systems where particles are larger than, say 1μm, X-ray computed microtomography [124] and laminography [125] present obvious advantages over the destructive methods used here. It would be difficult, however, to rely on these methods for identifying damage initiation sites at lower length scales, such as twinning-induced cracks. To prevent oxidation, the fracture surfaces of broken specimens were sprayed immediately after testing with a silicone mold release spray

then placed and held in a vacuum desiccator prior to being examined in SEM. It is worth noting that, even with extreme care, oxidation is such a major problem in magnesium that fracture surfaces can only be observed once. For this reason, the testing campaign has been paced to accommodate SEM observations of oxide-free fracture surfaces. Occasionally, EDS and WDS spectra of the second phases on the surface were recorded.

In addition to the SEM fractographs, the tensile (smooth and notched) specimens that were deformed until failure initiation (see above) were cut longitudinally using wire EDM. Observations were then made in optical microscopy and SEM in L–S and L–T planes, i.e., sections that contain the loading direction (L) and the short-transverse (S) or transverse direction (T), respectively. Samples containing the damage process zone were subsequently mounted in an epoxy resin to prepare metallographic sections. The method described for microstructural observations (Section 3.1) was followed. Magnesium and its alloys are among the most difficult metallic samples to prepare for microstructural examination. This is particularly true in heavily deformed specimens with features such as microcracks, microvoids and eventually macroscopic cracks. Extra care was thus taken to prepare the sections for damage observations.

3.4 Microtomography analysis

Tomography, which is based on radiography, employs similar principles as medical scanners but uses synchrotron radiation. Using numerical procedures, 2D scans could be utilized to reconstruct a 3D image of the microstructure with sub-micron resolutions. These 3D maps provide such rich information, which are instrumental for the understanding of a wide range of phenomena. Microtomography analysis was performed on notched bar specimens loaded along the T direction. The specimens

with highest (RN2) and moderate triaxiality (RN10 specimens, where the maximum strain to failure is obtained) are used for microtomography analysis. Samples were obtained form interrupted tests after incipient macroscopic crack formation. The specimens were cut longitudinally ($\parallel$ to T and along the L direction) to obtain samples from notch root (close to surface) and its middle (central) section. The tomography analysis was done as part of a collaborative study on fracture of magnesium alloys with Dr. T. Morgeneyer at Centre des Matriaux MINES, Paristech. The analyses were performed at the European Synchrotron Radiation Facility (ID19 line) using photon energy 19 keV to get high resolution images with the voxel size of 0.7 μm. Synchrotron radiation leads to a parallel beam geometry. For each section, 1500 radiographs are recorded to build a 3D image of the microstructure using filtered backprojection algorithm. The time required to take each radiograph is 0.7 s. The open-source image analysis software *"ImageJ"* is used to adjust the micrographs and 3D microstructure reconstruction.

This experiments enable investigating the effect of stress state triaxiality on damage initiation, its location with respect to notch geometry, prominent direction of macroscopic crack growth and state of damage at the onset of macroscopic crack initiation. The dependence of damage initiation location with respect to the notch geometry and local variation of triaxiality is facilitated using specimens from the center of the notch and its root.

4. INITIAL MICROSTRUCTURE

4.1 Initial microstructure: AZ31

Figure 10a shows 3D OM representation of initial microstructure of AZ31 plate. Analyses the size of 997 grains in different planes of the plate, using *ImageJ* image analysis software, revealed that the initial microstructure of the current AZ31 exhibits a dual grain size distribution with diameter of small grains approximately $3 - 4\mu m$ and large grains $\sim 10 - 12\mu m$. A histogram of grain size distribution in this alloy is presented in Figure 11. Small and recrystallized grains (formed during hot rolling at elevated temperature) are usually lumped together and form band-like features, which hare elongated perpendicular to S direction in L-S and T-S planes. Distribution of recrystallized grains in L-T plane is rather random, giving a transverse-isotropic appearance to this plane. Second phase particles (black colored) are also discernible in the microstructure. As a result of hot-rolling process, these particles are broken and elongated along the L direction. Few deformation twins are observed in the initial microstructure. Macroscopic texture measurement, shown in Figure 10b, indicates that the hot-rolled AZ31 plate exhibits a strong basal texture with c-axis of most grains aligned parallel to the S direction.

Figure 12 shows 3D SEM micrograph of the AZ31 plate. The preferred orientation of second phase particles (along the rolling direction) is clearly depicted in this figure. Three types of second-phases particles were observed in undeformed samples. The first type consists of intermetallic Al–Mn rich, probably Al_8Mn_5 dispersoids [126]. They appear as stringers elongated in the rolling direction or as isolated particles. Their composition was ascertained using EDS; See Figure 13a. The second type of particles consists of $Mg_{17}Al_{12}$ intermetallics with a cubic struc-

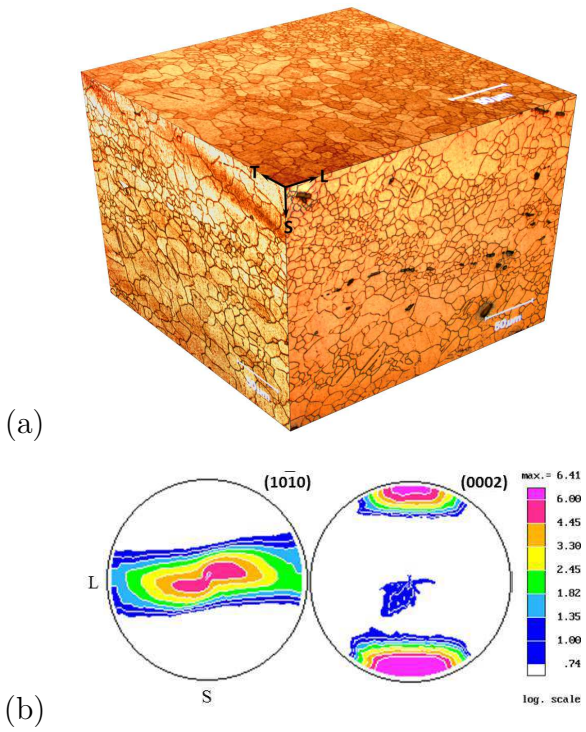

Figure 10: (a) Three dimensional representation of the initial microstructure of hot-rolled AZ31B plate exhibiting a dual grain size distribution. (b) XRD pole figures corresponding to (0002) and (10$\bar{1}$0) planes.

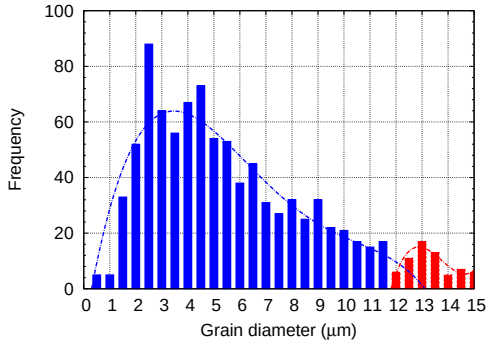

Figure 11: Grain size distribution in AZ31 plate. The histogram is obtained by measuring the size of ∼1000 grains in L–T, L–S and T–S plane.

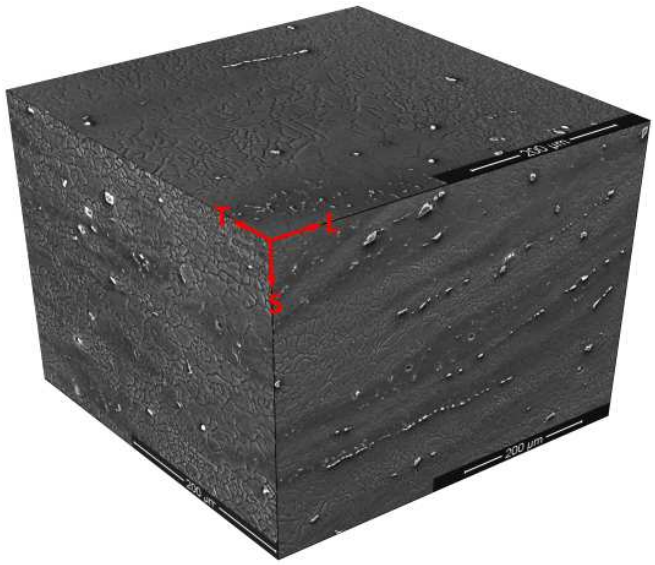

Figure 12: Three dimensional SEM representation of the initial microstructure of hot-rolled AZ31B plate showing preferred orientation of second-phase particles in the microstructure of the as-rolled material.

ture. They are present in two forms: fine, often sub-micron lamellar precipitates and larger equiaxed particles. The fine precipitates form most likely during cooling form hot-rolling temperatures. They appear mostly in regions of high Al content and decorate grain boundaries. On the other hand, the particles form during solidification. While larger than the precipitates, their number frequency is much smaller. As shown in Figure 13b, they can be found at grain boundaries or in the grain interior. The presence of both Al–Mn and $Mg_{17}Al_{12}$ intermetallics is expected in Mg–Al–Zn–Mn alloy systems [52]. A third type of particles was occasionally observed. They appeared as equiaxed and darker in SEM. The presence of an O peak in the EDS spectra suggests that these particles might be MgO oxides mixed with Mg–Al particles. The presence of oxide/intermetallic particles has recently been reported in [24] and will be further ascertained on fracture surfaces. There are also contrast bands in the microstructure, observed parallel to the rolling direction. Based on WDS

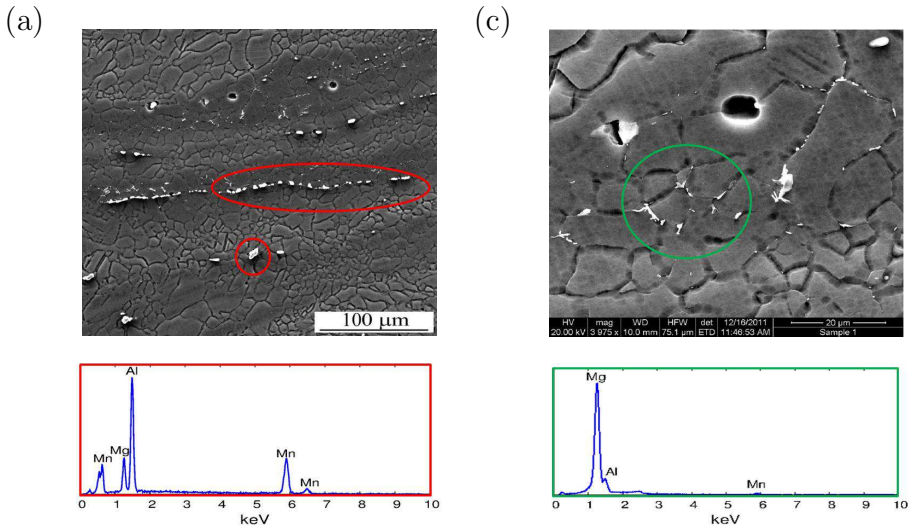

Figure 13: Various second phase particles with different morphology in the micostrucutre of as-received AZ31 alloy. The EDS analysis of particles, which are marked by lines, are presented below each micrograph.

micro-analysis, the variations in Al content is identified as the origin of these contrast bands. The observed compositional variation is assumed to be caused by high rates of solidification during casting.

4.2 Initial microstructure: WE43

Figure 14a shows the 3D OM representation of WE43 initial microstructure along the principal directions of the hot-rolled plate (namely L, T and S direction). As it is depicted in this figure, the distribution of grain size varies in different planes. For instance, some grains in the L–S plane are compressed in S direction and elongated along the rolling direction whereas L–T plane exhibits equiaxed grains. T–S plane has mainly equiaxed grains although few of its grains show squeezed morphology. In addition, grains in the T–S plane have considerable fluctuation in their size to such an extent that a dual grain size distribution is easily discernible in this plane. Other planes also accommodate a range of grain sizes although their grain size variations is

less intense. Second phase particles in the matrix or at grain boundaries (GB) can be observed as tiny black dots and bright points depending on their composition, lighting direction and microscope settings. The results of macroscopic texture measurement on the initial material, parallel to the T direction is presented in Figure 14b, where pole figures for two planes, i.e., $(10\bar{1}0)$ and (0002), are shown. As it is depicted in this figure, the presence of Yttrium (Y) and RE elements in WE43 leads to significant texture weakening compare to pure Mg and traditional Mg alloys such as AZ31. THenominal chemical composition of the WE43 plate are presented in Table 2.

Table 2: Nominal chemical composition of WE43 alloy used in this study [31].

Element / Alloy	Yttrium	Rare Earth	Zirconium	Magnesium
WE43	3.7–4.3 (%)	2.3–3.5 (%)	0.2 (%) min.	bal.

The basal pole in WE43 is also shifted towards the rolling (L) direction. Texture weakening at the presence of Y and Nd is expected based on the previous studies [46,127,128]. Grain size measurement was done utilizing *ImageJ* software. Figure 14c shows the grain size distribution in WE43 alloys, acquired by measuring the area of 352 grains in different planes. Noted that the reported grain diameters are calculated by assuming circular grains. According to this figure, WE43 exhibits a dual grain size distribution with diameter of small grains $D \sim 10\mu m$ and large grains around $D \sim 25\mu m$.

(a)

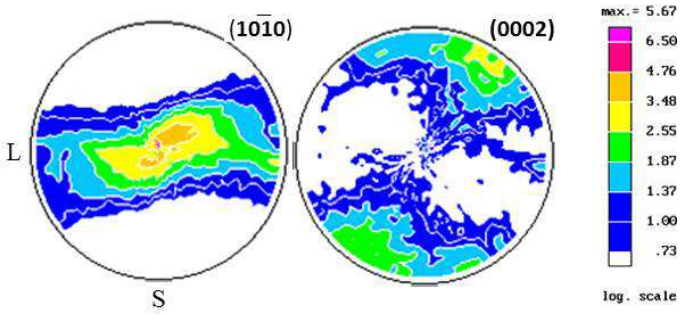

(b)

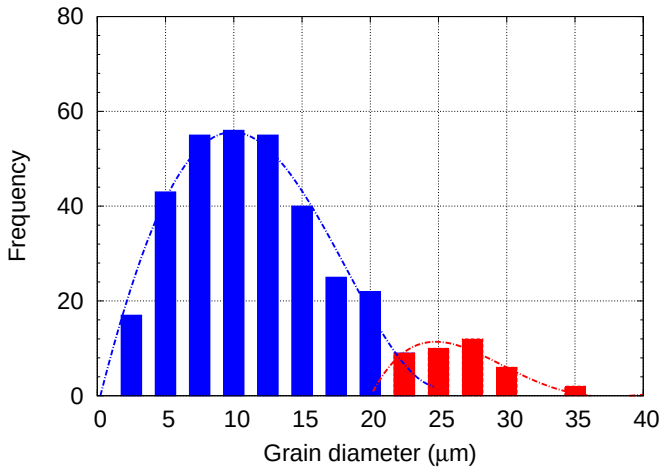

(c)

Figure 14: (a) Three dimensional optical microscope representation of initial microstructure of WE43 hot-rolled plate. (b) The XRD pole figures corresponding to (10$\bar{1}$0) and (0002) planes. (c) Grain size distribution in the microstructure of WE43 alloy. This data is based on measuring the size of 352 grains.

Figure 15 shows 3D SEM micrograph of WE43 plate. The preferred orientation of second phase particles (along the L direction in the L–S plane and parallel to T direction in the T–S plane) is clearly depicted in this figure. As it is shown, the L–T plane has a uniform distribution of second phase particles. Closer look reveals that the grain boundaries in this alloy are decorated with very fine particle. In addition to this GB particles, there are some large, round and bright particles, located at both grain interiors and at the vicinity of GBs. Utilizing EDS, the particles in this alloy are identified as those faceted particles that contain Mg-Y, Mg-Nd, Mg-Y-Nd. In addition, there are irregular-shaped, fine Mg-Zr particles which appear as clusters or individuals located in close proximity of each other. Ratio between the elements' peaks, phase diagrams' information (Mg-Nd and Mg-Y) and data from the literature [36, 129–131] are used to qualitatively identify these particles as $Mg_{41}Nd_5$, Mg_2Y, $Mg_{24}Y_5$, $\beta - Mg_{14}Nd2Y$ and $Mg - Zr$. These particles are distributed in an $\alpha - Mg$ matrix and its grain boundaries. High number density of particles at GBs is in accord with other experimental observations [87] and could rationalized by segregation of alloying elements at these interfaces [47]. It is worth noting that there might be nano-sized precipitates, such as Mg_2NdY and Mg_3Nd, present in the matrix which are not visible in the current SEM micrographs [87, 132].

Several regions with white contrast are also observed in the L–S and T–S planes. EDS mapping, presented in Figure 16 indicates that these bands are regions of Zr rich solid solution (Figure 16d). As shown in part (a) of this figure, the boundary of these contrast bands are also decorated with second phase particles, rich with Nd element. Nd is also present in the matrix as solid solution element although with lower concentration; see figure 16c for details of Nd distribution. According to part b of this figure, Yttrium element (Y) is uniformly distributed in matrix and second phase particles of this part of the microstructure.

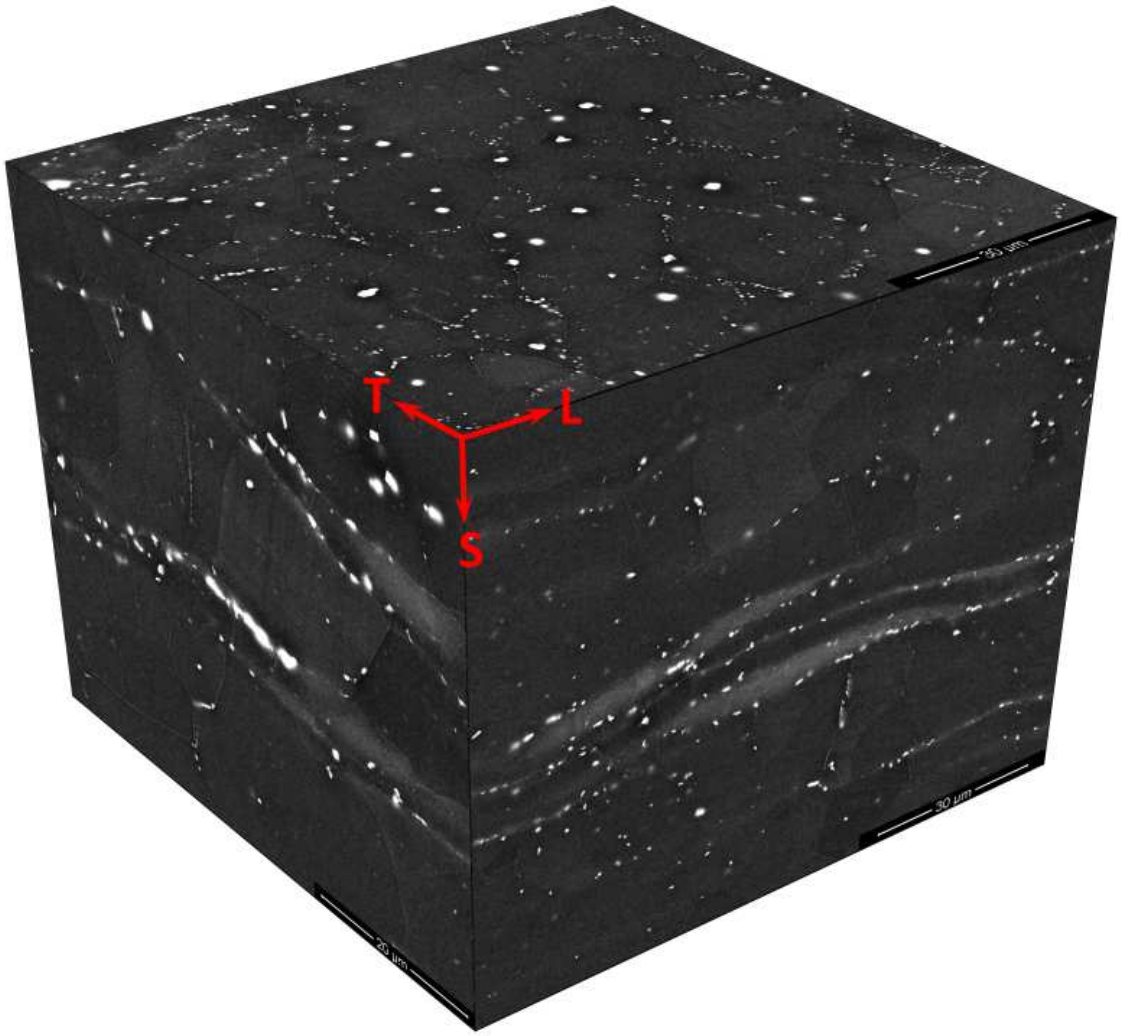

Figure 15: Three dimensional SEM representation of WE43 initial microstructure and spatial distribution of its second phase particles.

(a)

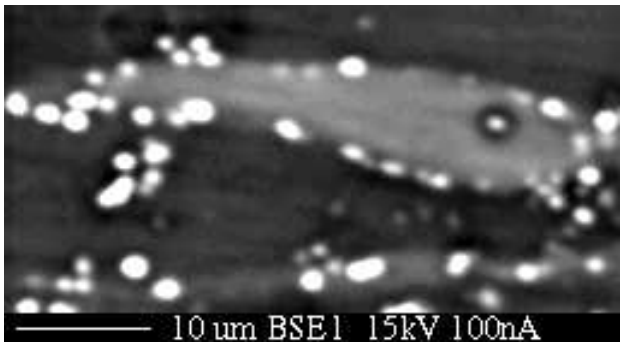

(b)

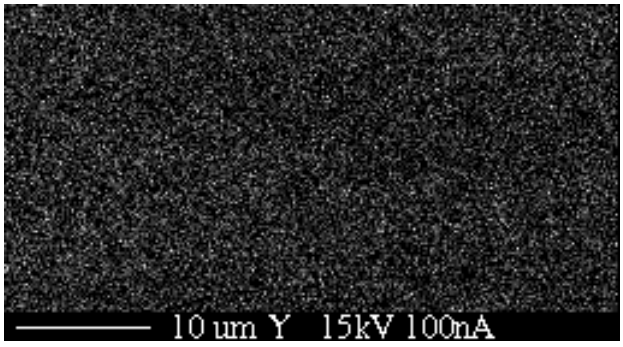

(c)

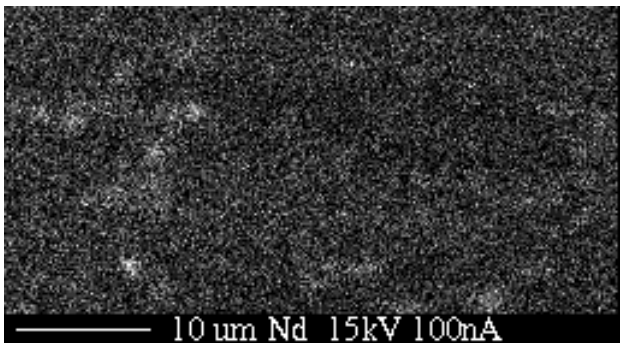

(d)

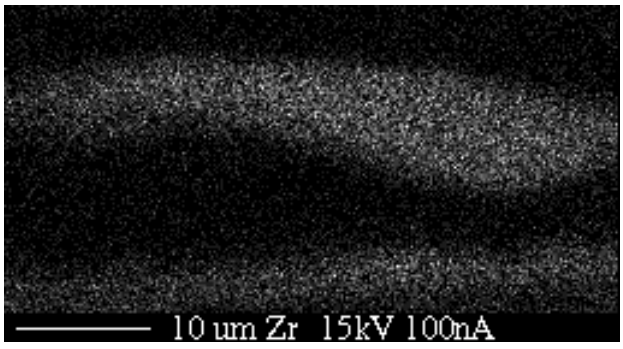

Figure 16: (a) SEM micrograph of WE43 alloy showing a typical contrast band in L–S plane. The boundaries of these contrast bands are decorated with second phase particles. EDS map of (b) Y, (c) Nd and (d) Zr.

5. MECHANICAL BEHAVIOR CHARACTERIZATION*

5.1 Flow behavior and anisotropy of AZ31

Typical nominal stress versus nominal strain responses of AZ31 in tension and compression parallel to the rolling (L) direction are shown in Figure 17a. This figure illustrates the unloading parts for the measurement of anisotropy ratios. The corresponding true stress–strain curves, depicted in Figure 17b, exhibit the usual tension–compression asymmetry. True-stress corrections were made so as to keep the same hardening rate as before necking. Better corrections are possible [133] but were not pursued here because the post-necking deformation is small. The compressive yield strength is considerably lower than in tension but the ultimate strengths are comparable.

Figure 18 shows typical results of plastic anisotropy evolution in AZ31 alloy for data presented in Figure 17. In compression along L direction, the relatively easy activation of extension twinning renders the material significantly more deformable along S (i.e., parallel to the c-axis) than along T (Figure 18a). The lack of deformability along T up to a strain of $\sim 5\%$ is a strong indicator of the limited number of deformation systems that are active post-yield. In fact, the formation of extension twins at the onset of plastic deformation also results in an unusual lateral contraction along the T direction; notice the initial decrease in ε_{T} in the inset of Figure 18a. This phenomenon is consistent with recent observations [134]. In subsequent stages of plastic flow, accumulated activity on other deformation systems, such as basal and prismatic $\langle a \rangle$ slip, induces enough plastic strain along T to overcome the negative

*Reprinted with permission from "Fracture strains, damage mechanisms and anisotropy in a magnesium alloy across a range of stress triaxialities" by Kondori, B. and Benzerga, A. A., 2014. Experimental Mechanics 54, 493-499, Copyright, Society for Experimental Mechanics 2013

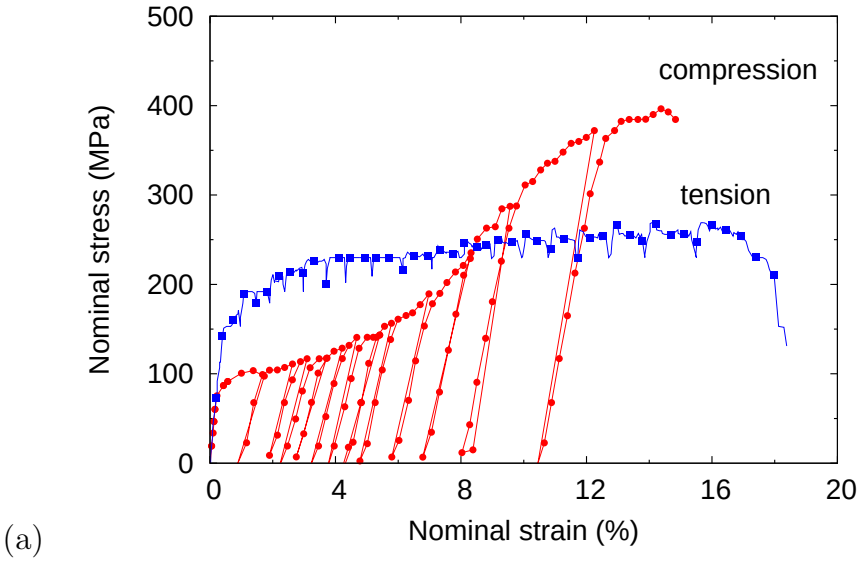

(a)

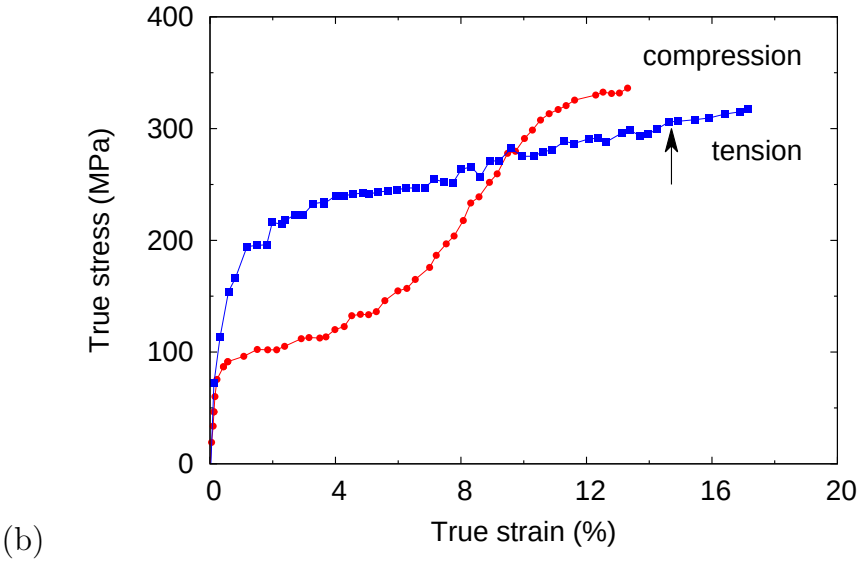

(b)

Figure 17: (a) Typical nominal stress versus nominal strain curves of AZ31 loaded parallel to L direction depicting full and partial unloadings in compression and tension, respectively, for R-value measurements. (b) True stress–strain curves. The arrow indicates the onset of necking. Post-necking corrections were applied keeping a similar hardening rate.

strain produced by extension twins and thus results in a net positive strain along this direction.

In tension parallel to L, on the other hand, the maximum lateral strain is along T (Figure 18b). This change is rationalized as follows. Under in-plane tensile loading, the polarity of extension twinning is such that it is not activated as easily as in compression. Instead, basal and prismatic slip are active from the outset of plastic deformation. These mechanisms, however, cannot accommodate the lateral strain along the S direction, only along T. To accommodate the lateral straining along S, i.e., the contraction along the c axis, contraction twinning and/or pyramidal slip must occur. The fact that the critical resolved shear stresses of these systems are relatively high explains the delay in their activation so that the T direction experiences more strain than the S direction. It is important to note that all deformation systems (slip and twinning) must be active in the early stages of plastic flow because some net deformation along S is measured from the outset.

The evolution of the anisotropy ratio R^{L} with strain is shown in Figure 18c, where the inverse of R^{L} is plotted for convenience. The error in R ratio measurement is large at strains below 0.1% (of order of R itself), but decreases rapidly ($0.2R$ at $\varepsilon_{\mathrm{L}} = 0.005$ and $0.02R$ at $\varepsilon_{\mathrm{L}} = 0.05$). For this reason, the ordinate axis is truncated for clarity. Also the inset shows the negative anisotropy ratio shortly after yielding. Figure 18c reveals two essential aspects of plastic flow anisotropy in AZ31B: (i) the existence of a steady state after a transient regime; and (ii) the extreme behavior during the transient. For instance, in compression values of $1/R^{\mathrm{L}}$ in excess of 10 are amenable to the lack of deformability along T (see Figure 18a). In tension $\parallel$ to L direction, the S direction is actually more deformable ($R^{\mathrm{L}} < 1$ as in compression) during the transient. In steady state, however, the anisotropy ratio is about 1.8 in tension and 0.35 in compression. The fact that $R^{\mathrm{L}} < 1$ in compression and $R^{\mathrm{L}} > 1$ in tension is consistent with the rationales provided above in what concerns the evolution of lateral strains.

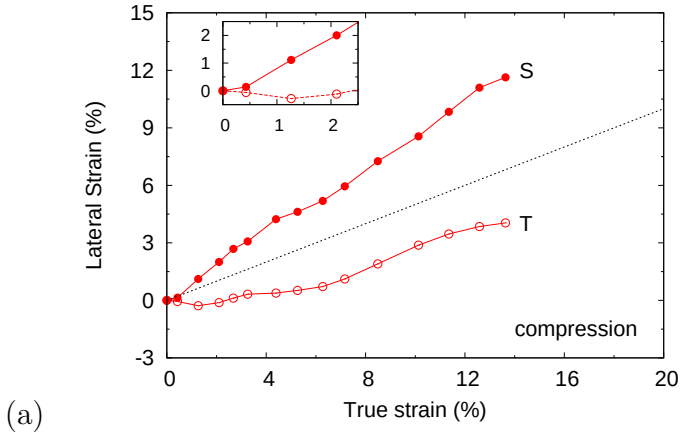

(a)

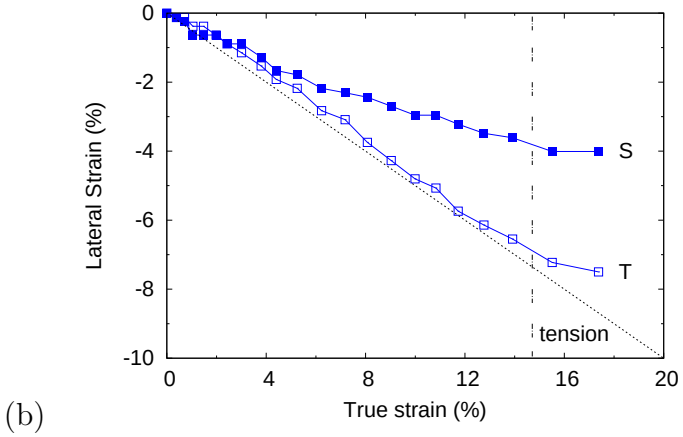

(b)

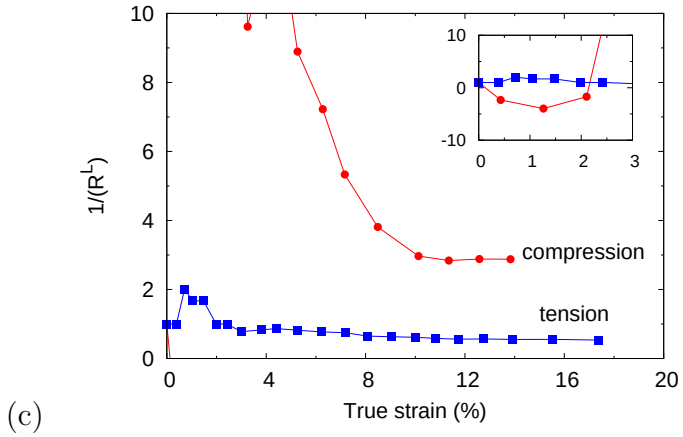

(c)

Figure 18: Lateral strain (along T or S as labeled) versus axial strain along L in (a) compression and (b) tension. Dotted lines point to a reference isotropic response. Inset in (a) shows the negative (contraction) strain along T in the early stages of compression. The necking strain is indicated by the vertical dashed line in (b). (c) Anisotropy ratio versus axial strain showing the transient and steady states. A detail of the transient (negative anisotropy ratio) is depicted in the inset. Values of $1/R^L$ larger than unity mean a greater ability to deform along S (parallel to the c-axis).

Interestingly, the evolution of anisotropic deformation is accompanied by a non-negligible dilatation. Figure 19 depicts the volumetric strain ε_{kk} (the sum of the three logarithmic strains $\varepsilon_{\mathrm{L}} + \varepsilon_{\mathrm{T}} + \varepsilon_{\mathrm{S}}$) versus the axial strain ε_{L}. A positive value of ε_{kk} indicates dilatation whereas a negative value indicates volume shrinkage up to experimental errors. Similar strain measurements were done on three different specimens in both tension and compression. The results were reproducible with little scatter. The error bars become larger in compression after a 0.1 strain due to barreling (not visible to the naked eye but quantified using top, center and bottom diameter measurements). The development of dilatational strains in tension was already evident in Figure 18b as the T-strain follows approximately the isotropic reference line while the S-strain is smaller. In a plastically incompressible material, the curves corresponding to the two lateral strains would be on either side of the dotted line so that the constraint $-(\varepsilon_{\mathrm{T}} + \varepsilon_{\mathrm{S}}) = \varepsilon_{\mathrm{L}}$ is satisfied. Figure 19 shows that there is a net increase in volume in both compression (2%) and tension (up to 6% after necking). A number of uniaxial tension and compression tests were performed to confirm the volume change. Result of such experiments are presented in Figure 20 indicating that increase in volume is detected in other specimens as well.

As mentioned before uniaxial experiments are performed along various directions of the Mg plates. Figure 21(a) depicts the true-stress versus true strain of AZ31 specimens compressed along three principal direction of the plate (i.e., L, T and S). Complex behavior of this alloy is clearly shown in this graph. The evolution of anisotropy ratios are also shown in part (b) of this figure. In this figure and for illustration purposes, anisotropy ratios for loading parallel to T and S are depicted whereas the inverse of anisotropy ratio along the L direction is shown.

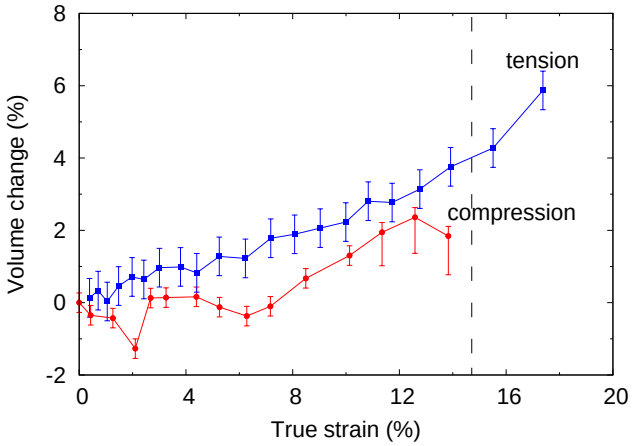

Figure 19: Relative volume change versus axial strain in compression and tension. Vertical dashed line indicates necking in tension.

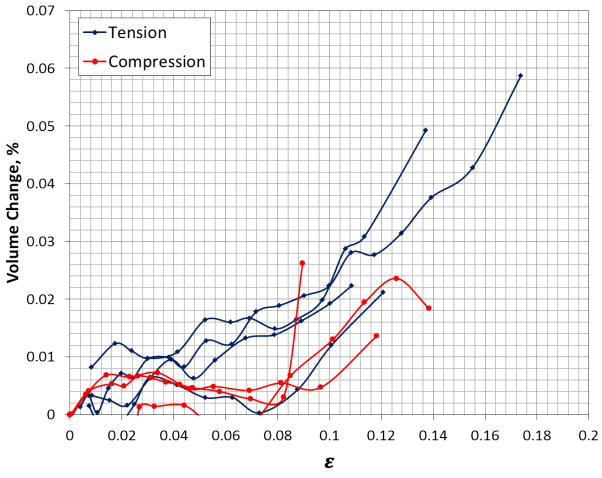

Figure 20: Relative volume change versus axial strain in compression and tension for a number of tests along rolling direction.

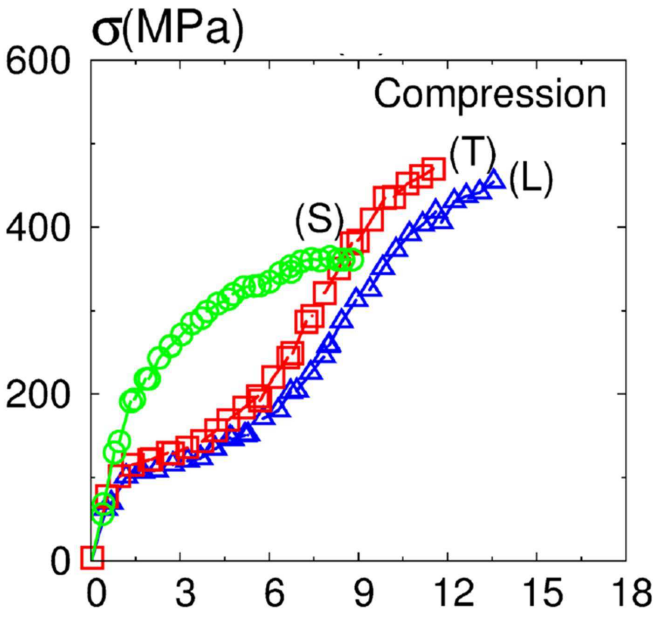

(a)

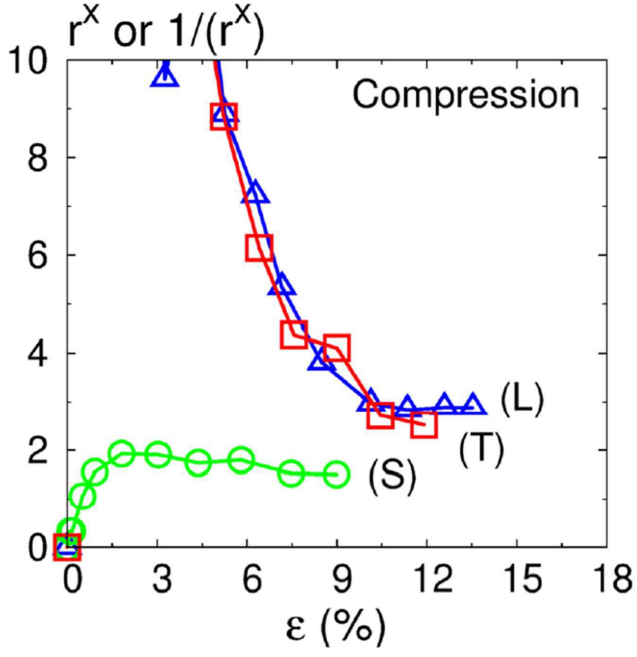

(b)

Figure 21: (a) True stress–strain behavior in compression for three loading orientations. (b) Anisotropy ratios $1/R_L$, R_T and R_s versus strain.

A summary of the flow stresses at different axial strains during uniaxial compression and tension of AZ31 specimens along various directions are presented in Table 3 and 5, respectively.

Table 3: Flow stress of AZ31 during uniaxial compression parallel to various directions of the plate.

Flow stress / Direction	σ_{yield}	$\sigma_{3\%}$	$\sigma_{6\%}$	$\sigma_{9\%}$	$\sigma_{12\%}$	σ_{UTS}
L	104.50	125.05	172.81	295.29	331.25	341.08
T	112.50	127.39	193.40	321.53	357.94	370.88
S	173.00	249.17	305.63	306.88	-	311.00
TS	83.00	122.13	164.48	188.02	218.87	234.29
LS	96.00	127.94	176.12	226.88	240.00	240.90
LT	108.50	122.86	178.95	301.77	360.64	364.50

Table 4: Evolution of anisotropy ratios in AZ31 during uniaxial compression parallel to various directions of the plate.

R^X / Direction	R_{yield}	$R_{3\%}$	$R_{6\%}$	$R_{9\%}$	$R_{12\%}$	R_{SS}
L	-0.50	0.03	0.10	0.20	0.24	0.31
T	-2.52	24.38	6.14	4.11	2.72	2.66
S	0.33	1.90	1.80	1.50	-	1.55
TS	1.00	4.36	3.98	2.29	2.67	2.28
LS	7.99	16.15	10.53	8.77	7.78	6.95
LT	1.00	0.05	0.11	0.21	0.36	0.42

Corresponding to such data, evolution of anisotropy ratios during uniaxial compression and tension are also given in Table 4 and 6, respectively.

Table 5: Tensile flow stress of AZ31 during uniaxial deformation parallel to various directions of the plate.

Direction \ Flow stress	σ_{yield}	$\sigma_{3\%}$	$\sigma_{6\%}$	$\sigma_{9\%}$	$\sigma_{12\%}$	σ_{UTS}
L	152.00	225.82	247.63	271.23	289.58	294.74
T	181.33	236.55	251.56	272.45	286.00	292.36
S	-	-	-	-	-	-
TS	58.00	123.48	185.48	-	-	185.66
LS	86.00	131.84	175.30	-	-	200.00
LT	184.75	239.72	273.84	286.86	295.87	306.01

Table 6: Evolution of anisotropy ratios in AZ31 during uniaxial tension parallel to various directions of the plate.

Direction \ R^X	R_{yield}	$R_{3\%}$	$R_{6\%}$	$R_{9\%}$	$R_{12\%}$	R_{SS}
L	1.00	1.29	1.30	1.58	1.78	1.70
T	1.01	0.67	0.48	0.42	0.36	0.39
S	-	-	-	-	-	-
TS	2.35	2.31	2.16	-	-	2.16
LS	2.95	3.38	2.64	-	-	2.24
LT	0.87	1.39	1.66	1.94	2.20	2.01

5.2 Flow behavior and anisotropy of WE43

Figure 22 presents the mechanical response of WE43 alloy under uniaxial compression along three different directions of the plate and their associated anisotropy ratios. The nominal stress-nominal strain response of WE43 along three principal directions (i.e. L, T and S) is shown in Figure 22a. The final stage of each experiment is accompanied with a load drop. This load-drop prior to failure in compression is slow and it covers a relatively large range of strains before final failure by splitting. In contrast to the response of pure Mg and common magnesium alloys such as AZ31 and ZK60 [22], there is no significant anisotropy in the yield and flow stress of WE43. The well-known S-shaped flow during compression along in-plane directions is also absent in these plots. Corresponding anisotropy ratios of these experiments are plotted in Figure 22b. This figure indicates that although the R^S is close to unity for loading along the (S) direction (i.e. lateral strains being independent of direction), there is considerable anisotropy in lateral strains when WE43 is compressed along the L and T directions. This anisotropy manifests itself as significant deviations of anisotropy ratios from unity (See Figure 22b). Note that in Figure 22b, the anisotropy ratios for loading along L ($\sim$1.8) and T ($\sim$0.5), are in fact indicative of a transversely isotropic behavior. This means that L and T direction in WE43 are nearly identical and the difference in their anisotropy ratios is caused by the adopted definitions (See Equation 3.4).

The uniaxial tension and compression response along the (L) direction are compared in Figure 23a. Here, the true stresses are plotted against trues strain in the bar. The load-drop region in the compression curve is replaced by a straight line that has the slope of flow stress immediately before the onset of softening. As it is depicted in this figure, the tension/compression asymmetry does not exist in WE43.

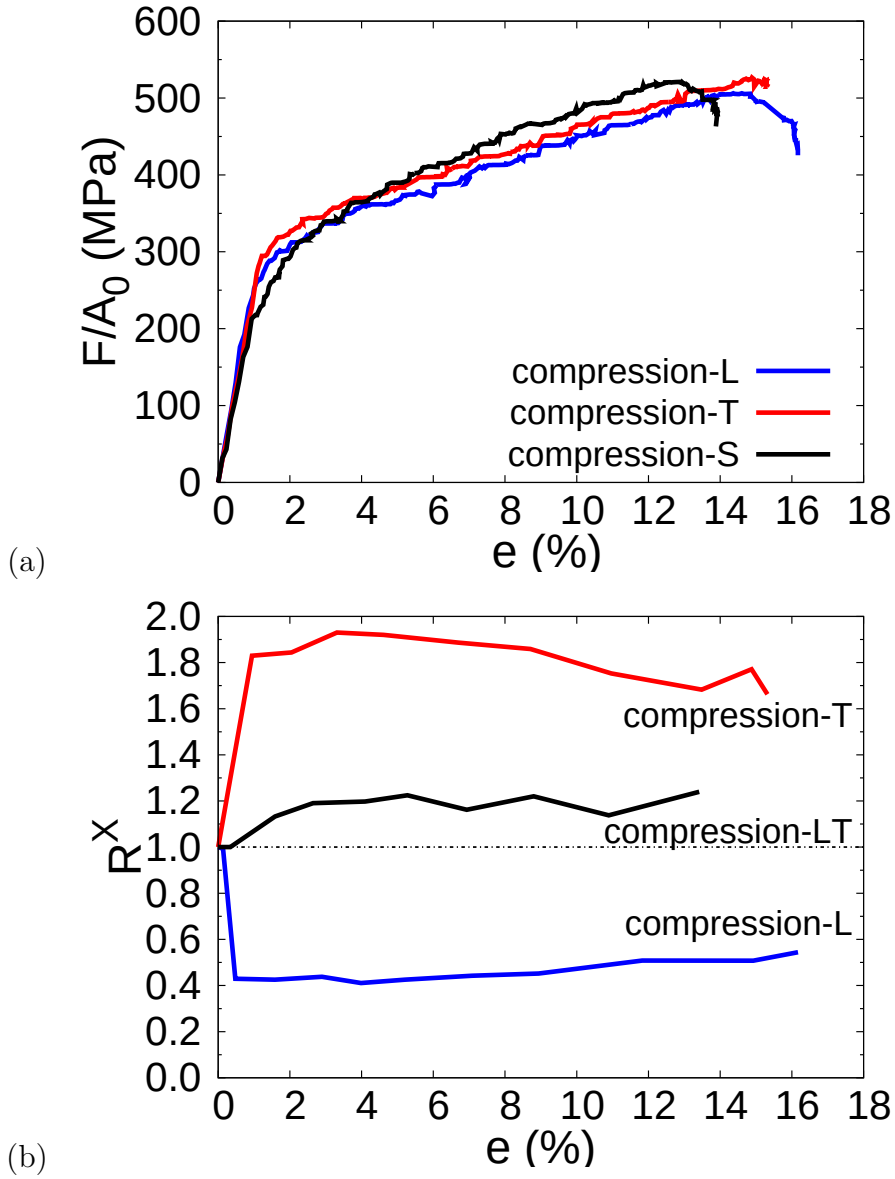

Figure 22: Nominal stress-strain behavior of WE43 along three principal directions (L, T and S) under compression. (b) Anisotropy ratios R^X (i.e. R^L, R^T and R^S) based on nominal strains versus nominal axial strain corresponding to the curves in part (a). The load-drop region in the compression curve is replaced by a straight line that has the slope of flow stress immediately before the onset of softening.

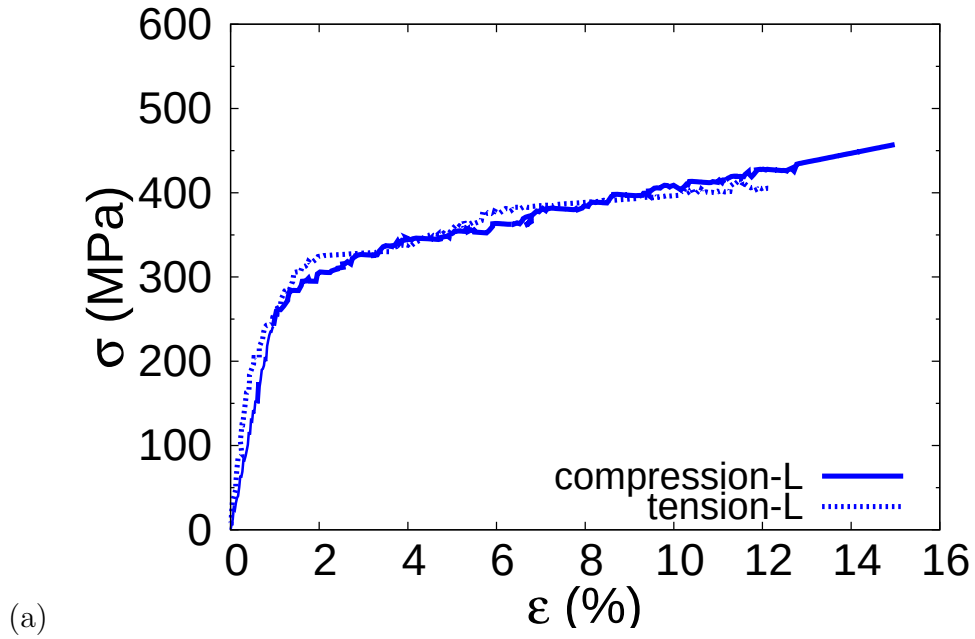

(a)

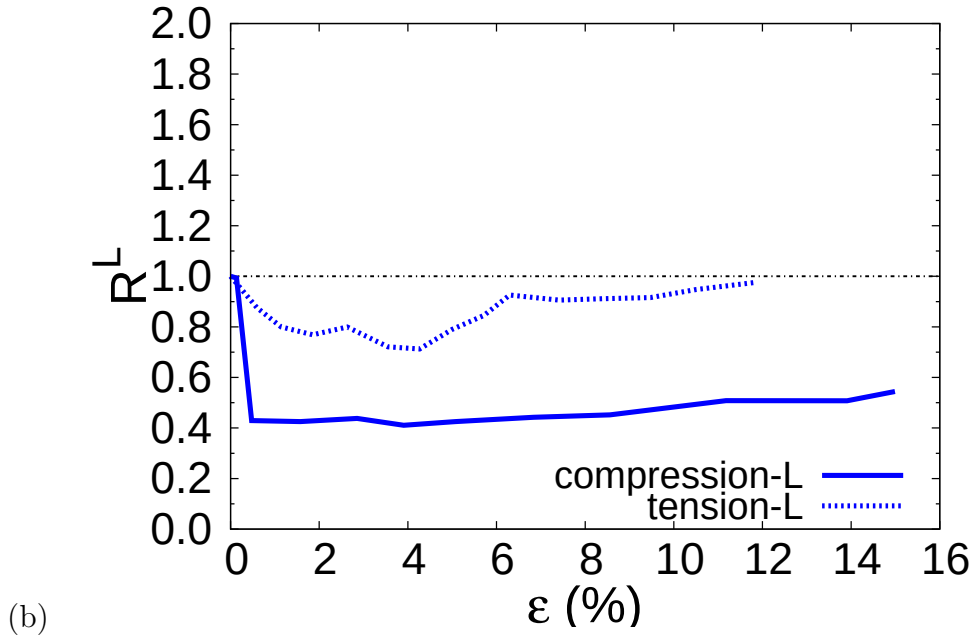

(b)

Figure 23: (a) True stress-strain behavior of WE43 in tension and compression along L direction and (b) associated anisotropy ratios (R^L) versus strain corresponding to curves presented in part (a).

Under uniaxial tension, the specimen fractures catastrophically with neither load drop prior to fracture nor a developed neck. Although flow properties under uniaxial tension and compression along L direction are very similar, the lateral strains and their ratios are significantly different in the two loading conditions; see Figure 23b). The results of this figure indicate that during tension, the lateral strains in WE43 are independent of direction and the initial circular cross-section retains its shape.

Similar to AZ31, uniaxial experiments of WE43 were done along six different directions. Flow stress and anisotropy ratios along these directions (three principal and three off-axis directions with 45° between the two principal directions) during compression experiments are presented in Tables 7 and 8, respectively. The data for tensile experiment is also presented in Tables 9 and 10. In addition, a summary of mechanical properties in all experiments are presented in Table 11. As it is shown in this table, the flow properties are more-or-less isotropic and tension/compression asymmetry is marginal. The only cases where the difference are considerable, are UTS data for LS and TS direction. This difference could be originated from limited ductility exhibited by specimens along these directions.

Table 7: Compressive flow stress of WE43 during uniaxial deformation along various directions of the plate.

Flow stress / Direction	σ_{yield}	$\sigma_{3\%}$	$\sigma_{6\%}$	$\sigma_{9\%}$	$\sigma_{12\%}$	σ_{UTS}
L	265.00	313.16	368.99	411.67	437.14	438.16
T	281.50	335.74	389.00	425.57	449.39	450.30
S	226.00	310.04	382.00	428.25	450.22	454.04
TS	228.00	310.01	358.32	394.98	416.20	409.49
LS	245.00	322.55	381.71	415.50	-	418.34
LT	263.50	313.70	367.67	398.90	423.84	434.49

Table 8: Evolution of anisotropy ratios in WE43 during uniaxial compression parallel to various directions of the plate.

R-ratio / Direction	R_{yield}	$R_{3\%}$	$R_{6\%}$	$R_{9\%}$	$R_{12\%}$	R_{SS}
L	0.71	0.40	0.44	0.47	0.50	0.52
T	1.91	1.92	1.91	1.85	1.73	1.69
S	1.00	1.22	1.19	1.22	1.23	1.21
TS	1.13	1.42	1.41	1.42	-	1.36
LS	1.08	1.37	1.54	-	-	1.43
LT	0.41	0.45	0.44	0.47	0.49	0.51

Table 9: Tensile flow stress of WE43 during uniaxial deformation along various directions of the plate.

Flow stress / Direction	σ_{yield}	$\sigma_{3\%}$	$\sigma_{6\%}$	$\sigma_{9\%}$	$\sigma_{12\%}$	σ_{UTS}
L	231.50	334.98	369.23	395.56	406.68	418.38
T	255.00	347.38	397.41	415.60	429.06	430.61
S	-	-	-	-	-	-
TS	222.00	307.30	337.10	-	-	337.10
LS	222.00	306.22	359.60	362.00	-	362.00
LT	254.50	359.80	393.92	425.81	437.93	439.56

Table 10: Evolution of anisotropy ratios in WE43 during uniaxial tension parallel to various directions of the plate..

R-ratio / Direction	R_{yield}	$R_{3\%}$	$R_{6\%}$	$R_{9\%}$	$R_{12\%}$	R_{SS}
L	0.69	0.69	0.82	0.89	0.98	0.98
T	1.25	1.08	1.00	0.97	0.94	0.94
S	-	-	-	-	-	-
TS	1.00	1.00	-	-	-	1.00
LS	1.26	1.00	-	-	-	1.00
LT	0.90	0.89	0.95	0.98	1.00	1.00

Table 11: Characteristics of mechanical response of WE43 under uiaxial loading along three principal directions and three off-axis directions, 45° between pairs of principal directions.

Property	Loading \ Direction	L	T	S	LT	LS	TS
Yield Strength (MPa)	Tension	231.5	255.0	–	254.5	224.0	222.0
	Compression	264.0	281.0	216.5	263.5	243.0	230.0
UTS (MPa)	Tension	418.4	430.6	–	439.6	358.0	337.0
	Compression	438.2	450.3	454.0	434.3	418.3	409.5
R-value†	Tension	0.98	0.94	–	1.00	1.00	1.00
	Compression	0.52	1.69	1.29	0.51	1.43	1.36

† reported R-values are measured at the end of deformation process and assumed to be steady state values.

The R-values in Table 11 are those acquired at the final stages of deformation when the R-values have reached a steady state (minimal change in their values as a function of strain) and before fracture. The R-values in tension are all close to unity which along with similar flow stresses at different directions suggest isotropy in this alloy under tension. In the case of compression, however, the R-values fall in a wide range between $\sim$ 0.5 and $\sim$1.8. These values suggest that circular cross section of the cylindrical pins becomes oval after compression.

The volumetric strain ε_{kk} (the sum of the three logarithmic strains $\varepsilon_{\mathrm{L}} + \varepsilon_{\mathrm{T}} + \varepsilon_{\mathrm{S}}$) was measured in each uniaxial test. These measurements versus the axial strain for tensile experiments carried out parallel to L, T and LT direction are reported in Figure 24. The compressive counterpart of these measurements for all six directions are presented in Figure 25. In all experiment, regardless of loading and its direction, a non-negligible dilatation is observed. Positive value of ε_{kk} indicates dilatation whereas a negative value indicates volume shrinkage up to experimental errors. Further study is required to reveal fundamental origins of such increases in volume.

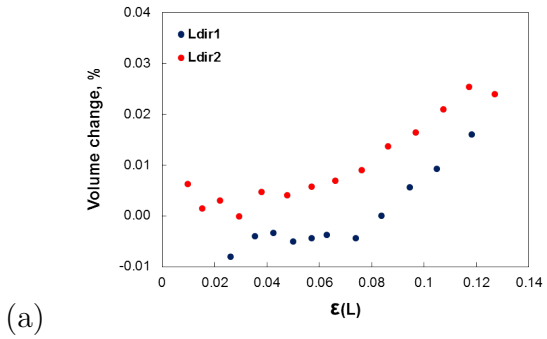

(a)

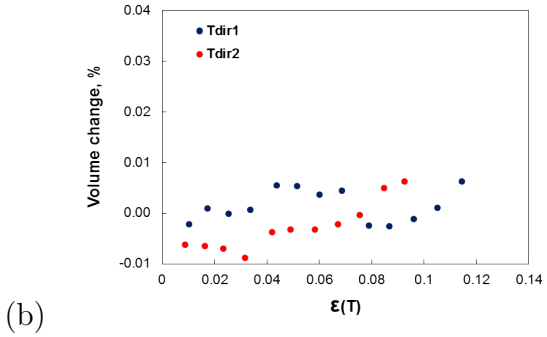

(b)

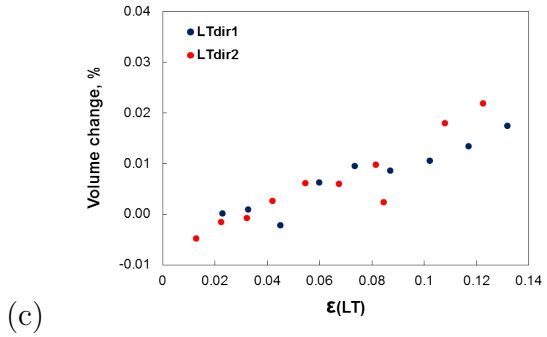

(c)

Figure 24: Relative volume change versus axial strain in tension parallel to (a) L, (b) T and (c) LT direction.

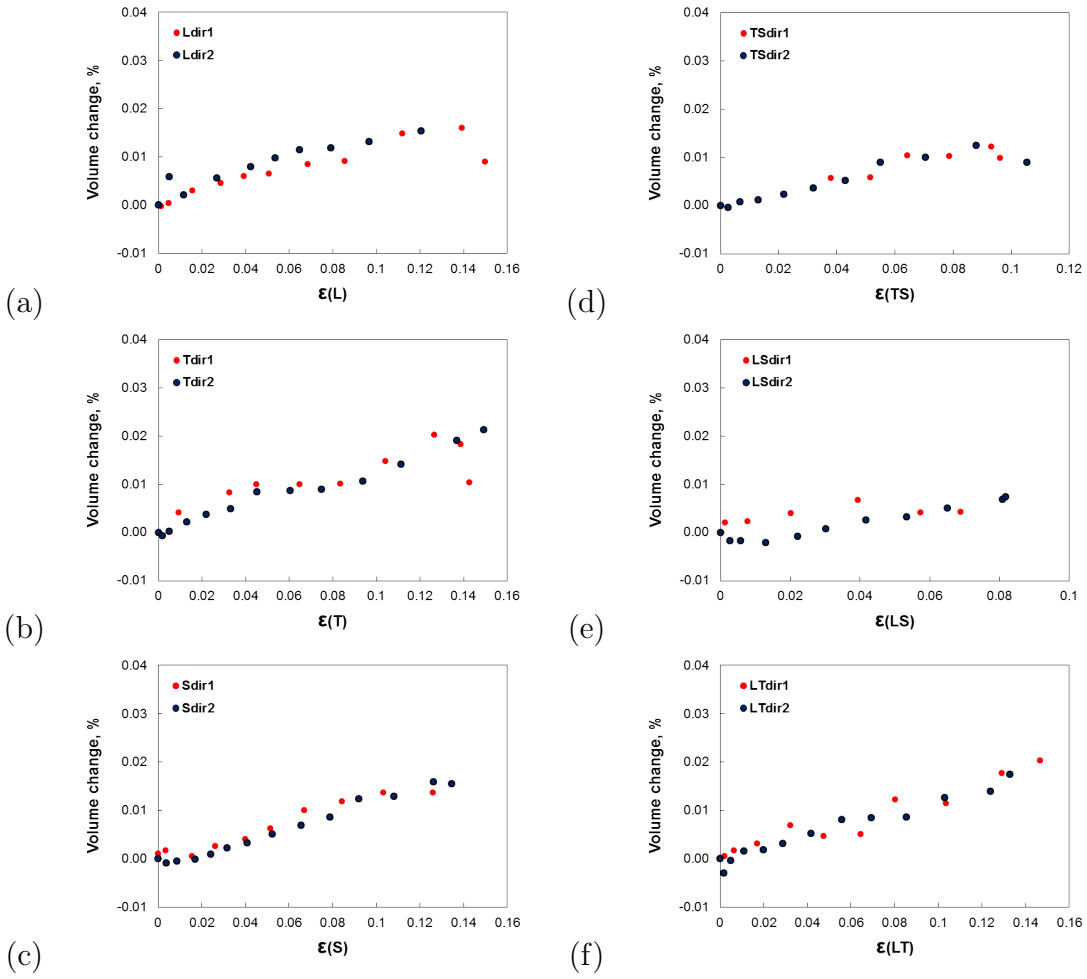

Figure 25: Relative volume change versus axial strain in compression parallel to (a) L, (b) T, (c) S, (d) TS, (e) LS and (f) LT direction.

6. DAMAGE AND FRACTURE CHARACTERIZATION*

6.1 Damage and fracture characterization of AZ31

In what follows the results of fracture experiments on uniaxial and notched bars with three different notch geometries along the L direction of the AZ31B plate are presented. The experimental observations and trends are explained and rationalized. Finally, the results of fracture tests on AZ31 along T and LT direction are presented. Since AZ31 with basal texture exhibits a behavior that is close to in-plane isotropy, the rationale proposed to justify the fracture behavior along L direction could also be applied to failure along T and LT direction.

Figure 26 shows the mechanical response of the three types of RN AZ31 specimens along L direction. Each response is given in terms of the applied load versus diameter reduction along the S direction (see Figure 8b above). Some expected scatter was observed on the maximum strains before load drop but there was less scatter on the limit loads. To illustrate the scatter in the response of different realizations, response of three different RN2 specimens are presented in Figure 27. Two tests in this figure were interrupted at macroscopic crack initiation. Only one test was taken to complete rupture (solid circle). For reference, the response of the smooth bar is also provided in Figure 26. For the the smooth bars, continuous measurement of $\Delta\Phi_S$ was acquired in addition to the discrete set of values made available on the basis of the anisotropy ratio measurements. However, since the radial extensometer is usually not located at the necked section the change in diameter recorded post-necking constitutes a lower bound.

*Reprinted with permission from "Effect of stress triaxiality on the flow and fracture of Mg alloy AZ31" by Kondori, B. and Benzerga, A. A., 2014. Metallurgical and Materials Transactions A, 2014. 45, 3292-3307, Copyright, Minerals, Metals & Materials Society and ASM International 2014

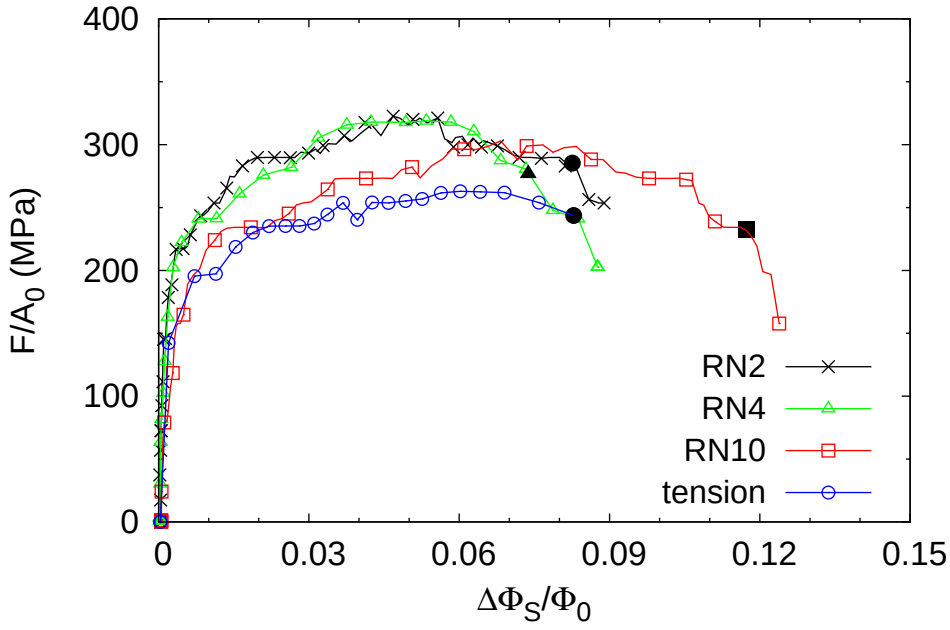

Figure 26: Force, divided by the initial cross-sectional area, versus relative reduction in diameter along S for the tensile (smooth and notched) specimens loaded along L direction. Filled symbols indicate the values used to define nominal strains at failure initiation (abrupt load drop).

In a plastically isotropic material the axial limit load increases with increasing the acuity of the notch as a result of notch-enhanced stress triaxiality [135]. In AZ31B this trend is observed in Figure 26; it is however weaker. Interestingly, there is barely any variation of the limit load between the RN4 and RN2 specimens. This observation hints at the interplay of plastic flow anisotropy and the achievable stress state triaxialities inside notches.

6.1.1 Effect of triaxiality on plastic anisotropy

The measured steady-state values of the anisotropy ratio R^{L} for fracture specimens are documented in Figure 28. The data for uniaxial tension bars and compression pins include those analyzed in detail in Section 5.1 and Figure 18. The values reported for the round notched specimens are according to definitions (3.10)

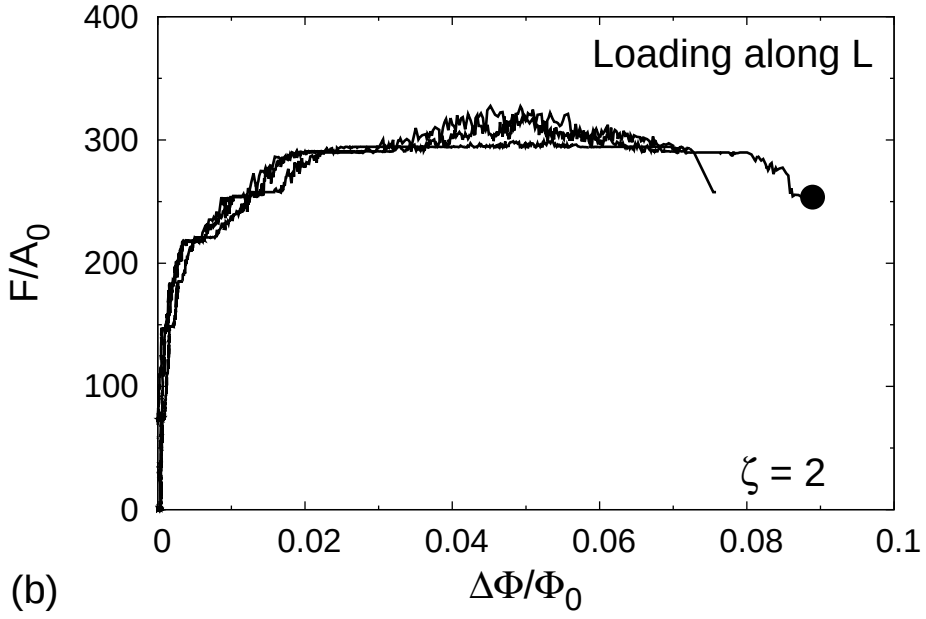

Figure 27: Force, divided by the initial cross-sectional area, versus relative reduction in diameter along S for the tensile (smooth and notched) specimens loaded along L direction. Filled symbols indicate the values used to define nominal strains at failure initiation (abrupt load drop).

at the abrupt load drop. The data in Figure 28 shows a clear trend of a decreasing anisotropy ratio with increasing stress triaxiality for positive (tensile) values of the latter. More precisely, the lateral direction of maximum deformability changes from T, under uniaxial loading, to S under triaxial loading. This holds for any amount of superposed lateral stress. As a consequence, $R^{\mathrm{L}} < 1$ in all notched bars. In addition, the anisotropy is stronger in the RN2 specimen (with the sharpest notch) than in the RN10 specimen (with the shallowest notch). For reference, the value of R^{L} in uniaxial tension averaged over all realizations is about 1.75.

The anisotropy ratios can also be measured post-mortem for specimens taken to complete rupture. In this case, the notation $R_{\mathrm{f}}^{\mathrm{L}}$ is used. Figure 28b documents

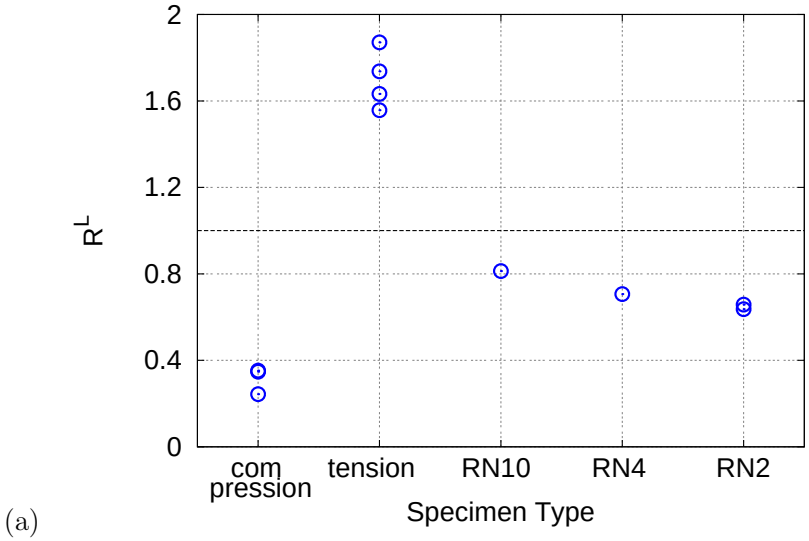

(a)

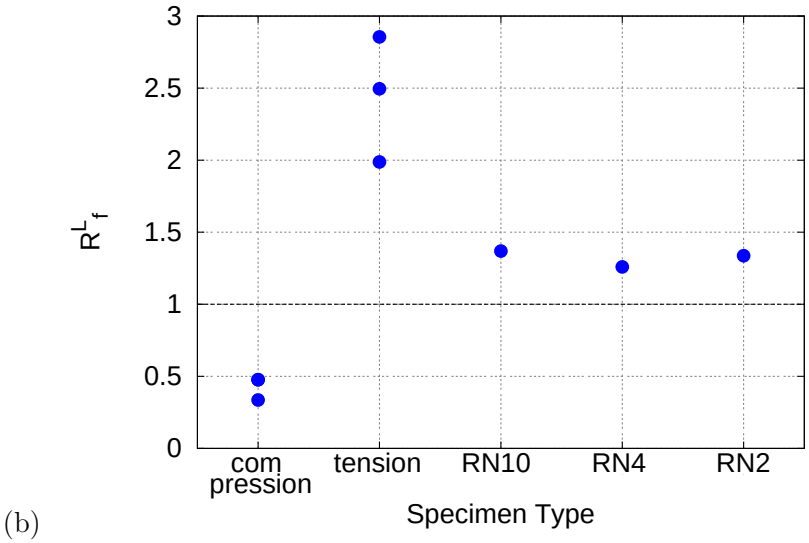

(b)

Figure 28: Anisotropy ratios R^{L} for various specimens measured (a) in steady-state, prior to crack initiation; and (b) post-mortem. For an isotropic material $R^{\mathrm{L}} = 1$ (horizontal dashed line).

the values for all specimen types. Two observations are noteworthy. First, the post-mortem anisotropy ratio is greater than the steady-state value, i.e., $R^{\mathrm{L}}_{\mathrm{f}} > R^{\mathrm{L}}$, irrespective of specimen type. Second, in the notched bars the above trend is such that $R^{\mathrm{L}}_{\mathrm{f}} > 1$ whereas $R^{\mathrm{L}} < 1$. This implies, in particular, that if measurements were

taken only after fracture one would have missed the fact that the deformability in notched bars is actually higher along the c-axis than perpendicular to it. Also, it must be emphasized that while R^{L} is representative of the material's deformation, $R^{\mathrm{L}}_{\mathrm{f}}$ also measures the signature of the overall dilation associated with the anisotropic crack growth process.

6.1.2 Fracture loci of AZ31 along rolling direction

The effect of stress triaxiality on fracture is best represented in a fracture locus. The latter depicts some measure of fracture against stress triaxiality. Figure 29 shows two fracture loci using either the strain to failure initiation, $\bar{\varepsilon}_{\mathrm{i}}$ of equation $(3.10)_4$, or the strain to complete fracture, $\bar{\varepsilon}_{\mathrm{f}}$ of equation $(3.10)_3$. Since the history of triaxiality evolution in the notched specimens is not known exactly, the failure strains are plotted against the specimen type. In uniaxial compression and tension, the triaxiality T (see Eq. 3.9) is $-1/3$ and $1/3$, respectively, before barreling or necking. For notched bars, there are more data points for $\bar{\varepsilon}_{\mathrm{i}}$ (Figure 29a) than for $\bar{\varepsilon}_{\mathrm{f}}$ (Figure 29b) since most tests were interrupted at crack initiation to enable the observation of damage mechanisms and ascertain the presence and location of the macroscopic crack. In uniaxial specimens, there are more data points for $\bar{\varepsilon}_{\mathrm{f}}$ since all of them fractured. Recall that the values of $\bar{\varepsilon}_{\mathrm{i}}$ in Figure 29a for uniaxial tension are lower-bound estimates. Upper-bound estimates for $\bar{\varepsilon}_{\mathrm{i}}$ are obviously the strains to complete fracture, $\bar{\varepsilon}_{\mathrm{f}}$. In fact, a tighter upper-bound estimate was obtained using the smooth bar test interrupted at incipient formation of shear failure then taking measurements inside the neck. Thus, the values provided for $\bar{\varepsilon}_{\mathrm{i}}$ in Figure 29a for tension are at most 4% below the actual values.

Details aside, the salient features from Figure 29 are as follows. First, the fracture loci exhibit a maximum at moderate stress triaxiality. The maximum ductility is

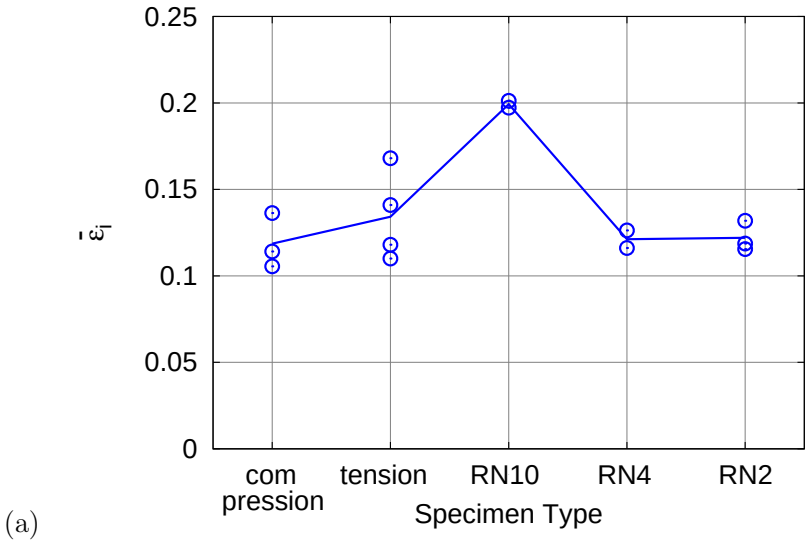

(a)

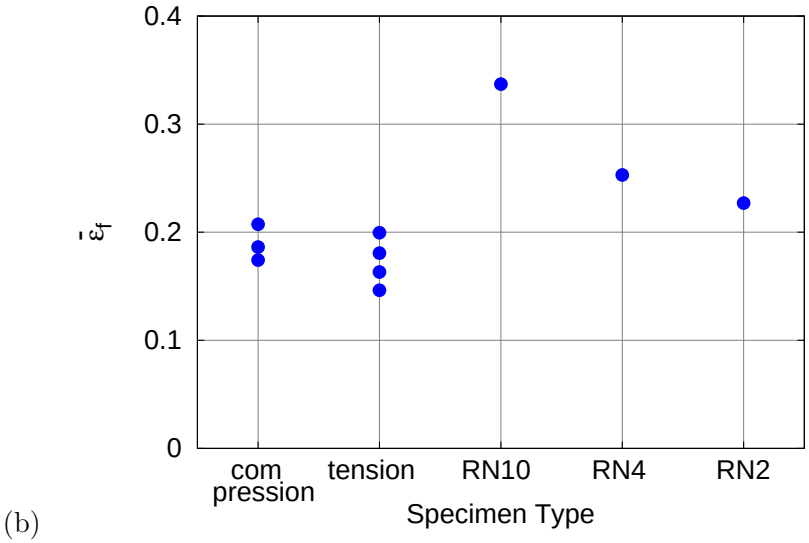

(b)

Figure 29: (a) Strain to failure initiation (nominally defined at the load drop) for all specimens tested. (b) Strains to complete fracture measured post-mortmem using top-view micropgaphs of failed specimens.

achieved in the RN10 specimen (shallow notch). Second, the strain to complete fracture $\bar{\varepsilon}_f$ is found to be greater in notched specimens than in initially smooth ones (Figure 29b). For $\bar{\varepsilon}_i$ the trend is similar, albeit weaker. Third, in any given specimen there is a difference between $\bar{\varepsilon}_f$ and $\bar{\varepsilon}_i$. This difference is large in notched bars and

small in initially smooth bars (the fact that the $\bar{\varepsilon}_{\mathrm{i}}$ values in the latter are lower bounds confirms the observation.) Finally, the strain to failure initiation does not vary between the RN4 and RN2 specimens (Figure 29a). As was already observed in Figure 26, the diameter reduction (at the abrupt load drop) in these two specimens is close to that of the smooth bars. Note that the reported strains to failure initiation account for anisotropy as per Figure 28 (i.e., $\Delta\Phi_{\mathrm{S}} \neq \Delta\Phi_{\mathrm{T}}$).

6.1.3 Fracture modes

Side-views of broken specimens loaded along the rolling direction (presented in Figure 30) showed that the macroscopic fracture path is slanted in uniaxial loading (compression and tension) and nominally flat in triaxial loading. All compression pins broke in two pieces. The normal to the fracture plane is contained in the L–S plane at $\approx \pm 45$ deg from the loading axis. Other ductile metals do not break in compression before some significant barreling. The latter usually leads to the development of tensile stresses on the outer boundary but since the stress state inside remains compressive, the main crack does not usually lead to the breaking of the specimen in fully separate pieces.

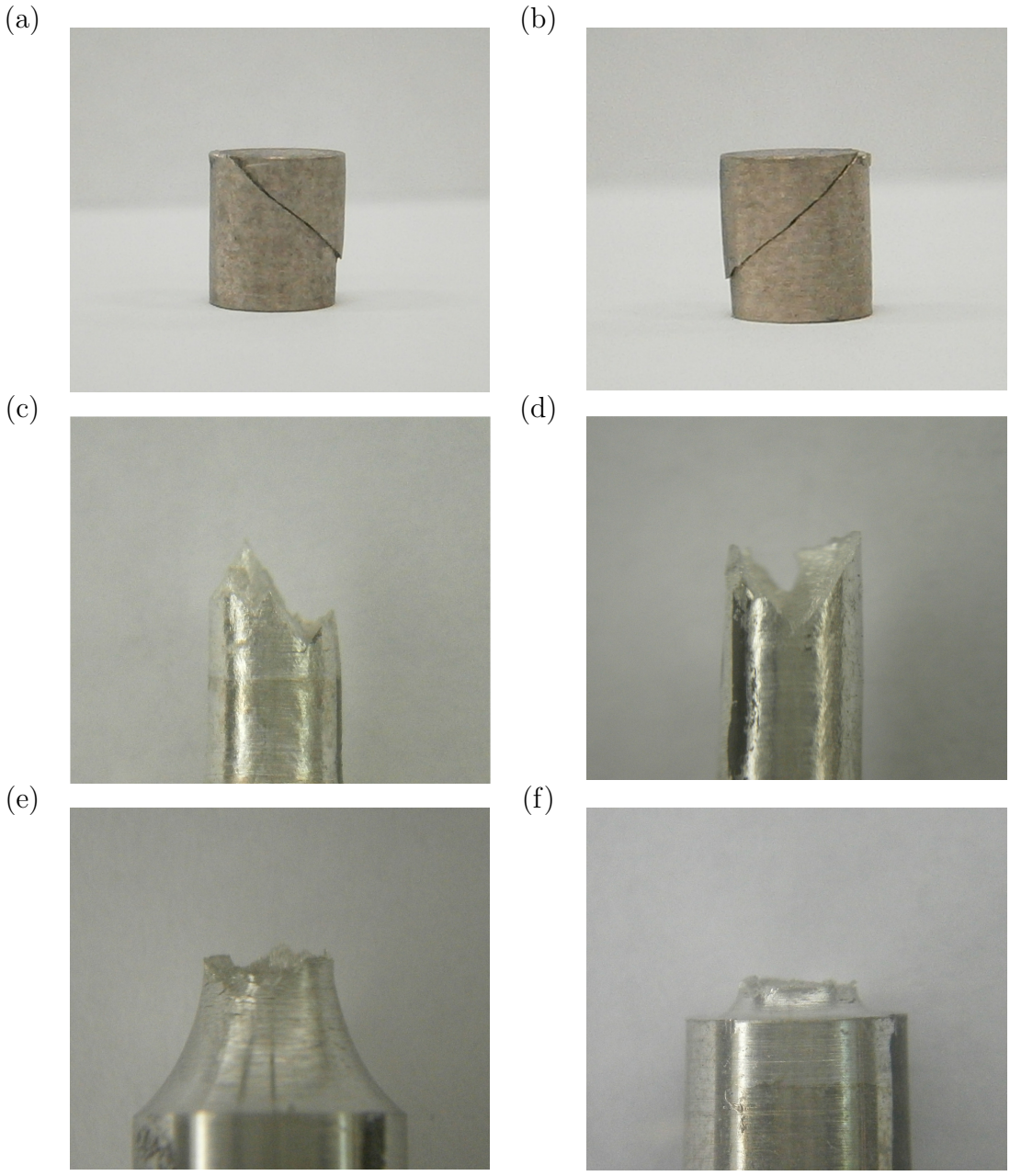

Figure 30: Macroscopic mode of failure in compression pins (a and b), uniaxial tensile bars (c and d), RN10 (e) and RN2 notched bars (f).

Shear failure also prevails in the *round* tensile specimens. As noted above, this is rarely observed in metals. The fracture surface in tension is rougher than in compression. The normal to the fracture plane may be contained in the L–S plane as in compression, or vary about that orientation leading to a somewhat conical fracture surface. The strong propensity for shear localization in the round tensile specimens is indicative of some destabilizing effects. The macroscopically flat fracture surfaces of notched specimens are more rough. Also, some secondary cracks are observed on the outer surface below and above the main crack; See Figure 99 in Appendix.I for illustrations. Detailed SEM micrographs will be analyzed after reporting on preferential and competing sites for damage initiation.

6.1.4 Damage initiation sites

Using the methods described in Section 3, two fundamental sites were identified for potential damage initiation: twins and second-phase particles. An attempt was made to observe each site in longitudinal sections as well as on the fracture surface. Figure 31 shows two examples of fully developed twin-sized voids in the vicinity of a nascent macroscopic crack (not shown). These observations were made in the only uniaxial tension test that was successfully interrupted prior to complete (shear) failure. The first microcrack (Figure 31a) is located about 30μm ahead of the macrocrack and appears to be arrested at the top and bottom grain boundaries. The second microcrack (Figure 31b) is farther away, at a distance about 90μm from the main crack, and seems to extend over two grains probably because of the coalescence of two microcracks. As subsequently shown, observations on the fracture surface suggest that these twin-sized voids are flat microcracks with a noncircular base. These features are reminiscent of those reported post fracture by Barnett [12] who indicated that the crack-like voids either consumed a region that appeared to

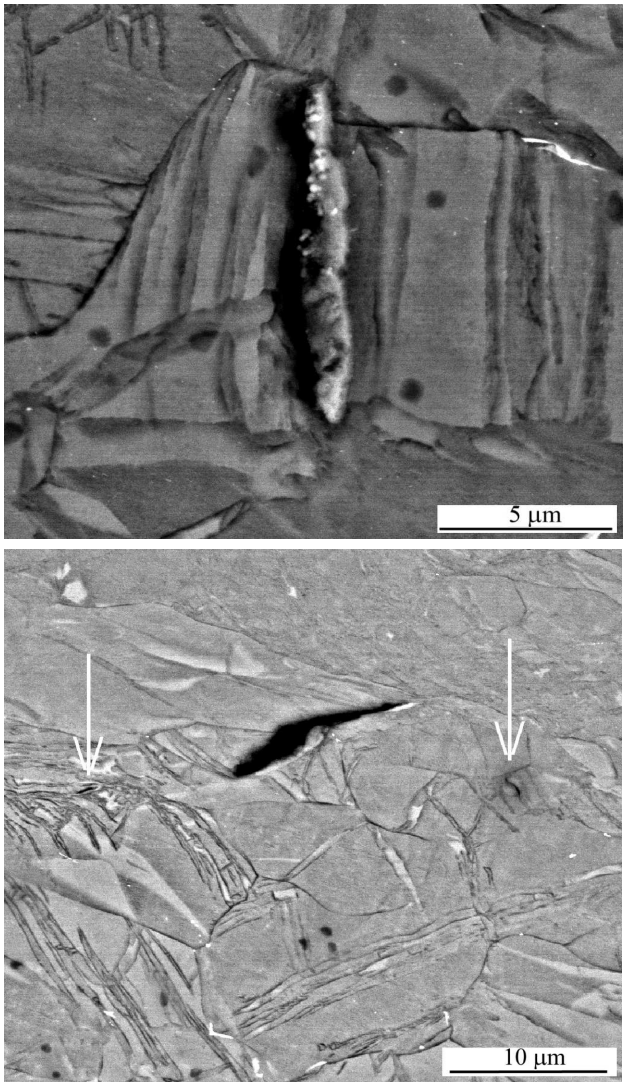

Figure 31: SEM micrograph of longitudinal section of a uniaxial tensile bar stopped at macroscopic crack formation showing (a) a twin-sized void near the tip of the macroscopic slanted crack and (b) other twin related microcracks with different sizes near the macroscopic crack.

have been occupied by a twin or, in rare cases, could be seen forming in the twin interior. The genesis of twin-sized voids is more difficult to ascertain. They may result from plastic strain accumulation inside the twin by basal and prismatic slip [4, 12] or by twin-boundary failure. The observation of void embryos in regions with large

twin frequency (white arrows in Figure 31b) suggests a correlation between twinning and void formation. On the other hand, since voids are not observed at all twin sites, concomitant factors may be necessary. Therefore, an alternative rationale for void formation in twins is the stress concentration resulting from twin intersections (Figure 31a) or twin-GB intersections. Note that the presence of crack-like voids of different sizes in a single cross-section indicates that void formation is a continuous process with a nucleation, growth and coalescence phases. The second site for damage initiation consists of a subgroup of the second-phase particles categorized in Section 4.1. There were enough particle residuals inside dimples to enable a limited, yet conclusive statistical analysis of the type of particles involved. Specifically, out of about 20 EDS analyses it was determined that about 25% were Al–Mn, 25% MgO and 50% pure Mn particles. Hence, the data shows that most particles leading to void formation are Mn particles; recall that none were identified on metallographic sections of undeformed material. Also, we found no evidence that the $Mg_{17}Al_{12}$ intermetallic particles were active nucleation sites. Figure 32 summarizes the three types of particles involved in void nucleation in AZ31B. Figure 32a illustrates void initiation at a stringer of Al–Mn. The micrograph was taken from the uniaxial tensile specimen deformed up to crack initiation. The slanted macrocrack shown is about 450μm long (the twin-sized void of Figure 31a is just ahead of its upper tip while the free surface is at the bottom). The fact that the crack opening is so much larger at the location of the particle than it is near the free surface suggests that the particle might have been the initiation point then the shear lip formed. In any case, the EDS spectrogram is actually not associated with this specific particle but with another Al–Mn particle inside a dimple (not shown for brevity). The micrograph in Figure 32b and its associated EDS spectrum unequivocally show that the Mn particles are involved in void nucleation. The assertion that these are pure Mn particles is

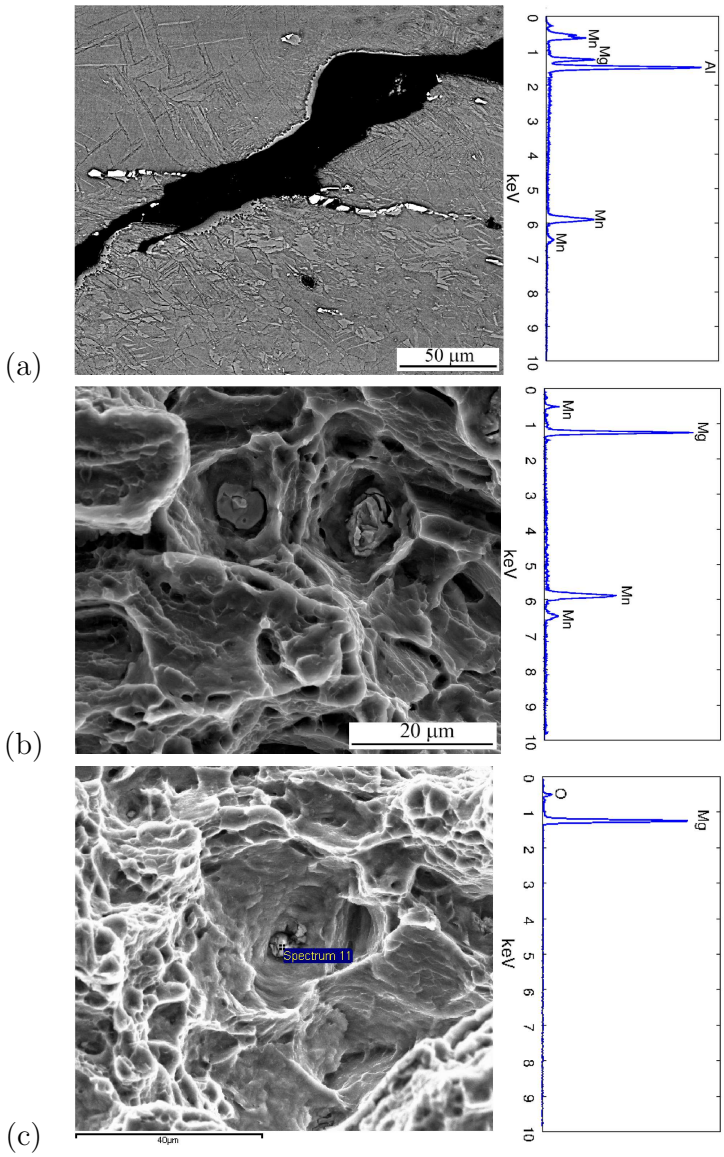

Figure 32: Three types of particles observed inside dimples and their EDS spectrograms. (a) Al-Mn particles (here in a smooth bar); (b) pure Mn particles (in a RN10 specimen); (c) Oxide particle (same RN10).

based on the phase diagram of a binary Mg–Mn system [52]. Thus the Mg peak must be the effect of the surrounding matrix. Finally, although oxidation of fracture surfaces can be an issue, as indicated earlier, Figure 32c clearly shows the presence

of an MgO particle (and not a film) inside the dimple.

6.1.5 Damage mechanisms

There is a clear transition in the fundamental damage mechanism with increasing stress triaxiality. This is illustrated in Figure 33. Under predominately uniaxial loading, the fracture surface exhibits mainly quasi-brittle features. Figure 33a shows for instance a deep crack in the small process zone of the smooth bar. The crack appears to have initiated at a deformation twin, such as that shown in Figure 31b. On the other hand, at a moderately low triaxiality (RN10 specimen) microvoid growth to coalescence becomes the dominant feature on the fracture surface, Figure 33b. This explains the higher strains to failure attained in RN10 specimens (see Figure 29). Upon further increase in the stress triaxiality (RN4 and RN2 specimens), the dimples become shallower, Figure 33c. As mentioned above, another common observation in RN4 and RN2 specimens concerns the flat facets that appear to be traces of twin-sized cracks, Figure 33c. Here, there are two coalescing cracks each confined to a grain. The presence of such cracks is consistent with our observation of twin-sized voids normal to the major loading axis (see Figure 31a).

The transition between the controlling mechanisms for damage initiation does not mean that only one of these mechanisms are active in a specific loading. In fact, both twin induced cracks and voids created on particles are observed in all studied deformations. The relative activity of each mechanism, however, is changed according to the applied loading. Figure 34 shows the side-view of a fractured RN2 specimen in the L–S plane where both damage initiation mechanisms are observed. Part (a) of this figure shows the overview of fractured specimen whereas part (b) and (c) present high magnification micrographs of the locations where damage is created on second phase particles or deformation twins, respectively. There are color coded

(a)

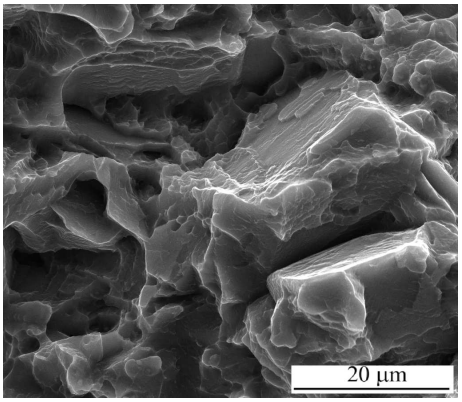

(b)

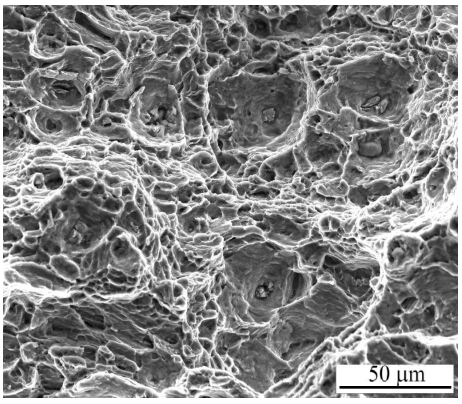

(c)

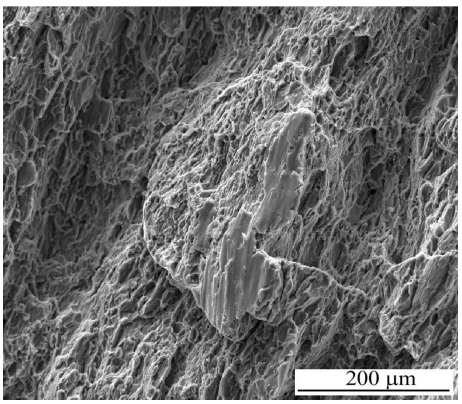

Figure 33: Salient features of the fracture surface under (a) uniaxial tension, (b) moderately triaxial tension (RN10), and (c) triaxial tension (RN2). The qualitative change in features illustrates a transition in microscopic damage mechanisms.

pictures in part (b) and (c) that helps the reader to identify the location of those specific features with respect to the fracture surface.

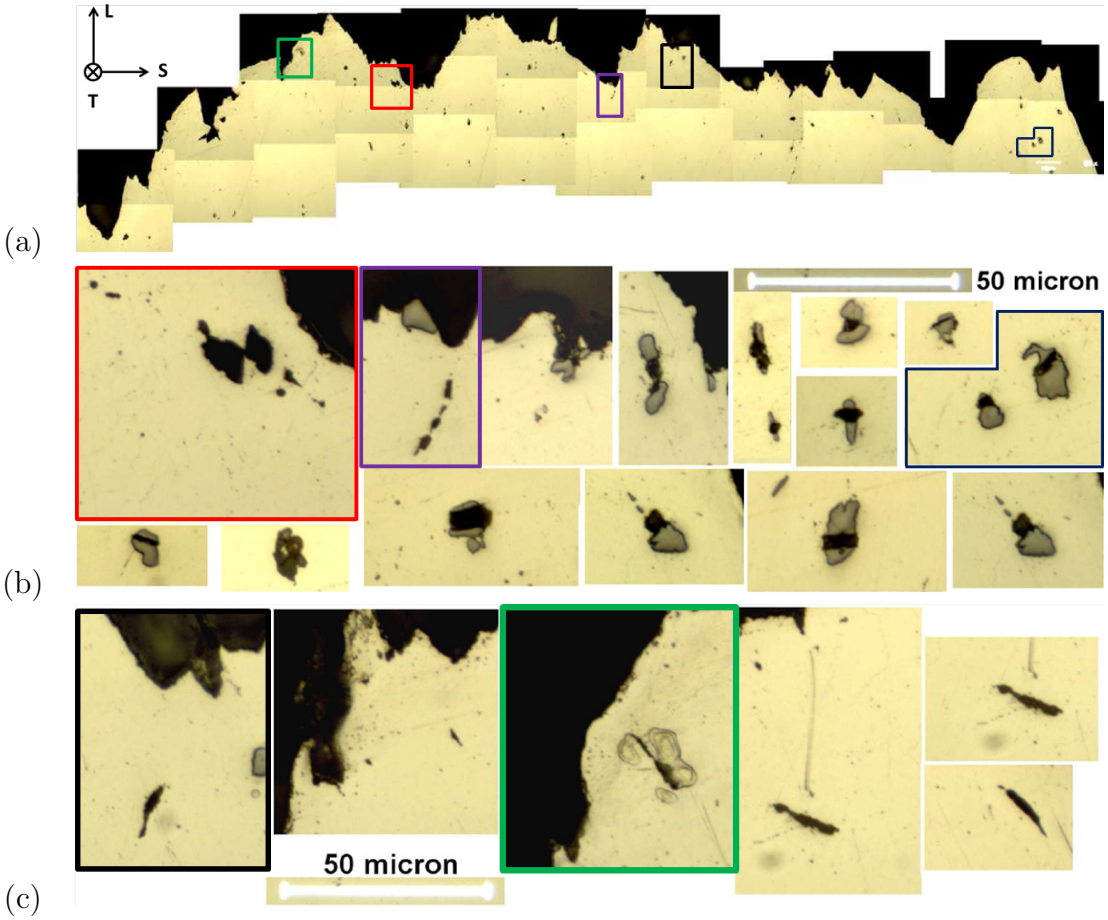

Figure 34: (a) Side-view of a fractured RN2 specimen sectioned parallel to L and S direction. Micrographs of voids nucleated on second phase particles and twin-induced microcracks are presented in part (b) and (c), respectively. The color-codes identify the location of some of the features with respect to the fracture surface in part (a).

6.1.6 Macroscopic crack growth and propagation

The top-view of the fracture surfaces in smooth and notched bars, loaded along the L direction, are presented in Figure 35. All of the fracture surfaces exhibit a number of splits running from along the T direction. Theses splits are along and less frequent at low triaxiality. As the triaxiality is increased, the splits become shorter while their number density increases. The neighboring splits are connected to each other through inclined planes, which is assumed to be related to shear localization. Recall that the anisotropy ratios (presented in Figure28) increase significantly after crack initiation and before fracture. This indicates that after crack initiation deformation along the T direction is more intense compared to that along S direction. Based on (i) the relative increase in rate of lateral deformation along T direction after crack initiation, (ii) the presence of splits that run parallel to T direction and (iii) the shear-like features connecting the splits, it was hypothesized that T direction is the direction of macroscopic crack propagation. After reaching to a critical distance, these cracks connect via shear localization in the L–S plane in the ligament region. To test this hypothesis, a series of fractography studies on the cracked and fractured specimens loaded along L direction in different planes were performed.

6.1.7 Macroscopic crack growth and propagation in RN10 specimens

The overview of the microstructure in L–T plane of an RN10 specimen after crack initiation and before fracture is presented in Figure 36. Depicted in this figure is a half of the specimen in which loading direction is vertical and crack is running horizontally, along the T direction.

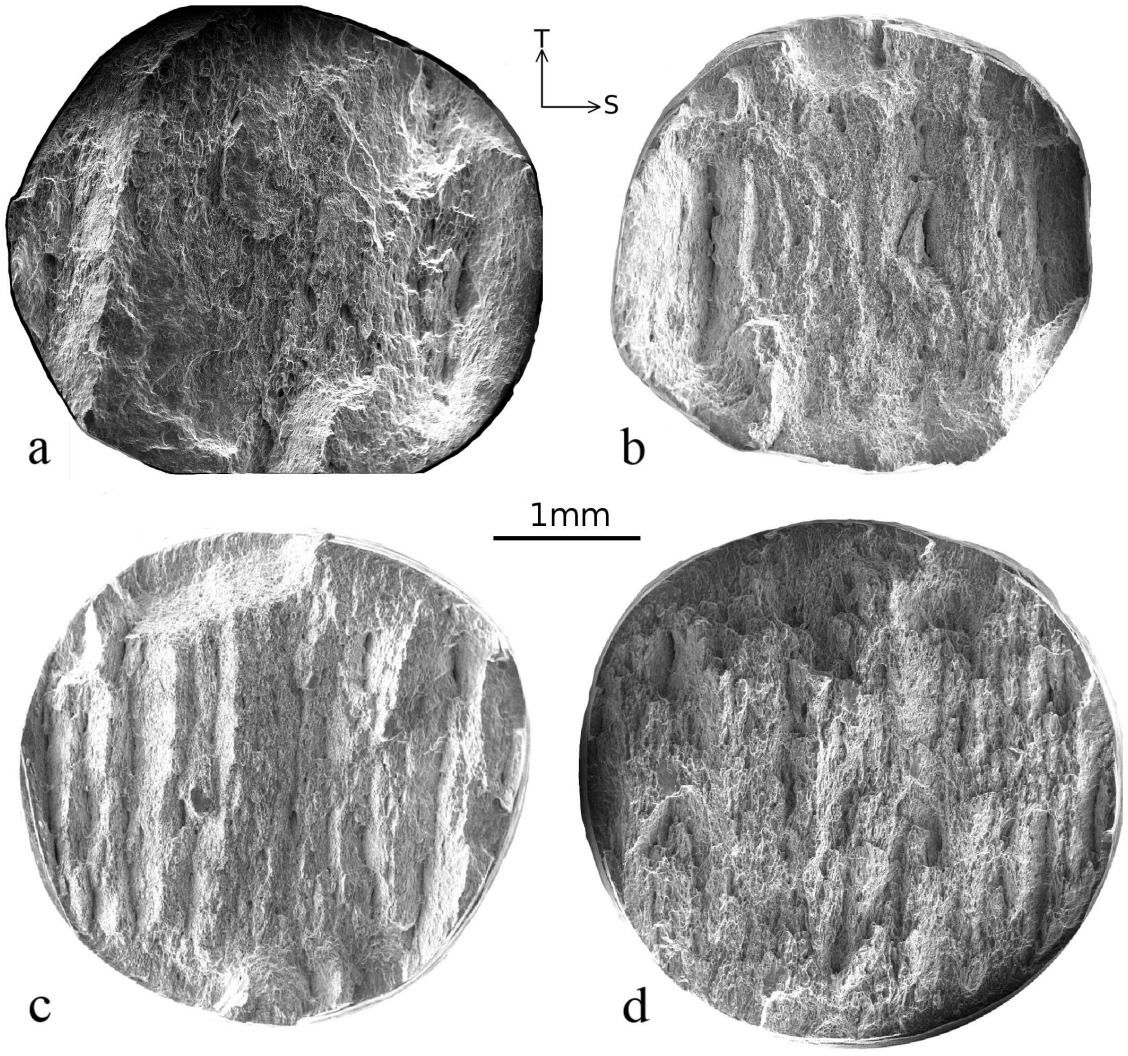

Figure 35: The top-view of the fracture surfaces of smooth and notched bars loaded along the L direction. These micrographs show the macroscopic features of the fracture surfaces. The presence of features called as splits, running along the T direction, are easily discernible in these graphs.

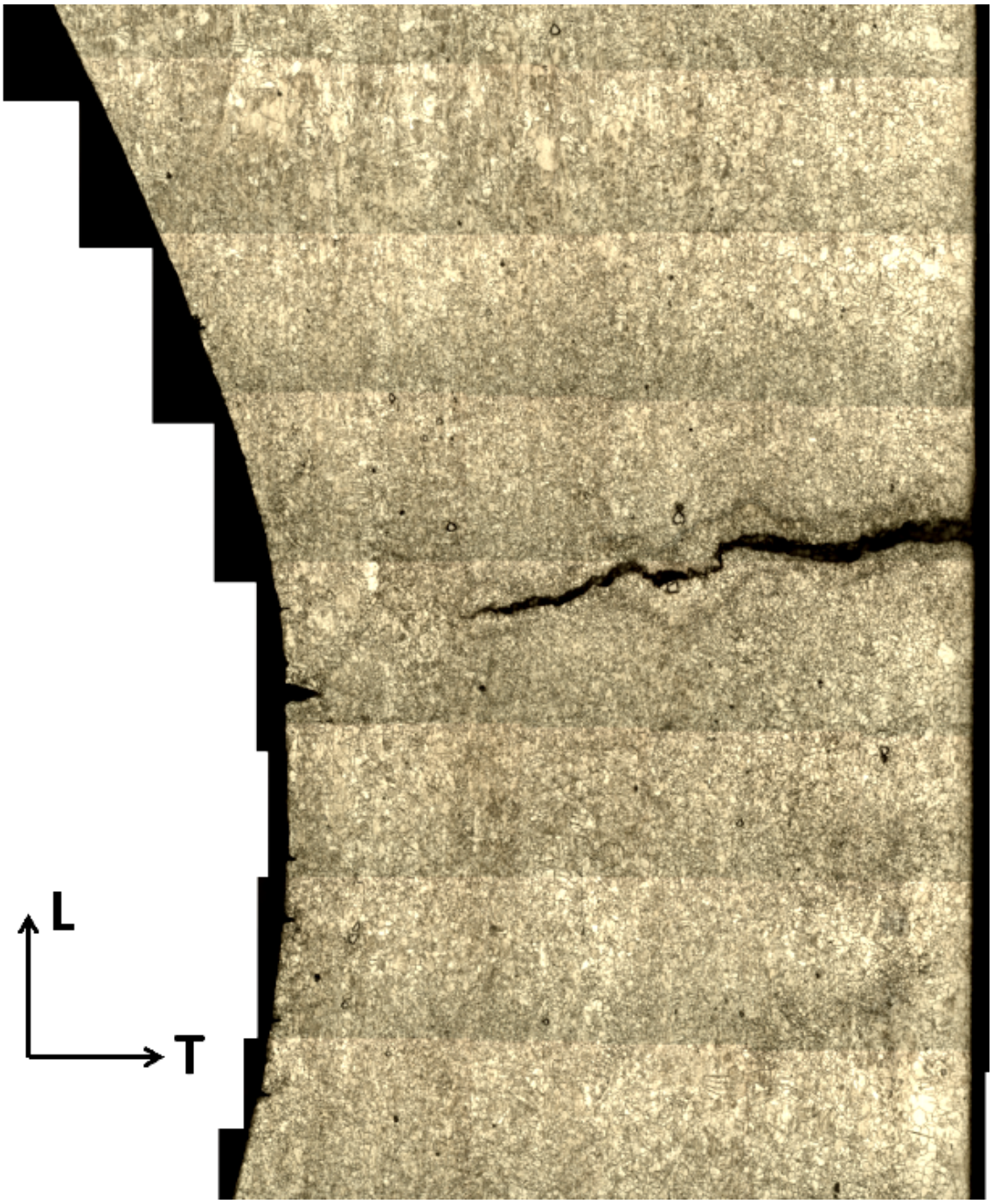

Figure 36: L–T view of the central section of an RN10 specimen loaded parallel to L direction, after macroscopic crack initiation and before fracture. Half of the specimen is shown in here. The macrocrack is formed inside the specimen and propagates toward the free surface along the T direction.

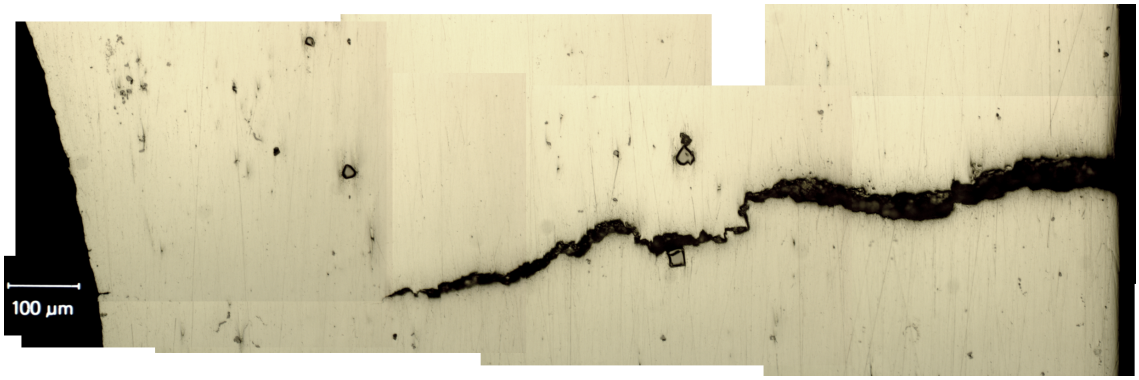

Figure 37: High magnification of the macroscopic crack in L–T plane presented in Figure 36 prior to etching.

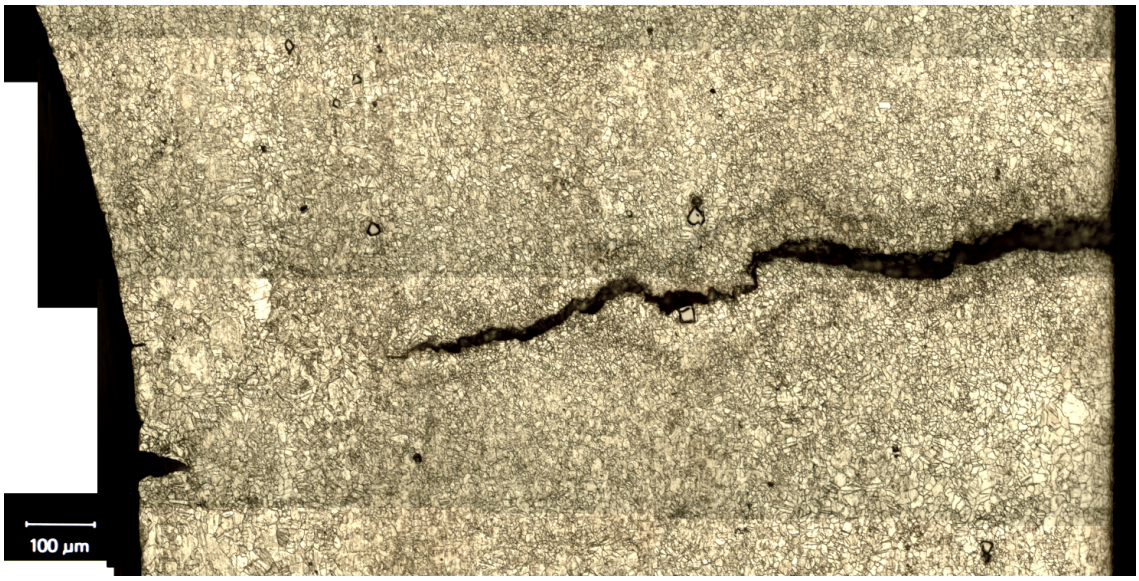

Figure 38: High magnification of the macroscopic crack in L–T plane presented in Figure 36 after etching.

Higher magnification micrographs of the features of this plane in unetched and etched (using both optical and SEM) condition are presented in Figures 37, 38 and 39, respectively.

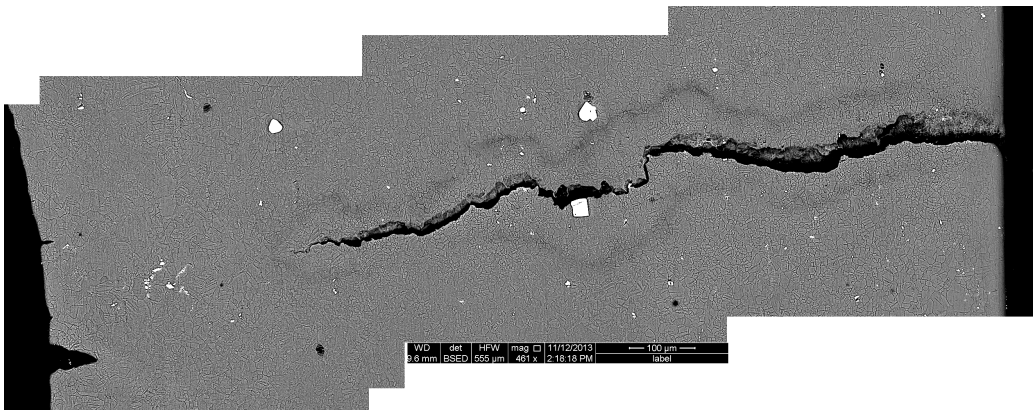

Figure 39: SEM micrograph of the macroscopic crack in L–T plane presented in Figure 36 after etching. In this figure, second phase particles and (partially) deformation twins are discernible.

From the maximum opening of the crack in these figures, it is inferred that, in RN10 specimens, crack is formed inside the specimen and propagates towards the surface ling the T direction.

The fracture surface of the fractured RN10 specimens was polished perpendicular to the loading direction (here, L direction) and was observed under optical microscope. The features of such surfaces after one and two rounds of metallography are presented in Figures 40 and 41, respectively. These figures suggest that the splits along T direction are the traces of crack propagating along the T direction. By comparing the features on fracture surface after first and those after second round of polishing, it is implied that some of the cracks along T direction could join each

other to form a large one.

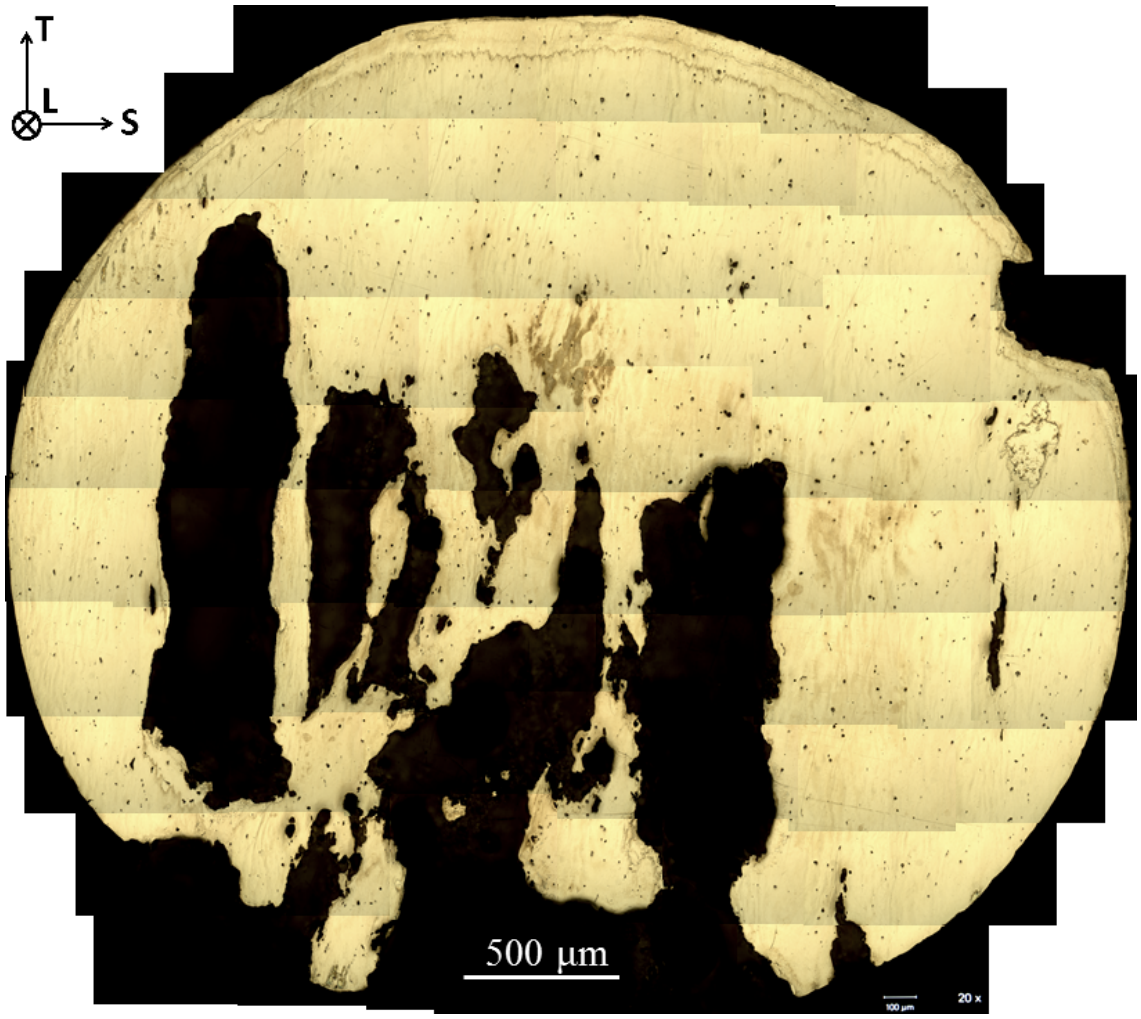

Figure 40: Top-view (T–S) of the fracture surface of an RN10 specimen loaded parallel to L direction. Some of the features on the fractures surface are destroyed by grinding and polishing perpendicular to L direction. Macrocracks propagate parallel to T direction.

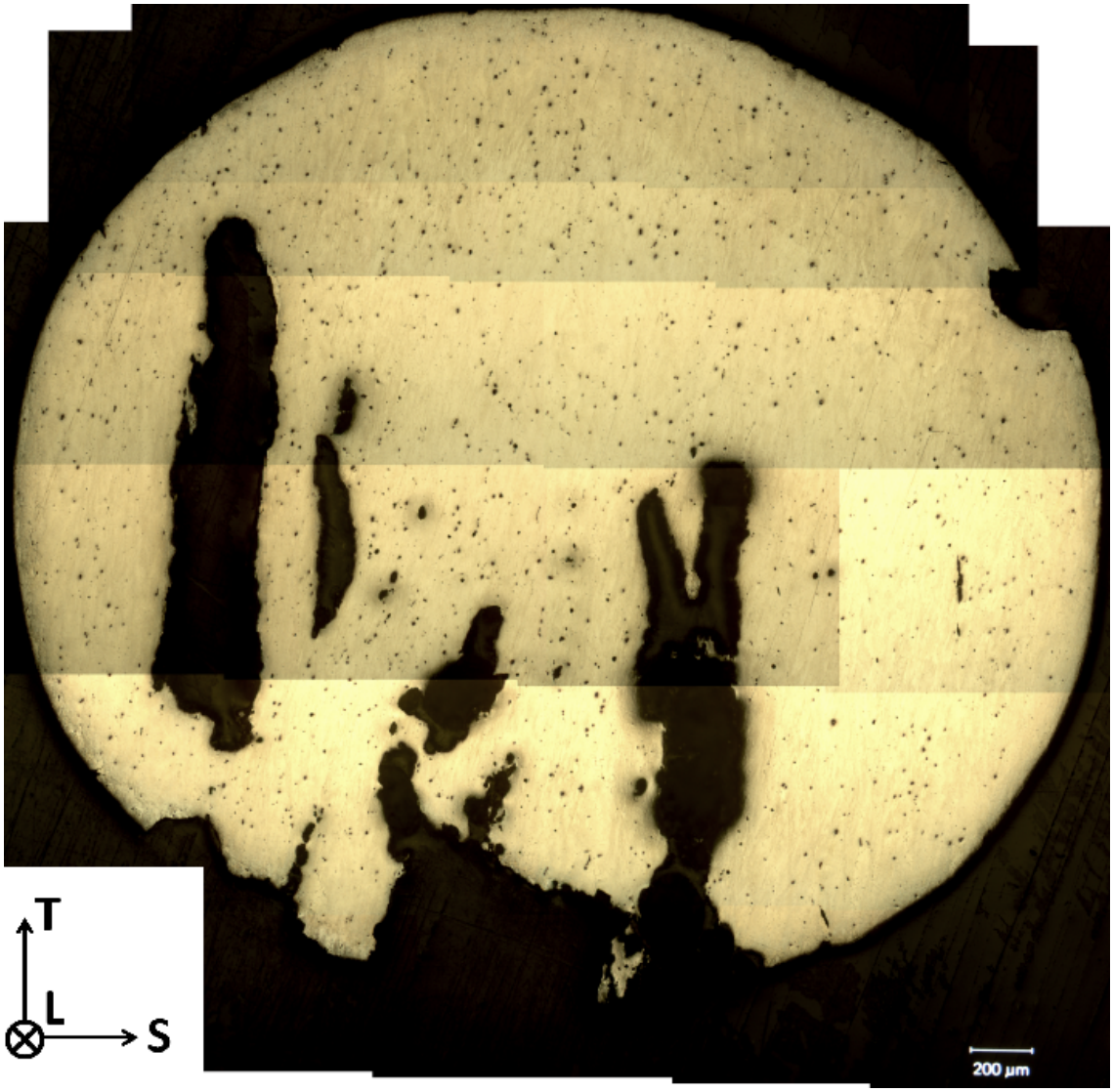

Figure 41: Top-view (T–S) of the fracture surface of an RN10 specimen loaded parallel to L direction. This micrograph is acquired from the sample presented in Figure 40 after an additional set of grinding and polishing perpendicular to L direction.

Based on the features in Figure 35, its was implied that shear localization in the ligament between the macrocracks lead to their coalescence. However, no clear evidence was offered to justify this conclusion. Metallography in L–S plane was persued to clarify this hypothesis. An interrupted RN10 specimen (the exact same one which was used to acquire images in Figures 36 to 39) were cut parallel to the loading direction and in the L–S plane to study the mechanisms by which the macrocracks join each other. Figures 42 to fig:RN10-LS-shear21 present the micrographs of this section. As depicted in Figure 42, zigzag cracks connected to the surface are observed at the two sides of the specimen. The shape of these cracks in the L–S plane indicates that they are driven by shear localization.

According to the micrographs shown in this section, one could rationalize the mechanism of crack propagation in AZ31-RN10 specimens. Initially, damage initiates inside the specimen toward the central region. Coalescence of voids and microcracks along the T direction leads to formation of macrocracks that propagate parallel to T direction. Growth of the macrocrack, which is closest to the notch root, leads to a plane-strain state of deformation in the region between free surface and macrocrack itself. Such deformation field in the ligament part promotes shear localization in L–S plane. Thus, the macrocrack connects to the free surface via an intense shear zone. Finally, the other macrocracks join each other by shear localization in the L–S plane and fracture occurs.

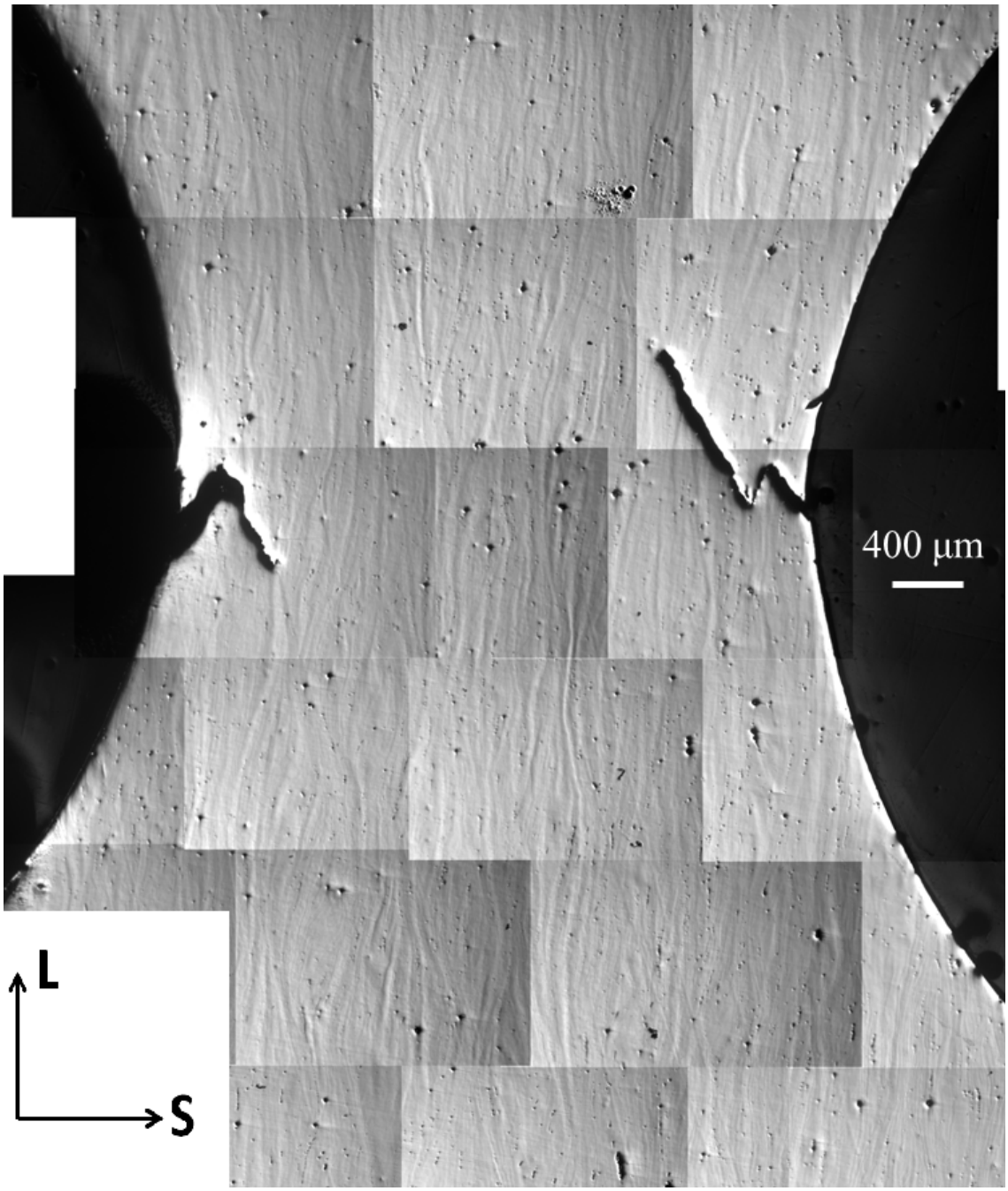

Figure 42: L–S view of the central section of the RN10 specimen loaded parallel to L direction, after macroscopic crack initiation and before fracture. The same specimen from which Figure 36 is acquired is employed to obtain this graph. Shear zones that connect macrocracks to the free surface are easily discernible on both sides of the specimen.

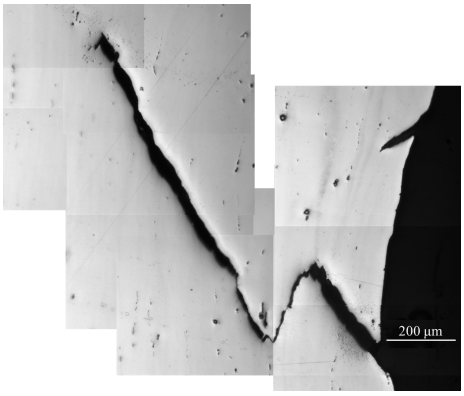

Figure 43: High magnification of the macroscopic crack in L–S plane, on the right-hand side of Figure 42 prior to etching.

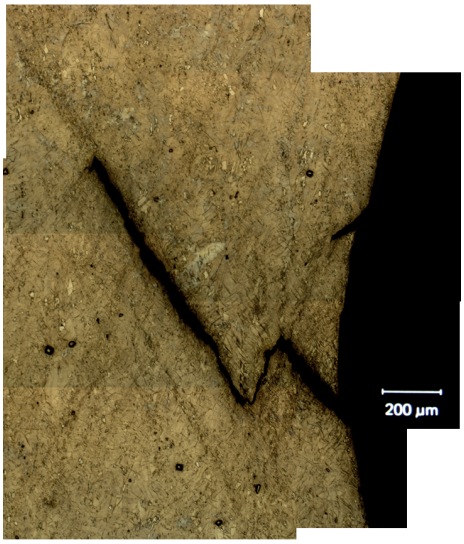

Figure 44: High magnification of the macroscopic crack in L–S plane, on the right-hand side of Figure 42 after etching.

For more detail on the morphology of the cracks in Figure 42, refer to their high magnification micrographs depicted in following figures before and after etching in Figure 43 to 46.

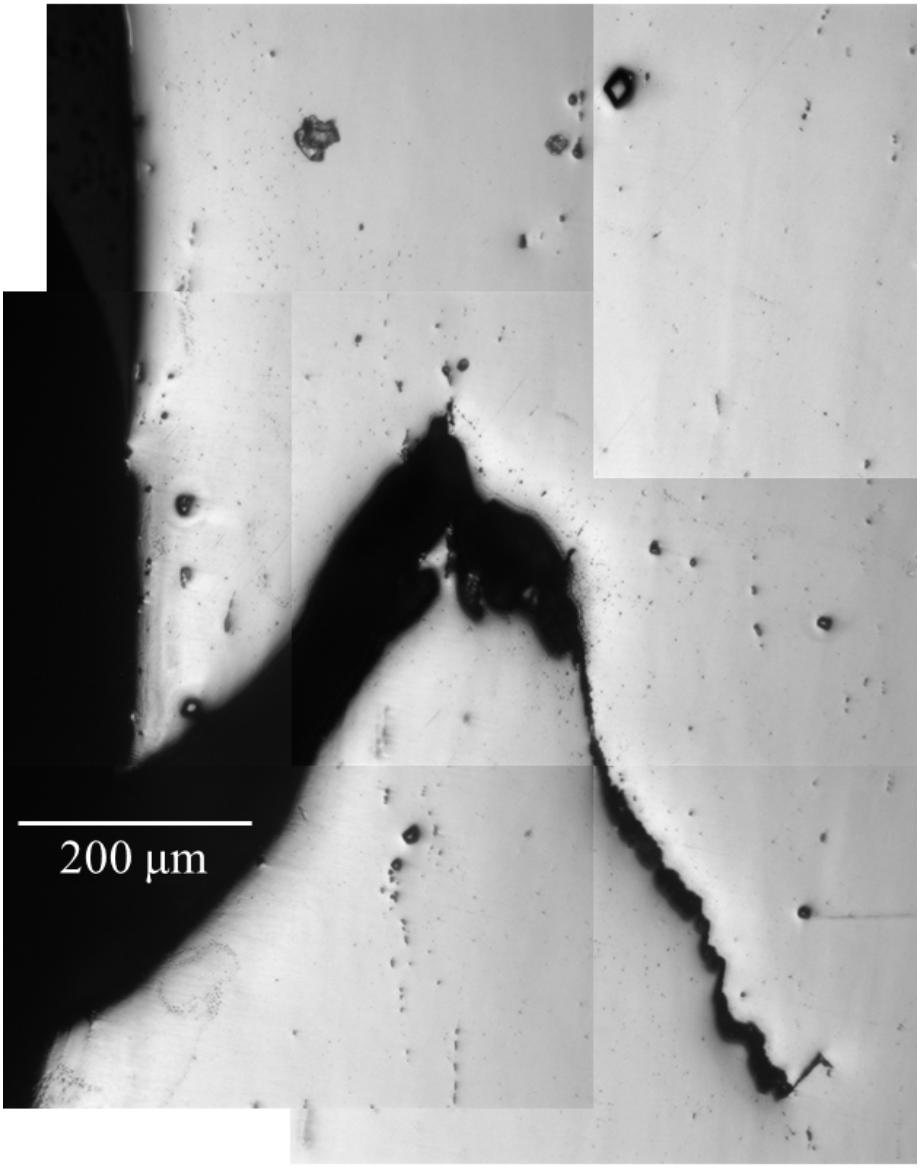

Figure 45: High magnification of the macroscopic crack in L–S plane, on the left-hand side of Figure 42 prior to etching.

Figure 46: High magnification of the macroscopic crack in L–S plane, on the left-hand side of Figure 42 after etching.

6.1.8 Macroscopic crack growth and propagation in RN2 specimens

The top-view of fractured RN2 specimens loaded along L direction, after grinding perpendicular to the loading direction and polishing, is shown in Figure 47. The feature on the fracture surface of RN2 specimens exhibit significant contrast to their RN10 counter parts although maintain some similarities. Similar to the RN10 specimens, the direction of macrocrack growth in RN2 specimens is parallel to T direction. Most of the cracks, however, are located near the notch root.

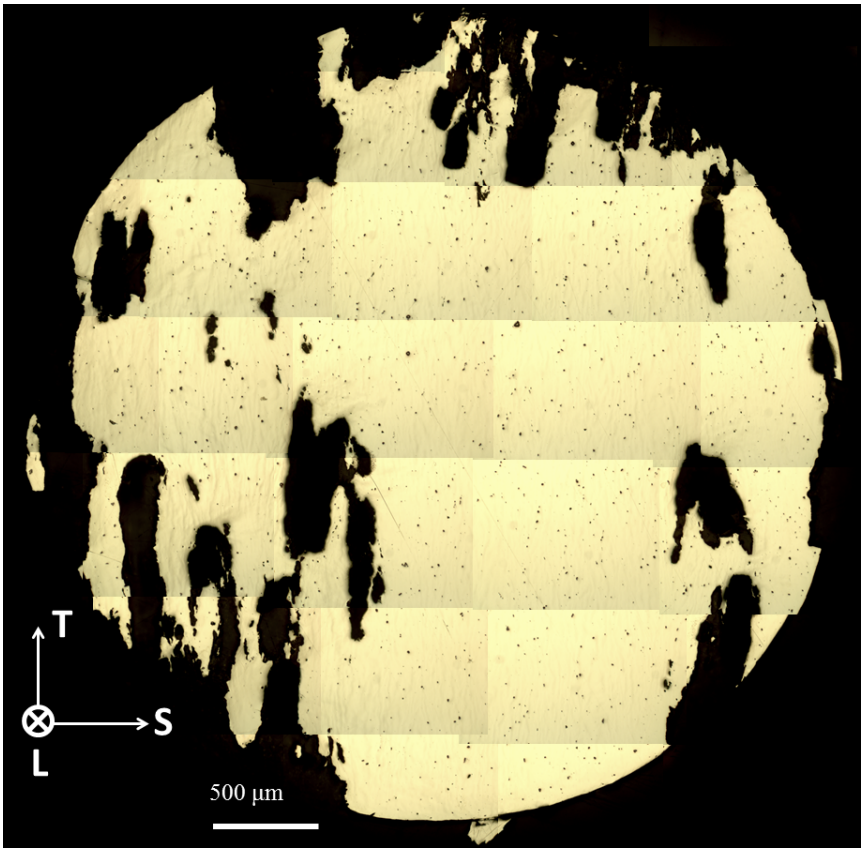

Figure 47: Top-view (T–S) of the fracture surface of an RN2 specimen loaded parallel to L direction. This micrograph is acquired from a broken RN2 specimen after grinding and polishing perpendicular to loading direction.

A schematic of the difference between formed macrocracks in RN10 and RN2 specimens loaded parallel to rolling direction is presented in Figure 48. According to the observations, macrocracks at low triaxialities tend to form in the central region of the specimen whereas high triaxiality promotes the formation of macrocracks near the notch-root. In both loading condition, the main direction of crack propagation is along the T direction.

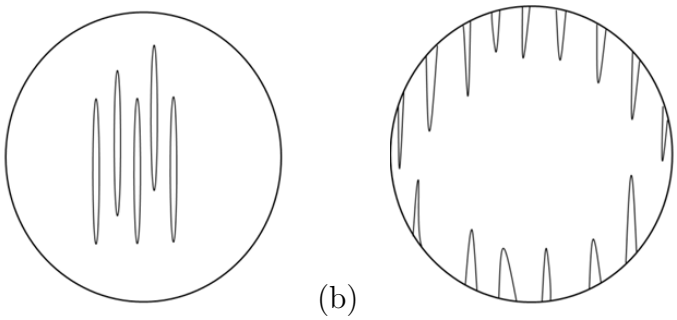

Figure 48: Schematic of macroscopic crack propagation in sample loaded parallel to L at (a) low and (b) high triaxiality. The direction of T in these figures is vertical whereas horizontal line represents S direction.

The side-view of the interrupted RN2 specimen loaded along L, after macroscopic crack initiation and before fracture, in the L–S plane reveals essentially the same information as its RN10 counterpart. The macrocracks (as shown in Figure 49, 50 and 51) indicate that macrocracks, which grow parallel to T direction connect to the free surface by an intense shear zone. In addition, macrocracks located in close vicinity of each other could join by shear localization.

The macroscopic mode of failure shown in Figure 30 suggests that crack propagation in AZ31 uniaxial tensile bars is driven mainly by shear localization. For

detailed micrographs in interrupted uniaxial bars and their crack morphology, refer to Appendix.II.

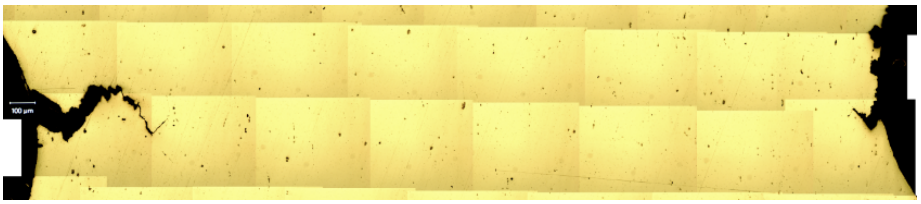

Figure 49: L–S view of the central section of the RN2 specimen loaded parallel to L direction, after macroscopic crack initiation and before fracture.

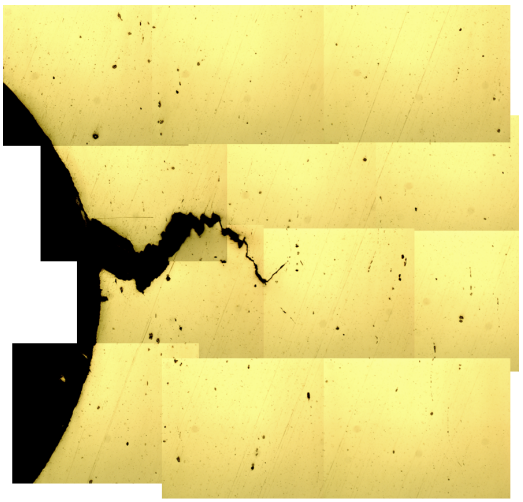

Figure 50: Higher magnification micrograph of the macroscopic crack on the left-hand side of Figure 49 prior to etching.

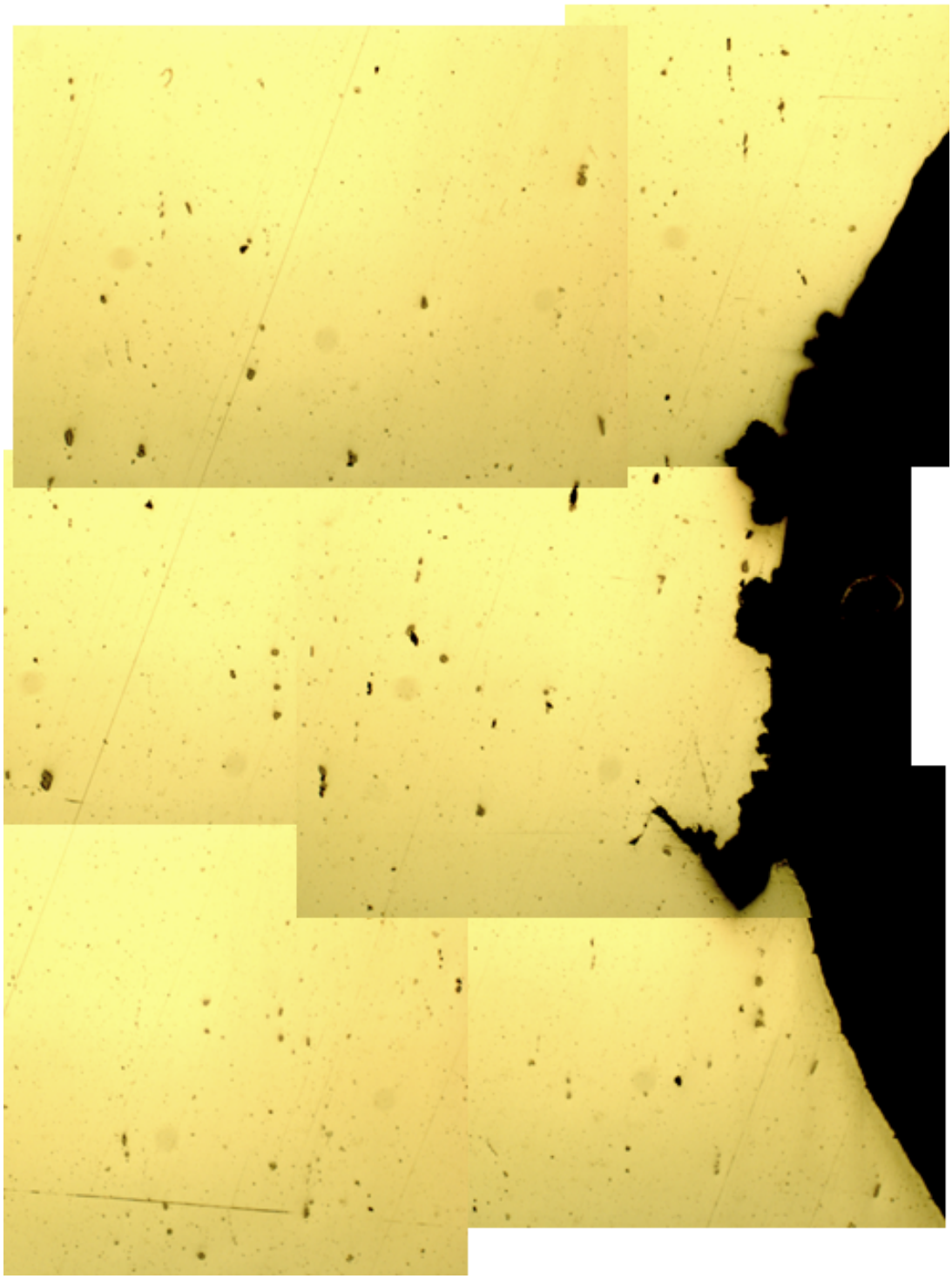

Figure 51: Higher magnification micrograph of the macroscopic crack on the right-hand side of Figure 49 prior to etching.

6.1.9 Salient features of the fracture surfaces

For completeness, the fractographs corresponding to the smooth, RN10 and RN2 specimens are now analyzed at higher resolutions. Figure 52 shows the salient features in the smooth bar. The overview in (a) shows an essentially slanted surface with a thin process zone (flat), (b) depicts a split in the thin process zone and (c) some deep and diamond-like shallow dimples; note the shear zone to the right of the figure. In some instances, second phase particles are observed at the center of dimples (d) suggesting some contribution of these particles to damage under uniaxial loading. However, this potential contribution is frustrated by the shear-like fracture and the predominance of twinning induced damage (e). At a finer scale, smaller dimples are seen, which appear to be the result of grain pull-out giving a granular morphology to the surface (f). Since fine particles are observed, it is hypothesized that these are the Mg-Al precipitates which may have caused local intergranular fracture. Such features have been observed in the literature [136].

The characteristic features of the fracture surface of the RN10 specimen are shown in Figure 53. The overview in (a) shows some coarse splits, one of which is shown in (b) at a higher magnification. Splits either result from the coalescence along T of multiple voids or from the joining of two shear cracks. Although less frequent in RN10 specimens, the flat facets are also observed (c) surrounded by dimples. The predominately dimpled character of the surface is evident in parts (d)–(f). In this region, most particles inside dimples are pure Mn particles.

Interestingly, the area frequency of deep dimples decreases in the RN2 specimen, Figure 54. Two features emerge: splits of shorter length (a) and flat facets (b). With the introduction of a sharp notch, the ratio θ of lateral stress to axial stress increases. One principal lateral stress is along S, which would favor the activation of softer

deformation systems, notably extension twinning. Since flat facets are less frequently observed at lower triaxialities, it is possible that these features originated from the coalescence of cracks growing along the boundaries of deformation twins, mostly extension twins, the formation of which is facilitated at higher triaxialities [22]. Other features on the fracture surface are similar to those observed in the process zone of the fracture surface of smooth bars. These include deep cracks with sizes close to the size of large grains (figure 54c and d), elongated dimples (figure 54d, e and f) and second phase particles at the center of dimples (figure 54e and f).

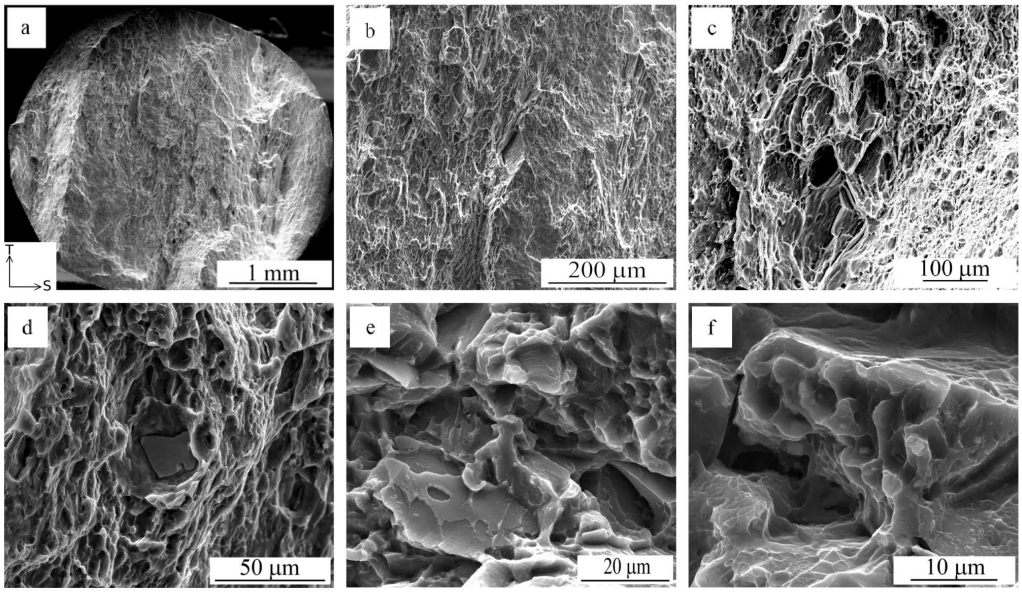

Figure 52: (a) Fracture surface of a smooth bar exhibiting (b) few splits, (c) diamond-like and sheared dimples, (d) a dimple with a particle inside, (e) quasi-brittle facets and (f) granular morphology.

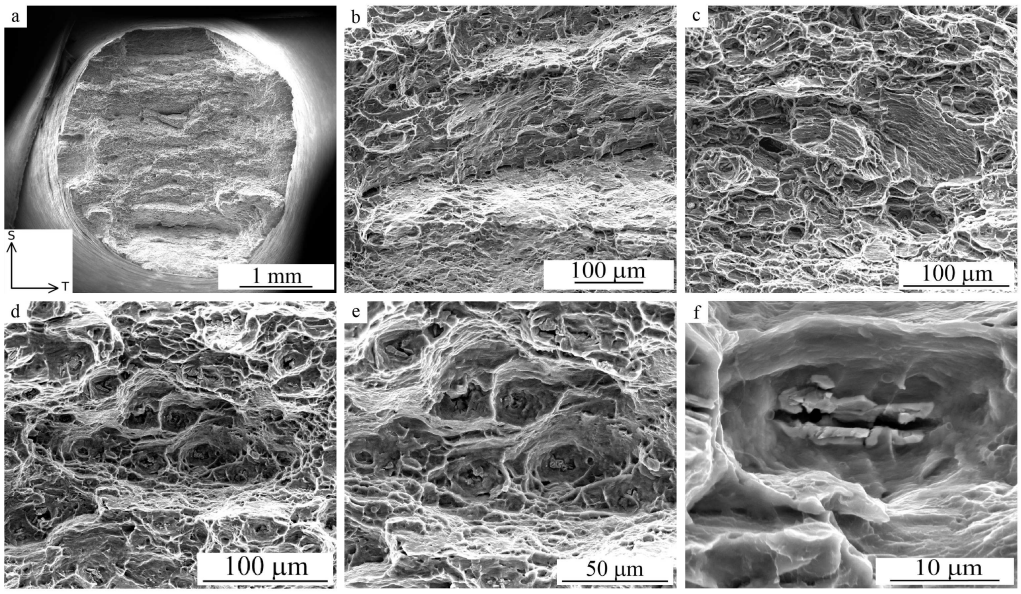

Figure 53: (a) Fracture surface of a shallow notched bar (RN10) exhibiting (b) few splits (c) rarely observed facets, and (d)–(f) commonly observed dimples.

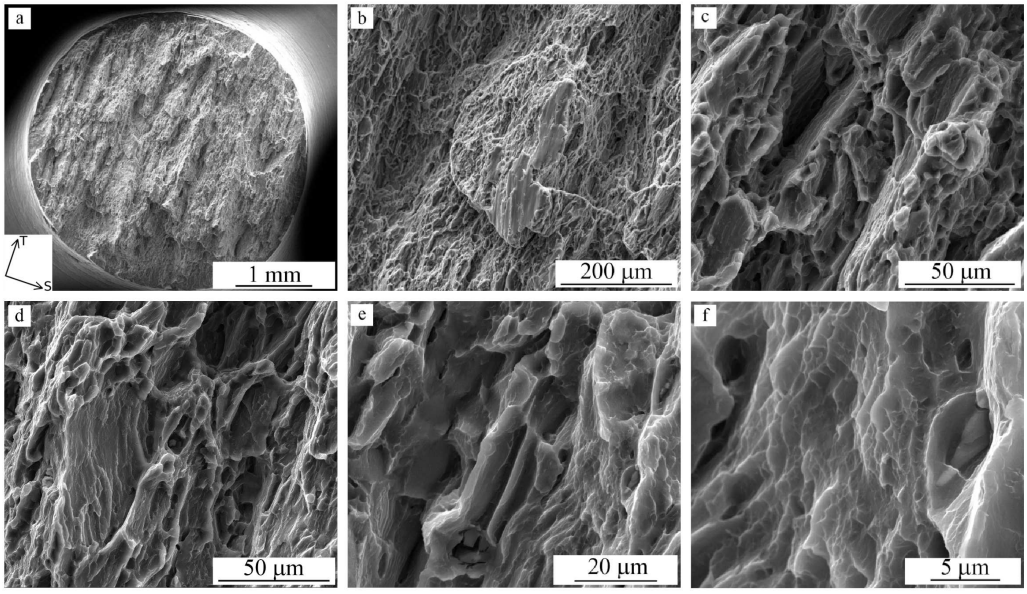

Figure 54: (a) Fracture surface of sharp notched bar (RN2) showing (b) large flat facets, (c) a magnified view of a split, and (d)–(f) other brittle-like features, including shallow dimples.

6.1.10 Anisotropy of fracture strains in AZ31

As it was noted before, the results presented in this section are all from loading parallel to the rolling direction. Based on the behavior of hot-rolled AZ31 (which is close to in-plane isotropy), however, the trends, mechanisms and justifications are applicable to loading in any in-plane direction such as T or LT direction. Figure 55 shows the fracture strains of AZ31 in a range of triaxialities loaded parallel to L, T and LT direction. As illustrated here, the failure strains are very close and trends are maintained. The marginal differences in the failure strains are associated with (i) the stochastic nature of fracture that leads to a certain degree of scatter in results; (ii) difference in the distribution of second phase particles along different directions of the plate and plastic anisotropy of the matrix (i.e. shift of the basal planes toward the rolling direction in the measured texture, which is caused by processing).

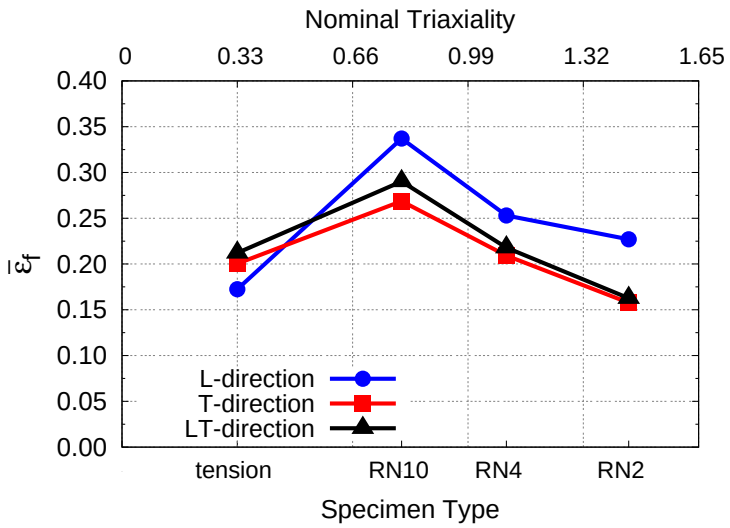

Figure 55: Fracture strains of AZ31 in a range of triaxialities loaded parallel to L, T and LT direction.

6.2 Damage and fracture characterization of WE43

To study the effect of stress state triaxiality on the deformation and fracture of WE43, uniaxial and notched bar experiments are performed on WE43 specimens with four different geometries. Applied load divided by initial minimum cross-section area versus normalized reduction of diameter along S direction under uniaxial and triaxial loading parallel to L direction are presented in figure 56. In these experiments, axial flow stress gradually increases after the elastic region to reached its maximum at fracture. Similar to the case of uniaxial tension, fracture in the notched bars occurs catastrophically (other materials usually exhibit a macroscopic load drop before fracture). Accommodated strain along S direction before final failure is reduced by increasing the triaxiality (i.e. going from uniaxial tension to RN2 specimens). Axial flow stress at a given reduction in diameter also increases by increasing notch acuity. The axial nominal stress at 0.01 reduction of diameter along S direction increases from 300 MPa to 350, 400 and 450 by going from uniaxial tension specimens to RN10, RN4 and RN2, respectively. It is expected for the axial limit load of a plastically isotropic material to increase with increasing notch acuity because of its enhanced stress triaxiality [135]. Precious works showed that the increase in the flow stress in AZ31 alloy by increasing triaxiality was much limited, an observation that was associated with activation of new and softer deformation mechanisms (See Ref. [18]).

The effect of stress state tiaxiality on activation of different deformation systems and eventually the macroscopic plastic anisotropy could be studied using anisotropy ratios (R^X). Anisotropy ratios are best in reflecting of these effects in polycrystalline materials with strong texture. None the less, useful information still could be implied from such data in WE43 with relatively weak texture. The strain ratios in specimens

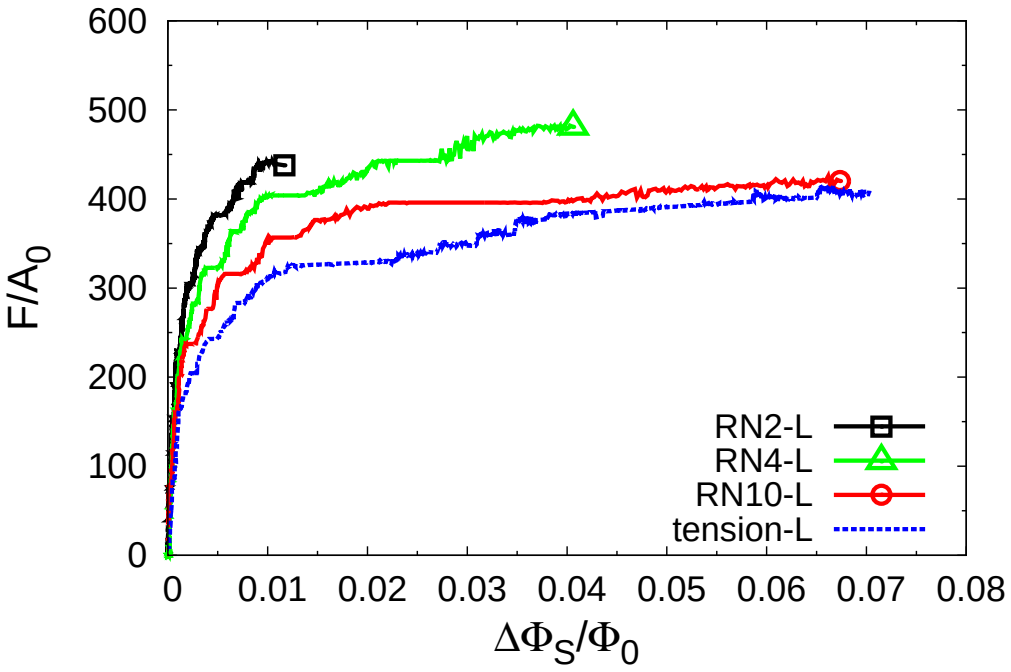

Figure 56: Force divided by initial cross-sectional area versus normalized reduction in diameter along S direction for uniaxial and notched specimens. Some curves are marked by a symbol at their end to make a better distinction between them.

with various geometries along L, T and LT direction are calculated post-mortem on fracture surfaces and based on equations 3.4_1, 3.4_2 and 3.4_3. The data is presented in Figure 57. As it is depicted in this figure, WE43 exhibits R-values close to unity under tensile loading, regardless of its stress state triaxiality. During tensile loading of WE43, there is marginal variation in lateral strains along different directions. It means that in the case of round specimens, the cross section will preserve its circular cross-section. Note that an isotropic material has R-value equal to unity. Under compressive loads, however, round specimens exhibit an oval cross section after fracture. This behavior could be related to activity of some dislocation or twinning

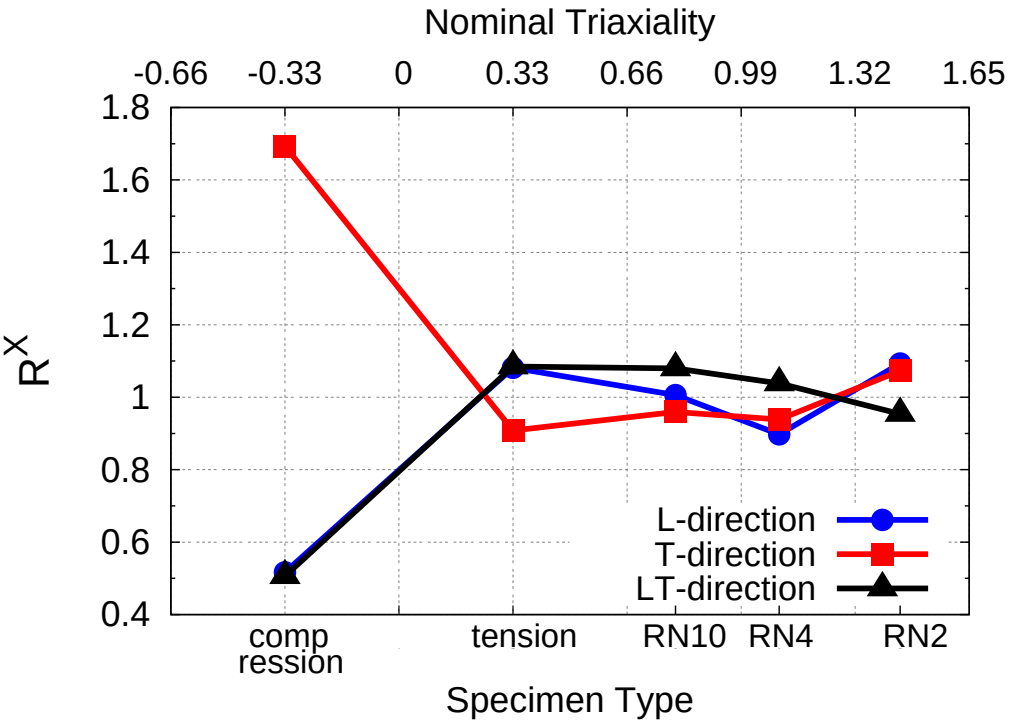

Figure 57: Anisotropy ratios R^X for various specimen geometries and loading directions measured postmortem. For an isotropic material $R^X = 1$.

variants under a certain loading direction instead of all of them. In addition, the flow stresses and R-values for loading along L, T and LT direction in compression and tension suggest transverse isotropy (isotropy in L–T plane) in WE43 alloy. Here, the apparent differences in the R-values originates from their definition.

Strain to fracture in WE43 alloy under various tensile loading conditions are shown in figure 58a. Approximate triaxiality for each specimen geometry, based on FE analysis of isotropic materials, are reported at the top horizontal scale. As illustrated in this figure, fracture locus of WE43, regardless of loading direction in the rolling plane, does not exhibit its maximum under uniaxial tension. This is in contrast to the response of most materials systems.

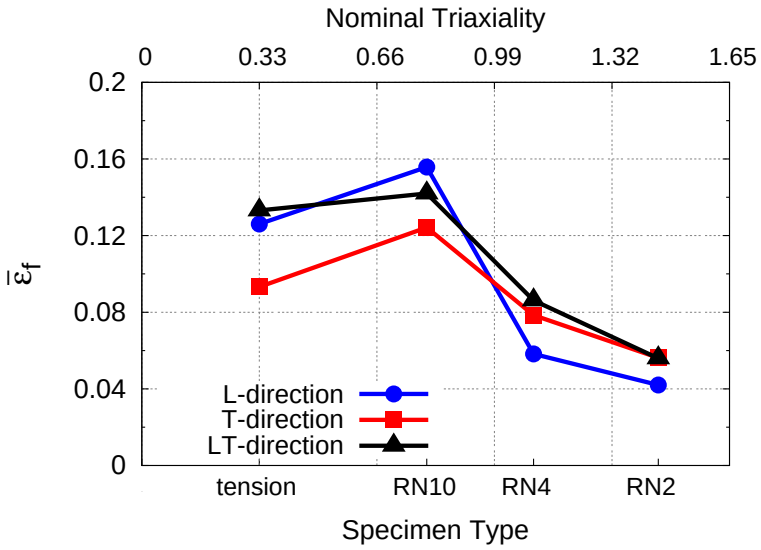

(a)

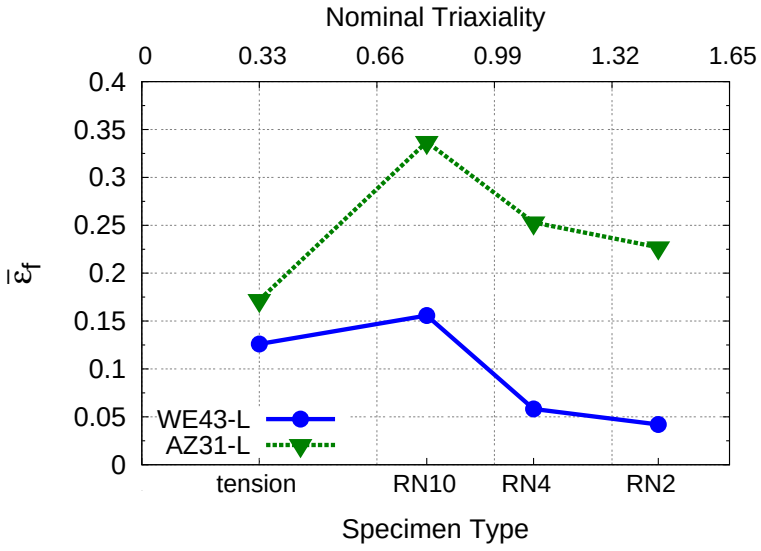

(b)

Figure 58: (a) Strain to complete fracture for three different in-plane direction (i.e. L, T and LT) measured postmortem using top view micrographs of failed specimens. (b) comparison between the fracture locus of WE43 and AZ31 in the studied range of triaxialities.

For each direction, by going from uniaxial tension bars to RN10 specimens with a shallow notch geometry, the strain to failure increases slightly. Thus, the maximum strain to failure in WE43 is achieved in RN10 notched bars with moderate triaxiality. After this maximum, however, the strain to failure is reduced significantly to average values as low as 4.2 % (for L direction) by increasing the stress triaxiality. This trend is universal for all in-plane specimens and the results are very close except for slight anisotropy in the strain to failure under uniaxial loading, where specimens along T exhibit the lowest strain to fracture.

To compare the properties of WE43 alloy with common magnesium alloys, results of same experiments on hot-rolled AZ31 plate with similar dimensions are presented in figure 58b. While WE43 and AZ31 exhibit comparable $\bar{\varepsilon}_f$ under uniaxial loading, the strain to failure under triaxial loading is severely diminished in WE43 compared to AZ31. For instance, RN2 specimens of AZ31 have average strain to failure $\bar{\varepsilon}_f$ four times higher than their WE43 counterparts. Note that AZ31 used in this comparison is an alloy with strong anisotropy, tension/compression asymmetry and strong basal texture (See Ref. [18, 22])while WE43 exhibits no tension/compression asymmetry, weakened texture and isotropic behavior in tension.

6.2.1 Fractography

To explore the microstrucutral mechanisms controlling the macroscopic fracture response of WE43, the fracture surface of different specimens are studied using SEM. The fracture surface of WE43 under uniaxial loading, presented in figure 59, exhibits a mixture of trans- and intergranular fracture (TGF and IGF, respectively) characteristics with the latter being more dominant. Faceted features and outline of grains on the fracture surface of WE43 alloy are clearly shown in the central region of figure 59a. These features are caused by advancement of macroscopic cracks along grain

(a) 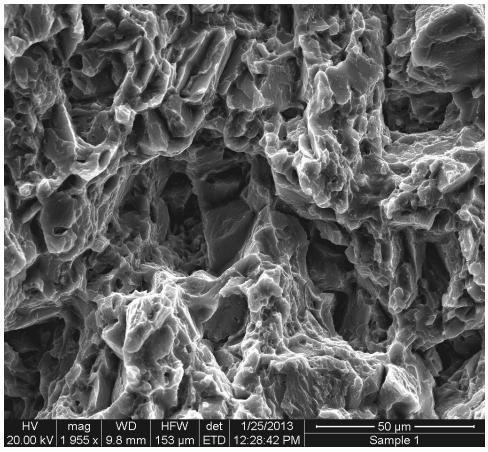

(b) 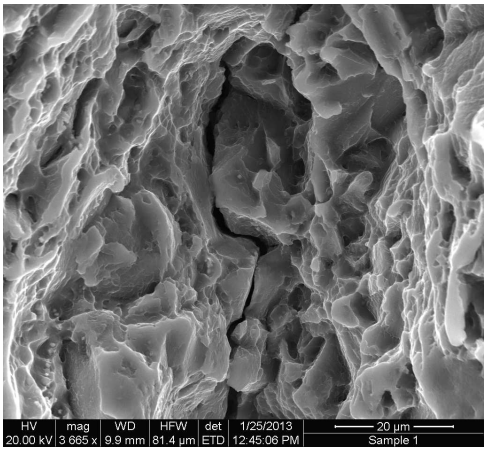

Figure 59: Fracture surface of a uniaxial tension specimen exhibiting (a) flat surfaces and outlines of grains on the fracture surface and (b) macroscopic cracks moving along grain boundaries. In both micrographs, shallow dimples cover a significant fraction of the fracture surface.

boundaries. Propagation of cracks along twin boundaries could also be responsible for some of the observed facets, as reported in References [23, 137]. The presence of shallow dimples covering significant portion of the studied area indicates that void growth in this alloy is truncated by early coalescence of voids/microcracks. There are small macroscopic cracks along the grain boundaries, as illustrated in figure 59b, providing further evidence for intergranular fracture (IGF) in WE43.

Increasing triaxiality enhances the IGF and TGF features on the fracture surface of WE43, as shown for the case of WE43-RN10 and RN2 specimens in figures 60 and 61, respectively. In these figures, smoother facets with high frequency are observed at higher trixialities. The presence of grains with their smooth facets on the fracture surface, as illustrated in figures 60b, 61a and 61b, is clear indication of IGF in the alloy and loading condition. In addition to grain boundaries, twin boundaries could also be preferred path for macroscopic crack advancement.

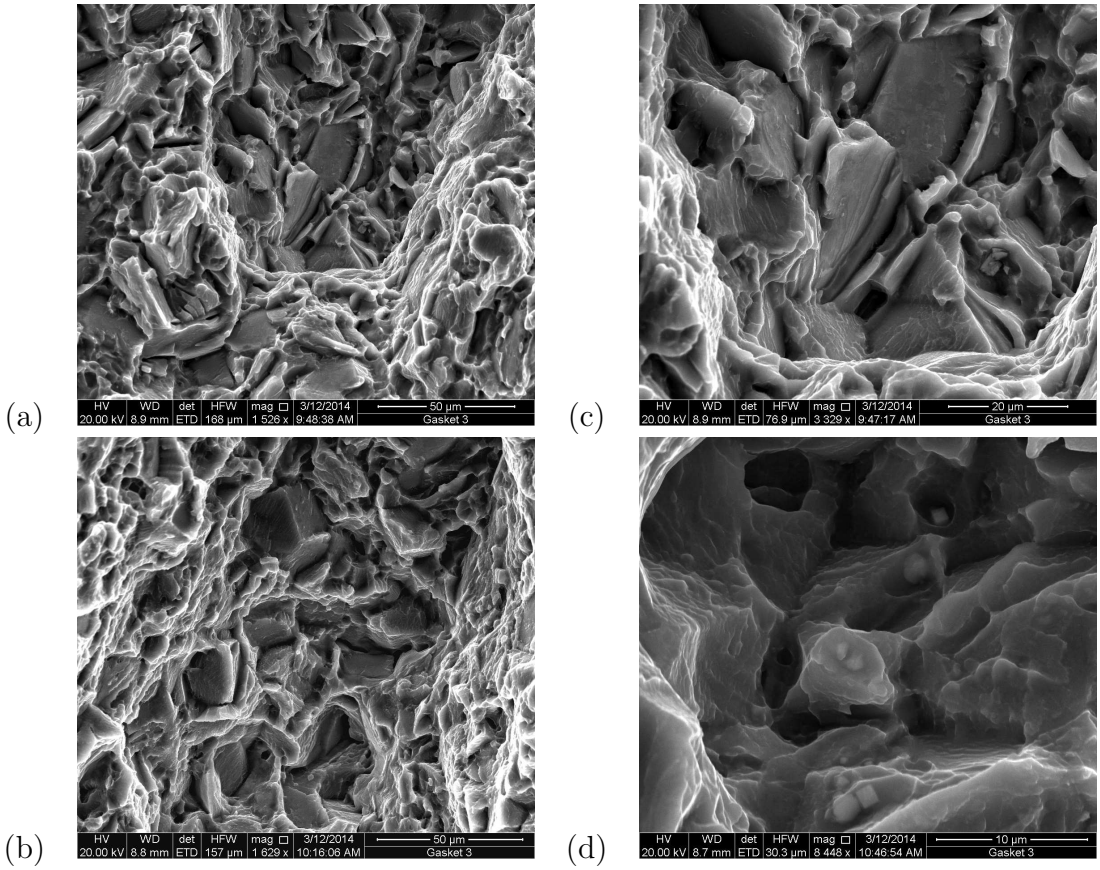

Figure 60: Fracture surface of a WE43-RN10 specimen exhibiting (a)&(c) facets with very smooth surfaces and (b) outline of grains on the fracture surface with smooth boundaries. (d) Second phase particles located at the end of shallow dimples and on smooth facets.

One should bear in mind that deformation twins could also act as damage initiation sites [12, 18] and lead to TGF. Figures 60a, 60c and 61c show faceted features parallel to each other suggesting twin boundaries as a preferred locations for either crack initiation or growth. Presence of numerous second phase particles on the fracture surface, as clearly depicted in figure 60d, indicates that second phase particles are also actively involved in damage initiation process. The particles are frequently

(a)

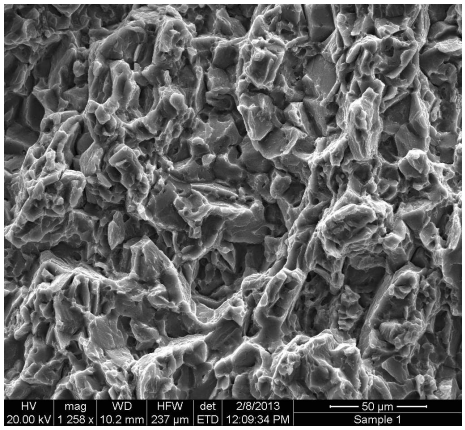

(b)

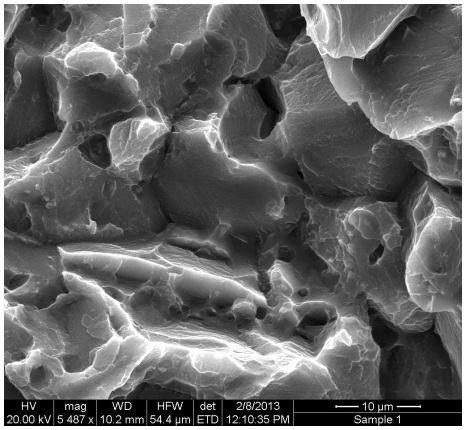

(c)

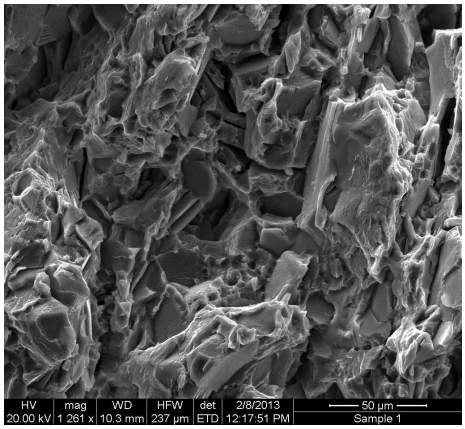

Figure 61: Fracture surface of a WE43-RN2 specimen showing (a)&(b) grain with their boundaries on the fracture surface and (c) smooth facets.

observed on the fracture surface. These particles are located at the center of shallow dimples or, sometimes, on flat and faceted features.

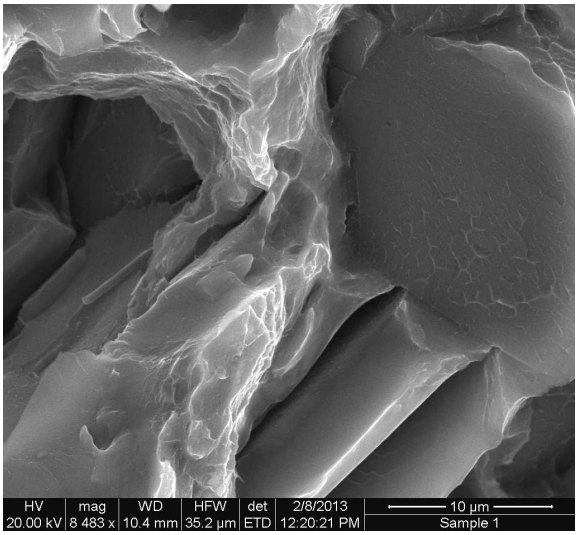

Figure 62: Cleavage-like fracture with ductile ridges and possibly twinning-induced cracks.

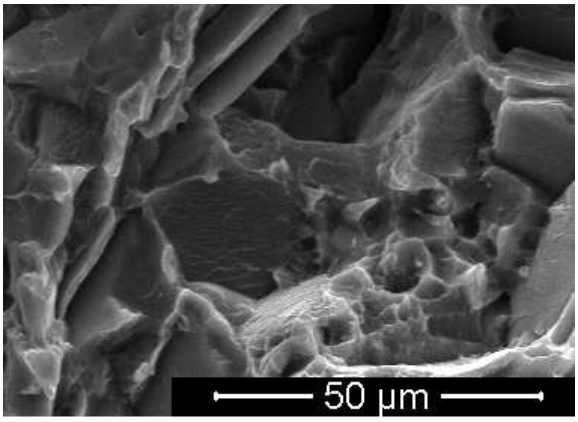

Figure 63: Frcture surface of a WE43-RN10 specimen showing a grain at its center. The boundary if this grain is decorated with second phase particles suggesting the role of these particles in intergranular fracture.

Figure 62 presents cleavage-like facets on the fracture surface of an RN2 specimen with ductile ridges and series of parallel cracks (most probably twinning-induced cracks) in their vicinity. This figure clearly shows the mixed nature of the fracture process in this alloy. The limited plasticity before final failure is evident from smooth cleavage-like features in this image.

In addition to particles shown in figure 60d, there are particles located at corners and edges of grains present on the fracture surfaces. This suggests that these grains are active damage initiation sites. The central region of figure 63 depicts the fracture surface of an RN10 specimen where the corner of the central grain is decorated with second phase particles.

6.2.2 Qualitative rationale for fracture locus of WE43

The low failure strains in the current WE43 alloy can be explained in light of Figures 62, 63, and other features on the fracture surface. After a critical strain, voids nucleate on the second-phase particles at appropriately-oriented GBs. The growth of these voids is truncated soon after their nucleation by early commencement of coalescence due to the spatial arrangement of particles at GBs. (See initial microstructure in Figure 64a for more details on the special arrangement of GB particles.) The above-mentioned rationale agrees with the features found on the fracture surfaces. Since the dependence of IGF on stress state triaxiality is known [138], one can expect a significant reduction of failure strain as the traixialities increases, which is also observed experimentally. Under uniaxial tension and compression, possible interference from shear localization reduces the strain that material can accommodate before final failure and leads to a maximum in fracture locus at moderate triaxialities.

(a)

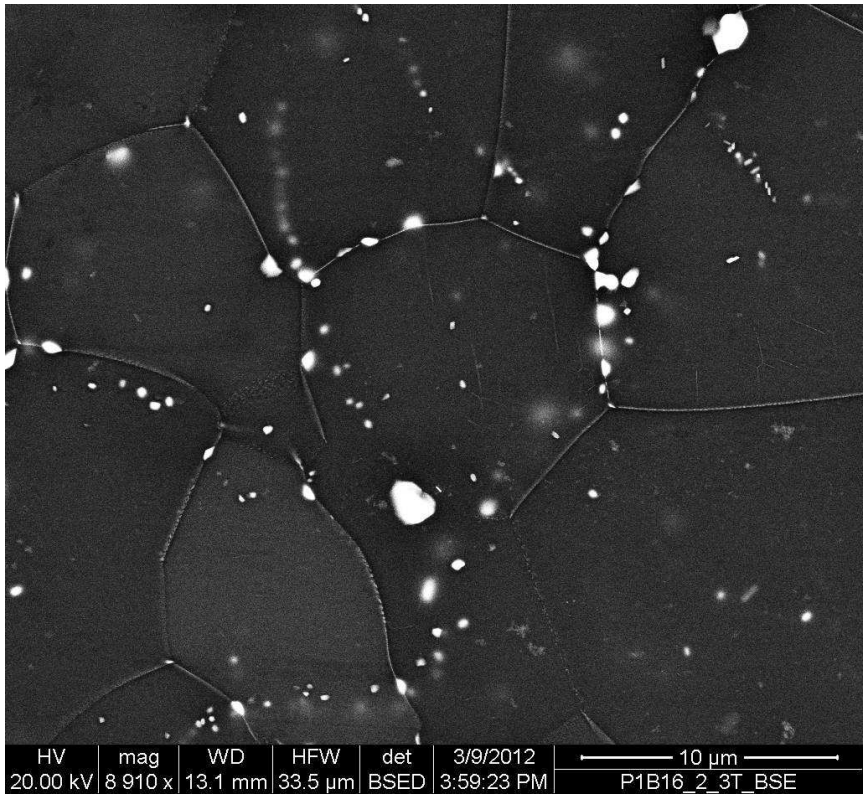

(b)

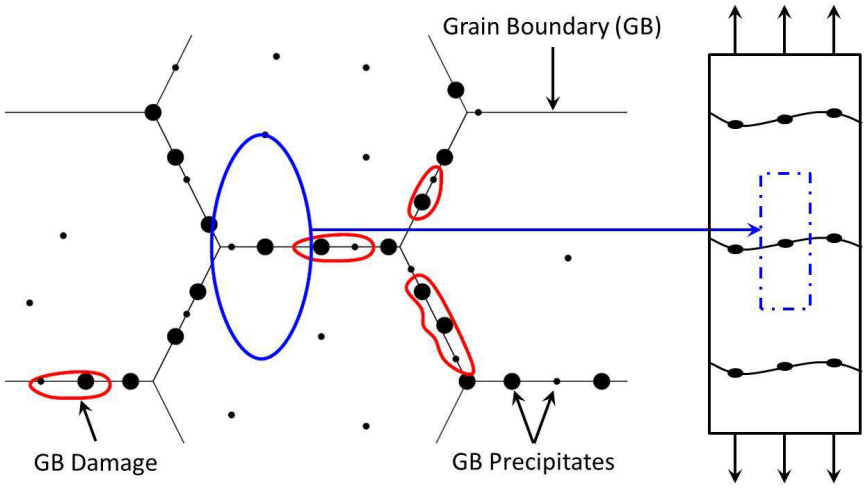

Figure 64: (a) Microstructure of WE43 in L-T plane showing second phase particles located mostly on GBs. (b) schematic of the microstructure and (c) idealized microstructure for study of intergranular fracture using models for ductile fracture.

The rationale proposed above is acceptable only if the ductile fracture mechanisms are operative in WE43. Although ductile fracture often occurs after significant plastic deformation, there are materials such as high strength alloys, metal matrix composites and un-clean alloys in which ductile fracture leads to fracture strains as low as 1% [139]. In the literature, fracture in magnesium alloys is often perceived as quasi-brittle, a conclusion which is based on the macro- and microstructural data from uniaxial loading experiments. Recent studies on fracture in Mg alloys [18, 22], however, showed that fracture under uniaxial loading is affected by structural instabilities, i.e., shear localization. Much higher failure strains in notched bar experiments, compared to their uniaxial counterparts, were measured. Higher ductility under such triaxial loading conditions was attributed to prevention of shear localization due to notch geometry as well as change in fracture mechanisms. Observation of (i) fracture surfaces covered by deep voids (Figures 11b and 13 in Ref. [18]), (ii) flat voids with limited opening, immediately ahead of a macroscopic cracks (Figure 9 in Ref. [18]) and (iii) high strain to failures in the absence of structural instabilities suggests the hypothesis that fracture in Mg alloys occurs by ductile fracture where limited void growth is interrupted by early coalescence of voids. In the following, WE43 material parameters and mechanisms of ductile fracture are utilized to rationalize experimentally observed fracture locus of WE43 via IGF.

To study ductile fracture, microstrucutre with complicated features is simplified to a Representative Volume Element (RVE) that carries the characteristics of the microstructure in an average sense. The RVE is often characterized by parameters such as (i) void volume fraction (f) that describes the amount of voids in microstrucutre; (ii) void aspect ratio (W), which represents the void shape characteristic; (iii) cell aspect ratio (λ) that characterizes the distribution of the voids; and finally (iv) ligament ratio (χ), which defines the ratio of the void diameter (perpendicular to the

loading direction) to the cell diameter. See Figure 65 for illustrations on these parameters. Only three of these parameters are independent and the geometry of the cell defines the relationship between them (e.g., for a spheroidal void inside a cylindrical cell, $\chi = [3f\lambda/W]^{\frac{1}{3}}$). Accordingly and by assuming that voids could initiate on all second phase particles, the microstructure of the WE43 in L–T plane, presented in Figure 64a, is simplified as one where second phase particles are mostly located on the grain boundaries (left picture in Figure 64b). Since those grains boundaries and their associated particles that are parallel to the loading direction do not play a substantial role in fracture, one could further idealize the microstructure as one presented in the right side of the Figure 64b. Using this idealization, χ_0 and λ_0 in the current WE43 alloy are calculated to be 0.25 and 1.77, respectively. The microstructure of this WE43 is not homogeneous and these parameters, in some locations, can be as high as of $\chi_0 = 0.35$ and $\lambda_0 = 5.25$. Here, only the grain boundaries that make an angle of $60 \leqslant \theta \leqslant 120$ degree with the loading direction are considered. In contrast to this microstructure, there is the matrix with homogeneously distributed voids that renders $\lambda_0 = 1$. A comparison between the RVE of microstructures with homogeneous and heterogeneous void distribution (similar to the one observed in WE43) is presented in Figure 65. It is clear from this picture that void nucleation from closely arranged particles can significantly reduce the ligament region that carries the load.

The void spacing significantly affects the strain to onset of coalescence [115] and it is the coalescence stage at the end of which fracture occurs. In fact, in many cases, the onset of coalescence could be identified as a failure criterion owing to the fact that material loses its load baring capacity rapidly and undergoes fracture soon after it. A fully analytical closed-form criterion for coalescence of voids by internal necking was recently developed by Benzerga and Leblond [93]. Using a modified version of the model in this reference [140] and presented in Equation 6.1, the stress

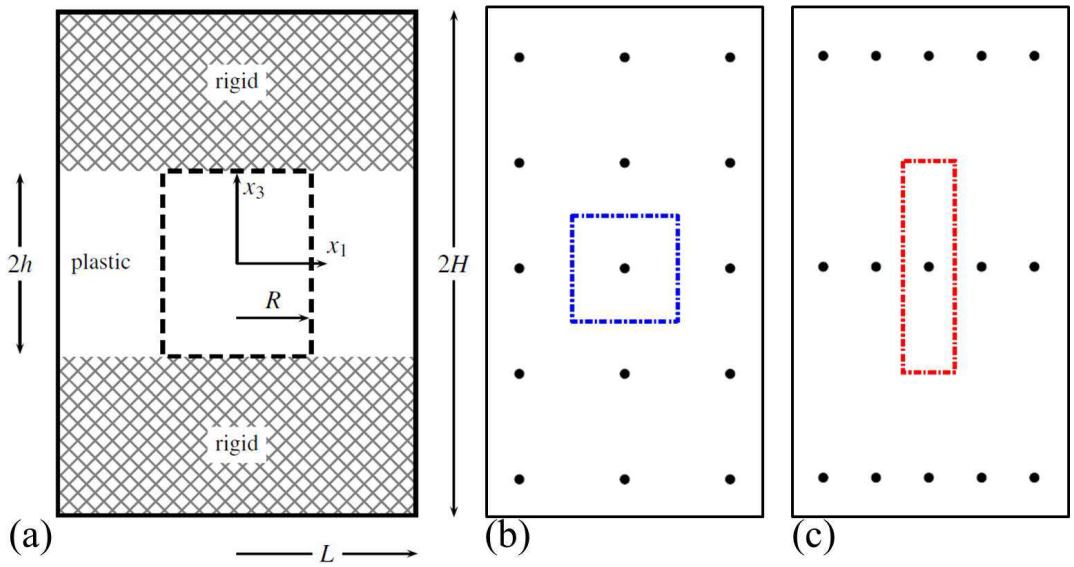

Figure 65: (a) RVE used to study coalescence of voids in fail via mechanisms of ductile fracture. (b) Shape of the RVE for homogeneous distribution of voids. (c) Shape of the RVE for heterogenous distribution of voids such that ductility properties of diminished. Idealization of the second phase particles on GBs as nucleation sites for voids in the current WE43 is close to such configuration (as shown in 64)

to the onset of coalescence (σ_c) normalized by the flow stress of the material ($\overline{\sigma}$) versus initial ligament ratio (χ_0) is calculated and presented in Figure 66.

$$\frac{\sigma_c}{\overline{\sigma}} = \frac{\beta}{\sqrt{3}}\left[2 - \sqrt{1+3\chi^4} + \ln\left(\frac{1+\sqrt{1+3\chi^4}}{3\chi^2}\right)\right] + \frac{\alpha}{3\sqrt{3}}\frac{\chi^3 - 3\chi + 2}{3\chi W} \tag{6.1}$$

with

$$\alpha = \frac{(C_0 + C_1\chi)W}{1 + (C_0 + C_1\chi)W}; \quad \beta = 0.9 \tag{6.2}$$

where

$$C_0 = -0.84; \quad C_1 = 12.9 \tag{6.3}$$

As it is illustrated here, a slight increase in χ_0 (which is bound between $0.0 \leqslant$

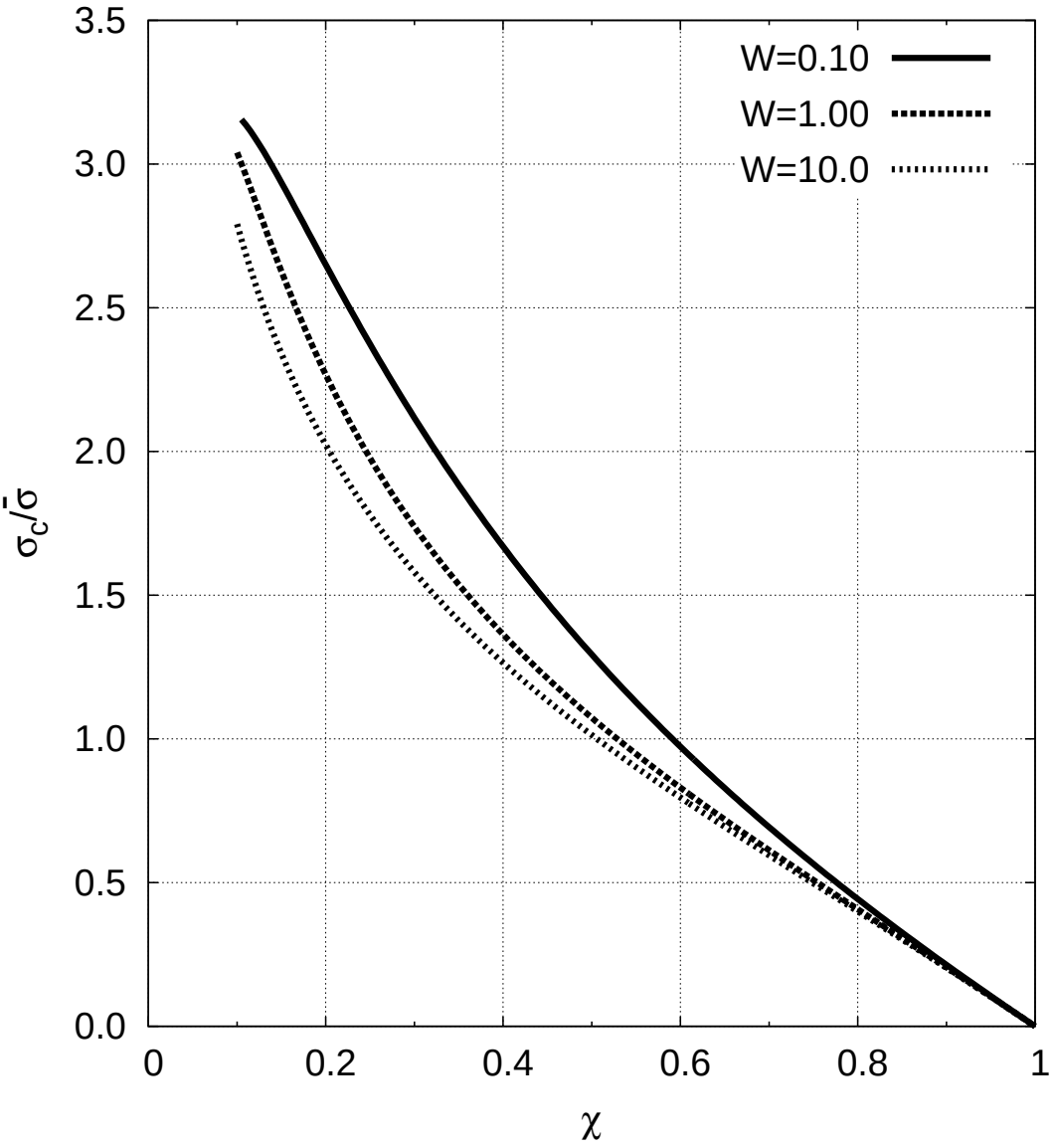

Figure 66: Evolution of coalescence stress 'σ_c' versus ligament parameter 'χ_0'. The trend of change in σ_c with χ_0 is almost the same for any void shape.

$\chi \leqslant 1.0$) leads to a significant drop in coalescence stress. According to the relationship between λ and χ, presented above, increasing λ from 1.0 (i.e., homogeneous distribution of voids) to 5.25 (i.e., locally measured from the distribution of second

phase particles on GBs in the current WE43 alloy) leads to a 173.8 % increase in parameter χ_0 and significant reduction of coalescence stress. Lower stresses required for coalescence are realizable at lower strains. Therefore, the failure strain of the materials is decreased significantly. The effect of void shape is presented in this figure as well. According to this figure, prolate voids lead to lower coalescence stress. Details aside, the trend of change in σ_c with χ_0 is almost the same for any void shape. Note that in this analysis, the change in void shape could drastically change void volume fraction, which is not kept constant. Thus, the effect of void shape presented here should be treated with care.

To rationalize the experimentally fracture locus, the effect of triaxiality of the evolution of microstrucutral variable should be studied. The effect of triaxiality on the evolution of ligament ratio and void shape during deformation of a model material is presented in Figure 67. These graphs are re-plotting of data in Ref. [79]. These graphs show the typical evolution of microstructure containing pre-existing voids during the void growth stage (omitting both nucleation and coalescence). As depicted in Figure 67a, the lateral growth of voids, which is manifested by increasing parameter χ, is substantially accelerated as the triaxiality is increased.

Voids experience minimal lateral growth under low traixiality of $T = 0.5$. In contrast to loading at low triaxiality, ligament ratio increases significantly at high triaxialities, which diminishes the load-bearing capacity of the material. Thus, one expects substantial reduction in strain to failure by increasing triaxialities, which is universally accepted. Such changes in the void growth dynamics also manifest themselves through evolution of void shape. As depicted in Figure 67b, the voids tend to elongate along the loading direction at low triaxialities, leading to increase in W. Under elevated triaxialities, however, the lateral growth of voids compared to their longitudinal extension is such that prolate voids evolve toward oblate ones.

This, partly, explains the deleterious effect of triaxiality on ductility. Finally, the knowledge from the above analysis is used to qualitatively describe the process of fracture in WE43 up to the onset of coalescence as the failure criterion. Figure 67c presents the coalescence stress as a function of void shape for various χ_0 values. The arrows in this figure schematically illustrate the evolution of microstructural variables during the course of deformation under Low (LT), High (HT) and Very High Triaxiality (VHT). There are two sets of arrows corresponding to (i) material with homogeneous distribution of voids (blue arrows) and (ii) matrix with heterogeneous distribution of voids similar to present WE43 alloy (red arrows). Both materials start with a similar void shape while the heterogeneous material has higher χ_0 and, consequently, lower coalescence stress. At low triaxialities (LT), plastic deformation leads to void elongation and significant increase in void aspect ratio (W). In this condition, lateral growth of voids are limited and χ does not change considerably. At high triaxiality (HT), lateral growth of voids is such that it balances their elongation and, as a result, W does not increase significantly while χ increases (switching from one line to others with lower coalescence stress). Under very high triaxialities (VHT), voids become flattened and χ is increased considerably. In WE43, voids nucleate on the closely spaced second phase particles at GBs. The newly nucleated voids have high χ and λ and reach the coalescence condition after limited deformation. At high traixiality, faster increase in χ leads to lower failure strain compared to low triaxiality cases. Finally, it is worth noting that, similar to the case of AZ31 [18], there are contributions from shear localization (although with less intensity). As for AZ31, the contribution from shear localization could be invoked to partically justify the experimentally observed maximum in failures strain at moderate triaxialities.

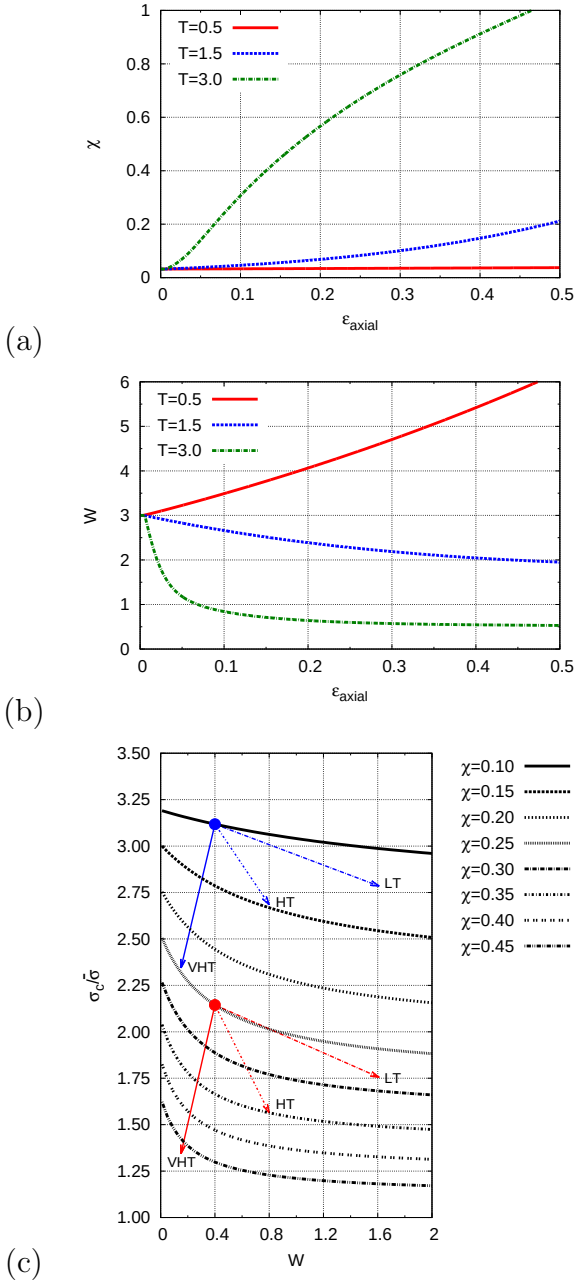

Figure 67: (a) Evolution of ligament parameter 'χ' during deformation under low, high and very high triaxialities. (b) Evolution of void ratio 'W' during deformation under low, high and very high triaxialities. (c) Effect of varying χ on the evolution of σ_c versus W. The blue and red arrows indicate the evolution of microstructure (W and χ) and σ_c for isotropic and heterogeneous distribution voids (on GBs), respectively. (VHT:=Very High Triaxiality, HT:=High Triaxiality and LT:Low Triaxiality)

7. MICROTOMOGRAPHY ANALYSIS

The fractography work presented in previous section, showed that, in AZ31, there is diffuse damage in the microstructure at incipient crack formation and after fracture. Second-phase particles and deformation twins were identified as the sites for void/microcrack initiation. It was shown that void near the fracture surface are not axially extended as it is expected based on information from most materials system such as copper and low-carbon steels. In addition, from the features on the fracture surface, which were mainly along the T direction, it was implied that direction of crack propagation in AZ31 alloy is parallel to the T direction. Metallography on the interrupted specimens in L–T and L–S corroborated this hypothesis. It was concluded that when macroscopic cracks reach to a critical distance from free surface or another crack, connect to it via shear localization in L–S plane.

Although valuable information are drawn from fractography data, their statistical representativeness could be questioned. It is especially important in the study of fracture, which is a stochastic phenomenon. In addition, the fractography data is in two dimensional by nature. Connecting such 2D data to the 3D state of damage in the material is not trivial. A three dimensional study on the state of damage at different triaxialities could provide further insight in the mechanism of damage and fracture. Therefore, microtomography analysis were performed on specimens loaded at different triaxialities. Samples for X-ray computed microtomography were prepared by sectioning notched specimens deformed up to incipient fracture along T direction. These samples are stopped at macroscopic crack initiation, which is identified by a sudden load-drop in the load-deflection curves. The specimens were cut in L–T planes into sections (i) close to the free surface and (ii) close to the center

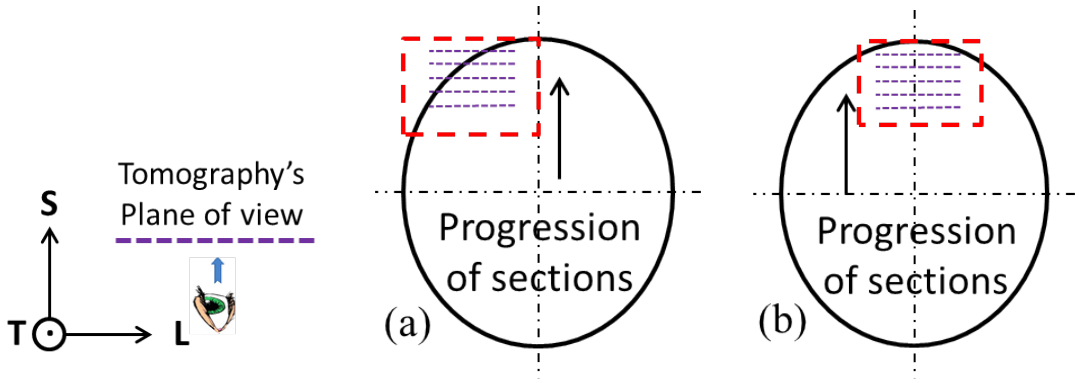

Figure 68: Schematic describing the location of each tomographic section and the order of images in the representation of results.

of the bar. Data from these analyses were used to acquire better understanding of void/microcrack growth and their interactions at coalescence,

Investigating the microstructure of RN10 and RN2 notched bars enabled the study of triaxiality effects on void/microcrack initiation, growth and coalescence. Tomography studies render a resolution of 0.7μm in which most second-phase particles are distinguishable. In this analysis, however, grain- and twin boundaries are not discernible. A schematic of the surface and central sections, plane of view and the order in which the micrographs are presented with respect to the geometry of the notched bars are shown in Figure 68. In this section, micrographs in each figure are ordered based on their closeness to the center of the bar (along the normal to the plane of view; i.e., S direction). For instance, in a single figure with four sub-figures, migcrograph in part (a) is taken from a location close to center of the bar whereas part (d) captures the microstructure close to the surface, which its normal is the S direction.

7.1 State of damage in AZ31 at moderate triaxialities

Figure 69 illustrates the microstructure of an AZ31-RN10 specimen.

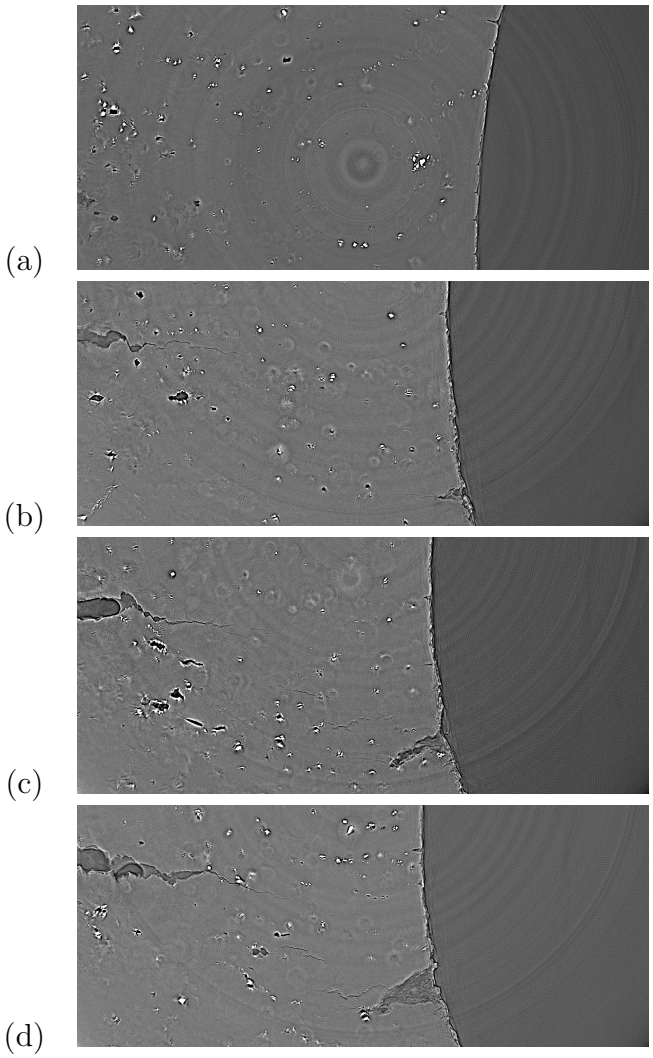

Figure 69: State of damage in an RN10 specimen loaded parallel to T direction and unloaded after macroscopic crack initiation. The micrographs are taken from a section near the free surface (black region). This section is similar to the one in part (a) of Figure 68. The width of each micrograph is 1435 μm.

(a)

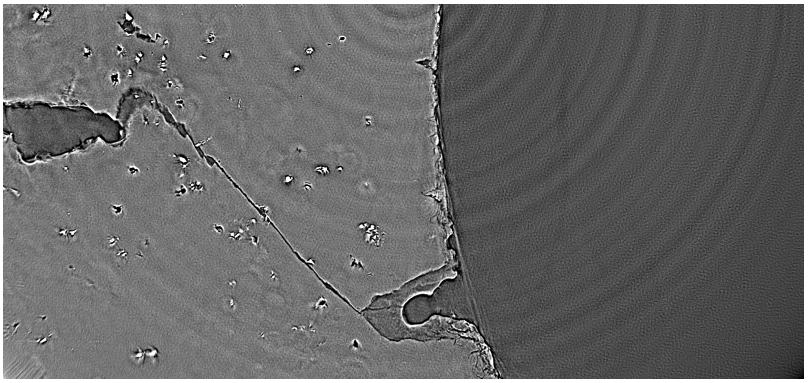

(b)

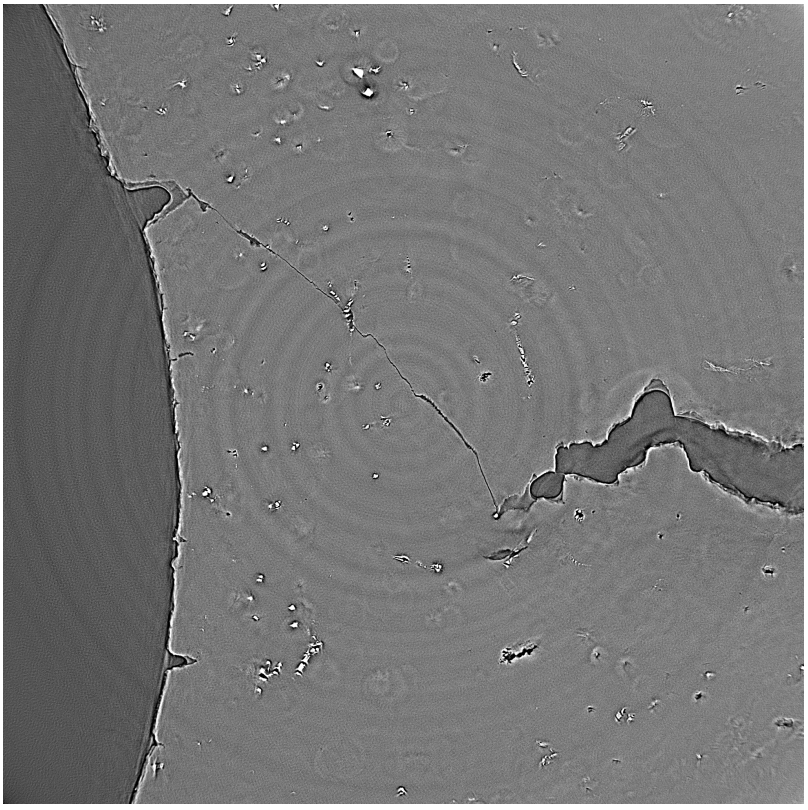

Figure 70: Formation of sheear lips in RN10 specimen. The microcracks connect to free surface when they reach to a critical distance from each other. The width of each micrograph is 1435 μm.

This figure depicts the microstructure near the notch root, similar to the schematic (a) in Figure 68. As depicted in these micrographs, most voids and the macroscopic crack in RN10 specimens are formed near the center of the specimen. Closer look indicates that majority of these voids are related to second-phase particles. When the macroscopic cracks get close to the free surface, large shear-lips (as shown in Figure 70 connects them to each other. Shear-lip formation usually occurs near the surface and in the L–S direction.

Micrographs of the central part of the RN10 specimen in the L–T plane is presented in Figure 71. Schematic (b) in Figure 68 illustrates the location of these micrographs. As described before and shown in part (a) of this figure, damage is more pronounced in the central region of these micrographs. It is possible for cluster of voids/microcracks to coalesce on each other and form macrocracks at separate regions of the sample. These macrocracks then connect to each other by shear localization and form a large macrocrack. Formation of such macrocracks via localization is depicted in Figure 71b-d. The micrographs in this section clearly show the extent of which damage is present in the last stages of deformation in Mg alloys. In addition, the importance of second-phase particles in damage initiation is demonstrated in all micrographs. Although there is limited axial voids growth, the number density and distribution of voids in the microstrucutre shows the ductile nature of fracture in this alloy.

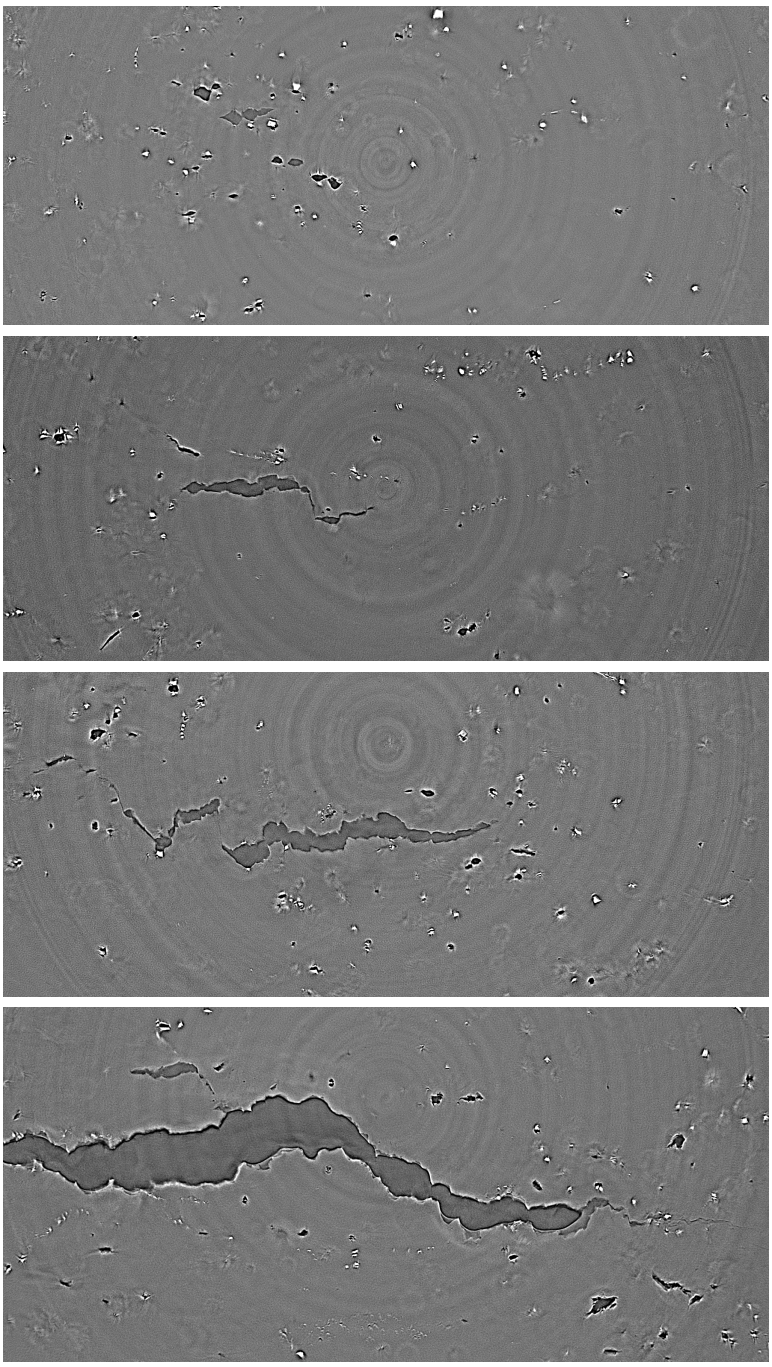

Figure 71: State of damage in an RN10 specimen loaded parallel to T direction and unloaded after macroscopic crack initiation. The micrographs are taken from a section near the center of the notched bar. This section is similar to the one in part (b) of Figure 68. The width of each micrograph is 1435 μm..

7.2 State of damage in AZ31 at high triaxialities

Tomography data of RN2 specimen is presented in this section. Similar to the previous section, microstructure near the notch root, similar to the schematic (a) in Figure 68, is shown in Figure 72.

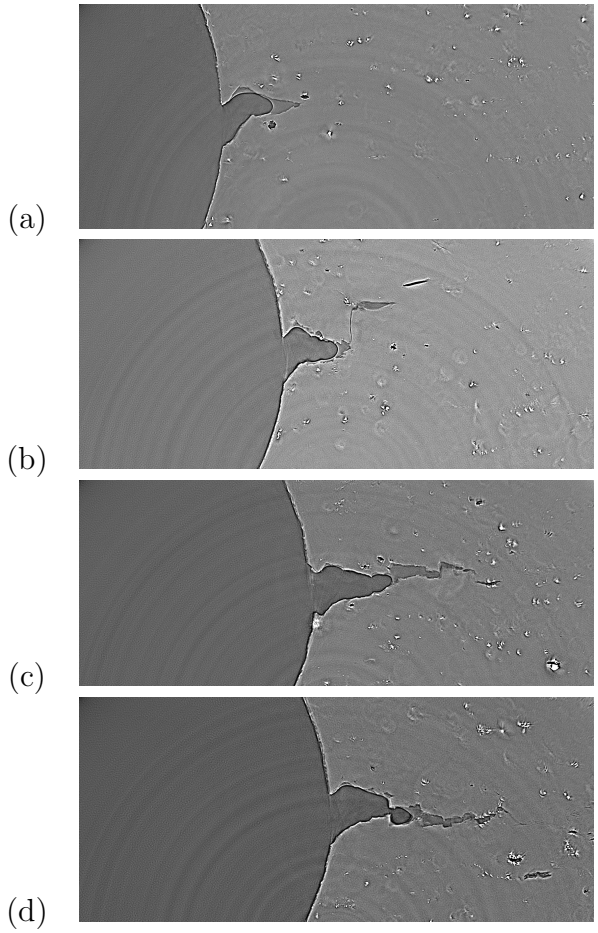

Figure 72: State of damage in an RN2 specimen loaded parallel to T direction and unloaded after macroscopic crack initiation. The micrographs are taken from a section near the free surface (black region). This section is similar to the one in part (a) of Figure 68. The width of each micrograph is 1435 μm.

(a)

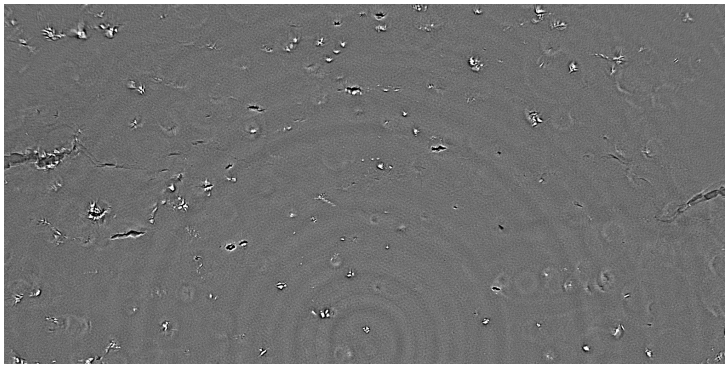

(b)

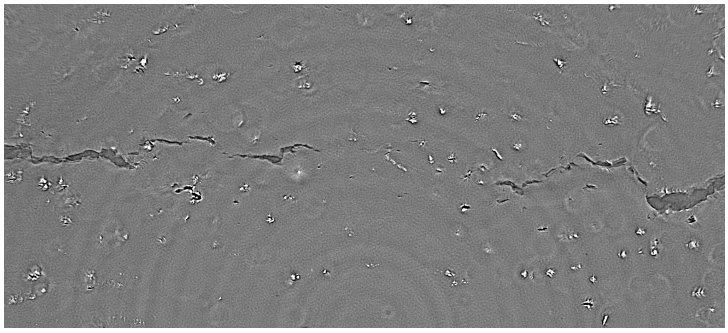

(c)

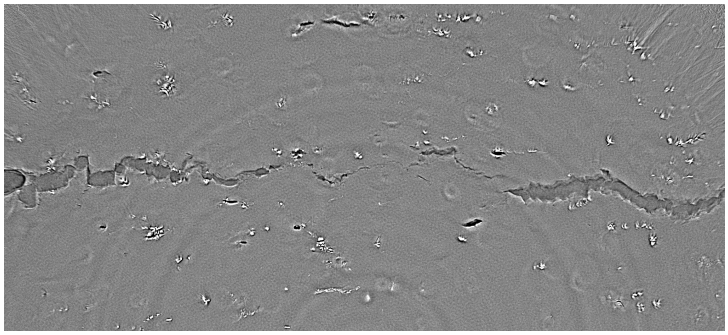

(d)

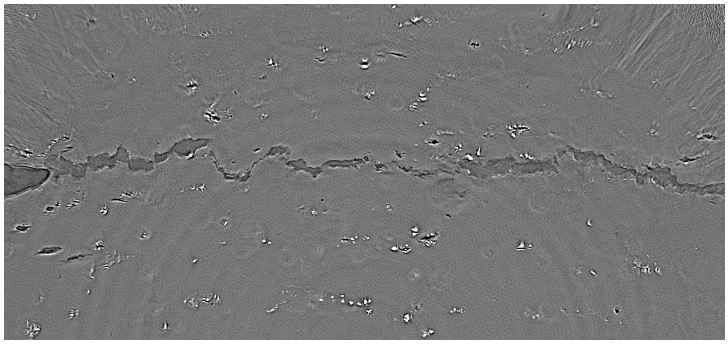

Figure 73: State of damage in an RN2 specimen loaded parallel to T direction and unloaded after macroscopic crack initiation. The micrographs are taken from a section near the center of the notched bar. This section is similar to the one in part (a) of Figure 68. The width of each micrograph is 1435 μm.

The central region of the bar in L–T planes are also shown in Figure 73; see the schematic (b) in Figure 68 for the location of these pictures with respect to the bar.

The most important observation in this set of micrographs is the frequent observation of voids with limited opening, even voids that are very close to the macroscopic crack. Compared to other materials system, where voids are significantly extended along the rolling direction, the voids/microcracks remain relative penny-shaped. Note that these features are captured after macroscopic crack initiation and close the final failure. The same was observed in the RN10 specimen but to a lesser extent. These micrographs indicate that there is limited void growth in AZ31 prior to failure.

As shown in Figure 72a and in contrast to the RN10 specimens, damaged regions are located near the free surface of RN2 specimens. Small cracks form near or on the surface. Moving along the S direction (normal to the plane of study) which is equivalent of going form Figure 72a to 72d, the cracks are extended towards the central region of the studied plane. As it was the case for RN10 specimens, void are mostly related to the second-phase particles. The micrographs in this figure also indicate that voids undergo limited axial growth before final failure. No large shear-lip was formed in RN2 specimens. There are, however, situations in which small microcracks with limited axial opening link up via very short shear region (Figure 72b and c). Similar trends were observed when the central region of the L–T section in RN2 specimens were studied. For more details, see Figure 73.

Investigating the voids in all of the presented micrographs suggests that, prior to coalescence, voids in AZ31 do not experience extensive axial growth compared to other material systems. This observation puts Mg in the class of technologically important materials in which fracture is controlled by early coalescence. High strength steels and Al alloys are among materials that fail with similar mechanism. Tomog-

raphy data also corroborated the conclusions of fractography on AZ31. Schematic illustration of the arrangement of microcracks in RN10 and RN2 specimens are recalled from Section sec:frac-AZ in Figure 48. In RN10 specimens loaded along T direction, damage forms predominantly in the central area of the sample and connects to the free surface via shear-lip formation. The direction of crack growth is along the L direction. Shear localization also connects the existing cracks. Microstrucutral investigations in L–T plane presents the best opportunity for observing crack growth and damage propagation. Alternatively, T–S planes' micrographs best illustrate the linkage of existing cracks by shear localization. In RN2 bars, however, damage is dominantly formed near notch root and macrocracks are formed near surface. These macrocracks propagate along L direction and connect to each other via shear zones. The mechanism of crack propagation and its trace, presented in Figure 48, is also proposed in previous sections based on tedious metallography.

7.3 Damage initiation from the surface

As previously mentioned, second-phase particles are the main mechanism for void and crack initiation. This contribution in creation of voids was illustrated in micrographs presented in the previous two sections. Figure 74 shows the role of second phase particles in initiation of surface cracks and their propagation. Part a of this figure shows the formation of a surface crack in an RN10 specimen at the location of second-phase particles. Figure 74b depicts a cracked formed in an RN2 specimen where a severely damaged cluster of second-phase particles are present. Figure 74c and d show the same figure presented in part b where second phase particles are present in the crack path.

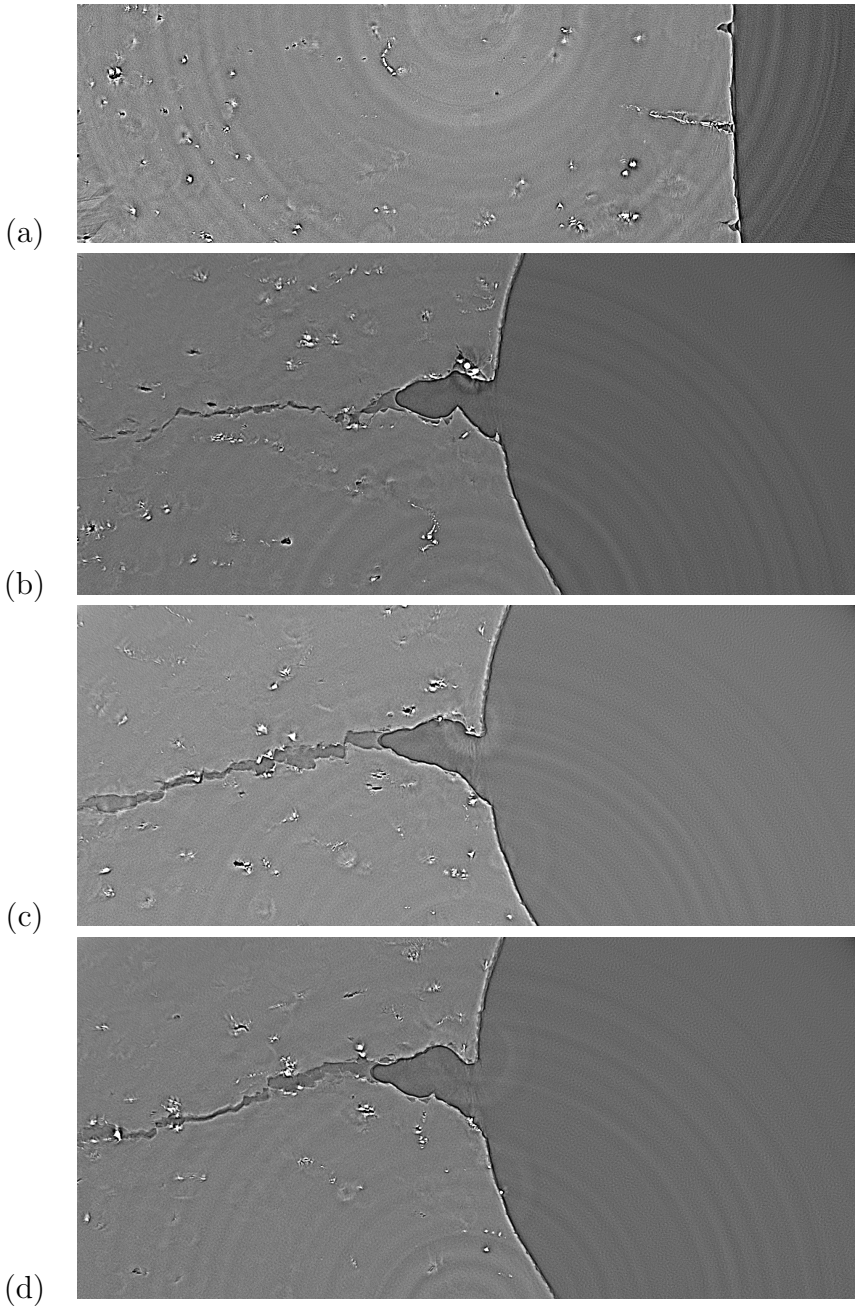

Figure 74: Tomograph of AZ31-RN10 specimen. Here, the role of second phase particles in initiation and propagation of surface cracks are illustrated. The width of each micrograph is 1435 μm.

8. CONSTITUTIVE MODELING OF PLASTIC ANISOTROPY

8.1 Identification of plastic anisotropy using Hill's 1948 criterion

Since void growth is a signature of plastic deformation of the matrix surrounding the voids, plasticity and ductile fracture are closely related. The HCP crystal structure and processing texture leave wrought magnesium alloys with a strong anisotropic behavior. Anisotropy of the matrix in Mg alloys is often invoked to justify their low ductility and poor formability [141]. However, recent analysis by Keralavarma and Benzerga showed that, when ductile fracture by void growth and coalescence it active in the material, certain types of matrix plastic anisotropy could significantly increase the strain to failure initiation [79]. Thus, accurate prediction of damage initiation and accumulation requires a proper constitutive model for plastic anisotropy. As mentioned before in Section 2.1, despite elastic isotropy [37], magnesium exhibits significant plastic anisotropy in its yield and flow strength as well as anisotropy ratios. Therefore, this section is dedicated to identifying the plastic anisotropy in the AZ31 and WE43.

To model yield and flow properties, a re-formulation of Hill's 1948 (Hill48) criterion [73] is adapted here. Among the advantages of Hill48 criterion are its simplicity and the fact that it could be fully identified base solely on the uniaxial experiments. For more details on the derivation of the model, see Section 2.3 and Ref. [75]. The yield function in this model reads as follows:

$$\mathcal{F} = \frac{3}{2}\,\sigma : \mathbb{p} : \sigma - \bar{\sigma}^2 = \frac{3}{2}\,\sigma^{'} : \mathbb{h} : \sigma^{'} - \bar{\sigma}^2 \tag{8.1}$$

where:

$\sigma^{'} = \sigma - 1/3\ tr(\sigma)\mathbf{I}$: The stress deviator;

$\mathbb{p}$: The forth order Hill's deviatoric anisotropy tensor;

$\mathbb{h}$: The forth order macroscopic anisotropy tensor in the space of deviatoric stresses;

$\bar{\sigma}$: The flow stress in an arbitrarily chosen reference direction.

In the equation 8.1, the relationship between $\mathbb{p}$ and $\mathbb{h}$ is as follows:

$$\mathbb{p} = \mathbb{J} : \mathbb{h} : \mathbb{J} \tag{8.2}$$

where $\mathbb{J}$ is the forth-order deviatoric projection operator $\mathbb{J} = \mathbb{I} - \frac{1}{3}\mathbf{I}\bigotimes\mathbf{I}$ with $\mathbb{I}$ and $\mathbf{I}$ being the forth- and second-order identity tensors, respectively. The plastic anisotropy of the matrix is, therefore, fully characterized by identifying the coefficients of the either of the anisotropy tensors (i.e., $\mathbb{p}$ or $\mathbb{h}$). Equation 8.3 shows the most general form of the deviatoric anisotropy tensor ($\mathbb{h}$) for the case of an orthotropic material with no tension–compression asymmetry.

$$\mathbb{h} = \begin{bmatrix} h_{11} & h_{12} & h_{13} & 0 & 0 & 0 \\ h_{12} & h_{22} & h_{23} & 0 & 0 & 0 \\ h_{13} & h_{23} & h_{33} & 0 & 0 & 0 \\ 0 & 0 & 0 & h_{44} & 0 & 0 \\ 0 & 0 & 0 & 0 & h_{55} & 0 \\ 0 & 0 & 0 & 0 & 0 & h_{66} \end{bmatrix} \tag{8.3}$$

For the current labeling of the plate, the directions 1, 2, 3, 4, 5 and 6 are assigned to L, T, S, TS, LS and LT, respectively. Assume that the principle directions of the plate (i.e., L, T, and S) coincide with the principle axes of orthotropy in the material. A direct consequence of this assumption is that off-diagonal components of anisotropy tensor vanish. Thus, it is the case that:

$$\mathbb{h} = \begin{bmatrix} h_L & 0 & 0 & 0 & 0 & 0 \\ 0 & h_T & 0 & 0 & 0 & 0 \\ 0 & 0 & h_S & 0 & 0 & 0 \\ 0 & 0 & 0 & h_{TS} & 0 & 0 \\ 0 & 0 & 0 & 0 & h_{LS} & 0 \\ 0 & 0 & 0 & 0 & 0 & h_{LT} \end{bmatrix} \tag{8.4}$$

In order to identify the anisotropy of the matrix using Hill48 model, all components of $\mathbb{h}$ matrix should be identified. There are two methods for such identification, (i) stress-based; and (ii) anisotropy ratio-based. The stress-based method utilizes the flow stresses as follows.

$$\frac{3}{2} \begin{bmatrix} \sigma_1^{'} \\ \sigma_2^{'} \\ \sigma_3^{'} \\ \sqrt{2}\sigma_4^{'} \\ \sqrt{2}\sigma_5^{'} \\ \sqrt{2}\sigma_6^{'} \end{bmatrix} \begin{bmatrix} h_L & 0 & 0 & 0 & 0 & 0 \\ 0 & h_T & 0 & 0 & 0 & 0 \\ 0 & 0 & h_S & 0 & 0 & 0 \\ 0 & 0 & 0 & h_{TS} & 0 & 0 \\ 0 & 0 & 0 & 0 & h_{LS} & 0 \\ 0 & 0 & 0 & 0 & 0 & h_{LT} \end{bmatrix} \begin{bmatrix} \sigma_1^{'} \\ \sigma_2^{'} \\ \sigma_3^{'} \\ \sqrt{2}\sigma_4^{'} \\ \sqrt{2}\sigma_5^{'} \\ \sqrt{2}\sigma_6^{'} \end{bmatrix} = \bar{\sigma}^2 \tag{8.5}$$

Here, shear components of the stress tensor are multiplied by $\sqrt{2}$ due to the fact that stress tensor is symmetric (i.e., $\sigma_{ij} = \sigma_{ji}$) and they appear twice in the original tensorial calculations. In the Voigt's notation, however, only three shear components are present and this difference is accounted for by the pre-factor. For material loaded along one of the principle axes of orthotropy (e.g., L direction), the yield criterion

becomes:

$$\frac{3}{2}\sigma^2 \begin{bmatrix} 2/3 \\ -1/3 \\ -1/3 \\ 0 \\ 0 \\ 0 \end{bmatrix} \begin{bmatrix} h_L & 0 & 0 & 0 & 0 & 0 \\ 0 & h_T & 0 & 0 & 0 & 0 \\ 0 & 0 & h_S & 0 & 0 & 0 \\ 0 & 0 & 0 & h_{TS} & 0 & 0 \\ 0 & 0 & 0 & 0 & h_{LS} & 0 \\ 0 & 0 & 0 & 0 & 0 & h_{LT} \end{bmatrix} \begin{bmatrix} 2/3 \\ -1/3 \\ -1/3 \\ 0 \\ 0 \\ 0 \end{bmatrix} = \bar{\sigma}^2 \qquad (8.6)$$

This equation leads to the following relation:

$$4h_L + h_T + h_S = 6(\frac{\bar{\sigma}}{\sigma_L})^2 \qquad \text{(for Loading} \parallel \text{L)} \qquad (8.7)$$

Applying the same analysis to loading parallel to other principal directions (i.e., T and S), it is the case that:

$$h_L + 4h_T + h_S = 6(\frac{\bar{\sigma}}{\sigma_T})^2 \qquad \text{(forLoading} \parallel \text{T)} \qquad (8.8)$$

$$h_L + h_T + 4h_S = 6(\frac{\bar{\sigma}}{\sigma_S})^2 \qquad \text{(forLoading} \parallel \text{S)} \qquad (8.9)$$

The off-axis loading of the material along directions other than the axis of orthotropy allows the identification of shear components of anisotropy tensor. Components of the stress tensor, equivalent to those developed in the material during uniaxial loading along off-axis directions (45° between pairs of principal directions) could be calculated using simple rotation of a second order matrix. Example of loading along LT direction is presented in what follows.

$$\sigma = \sigma \begin{bmatrix} 1/2 \\ 1/2 \\ 0 \\ 0 \\ 0 \\ -1/2 \end{bmatrix} \tag{8.10}$$

Since $\sigma_m = \frac{1}{3}\sigma$, the deviatoric stress is, thus, as the following.

$$\sigma^{'} = \sigma \begin{bmatrix} 1/6 \\ 1/6 \\ -2/6 \\ 0 \\ 0 \\ -3/6 \end{bmatrix} \tag{8.11}$$

Using the Hill48 yield criterion, it is the case that:

$$\frac{3}{2}\sigma^2 \begin{bmatrix} 1/6 \\ 1/6 \\ -2/6 \\ 0 \\ 0 \\ -\sqrt{2} \times 3/6 \end{bmatrix} \begin{bmatrix} h_L & 0 & 0 & 0 & 0 & 0 \\ 0 & h_T & 0 & 0 & 0 & 0 \\ 0 & 0 & h_S & 0 & 0 & 0 \\ 0 & 0 & 0 & h_{TS} & 0 & 0 \\ 0 & 0 & 0 & 0 & h_{LS} & 0 \\ 0 & 0 & 0 & 0 & 0 & h_{LT} \end{bmatrix} \begin{bmatrix} 1/6 \\ 1/6 \\ -2/6 \\ 0 \\ 0 \\ -\sqrt{2} \times 3/6 \end{bmatrix} = \bar{\sigma}^2 \tag{8.12}$$

The above equation leads to the following relation.

$$h_L + h_T + 4h_S + 18h_{LT} = 24(\frac{\bar{\sigma}}{\sigma_{LT}})^2 \qquad \text{(forLoading} \parallel \text{LT)} \qquad (8.13)$$

Similarly, one could also derive the relations for loading along LS and TS direction.

$$h_L + 4h_T + h_S + 18h_{LS} = 24(\frac{\bar{\sigma}}{\sigma_{LS}})^2 \qquad \text{(forLoading} \parallel \text{LS)} \qquad (8.14)$$

$$4h_L + h_T + h_S + 18h_{TS} = 24(\frac{\bar{\sigma}}{\sigma_{TS}})^2 \qquad \text{(forLoading} \parallel \text{TS)} \qquad (8.15)$$

Solving equation 8.7 to 8.15, simultaneously, the components of $\mathbb{h}$ (i.e. h_i) are calculated as follows:

$$h_L = \frac{\bar{\sigma}^2}{3}\left(\frac{5}{{\sigma_L}^2} - \frac{1}{{\sigma_T}^2} - \frac{1}{{\sigma_S}^2}\right) \qquad (8.16)$$

$$h_T = \frac{\bar{\sigma}^2}{3}\left(-\frac{1}{{\sigma_L}^2} + \frac{5}{{\sigma_T}^2} - \frac{1}{{\sigma_S}^2}\right) \qquad (8.17)$$

$$h_S = \frac{\bar{\sigma}^2}{3}\left(-\frac{1}{{\sigma_L}^2} - \frac{1}{{\sigma_T}^2} + \frac{5}{{\sigma_S}^2}\right) \qquad (8.18)$$

$$h_{TS} = \frac{\bar{\sigma}^2}{3}\left(\frac{4}{{\sigma_{TS}}^2} - \frac{1}{{\sigma_L}^2}\right) \qquad (8.19)$$

$$h_{LS} = \frac{\bar{\sigma}^2}{3}\left(\frac{4}{{\sigma_{LS}}^2} - \frac{1}{{\sigma_T}^2}\right) \qquad (8.20)$$

$$h_{LT} = \frac{\bar{\sigma}^2}{3}\left(\frac{4}{{\sigma_{LT}}^2} - \frac{1}{{\sigma_S}^2}\right) \qquad (8.21)$$

Using the above equations along with the data on yield/flow stresses from uniaxial tension or compression tests (presented in Section 5), the anisotropy of matrix could be characterized. This method requires six experiments along L, T, S, TS, LS and LT directions.

Another method to characterize the anisotropy of the matrix using Hill48 cri-

terion is to use anisotropy ratios. In the following, the derived equations for such identification is presented. In the Hill's model for anisotropy, an associative flow rule is considered. Using this flow rule, the Hill48 criterion leads to the following relations for the strain rate.

$$\mathbf{d} = \frac{3}{2}\frac{d_{eq}}{\sigma_{eq}}\mathbb{p} : \sigma = \frac{3}{2}\frac{d_{eq}}{\sigma_{eq}}\mathbb{J} : \mathbb{h} : \mathbb{J} : \sigma \tag{8.22}$$

Applying the above relation to uniaxial loading parallel to one of the principle directions of orthotropy (e.g., L direction), the strain rate tensor is identified as follows:

$$\begin{aligned}
\mathbf{d_L} &= \frac{3}{2}\frac{d_{eq}}{\sigma_{eq}} \times \sigma \\
&\begin{bmatrix} 2/3 & -1/3 & -1/3 & 0 & 0 & 0 \\ -1/3 & 2/3 & -1/3 & 0 & 0 & 0 \\ -1/3 & -1/3 & 2/3 & 0 & 0 & 0 \\ 0 & 0 & 0 & 1 & 0 & 0 \\ 0 & 0 & 0 & 0 & 1 & 0 \\ 0 & 0 & 0 & 0 & 0 & 1 \end{bmatrix} \begin{bmatrix} h_L & 0 & 0 & 0 & 0 & 0 \\ 0 & h_T & 0 & 0 & 0 & 0 \\ 0 & 0 & h_S & 0 & 0 & 0 \\ 0 & 0 & 0 & h_{TS} & 0 & 0 \\ 0 & 0 & 0 & 0 & h_{LS} & 0 \\ 0 & 0 & 0 & 0 & 0 & h_{LT} \end{bmatrix} \begin{bmatrix} 2/3 \\ -1/3 \\ -1/3 \\ 0 \\ 0 \\ 0 \end{bmatrix} \\
&= \frac{3}{2}\frac{d_{eq}}{\sigma_{eq}}\frac{\sigma}{9} \begin{bmatrix} 4h_L + h_T + h_S \\ -2h_L - 2h_T + h_S \\ -2h_L + h_T - 2h_S \\ 0 \\ 0 \\ 0 \end{bmatrix}
\end{aligned} \tag{8.23}$$

According to the anisotropy ratio defined in Section 3.3 and 3.4, The anisotropy

ratios for each of the loading directions are calculated as follows:

$$R^L = \frac{-2h_L - 2h_T + h_S}{-2h_L + h_T - 2h_S} \tag{8.24}$$

$$R^T = \frac{h_L - 2h_T - 2h_S}{-2h_L - 2h_T + h_S} \tag{8.25}$$

$$R^S = \frac{-2h_L + h_T - 2h_S}{h_L - 2h_T - 2h_S} \tag{8.26}$$

$$R^{TS} = \frac{18h_{TS} - (4h_L + h_T + h_S)}{2(4h_L + h_T + h_S)} \tag{8.27}$$

$$R^{LS} = \frac{18h_{LS} - (h_L + 4h_T + h_S)}{2(h_L + 4h_T + h_S)} \tag{8.28}$$

$$R^{LT} = \frac{18h_{LT} - (h_L + h_T + 4h_S)}{2(h_L + h_T + 4h_S)} \tag{8.29}$$

In the above identifications, it is assumed that the ratio of the lateral strain rates are equal to the ratio of lateral strains. By solving a set of five equations (two parallel to principle and three along off-axis directions) from the equation 8.24 to 8.29, simultaneously, the following relation are extracted for the components of $\mathbb{h}$ tensor (i.e. h_i). Here the Equation 8.26 is not considered, which removes the need for experiments along the S direction.

$$\frac{h_T}{h_L} = 1 - \frac{3(R^L R^T - 1)}{R^L R^T - 2R^L - 2} \tag{8.30}$$

$$\frac{h_S}{h_L} = 1 - \frac{3R^L(R^T - 1)}{R^L R^T - 2R^L - 2} \tag{8.31}$$

$$\frac{h_{TS}}{h_L} = -\frac{1}{2}\frac{(2R^{TS} + 1)(R^L + 1)}{R^L R^T - 2R^L - 2} \tag{8.32}$$

$$\frac{h_{LS}}{h_L} = -\frac{1}{2}\frac{(2R^{LS} + 1)(R^L + 1)R^L}{R^L R^T - 2R^L - 2} \tag{8.33}$$

$$\frac{h_{LT}}{h_L} = -\frac{1}{2}\frac{(2R^{LT} + 1)(R^L R^T + 1)}{R^L R^T - 2R^L - 2} \tag{8.34}$$

Using the experimental data presented in Section 5 and the above relations, the components of $\mathbb{h}$ tensor could be identified.

8.2 Application of Hill48 to Mg alloys

Using the relation derived in the previous section, the $\mathbb{h}$ tensor and its evolution during the course of deformation were identified for both AZ31 and WE43. It is worth noting that Hill48 is not able to account for tension/compression asymmetry. Thus, $\mathbb{h}$ tensor was identified for tension and compression, separately.

Table 12: Components of the $\mathbb{h}$ tensor and their evolution with deformation for AZ31, calculated based on anisotropy ratios, under uniaxial tension.

h_i	after yield	$\varepsilon = 3\%$	$\varepsilon = 6\%$	$\varepsilon = 9\%$	$\varepsilon = 12\%$	Steady State
h_L	1.00	1.08	1.15	1.16	1.18	1.17
h_T	1.00	0.96	0.82	0.91	0.93	0.92
h_S	1.00	0.71	0.56	0.45	0.36	0.40
h_{TS}	1.90	1.95	1.84	1.88	1.74	1.78
h_{LS}	2.31	2.43	1.82	1.72	1.66	1.60
h_{LT}	0.92	1.02	1.02	1.05	1.07	1.03
h	1.80	1.81	1.91	1.92	1.95	1.95

Table 13: Components of the $\mathbb{h}$ tensor and their evolution with deformation for AZ31, calculated based on flow stresses, under uniaxial tension.

h_i	after yield	$\varepsilon = 3\%$	$\varepsilon = 6\%$	$\varepsilon = 9\%$	$\varepsilon = 12\%$	Max Stress
h_L	0.73	0.28	0.66	-	-	1.08
h_T	0.13	0.10	0.60	-	-	1.11
h_S	2.96	4.80	2.77	-	-	0.57
h_{TS}	3.83	3.58	2.33	-	-	3.03
h_{LS}	3.93	3.61	2.34	-	-	2.56
h_{LT}	0.20	0.10	0.41	-	-	0.99
h	2.60	3.65	2.08	-	-	1.79

Table 14: Components of the $\mathbb{h}$ tensor and their evolution with deformation for AZ31, calculated based on anisotropy ratios, under uniaxial compression.

h_i	after yield	$\varepsilon = 3\%$	$\varepsilon = 6\%$	$\varepsilon = 9\%$	$\varepsilon = 12\%$	Steady State
h_L	-0.35	0.93	0.95	0.88	0.98	0.91
h_T	0.69	0.19	0.28	0.56	0.43	0.66
h_S	6.70	2.09	1.91	1.90	1.65	1.70
h_{TS}	1.00	3.24	2.98	1.86	2.11	1.85
h_{LS}	8.61	6.96	4.89	5.17	4.01	4.35
h_{LT}	4.53	0.58	0.60	0.72	0.76	0.86
h	2.55	1.95	1.92	1.83	1.84	1.77

The results of these identifications, using both stress- and anisotropy ratio-based, are presented in Table 12 to 18.

Table 15: Components of the $\mathbb{h}$ tensor and their evolution with deformation for AZ31, calculated based on flow stresses, under uniaxial compression.

h_i	after yield	$\varepsilon = 3\%$	$\varepsilon = 6\%$	$\varepsilon = 9\%$	$\varepsilon = 12\%$	Max Stress
h_L	1.26	1.26	1.29	1.08	1.00	0.98
h_T	0.98	1.19	0.89	0.76	0.72	0.68
h_S	-0.01	-0.23	-0.07	0.93	1.27	1.39
h_{TS}	1.78	1.06	1.14	2.96	2.72	2.49
h_{LS}	1.29	0.95	1.02	1.98	2.25	2.39
h_{LT}	1.12	1.30	1.14	0.97	0.75	0.77
h	2.18	2.46	2.36	1.80	1.84	1.83

Table 16: Components of the $\mathbb{h}$ tensor and their evolution with deformation for WE43, calculated based on anisotropy ratios, under uniaxial tension.

h_i	after yield	$\varepsilon = 3\%$	$\varepsilon = 6\%$	$\varepsilon = 9\%$	$\varepsilon = 12\%$	Steady State
h_L	0.87	1.01	-	-	-	1.03
h_T	1.21	0.80	-	-	-	0.91
h_S	1.33	1.15	-	-	-	0.97
h_{TS}	1.00	1.00	-	-	-	1.00
h_{LS}	1.37	0.89	-	-	-	0.94
h_{LT}	1.07	1.01	-	-	-	0.97
h	1.89	2.03	-	-	-	2.03

Table 17: Components of the $\mathbb{h}$ tensor and their evolution with deformation for WE43, calculated based on anisotropy ratios, under uniaxial compression.

h_i	after yield	$\varepsilon = 3\%$	$\varepsilon = 6\%$	$\varepsilon = 9\%$	$\varepsilon = 12\%$	Steady State
h_L	0.73	0.95	0.95	-	-	0.95
h_T	1.54	0.71	0.70	-	-	0.77
h_S	1.55	1.49	1.48	-	-	1.41
h_{TS}	1.00	1.32	1.33	-	-	1.24
h_{LS}	1.62	1.05	1.20	-	-	1.17
h_{LT}	0.90	0.83	0.80	-	-	0.83
h	1.87	1.98	1.97	-	-	1.97

Table 18: Components of the $\mathbb{h}$ tensor and their evolution with deformation for WE43, calculated based on flow stresses, under uniaxial compression.

h_i	after yield	$\varepsilon = 3\%$	$\varepsilon = 6\%$	$\varepsilon = 9\%$	$\varepsilon = 12\%$	Steady State
h_L	0.91	1.04	1.06	1.05	-	1.04
h_T	0.69	0.78	0.86	0.92	-	0.93
h_S	1.66	1.08	0.92	0.89	-	0.90
h_{TS}	1.47	1.03	1.08	1.12	-	1.19
h_{LS}	1.26	0.97	0.95	1.00	-	1.15
h_{LT}	0.89	0.99	1.03	1.11	-	1.05
h	1.91	2.02	2.02	1.98	-	1.95

Note that no uniaxial tension tests were done along the S direction. Since the stress-based method requires a set of six experiments, it is not possible to identify the $\mathbb{h}$ in tension based on the stresses. For AZ31 alloy, the compression flow stresses along the L direction was used as a replacement for tension along the S direction, since these two tests are almost equivalent in AZ31 with strong basal texture. In the anisotropy ratio-based method, only five set of experiments are sufficient and there is no need for results along the S direction.

8.3 Development of shear strains during off-axis uniaxial loading

During the loading of an anisotropic material parallel to directions other than principle axes of orthotropy, material could experience rotation, which is rooted in the anisotropy of the matrix. Development of such shear strains inside the material could introduce significant error in identification of anisotropy components from off-axis experiments. In the current study it was assumed that that no shear strains are developed in off-axis experiments along 45° between pairs of principle direction. Here, this assumption is tested. Consider uniaxial loading of a sample in the e_1-e_2 plane along a direction that makes angle θ with axis e_1. Here, e_1, e_2 and e_3 are the principle asex of orthotropy in the material. The stress state inside the gauge section due to such macroscopically applied deformation is as follows:

$$\sigma = \begin{bmatrix} \sigma & 0 & 0 \\ 0 & 0 & 0 \\ 0 & 0 & 0 \end{bmatrix} \tag{8.35}$$

where the coordinates coincide with the direction of the applied load. This stress in the coordinates system coinciding with the principle axes of orthotropy is calculated as follows:

$$\sigma^{'} = \mathbf{R}^T \sigma \mathbf{R} \tag{8.36}$$

where

$$\mathbf{R} = \begin{bmatrix} \cos\theta & \sin\theta & 0 \\ -\sin\theta & \cos\theta & 0 \\ 0 & 0 & 1 \end{bmatrix} \tag{8.37}$$

$$\sigma = \sigma \begin{bmatrix} \cos^2\theta\sigma & -\sin\theta\cos\theta\sigma & 0 \\ -\sin\theta\cos\theta\sigma & \sin^2\theta\sigma & 0 \\ 0 & 0 & 0 \end{bmatrix} \tag{8.38}$$

According to Equation 8.39, the strain rate tensor in Hill48 model is as follows.

$$\mathbf{d} = \frac{3}{2}\frac{d_{eq}}{\sigma_{eq}} \mathbb{J} : \mathbb{h} : \mathbb{J} : \sigma \tag{8.39}$$

$$= \frac{3}{2}\frac{d_{eq}}{\sigma_{eq}} \begin{bmatrix} \frac{2}{3}h_1 & -\frac{1}{3} & -\frac{1}{3} & 0 & 0 & 0 \\ -\frac{1}{3} & \frac{2}{3}h_2 & -\frac{1}{3} & 0 & 0 & 0 \\ -\frac{1}{3} & -\frac{1}{3} & \frac{2}{3}h_3 & 0 & 0 & 0 \\ 0 & 0 & 0 & h_4 & 0 & 0 \\ 0 & 0 & 0 & 0 & h_5 & 0 \\ 0 & 0 & 0 & 0 & 0 & h_6 \end{bmatrix} \begin{bmatrix} \cos^2\theta - \frac{1}{3} \\ \sin^2\theta - \frac{1}{3} \\ -\frac{1}{3} \\ 0 \\ 0 \\ -\cos\theta\sin\theta \end{bmatrix}$$

Thus

$$\mathbf{d} = \frac{3}{2}\frac{d_{eq}}{\sigma_{eq}} \begin{bmatrix} (\frac{2}{3}cos^2\theta - \frac{2}{9})h_1 + (-\frac{1}{3}sin^2\theta + \frac{1}{9})h_2 + \frac{1}{9}h_3 \\ (-\frac{1}{3}cos^2\theta + \frac{1}{9})h_1 + (\frac{2}{3}sin^2\theta - \frac{2}{9})h_2 + \frac{1}{9}h_3 \\ (-\frac{1}{3}cos^2\theta + \frac{1}{9})h_1 + (-\frac{1}{3}sin^2\theta + \frac{1}{9})h_2 - \frac{2}{9}h_3 \\ 0 \\ 0 \\ -\cos\theta\sin\theta h_6 \end{bmatrix} \tag{8.40}$$

The rate of shear deformation developed in the material for uniaxial loading parallel to a direction making a θ angle between the two principle directions is as follows:

$$\begin{aligned} d_{12}^{\theta} &= \frac{3}{2}\frac{d_{eq}}{\sigma_{eq}}\left[\cos 2\theta d_{12} + \frac{1}{2}\sin 2\theta(d_{22} - d_{11})\right] \\ &= \frac{3}{2}\frac{d_{eq}}{\sigma_{eq}}\left[\cos 2\theta d_{12} + \frac{1}{2}\sin 2\theta\left(\frac{1}{3}h_1 - \cos^2\theta h_1 - \frac{1}{3}h_2 + \sin^2\theta h_2\right)\right] \\ &= \frac{3}{2}\frac{d_{eq}}{\sigma_{eq}}\left[-\frac{1}{2}\cos 2\theta\sin 2\theta h_6 + \frac{1}{2}\sin 2\theta\left(-\frac{1}{6}h_1 + \frac{1}{6}h_2 - \frac{h_2 + h_1}{2}\cos 2\theta\right)\right] \\ &= \frac{3}{2}\frac{d_{eq}}{\sigma_{eq}}\left[-\frac{1}{2}\cos 2\theta\sin 2\theta h_6 + \frac{1}{2}\sin 2\theta\left(\frac{h_2 - h_1}{6} - \frac{h_2 + h_1}{2}\cos 2\theta\right)\right] \end{aligned} \tag{8.41}$$

For the maximum shear strain to be zero, it is the case that:

$$\cos 2\theta = \frac{h_2 - h_1}{6h_6 + 3(h_2 + h_1)} \tag{8.42}$$

Table 19 shows the components of $\mathbb{h}$ tensor in compression and tension at steady state, identified using anisotropy ratio method. This data is used in Table 20 to calculate the angle at which shear strains are zero. The results in Table 20 indicated that θ is always close to $\pi/4$. Therefore, no significant shear strain is developed inside the material. Generally and in order to avoid such rotations, it is a good practice to

use loading configurations that allow the rotation of grips during off-axis loading.

Table 19: Components of the $\mathbb{h}$ tensor and their evolution with deformation for AZ31, calculated based on steady state anisotropy ratios, under uniaxial compression and tension.

h_i	Compression	Tension
h_L	0.91	1.17
h_T	0.66	0.92
h_S	1.70	0.40
h_{TS}	1.85	1.78
h_{LS}	4.35	1.60
h_{LT}	0.86	1.03
h	1.77	1.95

Table 20: The angle θ (in degree) for which the shear strain in a uniaxially loaded specimen along an off-axis direction between pairs of L, T or S direction is zero.

direction	LT	LT	LS	LS	TS	TS
loading	Comp	Ten	Comp	Ten	Comp	Ten
$\cos 2\theta$	-0.0254	-0.0202	0.0234	-0.0539	0.0573	-0.0355
$\cos^{-1}(2\theta)$	1.5962	1.5910	1.5474	1.6247	1.5135	1.6063
$2\theta(deg)$	91.4535	91.1565	88.6598	93.0874	86.7151	92.0316
$\theta(deg)$	45.7268	45.5782	44.3299	46.5437	43.3576	46.0158

9. CONSTITUTIVE MODELING OF DUCTILE FRACTURE

The modeling strategy adopted in this work follows the philosophy put forth by Benzerga and Leblond [123]. It follows both the local [135] and, more generally, top-down approach [142] to fracture while improving previous methods; for example it offers a yield criterion for the onset microcrack/microvoid coalescence based on a fully analytical model. This strategy is similar to the Gurson-Tvergaard-Needleman modeling approach, which is applicable to isotropic materials only.

The utilized framework (KB model for void growth and LB model for void coalescence) relies on 3D constitutive relations in which anisotropic plasticity is coupled with anisotropic damage. To account for relevant ductile fracture mechanisms, the model evaluates criteria for growth and coalescence of voids inside an aniotropic matrix. Grounded in experimental evidence and literature data, pre-existing voids are considered in here. Parameter-free micromechanical models of void growth and coalescence will be used. The current modeling effort aims to study the effect of various microstrucutal parameters such as matrix plastic anisotropy, void shape and distribution on the overall fracture properties of materials under proportional loading condition (i.e., constant triaxiality). A series of parametric studies are performed to shed more light on the effect of such parameters on strain to failure via ductile fracture mechanisms. The range of triaxiality chosen for such studies are closed to those accessible via notched bar experiments ($0.5 \leqslant T \leqslant 1.5$. The reason for such choice is that loading of notched bars leads to the closest experimentally-achievable stress state to a proportional loading with constant triaxiality during deformation prior to fracture. The mistrostructural parameters of the current AZ31 and WE43 alloys are used to predict the fracture strains of these alloy at various triaxialities and

rationalize the experimentally measured ones. To achieve this, the evolution laws for micostrucutal variables of a material with pre-existing voids before microscale localization (that leads to void coalescence) is integrated for a material point. The integration continues until the yield function for void growth is equal to that of coalescence. An effective measure of accumulate strain is considered as failure strain (ε_f)

$$\varepsilon_f = \sqrt{\frac{2}{3}\varepsilon : \varepsilon} \tag{9.1}$$

An important step in this modeling approach is material's parameter identification. This pertains to anisotropic plasticity and void nucleation. In addition, experimental observations are needed to determine the initial values of microstructural parameters (such as void aspect ratio at initiation, initial particle volume fraction and shape), after which the micromechanical models will prescribe their evolution laws. Thus, the richness of the models will enable many parameter-sensitivity analyses to be conducted so as to formulate hypotheses on active damage mechanisms through detailed comparisons with experiments.

9.1 Plastic anisotropy

Since void growth is a signature of plastic deformation of the matrix surrounding the voids, plasticity and ductile fracture are closely related. HCP crystal structure, grain orientation, and the processing texture give magnesium alloys a pronounced anisotropic behavior. Anisotropy of the matrix in Mg alloys is often invoked to justify their low ductility and poor formability [141]. Recent analysis by Keralavarma and Benzerga [79], however, showed that if fracture is controlled by void growth and coalescence, certain types of anisotropy could be beneficial to ductility properties. Thus, accurate prediction of damage initiation and accumulation requires a constitutive model for plastic anisotropy that capture essential physics of the deformation.

The present study, utilizes a phenomenological description of yield based on modified Hill 1948 criterion [73], as presented in Ref. [75] and reviewed in Section 8. It is worth noting that Hill48 model is unable to account for tension/compression asymmetry, which is present in Mg alloys. However, in the current study where proportional loading in strictly tensile regime is utilized, Hill48 (characterized only by tensile experiments) could be employed to account for the matrix plastic anisotropy. More sophisticated models such as CPB06 [80] or those based on crystal plasticity could be utilized for improved representation of matrix anisotropy.

9.2 Void nucleation

Microvoids and microcracks are either pre-existing (i.e., as manufacturing defects) or induced during deformation. These microvoids and microcracks initiate on second phase particles and deformation twins, respectively. Any model intended to study ductile fracture requires a nucleation criterion. To account for void nucleation, several options are available. Lower-scale calculations, such as Molecular Dynamics (MD), could be explored to formulate physically-informed twin-crack nucleation criterion [143]. It is also possible to study the microstructure of the broken material immediately beneath the fracture surface to find voids and microcracks. The strain associated with the location of each void/crack could also be estimated from the lateral strains (measured using OM); this is similar to the method used in Ref [12] to identify the evolution of twin density with strain. Alternatively, the Beremin model, which utilizes both experiments and FE analysis with the aim of identifying a macroscopic criterion for nucleation, could be applied [95, 123]. In Beremin method, three types of circumferential notched cylindrical specimens are examined in order to vary the stress triaxiality in the notch region. The specimens are subjected to deformation to reach failure by crack initiation, which is identified by a

sudden load drop in the load–deflection curves. To avoid the complications caused by a developed macroscopic crack, the experiments should be stopped before crack initiation. The specimens are then sectioned parallel to the loading axis, and the locations of voids and their relationship to the particles are identified. The microvoids are categorized into those initiated by particle cracking and those nucleated by debonding of particles/matrix interface to identify the effect of nucleation mode. Finite element calculations are carried out for each specimen geometry using proper material's parameters to mimic plastic anisotropy and its hardening. All of the above mentioned methods require extensive experimental and computational work to identify a nucleation criterion. The microstructural studies on the initial material, however, indicates that many particles are cracked because of extensive deformation during the hot-rolling process and particles limited ductility. Therefore, pre-existing voids are assumed to be present in the microstructure prior to loading.

9.2.1 Void growth

Because of the relationship between material porosity and ductile failure, the ability to accurately describe the evolution of voids in a ductile metal is crucial in order to accurately predict the failure of the material. Unfortunately, computational constraints make it prohibitively expensive to model each of the micro-voids in most engineering structures; therefore, the method of explicitly tracking the evolution of each micro-void is not practical at this time. An alternative is to incorporate the effects of the micro-voids into the macroscopic, or average, properties (such as macroscopic stress, strain, yielding). Since the rate of dilatation of the porous solid is related to the void growth rate, plastic potentials for the porous solid must be developed in order to describe the void growth.

There have been attempts to take into account different types of anisotropy, e.g.,

anisotropy in the matrix material [75, 144] and void shape effect [92]. These models, however, either did not consider both effects together or at best considered superposition of the two effects [144]. Recent analysis by Keralavarma and Benzerga [79], however, showed that the combined effect is more subtle than simple superposition. Thus, the authors proposed a new model (in this document called as KB model) to mathematically represents such strong coupling between plastic anisotropy and void shape effect [79]. KB model, used in this study, is described bellow. The approximate yield function $\Psi^{\mathrm{KB}}(\boldsymbol{\Sigma}; f, W, \mathbf{e}_3, \mathbb{h})$, applicable to *non-axisymmetric* loadings, reads:

$$\Psi^{\mathrm{KB}} = C\frac{3}{2}\frac{\boldsymbol{\sigma} : \mathbb{H} : \boldsymbol{\sigma}}{\bar{\sigma}^2} + 2(g+1)(g+f)\cosh\left(\kappa\frac{\boldsymbol{\sigma} : \mathbf{X}}{\bar{\sigma}}\right) - (g+1)^2 - (g+f)^2 \quad (9.2)$$

where the macroscopic anisotropy tensor $\mathbb{H}$ is given by:

$$\mathbb{H} \equiv \mathbb{J} : \mathbb{h} : \mathbb{J} + \eta(\mathbf{X} \otimes \mathbf{Q} + \mathbf{Q} \otimes \mathbf{X}) \quad (9.3)$$

Here, $\mathbb{h}$ is the anisotropy tensor in the space of deviatoric stresses (as defined in equation 8.1) and $\mathbf{Q}$, $\mathbf{X}$ and $\mathbb{J}$ are transversely isotropic tensors given by:

$$\mathbf{X} \equiv \alpha_2(\mathbf{e}_1 \otimes \mathbf{e}_1 + \mathbf{e}_2 \otimes \mathbf{e}_2) + (1 - 2\alpha_2)\mathbf{e}_3 \otimes \mathbf{e}_3 \quad (9.4)$$

$$\mathbf{Q} \equiv -\frac{1}{3}(\mathbf{e}_1 \otimes \mathbf{e}_1 + \mathbf{e}_2 \otimes \mathbf{e}_2) + \frac{2}{3}\mathbf{e}_3 \otimes \mathbf{e}_3\,, \quad (9.5)$$

$$\mathbb{J} = \mathbb{I} - \frac{1}{3}\mathbb{J} \otimes \mathbb{J} \quad (9.6)$$

For more details on the parameters in the model, see Appendix.III.

Keralavarma and Benzerga [79] supplemented yield criterion (9.2) with evolution laws for the microstructural variables f, W and the void axis $\mathbf{e}_3$. The first two are in essence similar to those used in the model presented in Ref [92], but e_3 employs

an Eshelby concentration tensor for the spin following a proposal by [145]. The evolution laws are:

- Evolution of Porosity:

$$\dot{f} = (1-f)\Lambda \frac{\partial \Psi^{\mathrm{KB}}}{\partial \Sigma_{kk}}(\boldsymbol{\Sigma}) \tag{9.7}$$

  where Ψ^{KB} is the yield function and Λ is the plastic multiplier.

- Void shape evolution:

$$\begin{aligned} \dot{S} = \frac{3}{2}\left[1 + \left(\frac{9}{2} - \frac{T^2+T^4}{2}\right)(1-\sqrt{f})^2 \frac{\alpha_1 - \alpha_1^{\mathrm{G}}}{1-3\alpha_1}\right] \mathbf{e}_3 \cdot \mathbf{D}'^{\mathrm{p}} \cdot \mathbf{e}_3 \\ + \left(\frac{1-3\alpha_1}{f} + 3\alpha_2 - 1\right) \mathbf{I} : \mathbf{D}^{\mathrm{p}} \end{aligned} \tag{9.8}$$

  where $S \equiv \ln W$, T is the stress triaxiality ratio and $\alpha_1(f,W)$ and $\alpha_1^{\mathrm{G}}(f,W)$ are given in Appendix.III.

- Void axis evolution $\mathbf{e}_3$:

$$\dot{\mathbf{e}}_3 = \mathbf{W} \cdot \mathbf{e}_3 \tag{9.9}$$

  which assumes that the voids rotate with the material, $\mathbf{W}$ being the total material spin. This is clearly an approximation. An improved representation may be found in [79] on the basis of earlier work by [145].

9.2.2 Void coalescence

If void growth was assumed to proceed as described by a Gurson-like model [90] until coalescence (i.e., linkage with a neighboring void), then one could estimate void coalescence when the lateral void diameter, transverse to the main load, reaches the current lateral void spacing. This approach, however, leads to considerable overestimation of fracture properties. One of the first attempts to take into account the

coalescence of voids was carried out by Tvergaard and Needleman [91], who modified Gurson's spherical yield criterion to account for the onset of void coalescence leading to final material fracture. These two authors used this modified yield criterion in both numerical and finite element calculations to compare with experimental data of a copper rod fracturing under uniaxial tension (exhibiting cup-cone fracture). This modification by Tvegaard and Needleman on the pioneering work of Gurson is generally referred to as the GTN criterion in the literature.

An important difference, however, between the phenomenology of void coalescence revealed by the cell calculations and its representation in the GTN model is that the former points to a transition in the cell's deformation mode, from triaxial to purely uniaxial. For a rate-independent material, this transition is indicative of a localization, which is due to the onset of elastic unloading in regions above and below the void, with plastic flow being confined to the intervoid ligament. As a result, void growth becomes highly directional until fracture takes place. Thomason [117] posed a limit-analysis problem that was amenable to variational formulation with velocity fields that were consistent with a postlocalization response and ,thus, appropriate to the modeling of void coalescence. Thomason did not solve the problem in closed form, however, obtained approximate numerical solutions to which he proposed an empirical fit. Recently, Benzerga and Leblond [93] offered a closed form solution for this problem. A modification of this model, which more accurately captures coalescence in penny-shaped voids [140], is used as the criterion for onset of void coalescence in the present study. This yield criterion is as follows:

$$\Psi^{BL}(\boldsymbol{\sigma};\chi,W)=\begin{cases}\dfrac{(|\sigma_{33}|-t\Sigma^{surf})^2}{b^2{\Sigma^{vol}}^2}+4\dfrac{\sigma_{31}^2+\sigma_{32}^2}{l^2\tau^2}-1 & \text{for } |\sigma_{33}|\geq\Sigma^{surf}\\ \\ 4\dfrac{\sigma_{31}^2+\sigma_{32}^2}{l^2\tau^2}-1 & \text{for } |\sigma_{33}|\leq\Sigma^{surf}\end{cases} \tag{9.10}$$

where $\Sigma^{vol}(\chi)$, $\Sigma^{surf}(\chi,W)$ and $\tau(\chi)$ are functions of the microstructural parameters χ and W, given by:

$$\begin{aligned}\Sigma^{vol}(\chi)&=\frac{\bar{\sigma}}{\sqrt{3}}\left[2-\sqrt{1+3\chi^4}+\ln\frac{1+\sqrt{1+3\chi^4}}{3\chi^2}\right]\\ \Sigma^{surf}(\chi,W)&=\frac{\bar{\sigma}}{3\sqrt{3}}\frac{\chi^3-3\chi+2}{\chi W}\\ \tau(\chi)&=\frac{2\bar{\sigma}}{\sqrt{3}}(1-\chi^2)\end{aligned} \tag{9.11}$$

with

$$t=\frac{(t_0+t_1\chi)W}{1+(t_0+t_1\chi)W};\quad b=0.9 \tag{9.12}$$

where

$$t_0=-0.84;\quad t_1=12.9 \tag{9.13}$$

When there is no shear component in the applied macroscopic load (as it is the case in current study), the yield criterion becomes:

$$\begin{aligned}\Psi^{BL}(\Sigma;\chi,W)=\frac{|\sigma_{33}|}{\bar{\sigma}}&-\frac{b}{\sqrt{3}}\left[2-\sqrt{1+3\chi^4}+\ln\frac{1+\sqrt{1+3\chi^4}}{3\chi^2}\right]\\ &+\frac{t}{3\sqrt{3}}\left[\frac{\chi^3-3\chi+2}{\chi W}\right]\end{aligned} \tag{9.14}$$

The evolution equations are:

$$\dot{\chi} = \frac{3}{4}\frac{\lambda}{W}\left[\frac{3\gamma}{\chi^2} - 1\right] D^p_{\text{eq}} + \frac{\chi}{2\gamma}\,\dot{\gamma}, \tag{9.15}$$

$$\dot{W} = \frac{9}{4}\frac{\lambda}{\chi}\left[1 - \frac{\gamma}{\chi^2}\right] D^p_{\text{eq}} - \frac{W}{2\gamma}\,\dot{\gamma}, \tag{9.16}$$

$$\dot{\gamma} = \frac{1}{2(1-\chi_c)}\dot{\chi} \tag{9.17}$$

where λ represents the current value of the void spacing ratio, which is updated through:

$$\dot{\lambda} = \frac{3}{2}\lambda\, D^p_{\text{eq}}, \tag{9.18}$$

The void and cell axes were tacitly taken to rotate with the material as per (9.9). Here, evolution laws for coalesence are not used since the calculations are stopped after onset of coalescence.

Proper material's parameters pertaining to the flow in matrix are extracted from experiments and supplied to the models. Numerical computations using the above-mentioned framework (models for void growth and coalescence) require the introduction of elasticity, which is accounted for using an additive decomposition of the deformation rate tensor into elastic and plastic parts, $\mathbf{D} = \mathbf{D}^e + \mathbf{D}^p$. Assuming small elastic strains, a hypoelastic constitutive law may be used to write $\mathbf{D}^e = \mathbb{C}^{-1} : \dot{\boldsymbol{\sigma}}$, where $\mathbb{C}$ denotes the tensor of elasticity. During loading and after the onset of plasticity, the evolution laws for void growth are integrated for one material point. At each loading step, both yield criterion for growth and coalescence are evaluated. The integration continues up to the point where yield criterion for coalescence is satisfied prior to that of void growth. The accumulated equivalent strain ($\sqrt{(2/3)\varepsilon' : \varepsilon'}$, where

$\varepsilon^{'}$ is the deviatoric part of the total strain) at the onset of coalescence is identified as the strain to failure initiation (ε_i) and the integration is stopped. Although these calculations have not been implemented in a finite element software to solve boundary value problems, they could be extremely useful for parametric studies and predicting overall material behavior under various loading conditions and microstructural variables.

9.3 Parametric study

Prior to applying the described framework to predicting the fracture behavior of the current Mg alloys, it is employed in an parametric study to explore the effects of matrix properties and microstrucutral variables on the damage evolution and fracture properties of a model material. For this purpose, various matrix plastic anisotropies and their associated $\mathbb{h}$ tensor are utilized. The effect of various microstructural parameters, such as void shape (W) and cell aspect ratio (λ) on the overall properties are also investigated. These studies are utilized as a guideline for understanding fracture in anisotropic materials and its key influential parameters. For these purpose, the method described in the previous page is used to calculate the fracture strains and evolution of microstructural parameters.

9.3.1 Effect of anisotropy of the matrix

As it was mentioned in Section 8, plastic anisotropy of the matrix could be characterized by the six components of the $\mathbb{h}$ tensor (i.e., h_is). Using homogenization theory for a matrix containing spherical voids, a scalar invariant (called h) of the $\mathbb{h}$ tensor is identified such that it represents the effect of anisotropy on the ductility properties [75]. If the coordinates of the space in which the $\mathbb{h}$ tensor is presented are pointing toward the principal directions of orthotropy in the matrix, then, h admits

the following expression [75]:

$$h = 2\left[\frac{2}{5}\frac{h_L + h_T + h_S}{h_L h_T + h_T h_S + h_S h_L} + \frac{1}{5}\left(\frac{1}{h_{TS}} + \frac{1}{h_{LS}} + \frac{1}{h_{LT}}\right)\right]^{\frac{1}{2}} \tag{9.19}$$

According to this analysis, an isotropic matrix results in $h = 2$ whereas a matrix with $h > 2$ offers beneficial effects for ductility (compared to an isotropic matrix). When h associated with an anisotropy material is less than two, the ductility properties are diminished compared to an isotropic material.

In the case of spheroidal voids, the h alone is not sufficient to represent the effects of anisotropy. The orientation of voids in this case should be also considered. Thus, other invariants of the $\mathbb{h}$ tensor are introduced. These invariants are $\hat{h}_a$, $\hat{h}_t$, and $\hat{h}_q$. The following equations, for a material loaded along the e_3, define theses invariants [79].

$$\hat{h}_a = \frac{\hat{h}_{44} + \hat{h}_{55}}{2} \tag{9.20}$$

$$\hat{h}_t = \frac{\hat{h}_{11} + \hat{h}_{22} + \hat{h}_{66} + \hat{h}_{12}}{4} \tag{9.21}$$

$$\hat{h}_q = \frac{\hat{h}_{11} + \hat{h}_{22} + 4\hat{h}_{33} - 4\hat{h}_{23} - 4\hat{h}_{31} + 2\hat{h}_{12}}{6} \tag{9.22}$$

where h_{ij} above denote the Voigt-condensed components of the fourth-order tensor $\hat{\mathbb{h}}$; see also Equation 8.3. Here, $\hat{\mathbb{h}}$ is a formal inverse of tensor $\mathbb{h}$ and is defined as [75]:

$$\hat{\mathbb{p}} = \mathbb{J} : \hat{\mathbb{h}} : \mathbb{J}; \quad \hat{\mathbb{p}} : \mathbb{p} = \mathbb{p} : \hat{\mathbb{p}} = \mathbb{J} \tag{9.23}$$

In this section's calculations, the h_is for each studied anisotropy are entered in the calculations. As legend in the figures, different matrix anisotropies are labeled with their associated h factor. The information for these matrices are presented in

the tables presented after each graph.

The effect of plastic flow anisotropy of the matrix material, represented by the $\mathbb{h}$ tensor, on the failure strain of a model material with $f_0 = 10^{-5}$, $W_0 = 0.05$ and $\lambda_0 = 1.5$ is presented in Figure 75 (subscript zero denotes the initial value). Here, and as described in Section 8, $h = 2$ represents plastic isotropy. As shown in this figure, matrices with $h < 2$ lead to failure strains less than their isotropic counterparts. These are representative of materials in which anisotropy diminishes the ductility. Alternatively, and in contrast to the common perception in the literature, there are situations (i.e., $h > 2$) in which an anisotropy matrix improves the ductility.

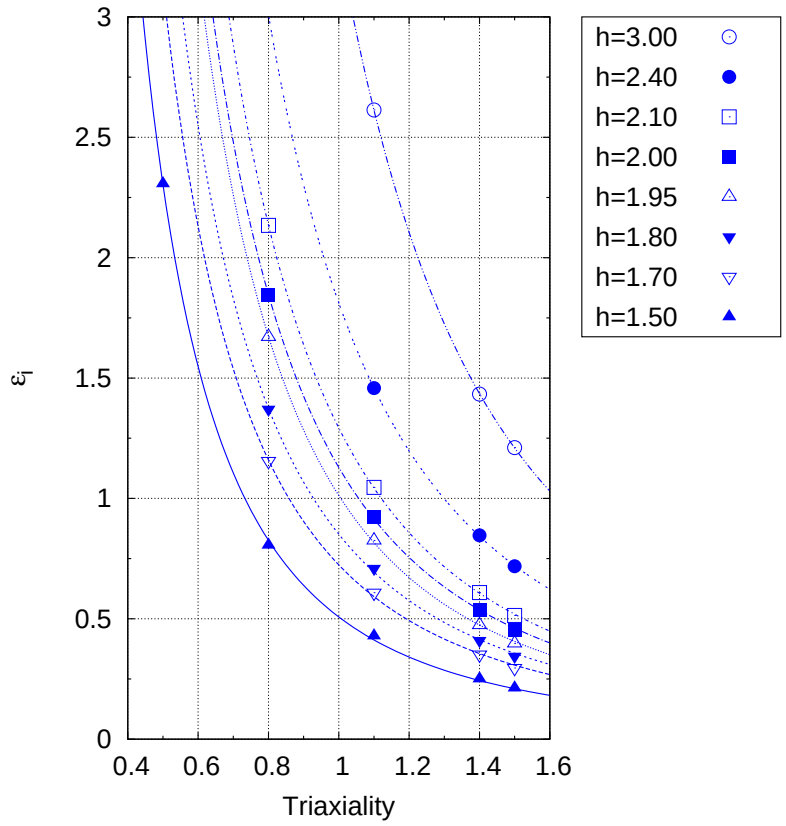

Figure 75: Strain at failure initiation versus triaxiality (T) for model materials with different matrix plastic anisitropy. Here $f_0 = 1.0 \times 10^{-5}$, $W_0 = 0.05$ and $\lambda_0 = 1.5$.

For instance, RVE with an anisotropic matrix characterized by $h = 3$ exhibits failure strain 2.82 times higher than the same RVE with an isotropic matrix. These results challenge the current and commonly-accepted understanding of plastic anisotropy in the literature, where plastic anisotropy is deemed as detrimental for ductility properties. According to the results in this figure, plastic anisotropy could be engineered to improve ductility. Details of the matrix characteristics in each of the studied cases are presented in Table 21.

Table 21: Details of the matrix characteristics in several matrices with various h factors studied in Figure 75.

Material	Plastic anisotropy components						Plastic anisotropy invariants			
	h_L	h_T	h_S	h_{TS}	h_{LS}	h_{LT}	$\hat{h}_a$	$\hat{h}_t$	$\hat{h}_q$	h
Mater. 1	1.00	1.00	1.00	0.25	0.25	0.80	2.63	2.51	1.00	3.00
Mater. 2	1.00	1.00	1.00	0.50	0.50	0.83	1.60	1.50	1.00	2.40
Mater. 3	1.00	1.00	1.00	0.80	0.80	1.00	1.13	1.13	1.00	2.10
Mater. 4	1.00	1.00	1.00	1.00	1.00	1.00	1.00	1.00	1.00	2.00
Mater. 5	1.17	0.92	0.40	1.78	1.60	1.03	0.80	1.07	1.04	1.95
Mater. 6	1.00	1.00	1.00	1.90	2.31	0.92	0.76	0.76	1.00	1.80
Mater. 7	0.80	1.20	1.60	1.90	2.80	1.00	0.68	0.62	1.01	1.70
Mater. 8	0.70	1.20	2.00	4.00	5.00	1.46	0.44	0.45	1.03	1.50

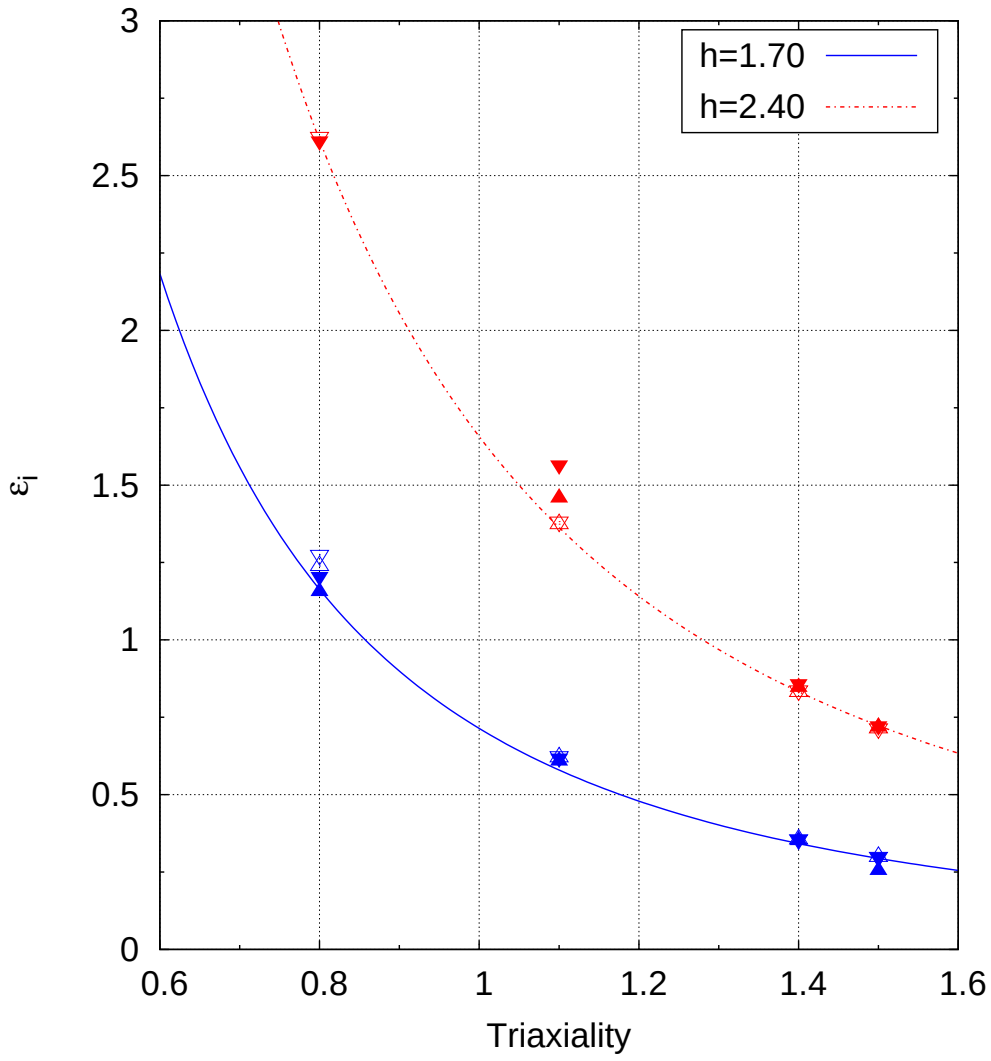

Figure 76: Coalescence strain versus triaxiality (T) for model materials with different realizations of matrix plastic anisotropy but similar h-factors ($h = 1.7$ and $h = 2.4$). Initial microstructural variable used in this calculation are: $f_0 = 1.0 \times 10^{-5}$, $W_0 = 0.05$ and $\lambda_0 = 1.5$. Mater. 7 and Mater. 2 are represented by ▲, Mater. 71 and Mater. 22 by ▼, Mater. 72 and Mater. 23 by △, Mater. 73 and Mater. 21 by ▽.

As mentioned in Section 8 and from data in Table 21, six h_is (h_1, ..., h_6) are involved in the identification of each matrix. Thus, several sets of h_is can lead to the same h factor. Therefore, multiple fracture loci might be represented by a single h factor in Figure 75. How these variations change the observed trends should be studied. The variation of fracture strain for materials with the same h factor but different realizations of matrix plastic anisotropies (i.e., matrices with nonidentical h_is) is explored in Figure 76. Details of the matrix characteristics in each of the studied cases are presented in Table 22 and 23. Despite minor differences, the results indicate that various sets of h_is that render a similar h factor lead to similar overall trends. The maximum margin in the results is obtained in the middle of the studied range of triaxialities, i.e. $T = 1.1$. From this figure, it could be concluded that in the studied range of triaxialities, h factor is able to captures the essential trends in the matrix plastic anisotropy effects on damage and fracture if ductile fracture mechanisms are operative.

Table 22: Details of the matrix characteristics in several matrices with $h = 1.7$ studied in Figure 76.

Material	Plastic anisotropy components						Plastic anisotropy invariants			
	h_L	h_T	h_S	h_{TS}	h_{LS}	h_{LT}	$\hat{h}_a$	$\hat{h}_t$	$\hat{h}_q$	h
Mater. 7	0.80	1.20	1.60	1.90	2.80	1.00	0.68	0.62	1.01	1.70
Mater. 71	1.00	1.00	1.00	1.86	1.86	1.86	0.54	0.77	1.00	1.70
Mater. 72	1.00	1.00	1.00	1.28	2.00	3.00	0.42	0.89	1.00	1.70
Mater. 73	1.00	1.00	1.00	1.00	3.27	3.27	0.31	1.00	1.00	1.70

Table 23: Details of the matrix characteristics in several matrices with $h = 2.4$ studied in Figure 76.

Material	Plastic anisotropy components						Plastic anisotropy invariants			
	h_L	h_T	h_S	h_{TS}	h_{LS}	h_{LT}	$\hat{h}_a$	$\hat{h}_t$	$\hat{h}_q$	h
Mater. 2	1.00	1.00	1.00	0.50	0.50	0.83	1.60	1.50	1.00	2.40
Mater. 21	1.00	1.00	1.00	1.00	0.31	1.00	1.00	2.10	1.00	2.40
Mater. 22	1.00	1.00	1.00	1.00	1.00	0.31	2.10	1.00	1.00	2.40
Mater. 23	1.00	1.00	1.00	1.00	0.48	0.48	2.08	1.00	1.00	2.40

To provide further insight on the effects of plastic anisotropy on fracture properties, the evolution of microstructural variables during deformation for materials with different plastic ansiotropy characteristics containing initially penny-shaped voids, is presented in Figure 77. See Table 21 for details on the matrix anisotropy. As shown in part (a) of this figure, the softening strain is decreased by reduction of the h factor. Lower softening strains could be attributed to the higher rates of void growth in matrices with smaller h factors, as depicted in Figure 77b. The evolution of cell aspect ratio does not vary with alterations of the matrix characteristics (Figure 77c). From the graphs presented in Figure 77d it is concluded that the evolution of ligament ratio (χ) is in accord with increments of f. Another variable of interest is void shape (W). Figure 78 illustrates the changes in the void aspect ratio during the course of deformation corresponding to Figure 77. Despite the universal trend of increasing W with strain in the current configuration (as depicted in Figure 78a), the dynamics of growth changes from case to case. Figure 78b clearly shows that the rate of increase in W is positive in material with $h > 2$ and negative in materials with $h < 2$. Note that the initial voids in these calculations are penny-shaped ($W_0 = 0.05$). Thus,

when voids open up, significant increments in W is detected, even if the situation promotes lateral growth more than the axial expansion.

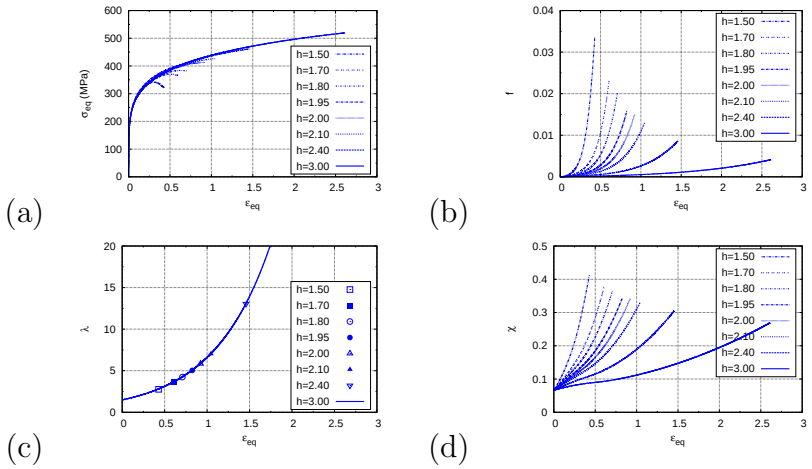

Figure 77: Mechanical response and evolution of microstructure with strain for materials with different matrix plastic anisotropy at triaxiality of $T = 1.1$ and flat oblate initial void ($W_0 = 0.05$). Here $f_0 = 1.0 \times 10^{-5}$ and $\lambda_0 = 1.5$

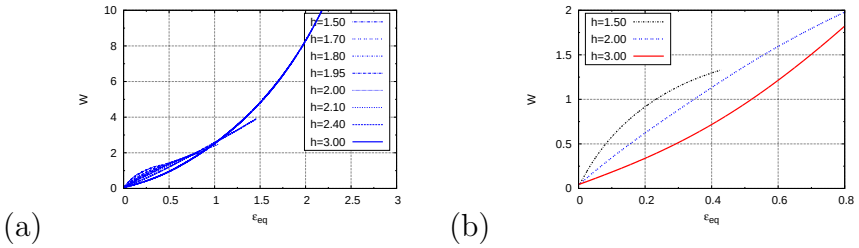

Figure 78: Details of the evolution of void shape with strain for materials with different matrix plastic anisotropy at triaxiality of T=1.1 and flat oblate initial void ($W_0 = 0.05$). Here $f_0 = 1.0 \times 10^{-5}$ and $\lambda_0 = 1.5$.

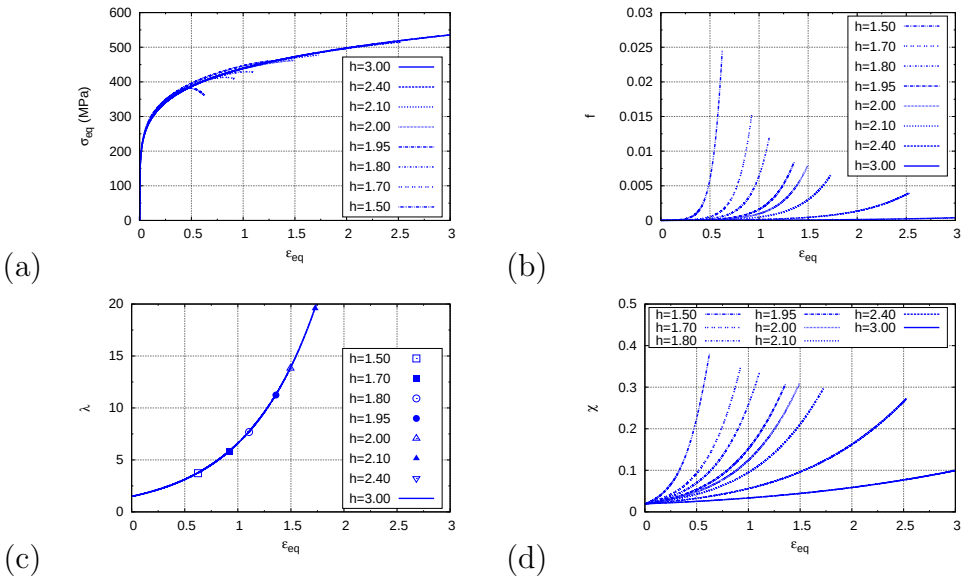

Figure 79: Mechanical response and evolution of microstructure with strain for materials with different matrix plastic anisotropy at triaxiality of $T = 1.1$ and prolate initial void ($W_0 = 2.0$). Here $f_0 = 1.0 \times 10^{-5}$ and $\lambda_0 = 1.5$

To clarify this effect, analysis similar to that performed in Figure 75 is carried out on material with the same microstrucral variables, but prolate voids in which $W_0 = 2.0$. Results of this analysis are presented in Figure 79 and 80. Despite similar trends in evolution of $\sigma_e q$, f, λ and χ of RVEs containing prolate and oblate voids, the evolution of W is significantly altered. In the material with initial prolate voids, $h < 2$ leads to extensive lateral void growth, which is substantially more detrimental than axial extension. Voids in in materials with $h > 2$, however, tend to undergo axial extension. This increased tendency for lateral void growth in anisotropic material with $h < 2$ could be the origin of diminished ductility in these matrices.

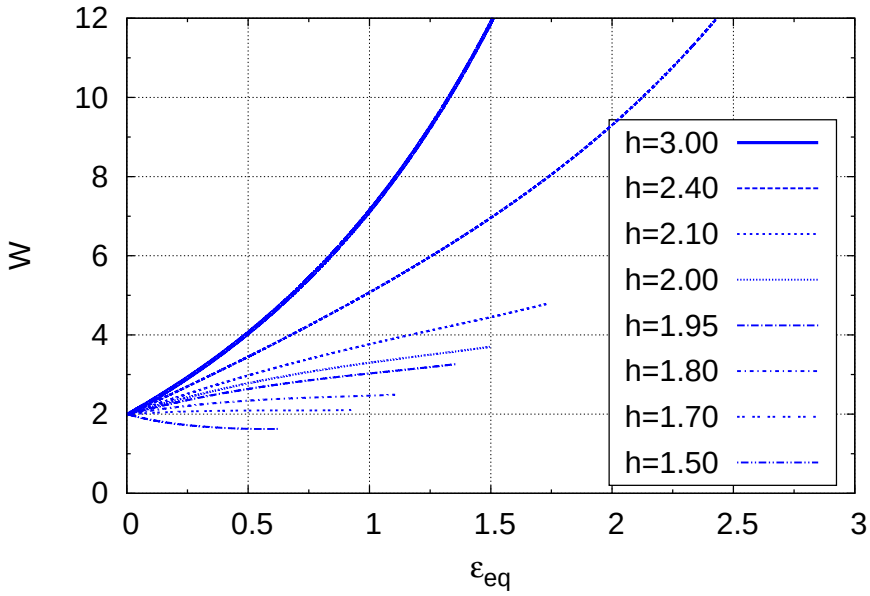

(a)

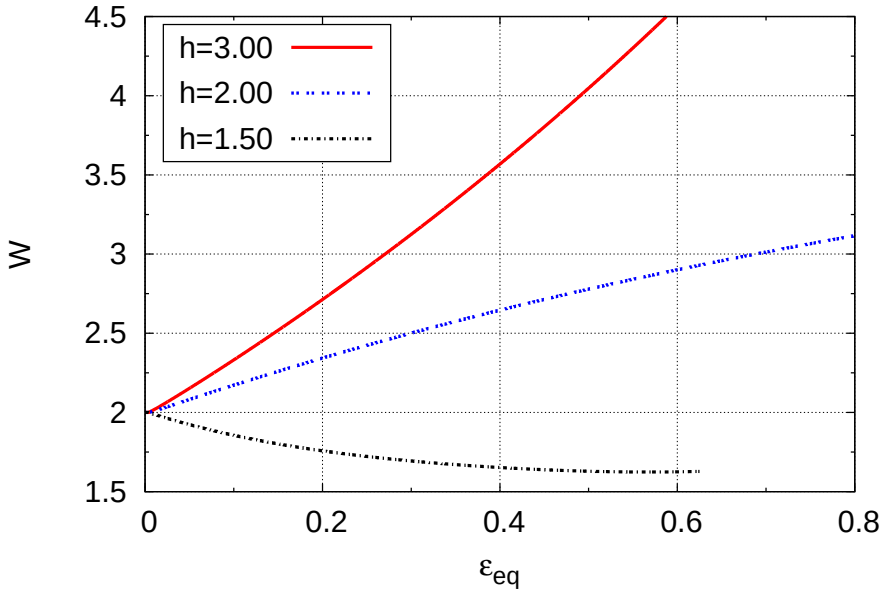

(b)

Figure 80: Details of the evolution of void shape with strain for materials with different matrix plastic anisotropy at triaxiality of $T = 1.1$ and initially prolate void ($W_0 = 2.0$). Here $f_0 = 1.0 \times 10^{-5}$ and $\lambda_0 = 1.5$

9.3.2 Effect of λ

Distribution of second-phase particles and their associated voids after nucleation in the microstructure could be altered by different techniques, such as adding alloying elements or performing various processing routes. Such effects are easily detected and have been studied by metallurgists. For instance, rolling usually leads to redistribution of second-phase particles and their elongation along the direction of rolling, which causes anisotropy in the initially isotropic microstructor. The changes in the microstructure are also reflected in the representative RVE of the material. Thus, investigation of these effects could provide guidance in altering the ductility of materials. Koplik and Needleman [115] studied the effect of cell shape, which reflect the influence of void distribution. The result of their analysis showed the strong influence of void spacing on the coalescence strain. It was also illustrated that the initial stress-strain response is controlled by void volume fraction. Note that if the matrix has a random distribution of voids, the rate of change in the void spacing upon loading is zero. Thus here a regular or quasi-regular distribution of voids is assumed. Justifications of this assumption are as follows: (i) Processed materials usually have a orientation dependent distribution of second-phase particles and voids; and (ii) considering the physics of the problem, even if the material has a random distribution of voids, wavelength of loading (caused by geometry of sample or loading itself) may select a subset of voids which nominally could be considered as an ordered aggregate.

To investigate the effects of void spacing on properties of a material failing via ductile fracture processes, strain to coalescence initiation versus triaxiality in materials with various void distribution characteristics are studied. The results of this analysis are presented in Figure 81.

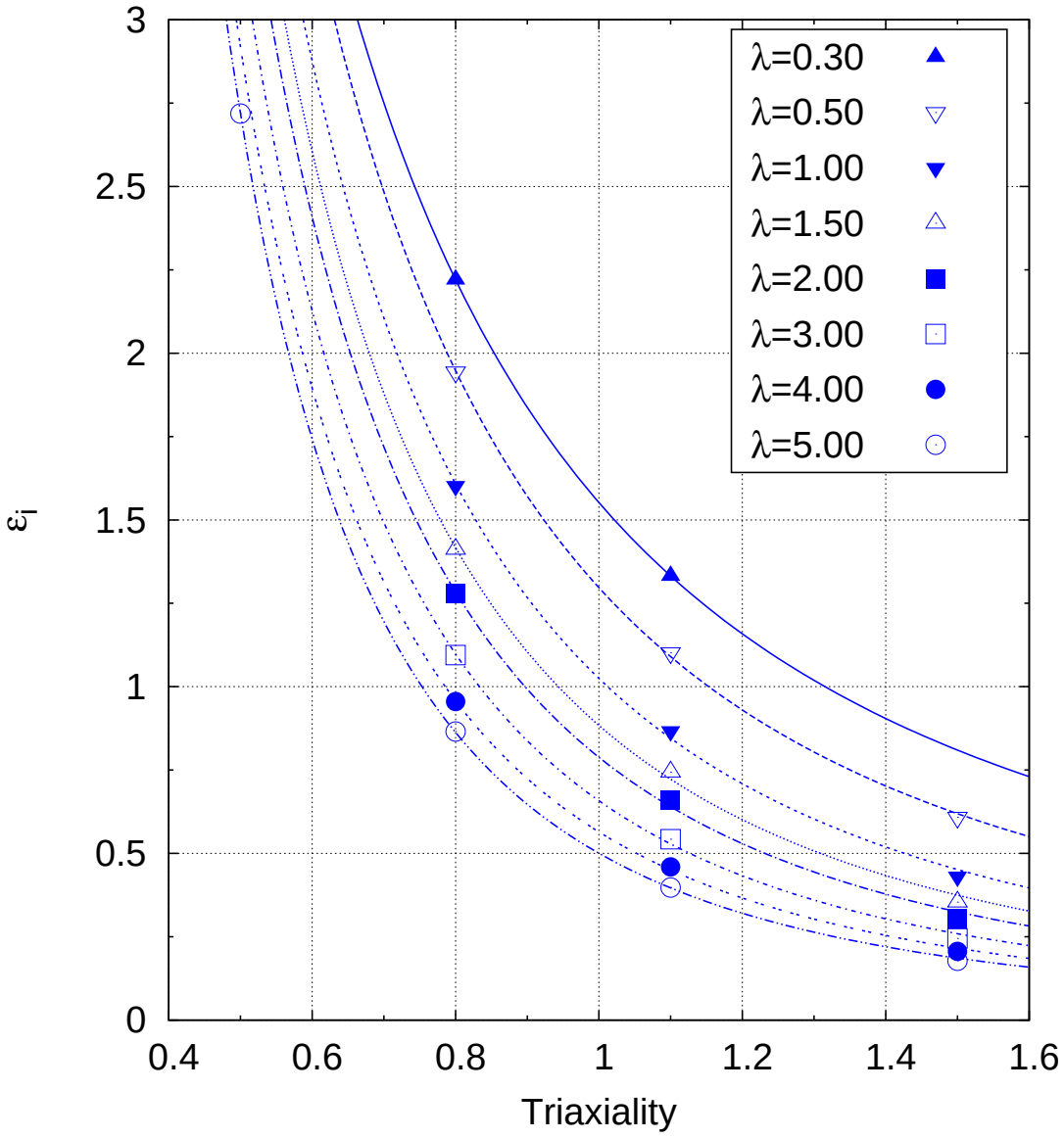

Figure 81: Coalescence strain versus triaxiality for model materials with different initial cell aspect ratios (λ_0). Here $h = 2.25$, $f_0 = 1.6 \times 10^{-4}$ and $W_0 = 0.05$.

In this analysis, the initial microstrucutal features are $h = 2.25$, $f_0 = 1.6 \times 10^{-4}$ and $W_0 = 0.05$. Note that $\lambda_0 = 1$ represents an initial homogeneous distribution of voids and an RVE with equal height and diameter. When voids are closely arranged perpendicular to the loading direction ($\lambda_0 > 1$), coalescence occurs after limited deformation. This situation is in contrast to one in which voids are arranged such that a RVE is 'fat', with diameter larger than its height ($\lambda_0 < 1$). As illustrated in Figure 81, the effect of void distribution on ductility is significant and is maximized at low triaxialities. At a triaixality of $T = 0.8$, coalescence strain for RVE with $\lambda_0 = 5.0$ and $\lambda_0 = 0.3$ are $\varepsilon_i = 0.866$ and $\varepsilon_i = 2.22$, respectively. Substantial increase in the failure strain is attributed to the increased distance between voids perpendicular to the loading direction, which postpones short-range interaction of voids and localization of deformation in the ligament between them.

To provide more details on the effect of λ, the evolution of microstructural features for the analysis presented in Figure 81 at the triaxiality of $T = 0.8$ is presented in Figure 82 and 83.

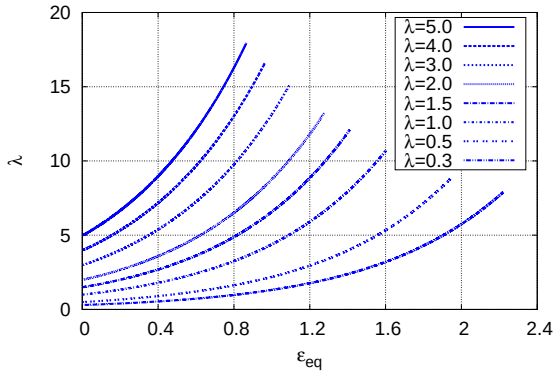

Figure 82: Evolution of cell aspect ratio (λ) with strain for materials with $h = 2.25$, $f_0 = 1.6 \times 10^{-4}$ and flat oblate initial void ($W_0 = 0.05$) at $T = 0.8$.

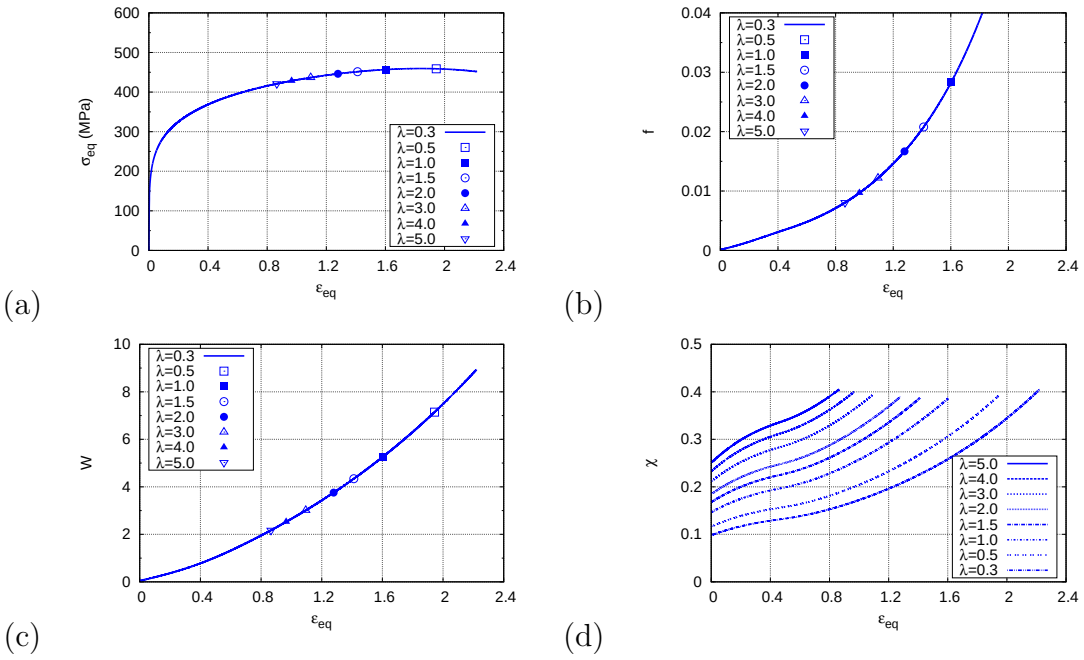

Figure 83: Mechanical response and evolution of microstructure with strain for materials with $h = 2.25$, $f = 1.6 \times 10^{-4}$ and flat oblate initial void ($W = 0.05$) at $T = 0.8$.

Figure 83 indicates that the cell aspect ratio only influenced the evolution of ligament ratio whereas other variables remain identical during deformation in all studied cases. Thus, stress strain response and dynamics of void growth are not affected by their distribution. In contrast, interaction between voids and onset of coalescence are strongly influenced by void spacing. These results are in agreement with conclusions in Ref. [115].

9.3.3 Effect of void shape

Void shape could also affect ductility properties. Several studies in the literature are dedicated to investigating these effects [146, 147]. According to the relationship between microstructural variables, changing one parameter representing the geometry of an RVE results in alteration of dependent parameters. Considering this fact, There are two ways to study the effect of void shape that mimics the physical aspect of the problem. For instance, one could choose to change void shape and maintain the relative spacing of the voids. By adopting this view, the change in void shape results in change in void volume fraction. This choice of variables is appropriate for investigating the effects of different nucleation mechanisms (i.e., particle cracking versus de-bonding at particle/matrix interface) in a fixed microstructure in which the distribution of second-phase particles is known. Alternatively, void shape could be changed by maintaining the void volume fraction. This choice significantly alters the ligament ratio χ and, in fact, reflects the effects of the ligament ratio (χ). This method facilitates studying the effect of distribution of void nucleation sites (due to processing, directionality, heat-treatment and ...)on the fracture properties. In what follows, these two effects are studied in further details.

9.3.3.1 Effect of void shape - constant void volume fraction

To study the effect of void shape when f is kept constant, coalescence strain for a model material at triaxialities between $0.5 \leqslant T \leqslant 1.5$ with $h = 2.25$, $f_0 = 1.0 \times 10^{-5}$, $\lambda_0 = 1.5$ and various Ws is predicted. The results, (presented in Figure 84), illustrate that reducing W from unity (i.e., spherical voids) to $W = 0.001$ leads to a significant drop in failure strain. This prediction could be rationalized in light of changes made to the geometry of RVE by altering W. Among the parameters that define an RVE, only three are independent; when one is changed, the dependent variables change

accordingly. This relationship could be calculated based on the shape of the RVE and its void. For example, in a cylindrical cell with a spheroidal void, it is the case that:

$$\chi = \left[\frac{3f\lambda}{2W}\right]^{\frac{1}{3}} \tag{9.24}$$

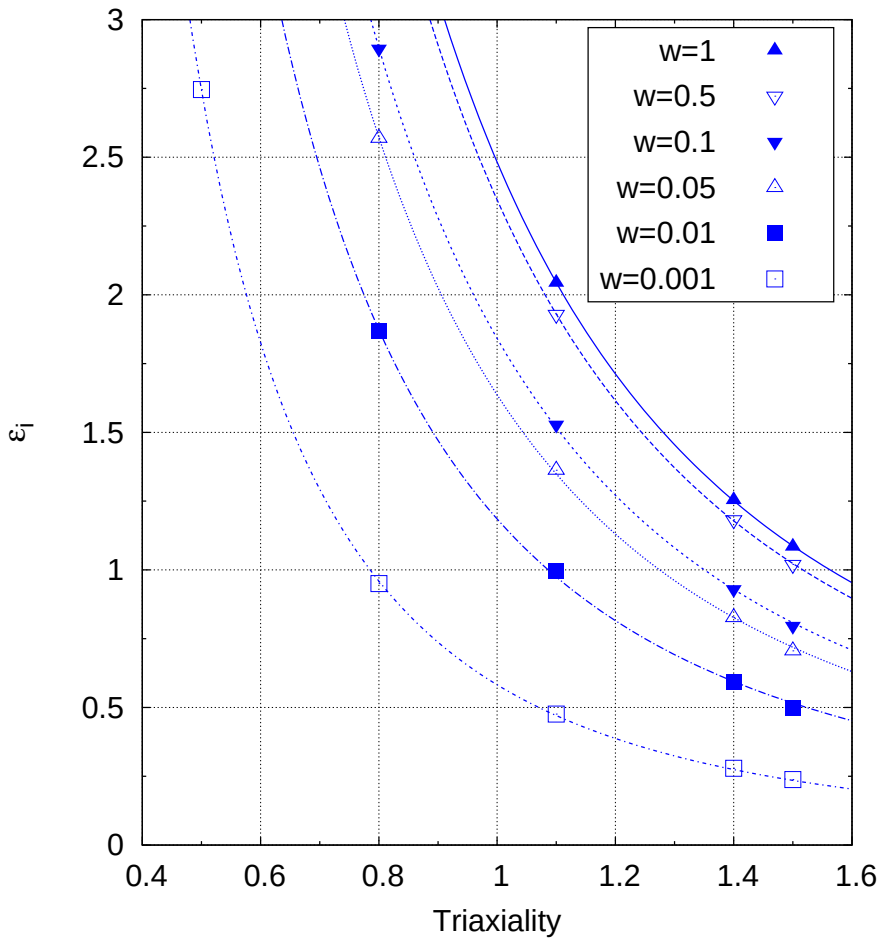

Figure 84: Strain to void coalescence versus triaxiality for model materials with constant void volume fraction but different initial void aspect ratios (λ_0). Here $h = 2.25$, $f_0 = 1.0 \times 10^{-5}$ and $\lambda_0 = 1.5$.

Thus, changing void shape and keeping the void volume fraction (f) constant, alters the χ parameter, which is very important for the onset of coalescence (Equation 9.14). This hypothesis is corroborated by the results presented in Figures 85 and 86 where the evolution of microstructural features during the course of deformation at triaxiality of T=0.8 is plotted. As shown in these figures, initial value of χ for different values of W is significantly altered. Note that initial f and λ remain constant in all realizations. In addition to the changes in ligament ratios, void shape effects the growth rate prior to coalescence.

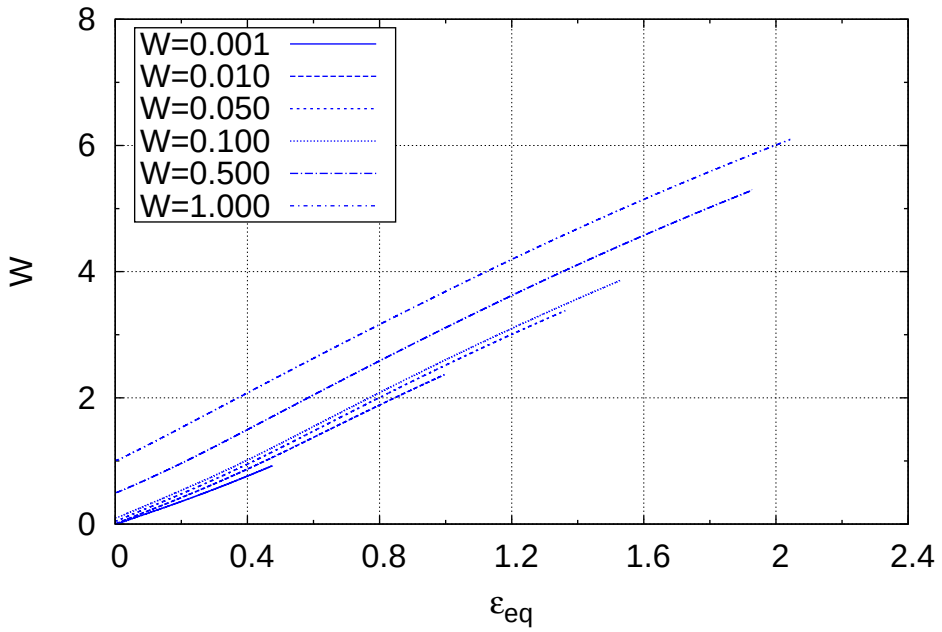

Figure 85: Evolution of void aspect ratio (W) with strain for materials with $h = 2.25$, $f = 1.0 \times 10^{-5}$, $\lambda = 1.5$ at $T = 1.1$.

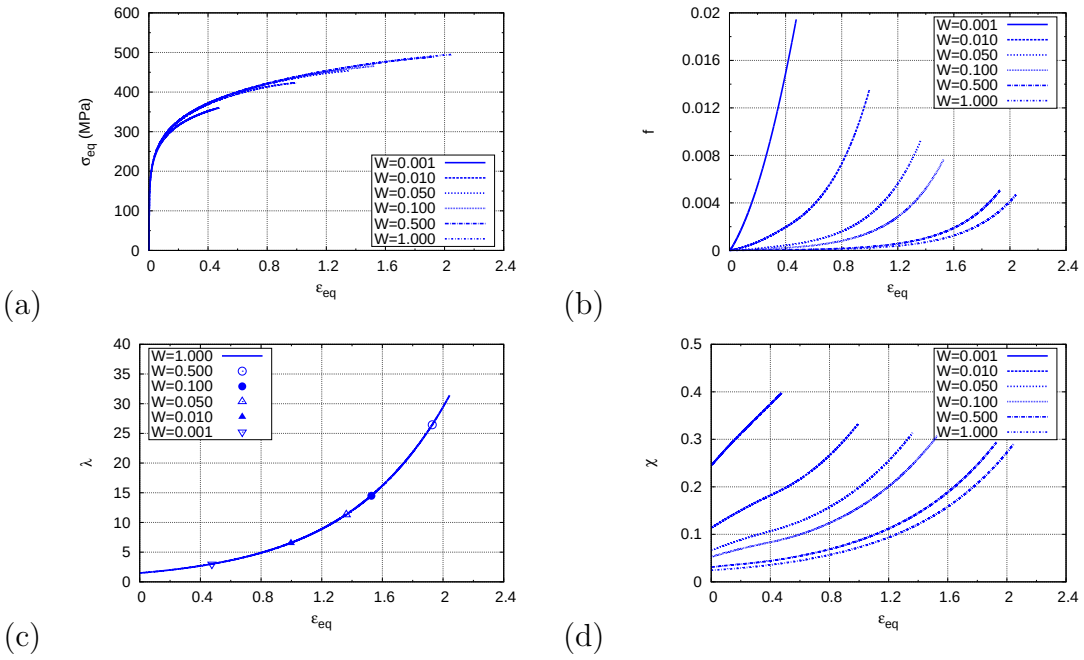

Figure 86: Mechanical response and evolution of microstructure with strain for materials with with $h = 2.25$, $f = 1.0 \times 10^{-5}$ and $\lambda = 1.5$ at $T = 0.8$.

9.3.3.2 Effect of void shape - constant χ

Alternative to the previous section's approach is to keep the ligament ratio constant and vary the void shape. This method assumes a fixed distribution of void nucleation sites in the material and an altered shape of the nucleated voids, which it could be caused by various nucleation mechanisms. The change in failure strains as a result of such void change is presented in Figure 87.

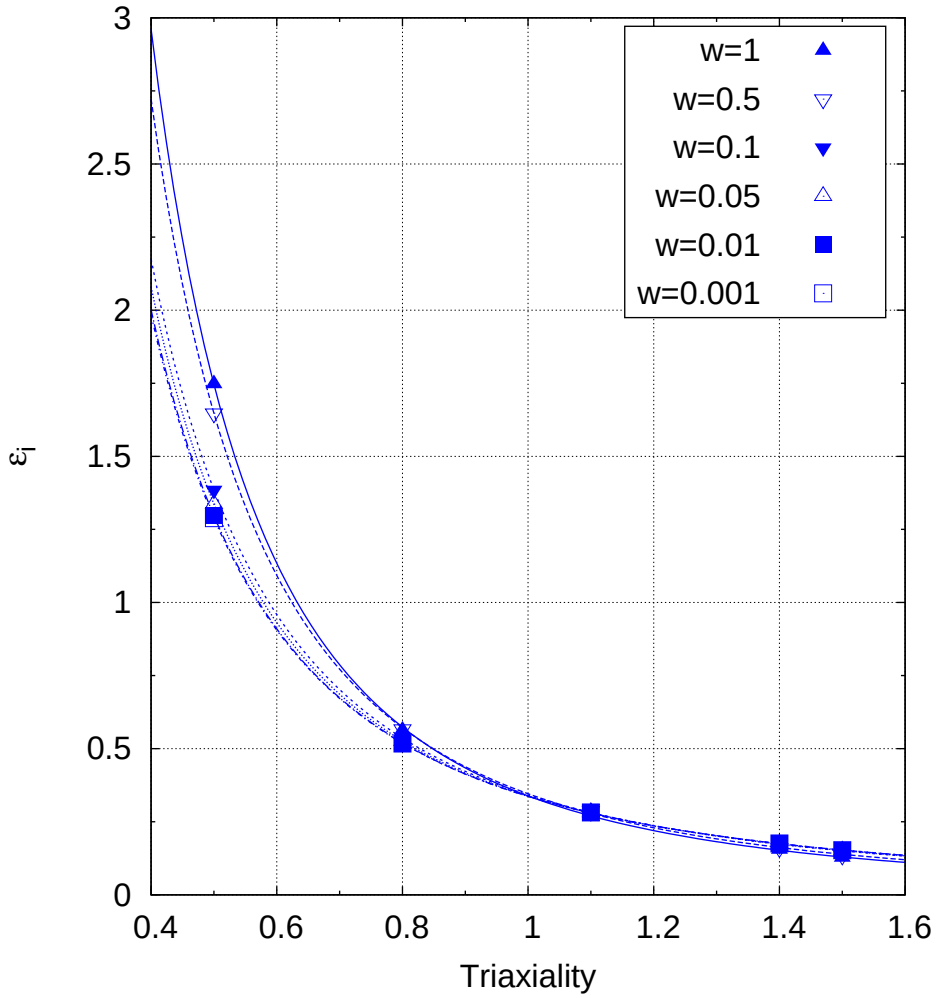

Figure 87: Coalescence strain versus triaxiality (T) for model materials with constant ligament aspect ratio (χ) but different initial void aspect ratios (W). Here $h = 1.7$, $f = 1.0 \times 10^{-5}$ and $\lambda = 1.5$.

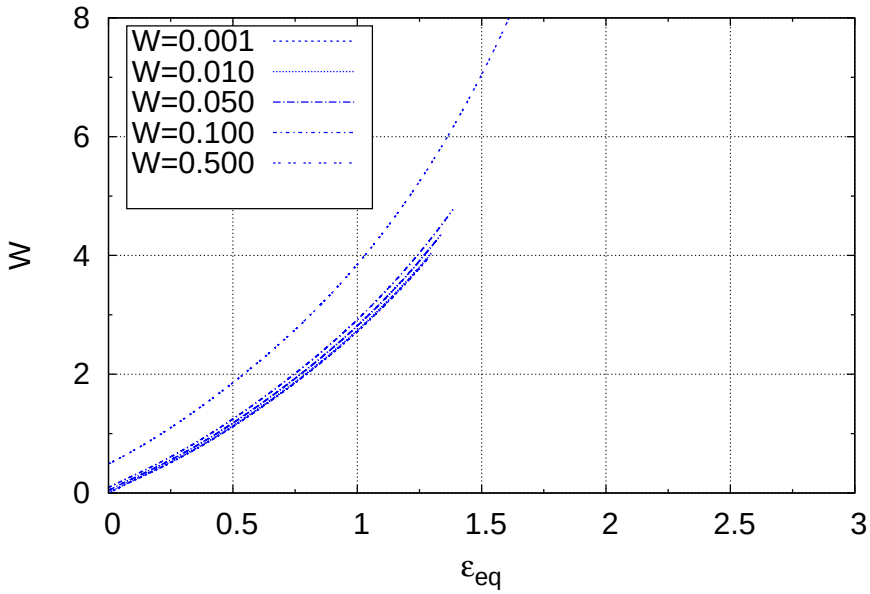

(a)

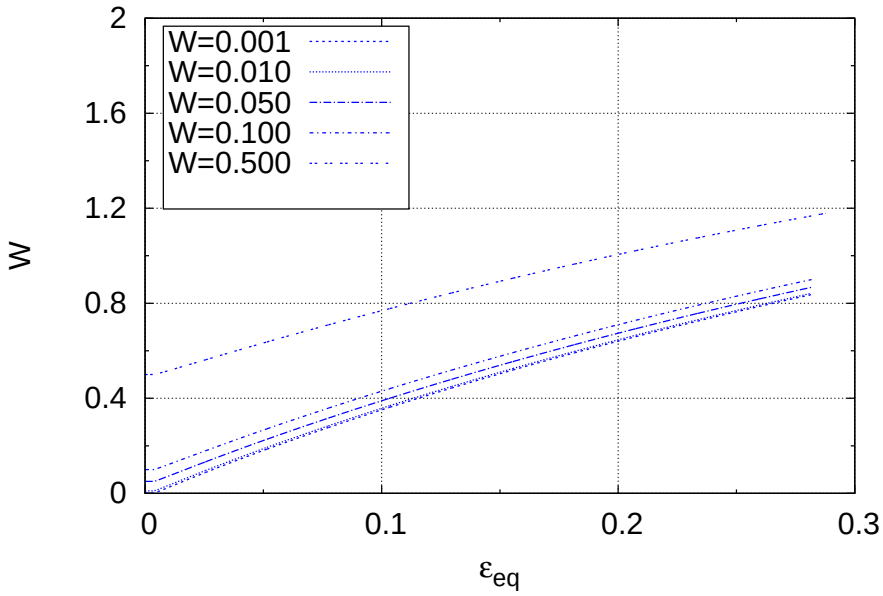

(b)

Figure 88: Evolution of void aspect ratio (W) with strain for materials with h=1.7, f=1.0×10^{-5}, $\lambda = 1.5$ at T=0.5 (a) and T=1.1 (b).

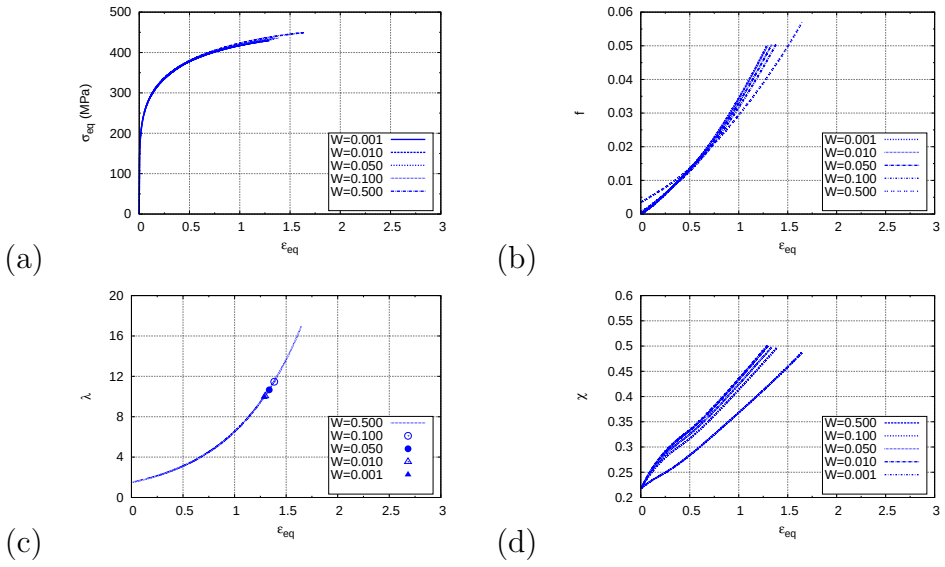

Figure 89: Mechanical response and evolution of microstructure with strain for materials with with h=1.7, f=1.0×10^{-5} and $\lambda = 1.5$ at T=0.5.

The evolution of features such as flow stress, void volume fraction, void shape, cell- and ligament-aspect ratio is presented in Figure 88, 89 (for T=0.5) and 90 (for T=1.1). These figures demonstrate that when χ is constant, the void shape has insignificant effect on ductility. The void shape effect of a constant ligament ratio is maximal at low traixialities in the studied range of triaxialities. Accordingly, oblate voids are more detrimental to ductility than their prolate counterparts. The void effect is reversed at high triaxialities ($T > 1.1$), with penny-shaped cracks as less detrimental for ductility.

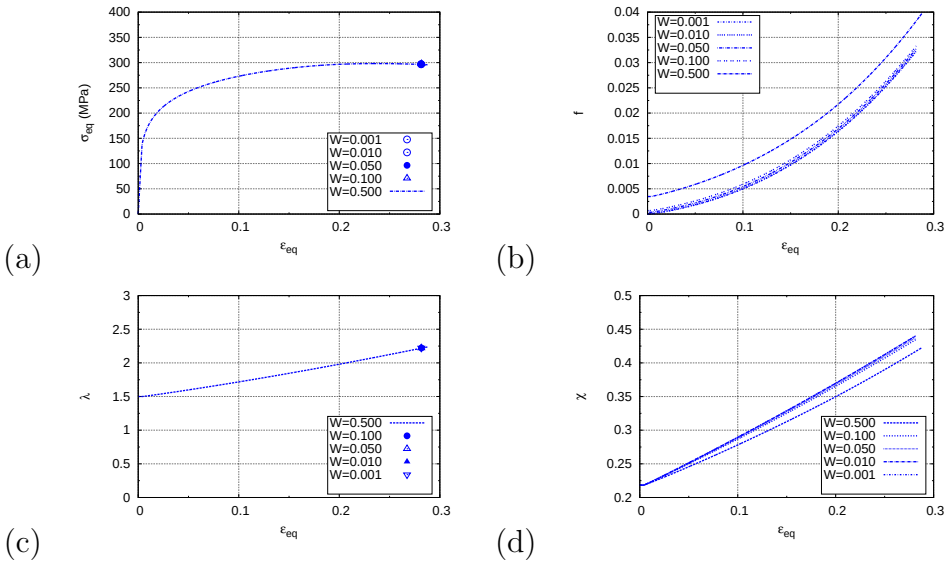

Figure 90: Mechanical response and evolution of microstructure with strain for materials with with h=1.7, f=1.0×10^{-5} and $\lambda = 1.5$ at T=1.1.

9.4 Application to magnesium alloys: AZ31 and WE43

9.4.1 Materials property identification of AZ31

To identify the material properties of AZ31 loaded along the L direction, image analysis software '*ImageJ*' was used. The volume fraction of the second-phase particles ($f_{part.} = 0.0078$) and their aspect ratio ($W_{part.} = 2.75$) were measured using the micrographs of the starting material. The cut-off area (area of the projection of the particle on to the plane of observation), below which the particles were not considered in these calculations, is 0.1 μm^2. Voronoi's cells were constructed on the location of these second-phase particles. The average size of cells associated with second-phase particles parallel and perpendicular the loading direction was measured and used to calculate the average cell aspect-ratio. Figure 91 shows the initial microstructure in various planes and its related Voronoi's cell. For loading along L direction (i.e., current analysis), the data from the L–S plane was employed, yielding $\lambda_{part.} = 0.87$. The aspect ratio calculated from micrographs of the L–T plane also rendered a similar number. The plane of study, used for identifying λ, should include the loading direction. Thus, the information from the T–S plane ($\lambda_{part.} = 1.0$). From these data and utilizing Equation 9.24, the ligament ratio associate to second phase particles was also calculated as $\chi = 0.155$.

Tomography data and micrographs from metallography of the interrupted and fractured specimens showed a high fraction of particles being actively involved in damage initiation process. According to these findings, second-phase particles were taken as the void initiation sites. This assumption leads to identical initial void-spacing and ligament ratio between voids and second phase particles ($\chi_{void} = \chi_{part.}$ & $\lambda_{void} = \lambda_{part.}$).

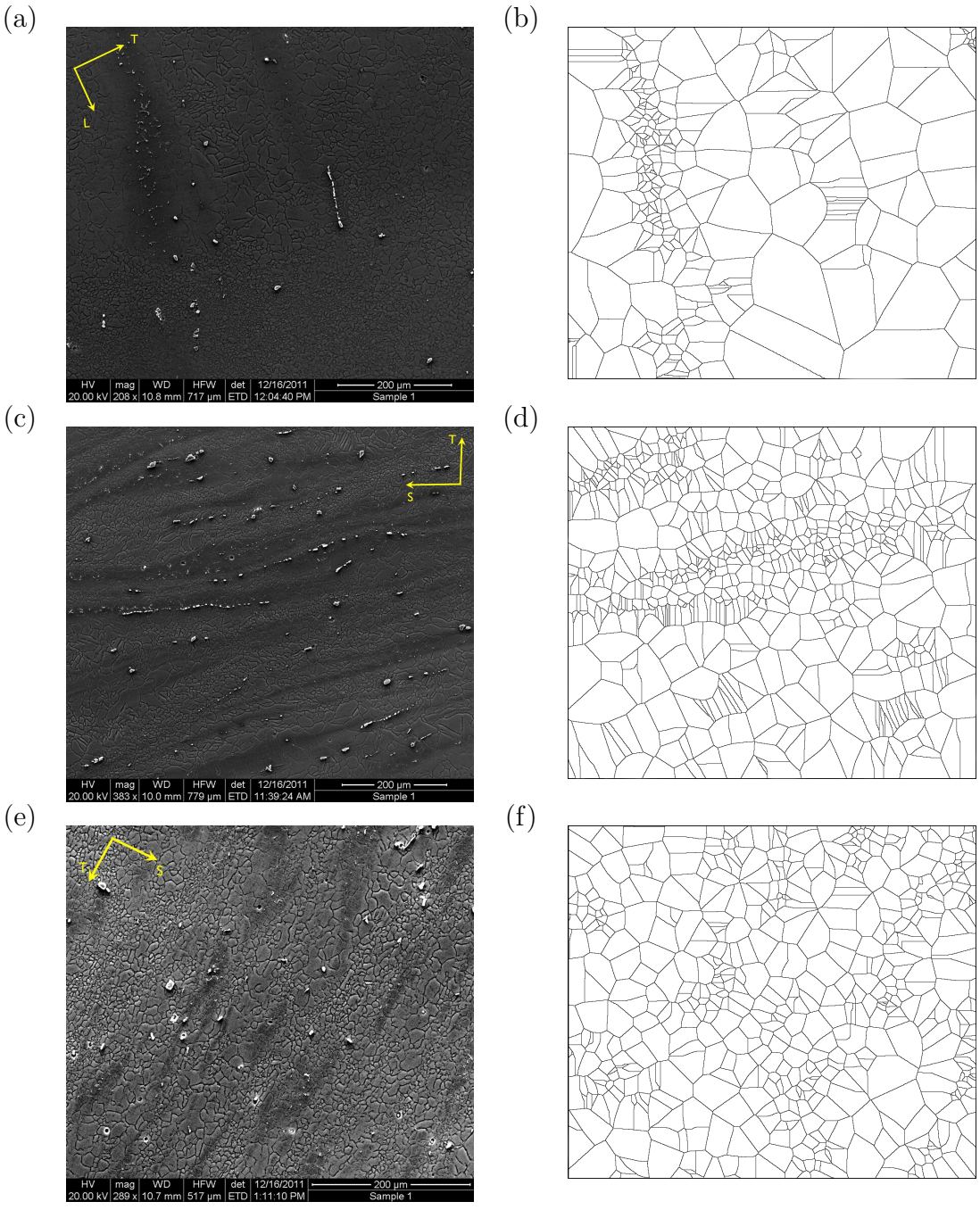

Figure 91: Microstructure (on the left) and its associated Voronoi's cells (on the right) for different planes in AZ31.

Last but not least, based on the limited opening of the voids at the end of deformation process, it was assumed that both voids or microcracks are initially penny-shaped. Thus, a $W_{void} = 0.05$ was assumed. Using initial W_{void}, λ_{void} $]\chi_{void}$ and utilizing Equation 9.24, the initial void volume fraction was calculated ($f_{void} = 0.000142$). A schematic of the algorithm followed for the identification of material parameters of AZ31 is presented in Figure 92.

Based on the literature data for elastic properties of Mg, elastic modulus of $E = 45GPa$ and Poisson's ratio of $\nu = 0.35$ was used for AZ31. Assuming a power law hardening, uniaxial tension results were used to characterize the flow properties of AZ31 along L direction.

$$\sigma = K\varepsilon_p^n \tag{9.25}$$

where K is material constant and equal to $K = 440.0$ MPa and n is hardening exponent $n = 0.18$. Here, ε_p represents the accumulated plastic strain. Based on the data in Section8, the characteristics of anisotropy after reaching a steady state were employed to represent the plastic anisotropy in the matrix. The components of anisitropic tensor employed in this model are as follows: $h_L = 1.18, h_T = 0.93, h_3 = 0.36, h_4 = 1.74, h_5 = 1.66, h_6 = 1.07, h = 1.95$.

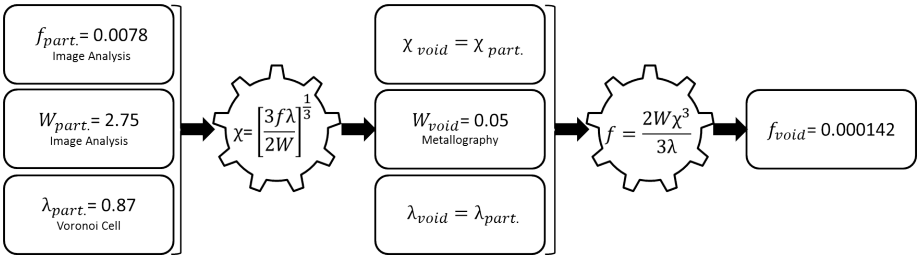

Figure 92: Schematic of the algorithm used to calculate microstructural parameters of AZ31.

9.4.2 Materials property identification of WE43

In Section 6.2.2, a rationale based on intergranular fracture in the current WE43 alloy was proposed to justify the experimentally measured fracture locus. According to that rationale, only the second-phase particles on the grain boundaries are contributing to damage initiation (Figure 93).

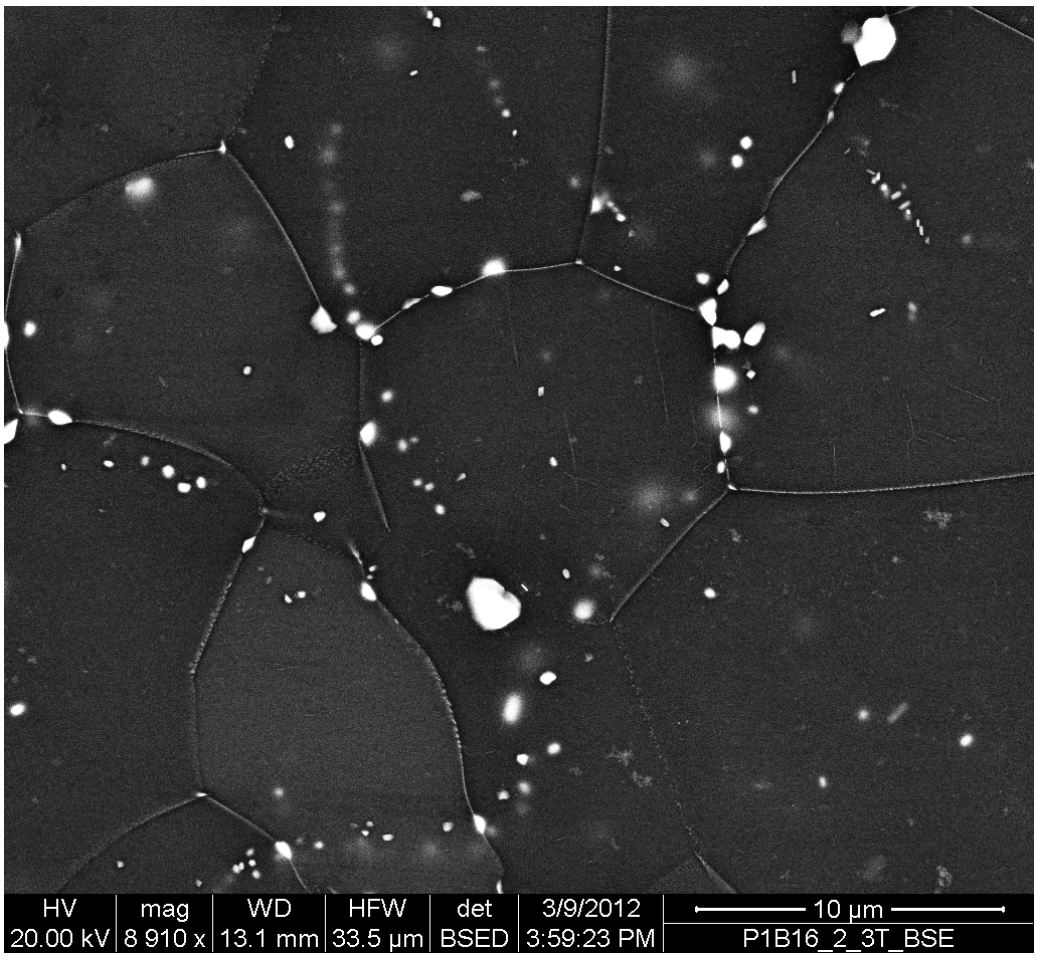

Figure 93: Microstructure of WE43 in L–T plane showing the presence of second phase particles on the grain boundaries.

Such qualitative rationale, however, was based only on the initial values of material parameters. For quantitative prediction of fracture, tracking the evolution of microstructural parameters during deformation is required. Motivated by fractographical observations and previously discussed IGF hypothesis, χ of the second-phase particles on the grain boundaries that make an angles of $60 \leqslant \theta \leqslant 120^{\circ}$ with the loading direction were measured in the L–T plane ($\chi_{part.} = 0.35$). The Λ of the second phase particles ($\lambda_{part.}$) was calculated using various methods and reported. To get $\lambda_{part.}$, one can divide the average grain size by the average distance between particles on GBs that make an angles of $60 \leqslant \theta \leqslant 120^{\circ}$ with the loading direction ($\lambda_{part.} = 5.25$). Alternatively, the average grain size divided by the average distance between particles on all GBs can be considered as the cell aspect ratio ($\lambda_{part.} = 4.39$). Finally, the average distance of all particles could be divided by the average distance between particles on GBs that make an angles of $60 \leqslant \theta \leqslant 120^{\circ}$ with the loading direction ($\lambda_{part.} = 1.77$).

As mentioned in previous section, it is assumed that voids are initially penny-shaped ($W_{void} = 0.05$) and these voids nucleate only on the second phase particles. Thus, $\chi_{part.} = \chi_{void}$ and $\lambda_{part.} = \lambda_{void}$. By comparing the predicted failure strains and those measured in experiments, $\lambda = 5.25$ was selected as the cell aspect ratio in the present WE43 alloys. Employing Equation 9.24, the GB's void volume fraction was calculated ($f_{void} = 0.000185$). Schematic of the algorithm followed for identification WE43 material parameters is presented in Figure 94.

Based on literature data for elastic properties of Mg, $E = 44$GPa, $\nu = 0.27$ are used for WE43 in the current model. Assuming a power law hardening and utilizing uniaxial tension experiments, flow properties of WE43 along L direction was characterized as follow:

$$\sigma = K\varepsilon_p^n \tag{9.26}$$

where K is material constant equal to $K = 615.0$ MPa and n is hardening exponent equal to $n = 0.16$. Here, ε_p represents the accumulated plastic strain. Based on the data in Section8, isotropic properties were used to represent the matrix ($h_1 = h_2 = h_3 = h_4 = h_5 = h_6 = h = 1.00$)

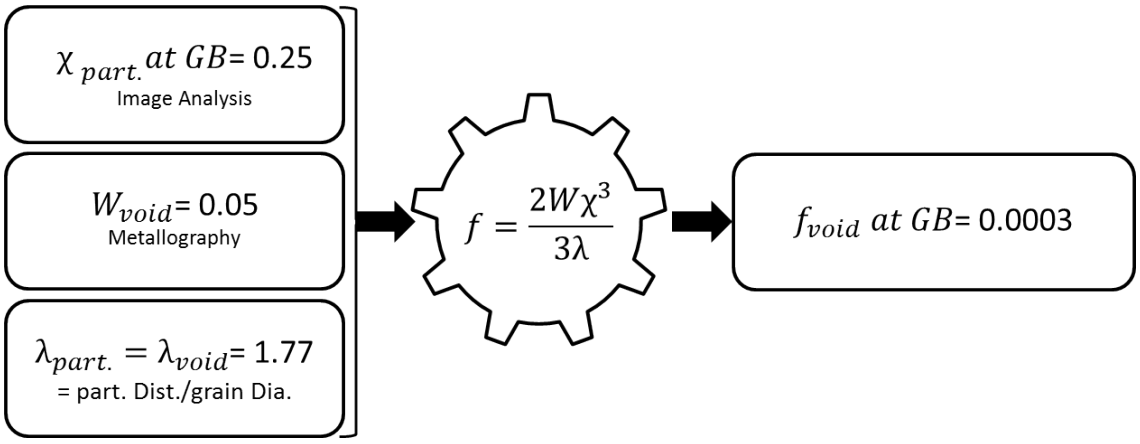

Figure 94: Schematic of the algorithm used to calculate microstructural parameters of WE43.

9.4.3 Modeling ductile fracture in Mg alloys

The proposed framework for void growth and coalescence was employed, using the material parameters of AZ31 and WE43, to predict the fracture locus of Mg notched bars loaded along the L direction. Current ductile fracture models for void growth and coalescence predict infinitely large fracture strains for uniaxial loading. In such loading conditions, the predicted lateral growth of voids is such that coalescence condition is never satisfied. Thus, in current analyses, the attention is focused on the notched bars. The equation governing the evolution of void shape is also modified by a pre-factor of $\eta = 0.43$ to match the parameter W with the experimentally measured ones. In fact, the evolution law for changes in void shape is analytically deriven but heuristically modified to quantitatively predict the experimental measurements. Thus, this partially heuristic law is amenable to modification based on experimental observations. The application of this pre-factor is justified as follows:

1. **void locking**: Experimental observations, presented in Figure 95, shows the role of second-phase particles in limiting void growth. This effect is know as void locking [103, 148]

2. **Effect of size on the rate of void growth:** Literature data indicates that voids smaller than a certain size, grow much slower that normal sized ones in the same matrix. In the present Mg alloys, the initiated penny-shaped voids have small size along the loading direction, which slows their longitudinal growth. Thus, application of a pre-factor that reduces the change in void shape is partly justified [149–151]

3. **Plastic anisotropy of the matrix:** Plastic anisotropy of the matrix can also affect the rate of shape change by constraining growth along certain directions.

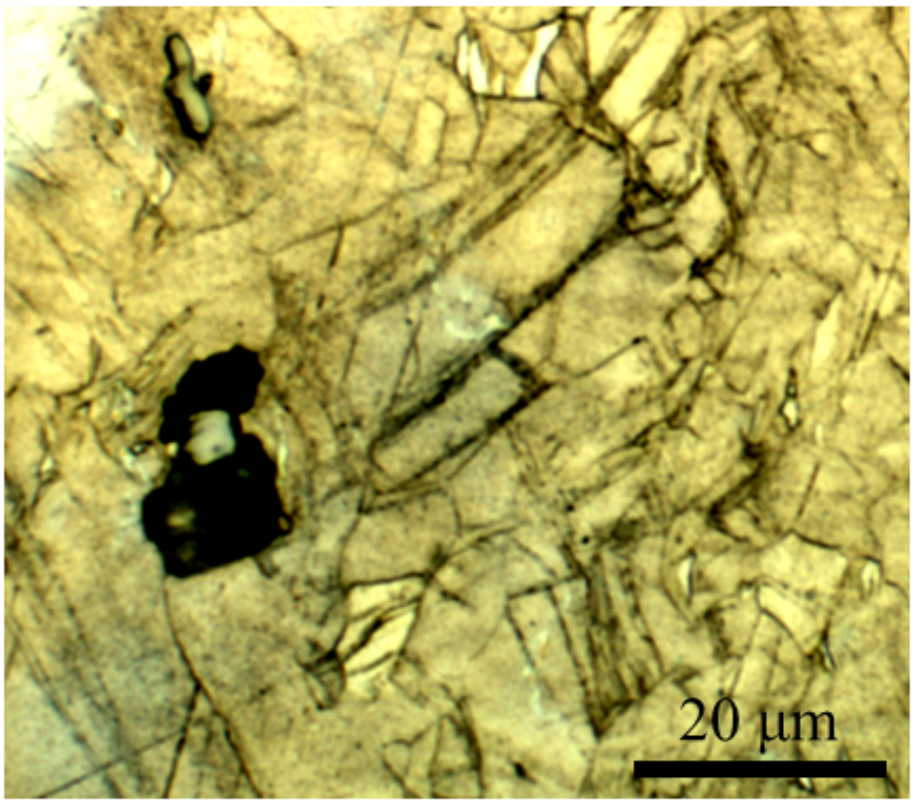

Figure 95: Evidence of void locking in AZ31. Loading direction in this micrograph is vertical.

The model with modified law for void-shape evolution was used to predict fracture strains under loading conditions the experimentally measured results. Figure 96 shows the predicted failure strains for both AZ31 and WE43 with same model parameters. Material parameters utilized for these results were calculated in previous two sections. The model could accurately predict the fracture behavior of WE43 alloy. Good agreement between the experimental results and current model predictions along with fractographical evidence suggests that fracture in WE43 could be represented by IGF and its microstructural features.

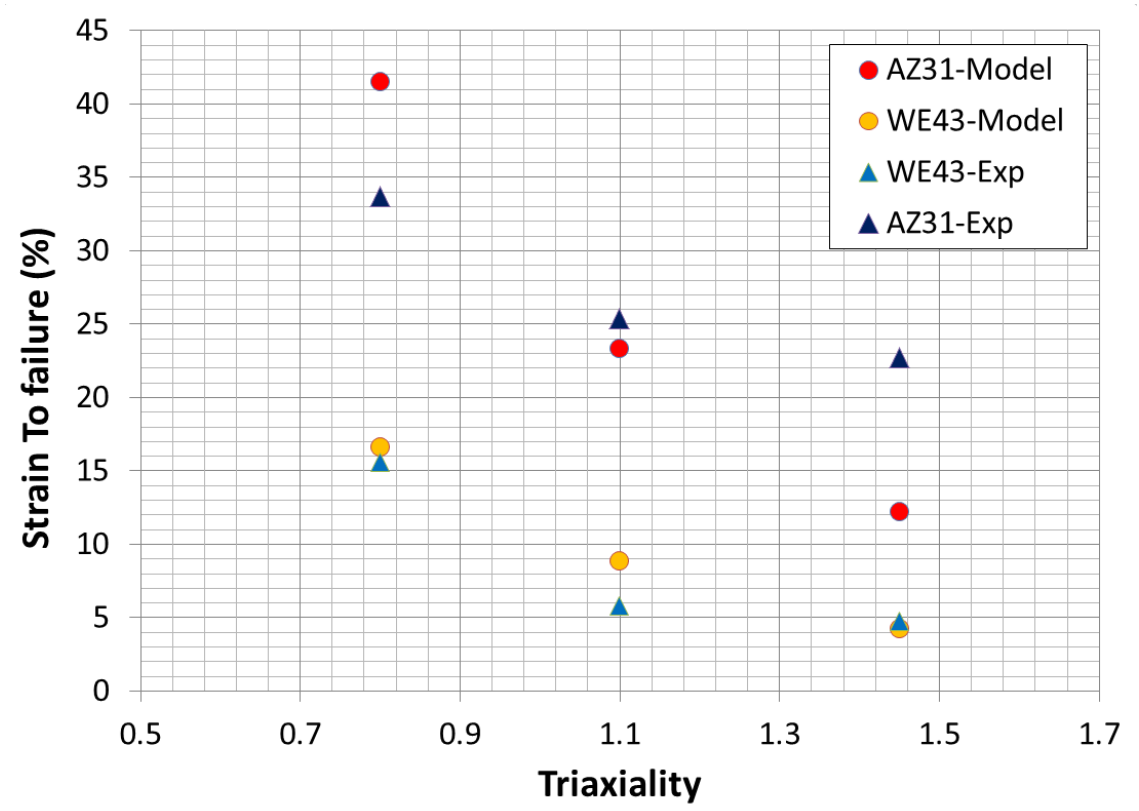

Figure 96: Comparison between predicted and experimentally measured fracture strains for AZ31 and WE43 specimens loaded parallel to L direction.

There is some mismatched between the experimentally measured and predicted fracture strain in AZ31. It should be noted that these calculation are performed for a material volume that do not fully account for the spatial variations in the various fields. This includes the variation of triaxiality within the actual specimen. The role of shear localization should also be noted. As presented in section 6.1.3, the mode of failure in AZ31's uniaxial bars is slanted. In such condition, shear localization truncates the stable deformation and leads to premature failure in a slanted mode.

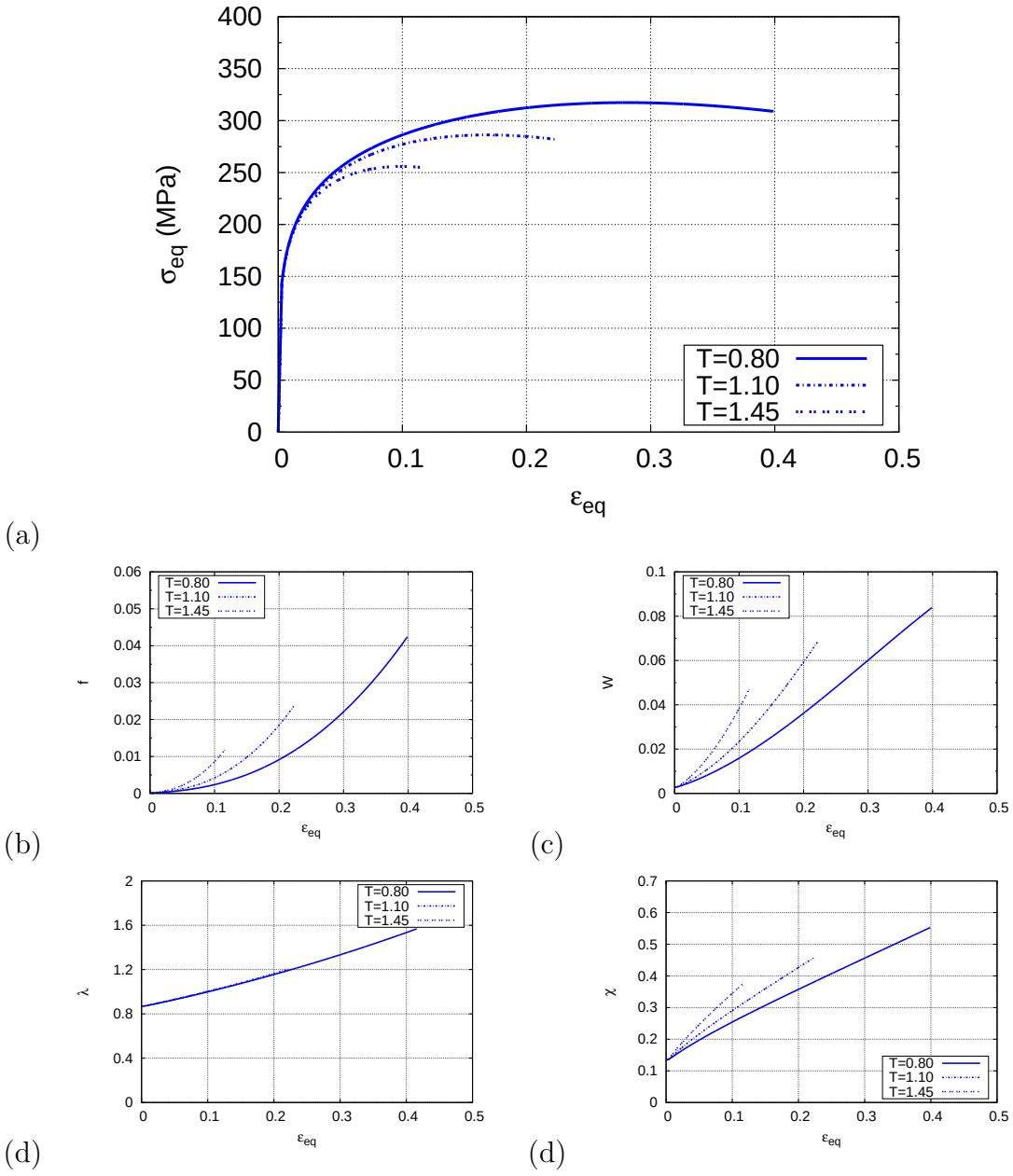

Figure 97: Predicted mechanical response and evolution of microstructure with strain for a material point with properties of AZ31 alloy used in this study.

Geometry of the sample in notched bars, however, forces the macroscopic crack to move along the minimum cross-section of the bar. This reduces the interference form shear localization but does not eliminated it completely. As depicted in Figure 30, there are large shear lips in the RN10 specimens. Although the macroscopic mode of failure is flat in those specimen, planes with slanted character are observed even with naked eye. As the notch becomes sharper (going form RN10 to RN2), the fracture surface becomes flatter and rarely exhibits shear-like features. Based on the above justification, more contribution form shear is expected at lower triaxialities. Since the current model does not account for shear effects, a mismatch between experiments and mode prediction at lower triaxialities is expected. Future work will focus on implementing the model in a Finite-Element software so that the Boundary-Value Problems (BVP) corresponding to the RN specimens can be solved, accounting for spatial variations of different field in specimen and shear localization.

To provide more information on the fracture in AZ31 and WE43, the predicted stress-strain response and the evolution of microstructural variables for the analysis presented in Figure 96 are presented in Figure 97 and 98.

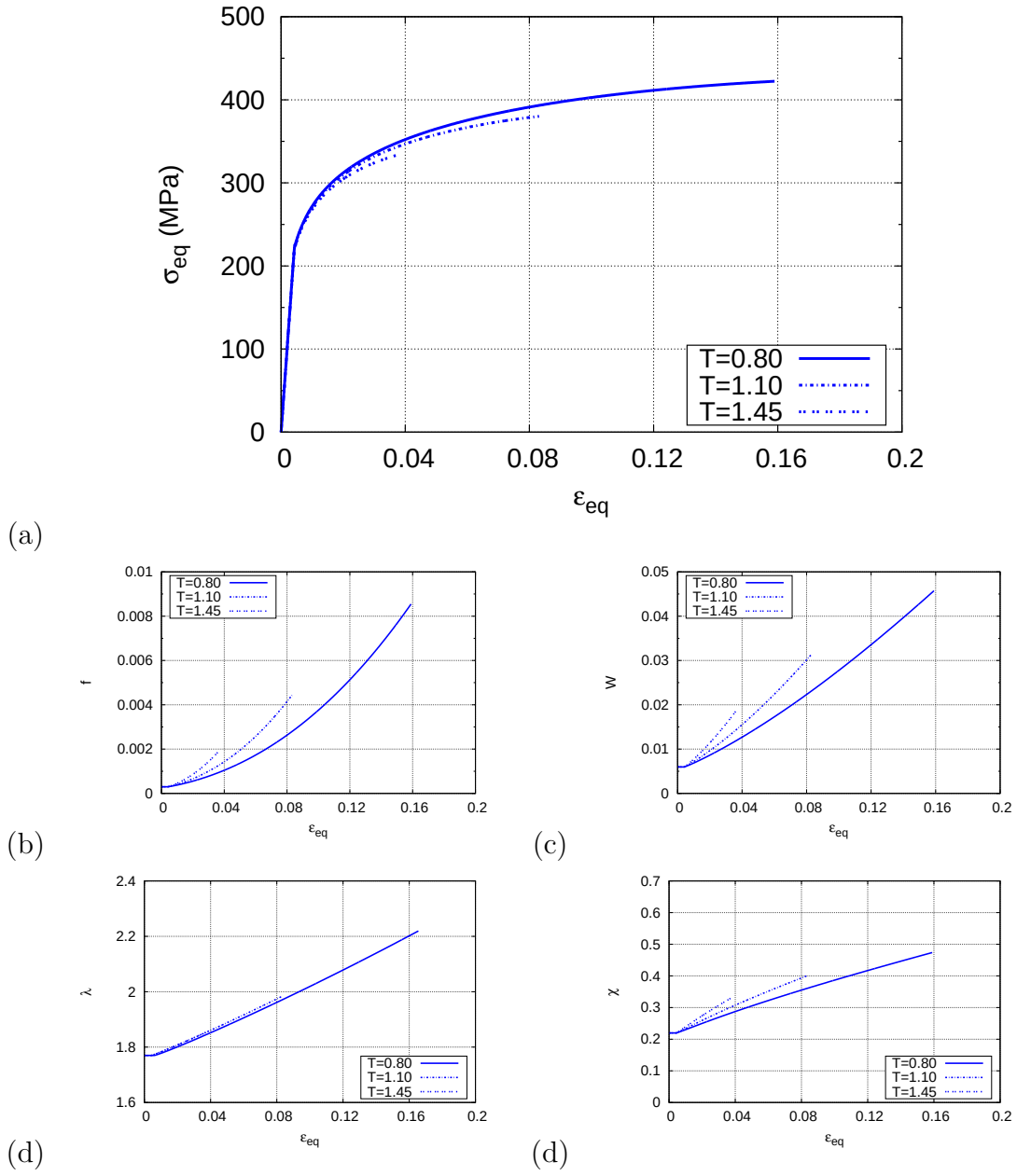

Figure 98: Predicted mechanical response and evolution of microstructure with strain for a material point with properties of WE43 alloy used in this study.

10. CONCLUSIONS

The processes of deformation, damage initiation and propagation to fracture in two magnesium alloys (AZ31 and WE43) at room temperature in a wide range of stress state triaxialities were studied. Performing experiments along different directions with respect to the initial macroscopic texture allowed the investigation of anisotropy in these properties. Detailed image analysis and fractography on cracked and fractured specimens enabled establishing connection between microscale phenomena and macroscopic response. The results yielded the following conclusions.

- Employing interrupted uniaxial tension and compression experiments along six different orientations and by using models in the literature, the plastic flow anisotropy of AZ31 and WE43 and their evolution during the course of deformation were characterized. In addition, a significant volume change during plastic deformation of both alloys was detected.

- Fracture studies showed that magnesium alloys such as AZ31 are more tolerant to damage compared to what was perceived based only on uniaxial experiments. Notched bar experiments showed that under triaxial loading condition (even in sharply notched bars), AZ31 exhibits larger strain to failure compared to its uniaxial counterparts.

- The fracture locus of AZ31, in the triaxiality range from 0.3 to 1.5, exhibits a maximum at moderate triaxialities. The increased ductility in notched bars was attributed to (i) transition from slanted (shear) to flat fracture in the macroscale; (ii) transition from twin-controlled to microvoid coalescence fracture at microscale; and (iii) activation of more deformation systems at high

triaxialities, which is a manifestation of loading effects on plastic anisotropy. During triaxial loading, the tensile stress parallel to the c-axis of hcp crystal structure is large enough to activate softer deformation systems (i.e. extension twinning).

- Depending on the loading condition and geometry of samples, ductile fracture in AZ31 could occur by either microvoid/crack nucleation to coalescence or by mechanical instability of the specimen (i.e., shear localization). Both of these mechanisms are important in practice. However, for the study of damage mechanism it is preferable to have a diffuse damage zone with know location. The damage process zone in shear failure is too small to infer any conclusive evidence of intrinsic damage mechanisms in uniaxial bars. On the other hand and by introduction of the notch, the fracture mode became flat, which facilitates the investigation of damage and fracture. This makes notched bars ideal specimens for investigating damage in Mg alloys.

- Based on microstructural evidence, it was concluded that macrocracks in AZ31 form in different regions of notched specimen, depending on the triaxiality. In moderate triaxialities (i.e., RN10 with shallow notch) macrocracks form in the central region and propagate along the transverse direction of the plate. When such macrocracks grow large enough, a plane-strain deformation state develops in the ligament between them, which promotes shear localization. Macrocracks, thus, join each other via shear zones in the L–S planes and final fracture follows. At high triaxialites, however, cracks form near the free surface and propagate parallel to the transverse direction. These cracks connect to the free surface almost immediately by shear localization in L–S plane.

- Results of the notched bar experiments indicate that WE43 and AZ31, in the

studied range of triaxialityies, exhibit significantly different sensitivity to stress-state triaxiality. In contrast to AZ31, which has weak sensitivity to triaxiality, the strain to failure in WE43 is reduced substantially when notch radius is decreased (i.e., increase in triaxiality). Based on the features on the fracture surface and considering the initial microstructure, the fracture locus of WE43 and its low failure strain in notched bars were justified by intergranular fracture initiated at second phase particles located on grain boundaries.

- A micromechanics-based continuum damage model was employed to rationalize the main experimental trends. The model has two components: (i) a shape-dependent void growth part; and (ii) a shape-dependent void/crack coalescence part. Parametric studies on the effects of various material-, loading- and microstructural variables were used to identify key parameters in the studied system. Proper matrix anisotropy and void spacing were identified to be the most important parameters in achieving high strain to failures.

- Utilizing the material and microstructural variables extracted from the image analysis, the model was employed to predict and rationalize the experimentally observed fracture strains and their trends. It was concluded that failure strain in WE43 is controlled by intergranular fracture. Fracture in notched AZ31 alloys was rationalized by early coalescence of initially penny-shaped voids/microcracks. During uniaxial loading, AZ31 fails by shear localization that truncates stable deformation of the matrix. The results provide the groundwork for understanding the effects of microstructural and loading variables on damage and fracture in magnesium alloys.

REFERENCES

[1] A. Stalmann, W. Sebastian, H. Friedrich, S. Schumann, K. Droder, Properties and processing of magnesium wrought products for automotive applications, Advanced Engineering Materials 3 (2001) 969–974.

[2] S. R. Agnew, C. N. Tome, D. W. Brown, T. M. Holden, S. C. Vogel, Study of slip mechanisms in a magnesium alloy by neutron diffraction and modeling, Scripta Materialia 48 (2003) 1003–1008.

[3] J. Koike, T. Kobayashi, T. Mukai, H. Watanabe, M. Suzuki, K. Maruyama, K. Higashi, The activity of non-basal slip systems and dynamic recovery at room temperature in fine-grained AZ31B magnesium alloys, Acta Materialia 51 (2003) 2055–2065.

[4] J. Koike, Enhanced deformation mechanisms by anisotropic plasticity in polycrystalline Mg alloys at room temperature, Metallurgical and Materials Transactions A. 36A (2005) 1689–1696.

[5] S. B. Yi, C. H. J. Davies, H. G. Brokmeier, R. E. Bolmaro, K. U. Kainer, J. Homeyer, Deformation and texture evolution in AZ31 magnesium alloy during uniaxial loading, Acta Materialia 54 (2006) 549–562.

[6] X. Gao, J. F. Nie, Characterization of strengthening precipitate phases in a Mg-Zn alloy, Scripta Materialia 56 (2007) 645–648.

[7] L. Capolungo, I. J. Beyerlein, C. N. Tome, Slip-assisted twin growth in hexagonal close-packed metals, Scripta Materialia 60 (2009) 32–35.

[8] M. Al-Maharbi, I. Karaman, I. J. Beyerlein, D. Foley, K. T. Hartwig, L. J. Kecskes, S. N. Mathaudhu, Microstructure, crystallographic texture, and plastic anisotropy evolution in an Mg alloy during equal channel angular extrusion processing, Materials Science and Engineering:A 528 (2011) 7616–7627.

[9] S. R. Agnew, O. Duygulu, Plastic anisotropy and the role of non-basal slip in magnesium alloy AZ31B, International Journal of Plasticity 21 (2005) 1161–1193.

[10] M. R. Barnett, Twinning and the ductility of magnesium alloys Part I: "tension" twins, Materials Science and Engineering:A 464 (2007) 1–7.

[11] L. Jiang, J. J. Jonas, R. K. Mishra, A. A. Luo, A. K. Sachdev, S. Godet, Twinning and texture development in two Mg alloys subjected to loading along three different strain paths, Acta Materialia 55 (2007) 3899–3910.

[12] M. R. Barnett, Twinning and the ductility of magnesium alloys Part II. "contraction" twins, Materials Science and Engineering:A 464 (2007) 8–16.

[13] H. Somekawa, T. Mukai, Effect of texture on fracture toughness in extruded AZ31 magnesium alloy, Scripta Materialia 53 (2005) 541–545.

[14] D. Ando, J. Koike, Y. Sutou, Relationship between deformation twinning and surface step formation in AZ31 magnesium alloys, Acta Materialia 58 (2010) 4316–4324.

[15] A. Yamashita, Z. Horita, T. G. Langdon, Improving the mechanical properties of magnesium and a magnesium alloy through severe plastic deformation, Materials Science and Engineering:A 300 (2001) 142–147.

[16] S. S. Park, G. T. Bae, D. H. Kang, I.-H. Jung, K. S. Shin, N. J. Kim, Microstructure and tensile properties of twin-roll cast Mg-Zn-Mn-Al alloys, Scripta Materialia 57 (2007) 793–796.

[17] D. C. Foley, M. Al-Maharbi, K. T. Hartwig, I. Karaman, L. J. Kecskes, S. N. Mathaudhu, Grain refinement vs. crystallographic texture: Mechanical anisotropy in a magnesium alloy, Scripta Materialia 64 (2011) 193–196.

[18] B. Kondori, A. A. Benzerga, Effect of stress triaxiality on the flow and fracture of Mg alloy AZ31, Metallurgical and Materials Transactions A. 45 (2014) 3292–3307.

[19] R. A. Lebensohn, C. N. Tome, A self-consistent anisotropic approach for the simulation of plastic deformation and texture development of polycrystals: Application to zirconium alloys, Acta Metallurgica et Materialia 41 (1993) 2611–2624.

[20] T. E. Davidson, J. C. Uy, A. P. Lee, Tensile fracture characterization of metals under hydrostatic pressures to 23 kilobars, Acta Metallurgica 14 (1966) 937–948.

[21] A. Sankaran, S. V. Madam, A. Nouri, M. R. Barnett, Attaining high compressive strains in pure Mg at room temperature by encasing with pure Al, Scripta Materialia 66 (2012) 725–728.

[22] B. Kondori, A. A. Benzerga, Fracture strains, damage mechanisms and anisotropy in a magnesium alloy across a range of stress triaxialities, Experimental Mechanics 54 (2014) 493–499.

[23] D. Ando, J. Koike, Y. Sutou, The role of deformation twinning in the fracture behavior and mechanism of basal textured magnesium alloys, Materials Science and Engineering:A 600 (2014) 145–152.

[24] M. Lugo, M. A. Tschopp, J. B. Jordon, M. F. Horstemeyer, Microstructure and damage evolution during tensile loading in a wrought magnesium alloy, Scripta Materialia 64 (2011) 912–915.

[25] H. Somekawa, A. Singh, T. Inoue, K. Tsuzaki, Crack propagation behaviour in magnesium binary alloys, The Philosophical Magazine 94 (2014) 3317–3330.

[26] H. Somekawa, A. Singh, T. Mukai, Fracture mechanism of a coarse-grained magnesium alloy during fracture toughness testing, Philosophical Magazine Letters 89 (2009) 2–10.

[27] S. Lee, S. Lee, D. Kim, Effect of Y, Sr, and Nd additions on the microstructure and microfracture mechanism of squeeze-cast AZ91-X magnesium alloys, Metallurgical and Materials Transactions A. 527 (1998) 1221–1235.

[28] B. Kim, J. Do, S. Lee, I. Park, In situ fracture observation and fracture toughness analysis of squeeze cast AZ51-xSn magnesium alloys, Materials Science and Engineering:A 527 (2010) 6745–6757.

[29] J. R. Rice, The localization of plastic deformation, in: W. T. Koiter (Ed.), 14th International Congress of Theoretical and Applied Mechanics, North–Holland, Amsterdam, 1976, pp. 207–220.

[30] M. Marya, L. G. Hector, R. Verma, W. Tong, Microstructural effects of AZ31 magnesium alloy on its tensile deformation and failure behaviors, Materials Science and Engineering:A 418 (2006) 341–356.

[31] Magnesium Elektron Ltd, Elektron43 preliminary datasheet, URL: http://www.magnesium-elektron.com/data/downloads/DS043.pdf, Magnesium Elektron Ltd, Swinton, England, Accessed: 09/15/2014 (2011).

[32] B. Lee, S. Park, S. Hong, K. Park, C. Lee, Role of initial texture on the plastic anisotropy of Mg-3Al-1Zn alloy at various temperatures, Materials Science and Engineering:A 528 (2011) 1162–1172.

[33] H. E. Friedrich, B. L. Mordike, Magnesium Technology: Metallurgy, Design Data, Applications, Springer, New York, 2006.

[34] B. L. Mordike, T. Ebert, Magnesium properties - applications - potential, Materials Science and Engineering:A 302 (2001) 37–45.

[35] B. R. Powell, P. E. Krajewski, A. A. Luo, Magnesium alloys for lightweight powertrains and automotive structures, in: Materials, Design and Manufacturing for Lightweight Vehicles, Woodhead Publishing in Materials, CRC Press, Boca Raton, FL, 2010, pp. 114–173. doi:10.1533/9781845697822.1.114.

[36] S. Delfino, A. Saccone, R. Ferro, Phase relationships in the neodymium-magnesium alloy system, Metallurgical Transactions 21 (1990) 2109–2114.

[37] L. Wu, S. R. Agnew, D. W. Brown, G. M. Stoica, B. Clausen, A. Jain, D. E. Fielden, P. K. Liaw, Internal stress relaxation and load redistribution during the twinning–detwinning-dominated cyclic deformation of a wrought magnesium alloy, ZK60A, Acta Materialia 56 (2008) 3699–3707.

[38] S. R. Agnew, J. F. Nie, Preface to the viewpoint set on: The current state of magnesium alloy science and technology, Scripta Materialia 63 (2010) 671–673.

[39] D. W. Brown, S. R. Agnew, M. A. M. Bourke, T. M. Holden, S. C. Vogel, C. N. Tome, Internal strain and texture evolution during deformation twinning in magnesium, Materials Science and Engineering:A 399 (2005) 1–12.

[40] S. Mezbahul-Islam, A. O. Mostafa, M. Medraj, Essential magnesium alloys binary phase diagrams and their thermochemical data, Journal of Materials (2014) 1–33.

[41] Q. D. Wang, Y. Z. Lu, X. Zeng, W. J. Ding, Y. P. Zhu, Q. H. Li, J. Lan, Study on the fluidity of AZ91+xRE magnesium alloy, Materials Science and Engineering:A 271 (1999) 109–115.

[42] Y. Z. Lu, Q. D. Wang, X. Q. Zeng, W. J. Ding, C. Q. Zhai, Y. P. Zhu, Effects of rare earths on the microstructure, properties and fracture behavior of Mg-Ag alloys, Materials Science and Engineering:A 278 (2000) 66–76.

[43] Z. G. Y., Z. H., G. M., W. D., Mechanism of effects of rare earths on microstructure and properties at elevated temperatures of AZ91 magnesium alloy, Journal of Rare Earth 25 (2007) 348–351.

[44] Y. X. Wang, S. K. Guan, X. Q. Zeng, W. J. Dine, Effects of RE on the microstructure and mechanical properties of Mg-8Zn-4Al magnesium alloy, Materials Science and Engineering:A 416 (2006) 109–118.

[45] E. A. Ball, P. B. Prangnell, Tensile-compressive yield asymmetries in high-strength wrought magnesium alloys, Scripta Materialia 31 (1994) 111–116.

[46] J. Bohlen, M. R. Nuernberg, J. W. Senn, D. Letzig, S. R. Agnew, The texture and anisotropy of magnesium-zinc-rare earth alloy sheets, Acta Materialia 55 (2007) 2101–2112.

[47] J. P. Hadorn, K. Hantzsche, S. Yi, J. Bohlen, D. Letzig, J. A. Wollmershauser, S. R. Agnew, Role of solute in the texture modification during hot deformation of Mg-rare earth alloys, Metallurgical and Materials Transactions A. 43 (2012) 1347–1362.

[48] S. Sandloebes, Z. Pei, M. Friak, L.-F. Zhu, F. Wang, S. Zaefferer, D. Raabe, J. Neugebauer, Ductility improvement of Mg alloys by solid solution: Ab initio modeling, synthesis and mechanical properties, Acta Materialia 70 (2014) 92–104.

[49] S. Celotto, T. J. Bastow, Study of precipitation in aged binary Mg-Al and ternary Mg-Al-Zn alloys using 27Al NMR spectroscopy, Acta Materialia 49 (2001) 41–51.

[50] M. M. Avedesian, B. H., Magnesium and Magnesium Alloys (ASM Specialty Handbook), ASM Specialty Handbook, Butterworth-Heinemann, Oxford, 1999.

[51] H. Okamoto, Mg-Y (Magnesium-Yttrium), Journal of Phase Equilibria and Diffusion 31 (2010) 199–199.

[52] N. Hort, Y. D. Huang, K. U. Kainer, Intermetallics in magnesium alloys, Advanced Engineering Materials 8 (2006) 235–240.

[53] I. Polmear, Light Alloys: Metallurgy of the Light Metals, Metallurgy and Materials Science Series, Butterworth-Heinemann, Oxford, 1995.

[54] M. Asgar-Khan, M. Medraj, Thermodynamic description of the Mn, Al-Mn and Mg-Al-Mn systems using the modified quasichemical model for the liquid phases, Materials Transactions 50 (2009) 1113–1122.

[55] A. Luque, M. Ghazisaeidi, W. A. Curtin, Deformation modes in magnesium (0001) and $(0\,1\,\bar{1}\,1)$ single crystals: Simulations versus experiments, Modelling and Simulation in Materials Science and Engineering 21 (2013) 1–15.

[56] A. H. Cottrell, B. A. Bilby, A mechanism for the growth of deformation twins in crystals, The Philosophical Magazine 42 (1951) 573–581.

[57] J. W. Christian, S. Mahajan, Deformation twinning, Progress in Materials Science 39 (1995) 1–157.

[58] S. Mahajan, D. F. Williams, Deformation twinning in metals and alloys, International Metallurgical Reviews 18 (1973) 43–61.

[59] A. Jain, S. R. Agnew, Modeling the temperature dependent effect of twinning on the behavior of magnesium alloy AZ31B sheet, Materials Science and Engineering:A 462 (2007) 29–36.

[60] Q. Ma, H. El Kadiri, A. Oppedal, J. Baird, B. Li, M. Horstemeyer, S. Vogel, Twinning effects in a rod-textured AM30 magnesium alloy, International Journal of Plasticity 29 (2012) 60–76.

[61] F. Kabirian, A. S. Khan, T. Gnupel-Herlod, Visco-plastic modeling of mechanical responses and texture evolution in extruded AZ31 magnesium alloy for various loading conditions, International Journal of Plasticity 68 (2015) 1–20.

[62] J. Zhang, S. P. Joshi, Phenomenological crystal plasticity modeling and detailed micromechanical investigations of pure magnesium, Journal of the Mechanics and Physics of Solids 60 (2012) 945–972.

[63] R. Sanchez-Martin, M. T. Prez-Prado, J. Segurado, J. Bohlen, I. Gutirrez-Urrutia, J. Llorca, J. M. Molina-Aldareguia, Measuring the critical resolved shear stresses in Mg alloys by instrumented nanoindentation, Acta Materialia 71 (2014) 283–292.

[64] M. H. Yoo, Slip, twinning, and fracture in hexagonal close-packed metals, Metallurgical Transactions 12 (1981) 409–418.

[65] P. W. Flynn, J. Mote, J. E. Dorn, On the thermally activated mechanism of prismatic slip in magnesium single crystals, Transactions of the Metallurgical Society of AIME 221 (1961) 1148–1154.

[66] R. E. Reedhill, W. D. Robertson, Deformation of magnesium single crystals by nonbasal slip, Transactions of the American Institute of Mining and Metallurgical Engineers 209 (1957) 496–502.

[67] S. R. Agnew, M. H. Yoo, C. N. Tome, Application of texture simulation to understanding mechanical behavior of Mg and solid solution alloys containing Li or Y, Acta Materialia 49 (2001) 4277–4289.

[68] M. H. Yoo, J. R. Morris, K. M. Ho, S. R. Agnew, Nonbasal deformation modes of HCP metals and alloys: Role of dislocation source and mobility, Metallurgical and Materials Transactions A: Physical Metallurgy and Materials Science 33 (2002) 813–822.

[69] T. Obara, H. Yoshinga, S. Morozumi, $\{11\bar{2}2\}< 1123 >$ slip system in magnesium, Acta Metallurgica 21 (1973) 845–853.

[70] S. R. Agnew, O. Duygulu, A mechanistic understanding of the formability of magnesium: Examining the role of temperature on the deformation mechanisms, Vol. 419, 2003, pp. 177–188.

[71] Z. Zhang, P. Cizek, M. Barnett, A critical test of twin-induced softening in a magnesium alloy extruded to a strain of 0.7 at room temperature, Scripta Materialia 67 (2012) 1015–1018.

[72] A. Khosravani, J. Scott, M. P. Miles, D. Fullwood, B. L. Adams, R. K. Mishra, Twinning in magnesium alloy AZ31B under different strain paths at moderately elevated temperatures, International Journal of Plasticity 45 (2013) 160–173.

[73] R. Hill, A theory of yielding and plastic flow of anisotropic solids, Proceedings of the Royal Society of London A 193 (1948) 281–297.

[74] A. P. Karafillis, M. C. Boyce, A general anisotropic yield criterion using bounds and a transformation weighting tensor, Journal of the Mechanics and Physics of Solids 41 (1993) 1859–1886.

[75] A. A. Benzerga, J. Besson, Plastic potentials for anisotropic porous solids, European Journal of Mechanics 20A (2001) 397–434.

[76] J. P. Boehler, Applications of Tensor Functions in Solid Mechanics, Springer, Wien, 1987.

[77] W. F. Hosford, The Mechanics of Crystals and Textured Polycrystals, Oxford University Press, Oxford, 1993.

[78] V. Vitek, M. Mrovec, J. L. Bassani, Influence of non-glide stresses on plastic flow: From atomistic to continuum modeling, Materials Science and Engineering:A 365 (2004) 31–37.

[79] S. M. Keralavarma, A. A. Benzerga, A constitutive model for plastically anisotropic solids with non-spherical voids, Journal of the Mechanics and Physics of Solids 58 (2010) 874–901.

[80] O. Cazacu, B. Plunkett, F. Barlat, Orthotropic yield criterion for hexagonal closed packed metals, International Journal of Plasticity 22 (2006) 1171–1194.

[81] R. Gehrmann, M. M. Frommert, G. Gottstein, Texture effects on plastic deformation of magnesium, Materials Science and Engineering:A 395 (2005) 338–349.

[82] N. Stanford, M. R. Barnett, Solute strengthening of prismatic slip, basal slip and $\{10\bar{1}2\}$ twinning in Mg and Mg-Zn binary alloys, International Journal of Plasticity 47 (2013) 165–181.

[83] J. D. Robson, N. Stanford, M. R. Barnett, Effect of precipitate shape and habit on mechanical asymmetry in magnesium alloys, Materials Science and Engineering:A 44 (2013) 2984–2995.

[84] S. R. Agnew, R. P. Mulay, F. J. Polesak, III, C. A. Calhoun, J. J. Bhattacharyya, B. Clausen, In situ neutron diffraction and polycrystal plasticity modeling of a Mg-Y-Nd-Zr alloy: Effects of precipitation on individual deformation mechanisms, Acta Materialia 61 (2013) 3769–3780.

[85] J. D. Robson, N. Stanford, M. R. Barnett, Effect of precipitate shape on slip and twinning in magnesium alloys, Acta Materialia 59 (2011) 1945–1956.

[86] Z. Leng, J. Zhang, J. Sun, H. Shi, S. Liu, L. Zhang, M. Zhang, R. Wu, Notch tensile behavior of extruded Mg-Y-Zn alloys containing long period stacking ordered phase, Materials & Design 600 (2014) 495–499.

[87] N. Kumar, N. Dendge, R. Banerjee, R. S. Mishra, Effect of microstructure on the uniaxial tensile deformation behavior of Mg-4Y-3RE alloy, Materials Science and Engineering:A 590 (2014) 116–131.

[88] S. Sandloebes, S. Zaefferer, I. Schestakow, S. Yi, R. Gonzalez-Martinez, On the role of non-basal deformation mechanisms for the ductility of Mg and Mg-Y alloys, Acta Materialia 59 (2011) 429–439.

[89] J. J. Jonas, S. Mu, T. Al-Samman, G. Gottstein, L. Jiang, E. Martin, The role of strain accommodation during the variant selection of primary twins in magnesium, Acta Materialia 59 (2011) 2046–2056.

[90] A. L. Gurson, Continuum theory of ductile rupture by void nucleation and growth: Part I – yield criteria and flow rules for porous ductile media, Journal of Engineering Materials and Technology 99 (1977) 2–15.

[91] V. Tvergaard, A. Needleman, Analysis of the cup–cone fracture in a round tensile bar, Acta Metallurgica 32 (1984) 157–169.

[92] M. Gologanu, J.-B. Leblond, G. Perrin, J. Devaux, Recent extensions of Gurson's model for porous ductile metals. Part I: Gurson-like models incorporating the influence of void shape, in: P. Suquet (Ed.), Continuum Micromechanics, Springer, Verlag, 1995, pp. 61–97.

[93] A. Benzerga, J.-B. Leblond, Effective yield criterion accounting for microvoid coalescence, Journal of Applied Mechanics 81 (2014) 1–7.

[94] A. S. Argon, J. Im, Separation of second phase particles in spheroidized 1045 steel, Cu-0.6pct Cr alloy, and maraging steel in plastic straining, Metallurgical Transactions 6 (1975) 839–851.

[95] F. M. Beremin, Cavity formation from inclusions in ductile fracture, Metallurgical Transactions 12A (1981) 723–731.

[96] G. Le Roy, J. D. Embury, G. Edward, M. F. Ashby, A model of ductile fracture based on the nucleation and growth of voids, Acta Metallurgica 29 (1981) 1509–1522.

[97] L. Babout, Y. Brechet, E. Maire, R. Fougres, On the competition between particle fracture and particle decohesion in metal matrix composites, Acta Materialia 52 (2004) 4517–4525.

[98] M. N. Shabrov, E. Sylven, S. Kim, D. H. Sherman, L. Chuzhoy, C. L. Briant, A. Needleman, Void nucleation by inclusion cracking, Metallurgical and Materials Transactions A. 35A (2004) 1745–1755.

[99] T. Pardoen, I. Doghri, F. Delannay, Experimental and numerical comparison of void growth models and void coalescence criteria for the prediction of ductile fracture in copper bars, Acta Materialia 46 (1998) 541–552.

[100] R. D. Thomson, J. W. Hancock, Local stress and strain fields near a spherical elastic inclusion in a plastically deforming matrix, International Journal of Fracture 24 (1984) 209–228.

[101] A. Needleman, A continuum model for void nucleation by inclusion debonding, Journal of Applied Mechanics 54 (1987) 525.

[102] M. N. Shabrov, A. Needleman, An analysis of inclusion morphology effects on void nucleation, Modelling and Simulation in Materials Science and Engineering 10 (2002) 163–183.

[103] K. Siruguet, J.-B. Leblond, Effect of void locking by inclusions upon the plastic behavior of porous ductile solids–I: Theoretical modeling and numerical study of void growth, International Journal of Plasticity 20 (2004) 225–254.

[104] N. A. Fleck, J. W. Hutchinson, V. Tvergaard, Softening by void nucleation and growth in tension and shear, Journal of the Mechanics and Physics of Solids 37 (1989) 515–540.

[105] P. F. Thomason, Ductile Fracture of Metals, Pergamon Press, Oxford, 1990.

[106] B. Marini, F. Mudry, A. Pineau, Experimental study of cavity growth in ductile rupture, Engineering Fracture Mechanics 22 (1985) 989–996.

[107] F. A. McClintock, A criterion for ductile fracture by the growth of holes, Journal of Applied Mechanics 35 (1968) 363–371.

[108] J. R. Rice, D. M. Tracey, On the enlargement of voids in triaxial stress fields, Journal of the Mechanics and Physics of Solids 17 (1969) 201–217.

[109] V. Tvergaard, Influence of voids on shear band instabilities under plane strain conditions, International Journal of Fracture 17 (1981) 389–407.

[110] V. Tvergaard, On localization in ductile materials containing spherical voids, International Journal of Fracture 18 (1982) 237–252.

[111] M. Gologanu, J.-B. Leblond, J. Devaux, Approximate models for ductile metals containing non-spherical voids – case of axisymmetric prolate ellipsoidal cavities, Journal of the Mechanics and Physics of Solids 41 (11) (1993) 1723–1754.

[112] M. Gologanu, J.-B. Leblond, J. Devaux, Approximate models for ductile metals containing non–spherical voids — case of axisymmetric oblate ellipsoidal cavities, Journal of Engineering Materials and Technology 116 (1994) 290–297.

[113] G. Rousselier, Ductile fracture models and their potential in local approach of fracture, Nuclear Engineering and Design 105 (1987) 97–111.

[114] A. Needleman, Void growth in an elastic–plastic medium, Journal of Applied Mechanics 39 (1972) 964–970.

[115] J. Koplik, A. Needleman, Void growth and coalescence in porous plastic solids, International Journal of Solids and Structures 24 (8) (1988) 835–853.

[116] P. F. Thomason, A theory for ductile fracture by internal necking of cavities, Journal of the Institute of Metals 96 (1968) 360–376.

[117] P. F. Thomason, Three–dimensional models for the plastic limit–loads at incipient failure of the intervoid matrix in ductile porous solids, Acta Metallurgica 33 (1985) 1079–1085.

[118] A. A. Benzerga, J. Besson, A. Pineau, Coalescence–controlled anisotropic ductile fracture, Journal of Engineering Materials and Technology 121 (1999) 221–229.

[119] Magnesium Elektron Ltd, Elektron AZ31B sheet, plate & coil, URL: http://www.magnesium-elektron.com/data/downloads/DS482.pdf, Magnesium Elektron Ltd, Swinton, England, Accessed: 09/15/2014 (2006).

[120] R. T. DeHoff, Measurement of number and average size in volume, in: R. T. DeHoff, F. N. Rhines (Eds.), Quantitative Microscopy, McGraw-Hill, New York, 1968, pp. 128–148.

[121] A. A. Benzerga, J. Besson, A. Pineau, Anisotropic ductile fracture. Part I: Experiments, Acta Materialia 52 (2004) 4623–4638.

[122] A. A. Benzerga, J. Besson, A. Pineau, Anisotropic ductile fracture. Part II: Theory, Acta Materialia 52 (2004) 4639–4650.

[123] A. A. Benzerga, J.-B. Leblond, Ductile fracture by void growth to coalescence, Advances in Applied Mechanics 44 (2010) 169–305.

[124] A. Hosokawa, D. S. Wilkinson, J. Kang, E. Maire, Onset of void coalescence in uniaxial tension studied by continuous X-ray tomography, Acta Materialia 61 (2013) 1021–1036.

[125] D. Steglich, T. F. Morgeneyer, Failure of magnesium sheets under monotonic loading: 3D examination of fracture mode and mechanisms, International Journal of Fracture 183 (2013) 105–112.

[126] T. Laser, M. R. Nurnberg, A. Janz, C. Hartig, D. Letzig, R. Schmid-Fetzer, R. Bormann, The influence of manganese on the microstructure and mechanical properties of AZ31 gravity die cast alloys, Acta Materialia 54 (2006) 3033–3041.

[127] R. Xin, B. Song, K. Zeng, G. Huang, Q. Liu, Effect of aging precipitation on mechanical anisotropy of an extruded Mg-Y-Nd alloy, Materials & Design 34 (2012) 384–388.

[128] K. Hantzsche, J. Bohlen, J. Wendt, K. U. Kainer, S. B. Yi, D. Letzig, Effect of rare earth additions on microstructure and texture development of magnesium alloy sheets, Scripta Materialia 63 (2010) 725–730.

[129] J. Grobner, R. Schmid-Fetzer, Thermodynamic modeling of the Mg-Ce-Gd-Y system, Scripta Materialia 63 (2010) 674–679.

[130] F. G. Meng, J. Wang, H. S. Liu, L. B. Liu, Z. P. Jin, Experimental investigation and thermodynamic calculation of phase relations in the Mg-Nd-Y ternary system, Materials Science and Engineering:A 454-455 (2007) 266–273.

[131] A. Kielbus, M. Stopyra, R. Jarosz, Influence of sand-casting parameters on microstructure and properties of magnesium alloys, Archives of Metallurgy and Materials 58 (2013) 635–640.

[132] I.-B. Kim, J.-Y. Hong, B.-G. Hong, K.-H. Kim, Precipitation behavior of Mg-Y-Nd-Zr alloy, Materials Science Forum 449-452 (2004) 649–652.

[133] S. Basu, A. A. Benzerga, On the path-dependence of the fracture locus in ductile materials – experiments, unpublished data (2013).

[134] Y. B. Chun, C. H. J. Davies, Negative lateral strain ratio induced by deformation twinning in magnesium alloy AZ31, Materials Science and Engineering:A 528 (2011) 4941–4946.

[135] A. Pineau, Development of the local approach to fracture over the past 25 years: Theory and applications, International Journal of Fracture 138 (2006) 139–166.

[136] H. Watanabe, Effect of second-phase precipitates on local elongation in extruded magnesium alloys, Journal of Materials Engineering and Performance 22 (2013) 1–5.

[137] K. Hazeli, H. Askari, J. Cuadra, F. Streller, R. Carpick, H. Zbib, A. Kontsos, Microstructure-sensitive investigation of magnesium alloy fatigue, International Journal of Plasticity 68 (2015) 55–76.

[138] T. Pardoen, J. W. Hutchinson, Micromechanics-based model for trends in toughness of ductile metals, Acta Materialia 51 (2003) 133–148.

[139] F. Dominique, A. Pineau, A. Zaoui, Mechanical Behaviour of Materials: Volume II: Fracture Mechanics and Damage (Solid Mechanics and its Applications), Solid Mechanics and its Applications (Book 191), Butterworth-Heinemann, Oxford, 2013.

[140] M. E. Torki, A. A. Benzerga, J.-B. Leblond, On void coalescence under combined tension and shear, Journal of Applied Mechanics Submitted.

[141] X. Chen, D. Shang, R. Xiao, G. Huang, Q. Liu, Influence of rolling ways on microstructure and anisotropy of AZ31 alloy sheet, Transactions of Nonferrous Metals Society of China S 20 (2010) 589–593.

[142] J. W. Hutchinson, A. G. Evans, Mechanics of materials: Top-down approaches to fracture, Acta Materialia 48 (2000) 125–135.

[143] J. Wang, I. J. Beyerlein, J. P. Hirth, Nucleation of elementary $\{\bar{1}011\}$ $\{\bar{1}013\}$ twinning dislocations at a twin boundary in hexagonal close-packed crystals, Modelling and Simulation in Materials Science and Engineering 20 (2012) 024001.

[144] S. M. Keralavarma, A. A. Benzerga, An approximate yield criterion for anisotropic porous media, Comptes Rendus Mecanique 336 (2008) 685–692.

[145] M. Kailasam, P. Ponte Castaneda, A general constitutive theory for linear and nonlinear particulate media with microstructure evolution, Journal of the Mechanics and Physics of Solids 46 (3) (1998) 427–465.

[146] T. Pardoen, J. W. Hutchinson, An extended model for void growth and coalescence, Journal of the Mechanics and Physics of Solids 48 (2000) 2467–2512.

[147] A. A. Benzerga, Micromechanics of coalescence in ductile fracture, Journal of the Mechanics and Physics of Solids 50 (2002) 1331–1362.

[148] K. Siruguet, J.-B. Leblond, Effect of void locking by inclusions upon the plastic behavior of porous ductile solids–part II: Theoretical modeling and numerical study of void coalescence, International Journal of Plasticity 20 (2004) 255–268.

[149] J. Segurado, J. Llorca, An analysis of the size effect on void growth in single crystals using discrete dislocation dynamics, Acta Materialia 57 (2009) 1427–1436.

[150] B. Liu, X. Qiu, Y. Huang, K. C. Hwang, M. Li, C. Liu, The size effect on void growth in ductile materials, Journal of the Mechanics and Physics of Solids 51 (2003) 1171–1187.

[151] B. Liu, Y. Huang, M. Li, K. C. Hwang, C. Liu, A study of the void size effect based on the taylor dislocation model, International Journal of Plasticity 21 (2005) 2107–2122.

APPENDIX I

SECONDARY CRACKS ON THE OUTER SURFACE OF AZ31 SPECIMENS

(a)

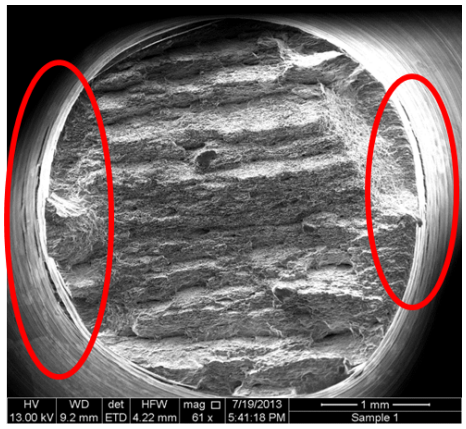

(b)

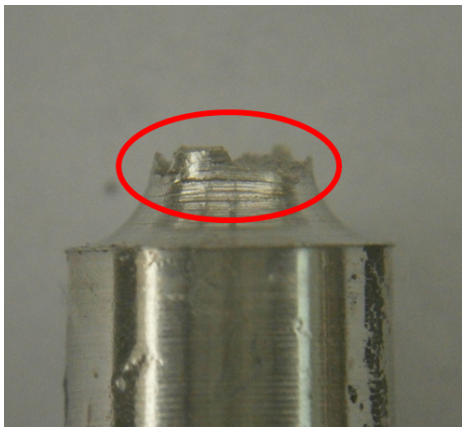

Figure 99: (a) Top- and (b) side-view of the fracture surface of an AZ31-RN10 notched bars showing the presence of secondary cracks on the outer surface, below and above the main crack.

APPENDIX II

CRACK PROPAGATION IN AZ31 UNIAXIAL BARS

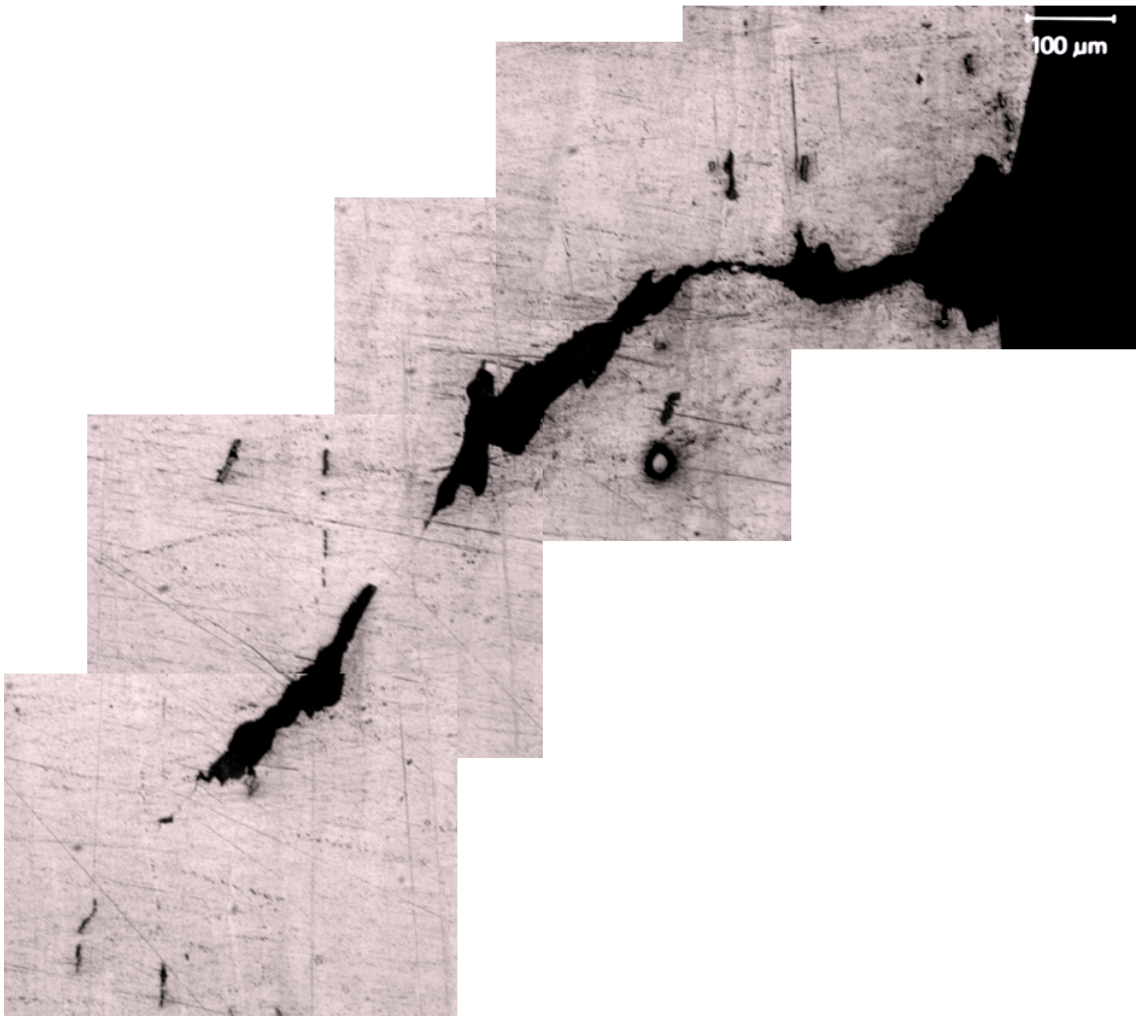

Figure 100: Side-view of a macroscopic after crack initiation and before final failure.

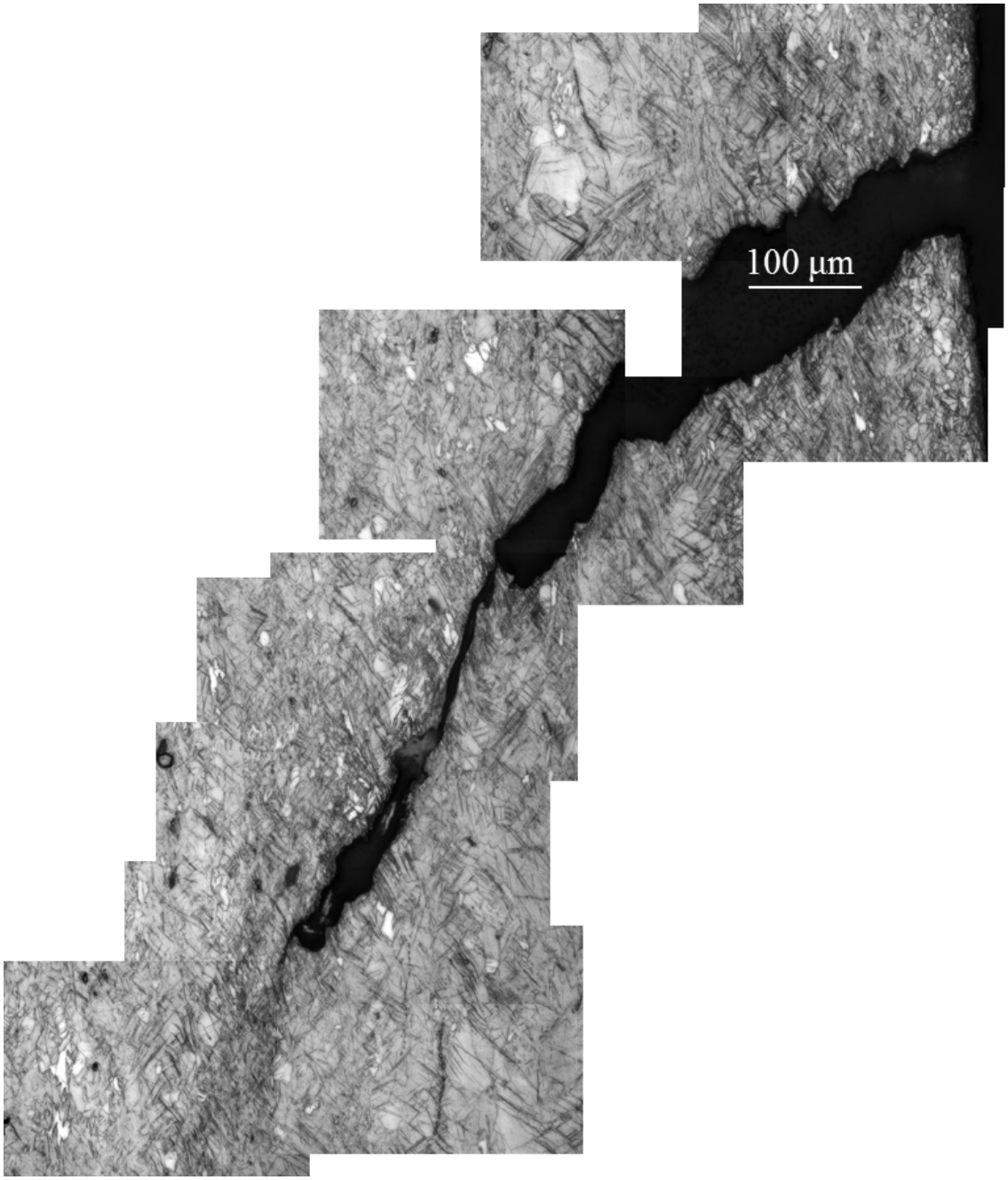

Figure 101: Side-view of a macroscopic after crack initiation and before final failure.

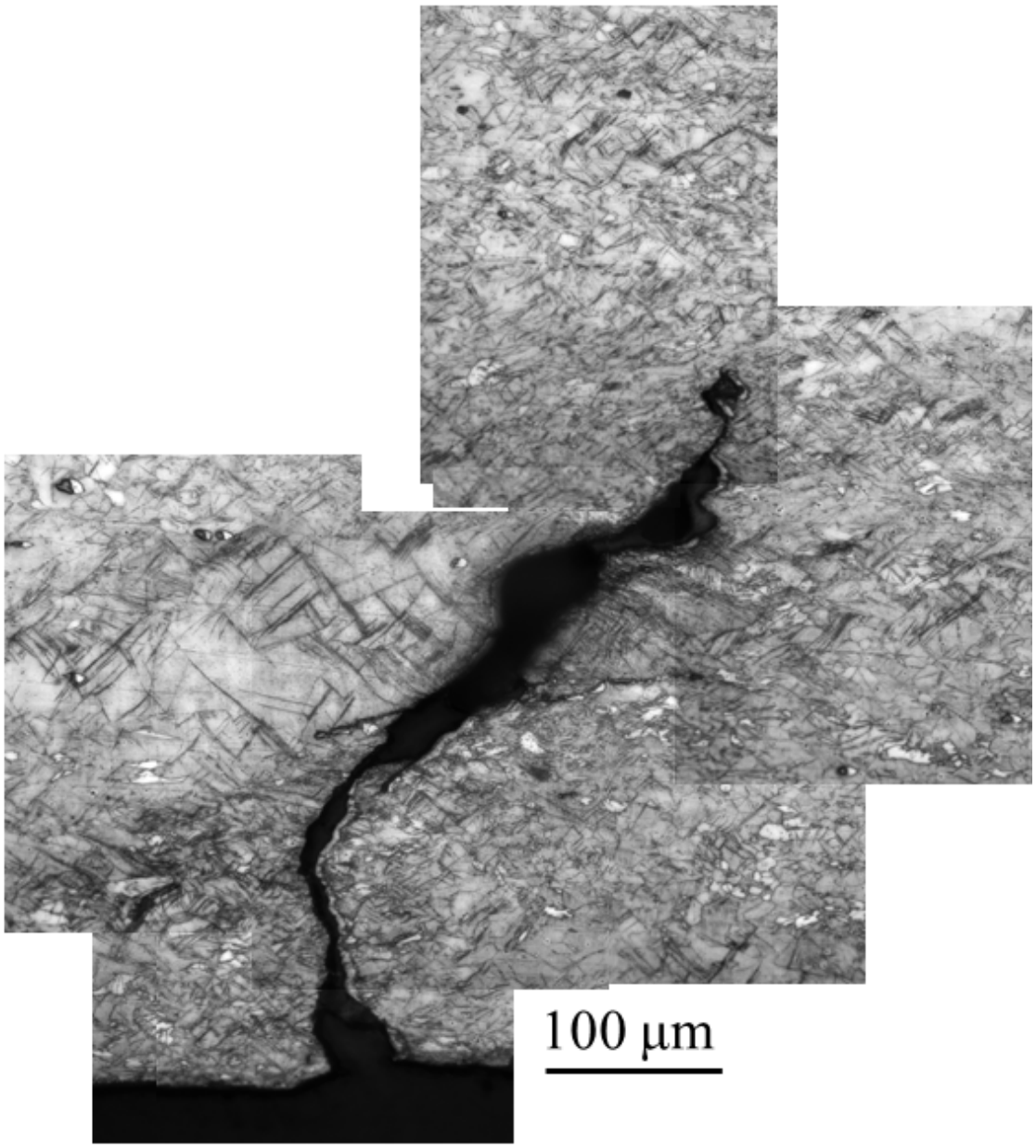

Figure 102: Side-view of a macroscopic after crack initiation and before final failure.

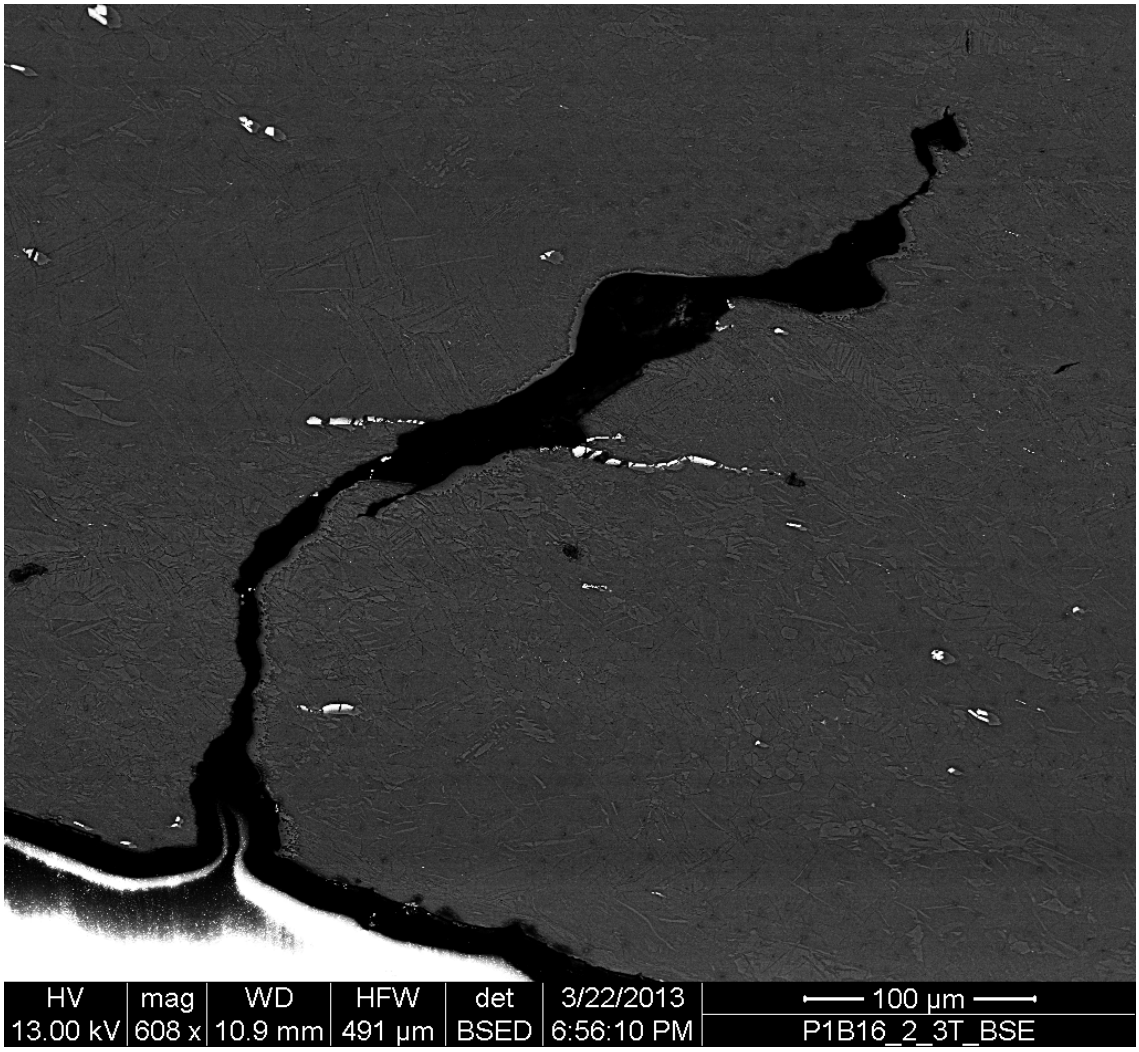

Figure 103: Side-view of a macroscopic after crack initiation and before final failure.

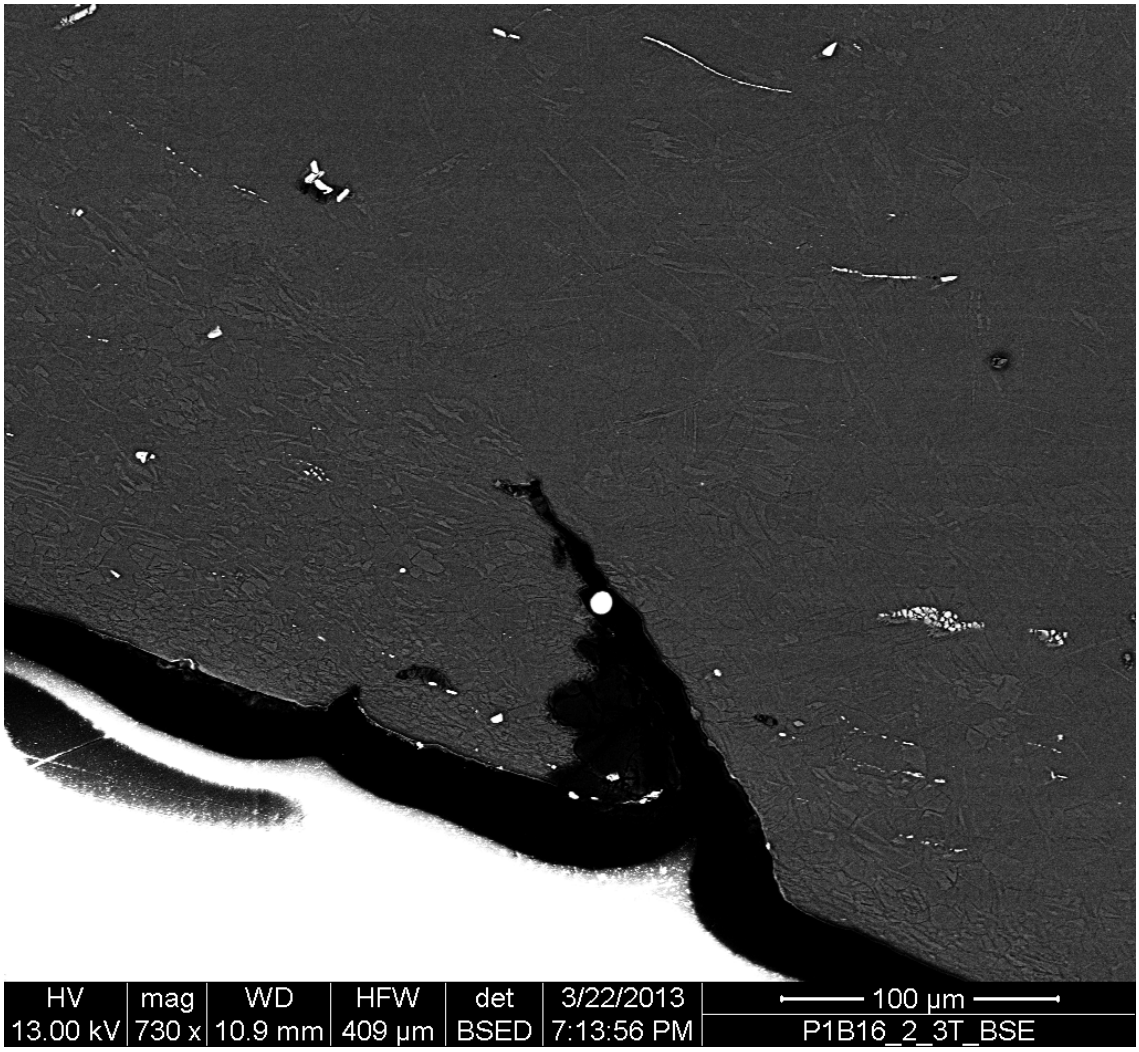

Figure 104: Side-view of a macroscopic after crack initiation and before final failure.

APPENDIX III

PARAMETERS OF THE VOID GROWTH MODEL

There are six parameters which depend on the microstructural variables f and w and on the anisotropy tensor $\mathbb{h}$: C, g, κ, η and α_2, listed by order of appearance in criterion (9.2) and α_1, which appears in the evolution law of W.

$$g = 0 \quad \text{(p)}; \qquad g = \frac{e_2^3}{\sqrt{1-e_2^2}} = f\frac{e_1^3}{\sqrt{1-e_1^2}} = f\frac{(1-w^2)^{\frac{3}{2}}}{w} \quad \text{(o)} \tag{10.1}$$

We recall that e_1 and e_2 are the eccentricities of the void and the outer boundary of the RVE, respectively. Both are implicit functions of f and w. Next, the full expression of κ was provided by [79] but can be simplified into:

$$\kappa = \begin{cases} \dfrac{3}{h}\left\{1 + \dfrac{h_{\mathrm{t}}}{h^2 \ln f} \ln \dfrac{1-e_2^2}{1-e_1^2}\right\}^{-1/2} & \text{(p)} \\ \dfrac{3}{h}\left\{1 + \dfrac{(g_f - g_1) + \frac{4}{5}(g_f^{5/2} - g_1^{5/2}) - \frac{3}{5}(g_f^5 - g_1^5)}{\ln(g_f/g_1)}\right\}^{-1} & \text{(o)} \end{cases} \tag{10.2}$$

where shorthand notations are used for:

$$g_f \equiv \frac{g}{g+f}, \quad g_1 \equiv \frac{g}{g+1}$$

$$\alpha_2 = \begin{cases} \dfrac{(1+e_2^2)}{(1+e_2^2)^2 + 2(1-e_2^2)} & \text{(p)} \\ \dfrac{(1-e_2^2)(1-2e_2^2)}{(1-2e_2^2)^2 + 2(1-e_2^2)} & \text{(o)} \end{cases} \tag{10.3}$$

$$\eta = -\frac{2}{3h_{\rm q}}\frac{\kappa Q^*(g+1)(g+f){\rm sh}}{(g+1)^2+(g+f)^2+(g+1)(g+f)[\kappa H^*{\rm sh}-2{\rm ch}]},$$
$$C = -\frac{2}{3}\frac{\kappa(g+1)(g+f){\rm sh}}{(Q^*+\frac{3}{2}h_{\rm q}\eta H^*)\eta}, \quad {\rm sh}\equiv\sinh(\kappa H^*), \quad {\rm ch}\equiv\cosh(\kappa H^*) \tag{10.4}$$

where $H^* \equiv 2\sqrt{h_{\rm q}}(\alpha_1-\alpha_2)$ and $Q^* \equiv \sqrt{h_{\rm q}}(1-f)$.

$$\alpha_1 = \begin{cases} \left[e_1-(1-e_1^2)\tanh^{-1}e_1\right]/(2e_1^3) & \text{(p)} \\ \left[-e_1(1-e_1^2)+\sqrt{1-e_1^2}\sin^{-1}e_1\right]/(2e_1^3) & \text{(o)} \end{cases} \tag{10.5}$$

Note that the expressions of α_2 and α_1 are identical to those given by [92] for isotropic matrices. The dependence of the criterion parameters upon anisotropy tensor $\mathbb{h}$ enters through one invariant, h, and two transversely isotropic invariants, $h_{\rm t}$ and $h_{\rm q}$, of that tensor. When expressed in the basis associated with the principal directions of orthotropy*, invariant h is given by (9.19) while $h_{\rm t}$ and $h_{\rm q}$ are given by:

$$h_{\rm t} = \frac{1}{5}\left[-\frac{13}{12}(\hat{h}_{\rm L}+\hat{h}_{\rm T})+\frac{8}{3}\hat{h}_{\rm S}+4(\hat{h}_{\rm TS}+\hat{h}_{\rm SL})-\frac{7}{2}\hat{h}_{\rm LT}\right] \tag{10.6}$$

and

$$h_{\rm q} \equiv \frac{2}{3}\mathbf{Q}:\hat{\mathbb{h}}:\mathbf{Q} \tag{10.7}$$

Here, the $\hat{h}_i$ are the components of $\hat{\mathbb{h}}$ expressed using Voigt's condensation and $\hat{\mathbb{h}}$ is formal inverse of $\mathbb{h}$. $h_{\rm q}$ only appears in the expressions of C and η (it was denoted $\hat{h}_q$ in [79]).

*In the context of this section, this means replacing indices 1 to 6 in (9.19) with L, T, S, TS, SL and LT, respectively.